

# Hydration and thermal decomposition of cement/calcium sulphate based materials

A.C.J. de Korte

/ Department of the Built Environment

**bouwstenen 201**



HYDRATION AND THERMAL  
DECOMPOSITION OF  
CEMENT/CALCIUM-SULPHATE  
BASED MATERIALS

De promotiecommissie is als volgt samengesteld:

Voorzitter: prof.ir. E.S.M. Nelissen  
1<sup>e</sup> Promotor: prof.dr.ir. H.J.H. Brouwers  
Co-promotor: prof.dr.ir. J.A.M. Kuipers  
leden: Prof.Dr. H-U. Hummel  
(Friedrich-Alexander-Universität Erlangen-Nürnberg)  
prof.dr.ir. J.J.N. Lichtenberg  
prof.dr. A.P. Philipse (Universiteit Utrecht)  
prof.dr. S. Torquato (Princeton University)  
adviseur dr.ir. G.J.L. van der Wegen (SGS Intron)

CIP-DATA LIBRARY TECHNISCHE UNIVERSITEIT EINDHOVEN

Hydration and thermal decomposition of cement/calcium sulphate based materials / by  
A.C.J. de Korte

A catalogue record is available from the Eindhoven University of Technology Library

ISBN: 978-90-386-3862-1

Bouwstenen 201

NUR 955

Copyright 2015 by Ariën de Korte

Cover design: Ariën de Korte

Printed by: Proefschriftmaken.nl || Uitgeverij BOXPress

Published by: Uitgeverij BOXPress, 's-Hertogenbosch

All rights reserved. No part of this publication may be reproduced, stored in a retrieval system or transmitted by any means, electronic, mechanical, photocopying, recording or otherwise without the prior written permission of the author.

Typeset with the L<sup>A</sup>T<sub>E</sub>X Documentation System.

Author email: [a.c.j.dekorte@gmail.com](mailto:a.c.j.dekorte@gmail.com)

# HYDRATION AND THERMAL DECOMPOSITION OF CEMENT/CALCIUM-SULPHATE BASED MATERIALS

PROEFSCHRIFT

ter verkrijging van de graad van doctor  
aan de Technische Universiteit Eindhoven,  
op gezag van de rector magnificus prof.dr.ir. F.P.T. Baaijens,  
voor een commissie aangewezen door het College voor Promoties,  
in het openbaar te verdedigen op donderdag 8 juni 2015 om 14:00 uur

door

Arie Cornelis Johannis De Korte

geboren te Wageningen

Dit proefschrift is goedgekeurd door de promotor en de samenstelling van de promotiecommissie is als volgt:

Voorzitter: prof.ir. E.S.M. Nelissen  
1<sup>e</sup> Promotor: prof.dr.ir. H.J.H. Brouwers  
Co-promotor: prof.dr.ir. J.A.M. Kuipers  
leden: Prof.Dr. H-U. Hummel  
(Friedrich-Alexander-Universität Erlangen-Nürnberg)  
prof.dr.ir. J.J.N. Lichtenberg  
prof.dr. A.P. Philipse (Universiteit Utrecht)  
prof.dr. S. Torquato (Princeton University)  
adviseur dr.ir. G.J.L. van der Wegen (SGS Intron)

## Preface

*It all happened in the summer of 2006.* This could have been the start of a fairy tale, but in fact it is the start of preface of PhD-thesis. I am deviating from the story, I wanted to tell. In the summer of 2006, I was working on my master-thesis, actually my graduation project for becoming a 'ingenieur'(/engineer), when Professor Jos Brouwers asked me if I would be interesting in doing a PhD with him. He was at that time busy to get a new European-funded project started. I want to thank Jos for asking me to become a PhD and for your guidance of my research in the last ten years.

The project was an 6<sup>th</sup> FP Integrated European project, named "Integrated Safe and Smart Building concept" (ISSB, Proposal No. 026661-2). It focused on the improvement of gypsum plasterboards, especially on the improvement of the fire behaviour of such boards. The projects contained of two PhD's in Twente and 22 research partners in ten European countries. I would focus on the computer modelling of hydration and fire behaviour of gypsum-based materials and Jeffrey Bakker would improve the gypsum mixtures with the help of experiments. After Jeffrey unfortunately stopped, Qingliang Yu replaced him a year after I started. Together we visited several project meetings and conferences and we had several discussions on work, private matters and differences between Europa and China. Also after his move to Eindhoven, the discussions remained. Dr. Qingliang Yu thank you for our discussions and support in the last seven years.

I would also like to thank the members of my PhD defence committee - Prof. Dr. ir. J.A.M. Kuipers, Prof. Dr. H-U. Hummel, Prof. Dr. ir. J.J.N. Lichtenberg, Prof. Dr. A.P. Philipse, Prof. Dr. S. Torquato and Dr. Ir. G.J.L. van der Wegen - for accepting and reviewing this PhD thesis.

To my fellow-PhD's during the six years in Twente (Arjen, Frederick, Jimmy, Jeroen, Marlijn, Ronald, Frank, Stefan, Anneloes, Tijs, Jasper, Carissa, Wei, Ibsen, Hendrik, Bram, Tatsiana, Mieke, Erwin, Marieke, Götz, Martin, Inge, Albertus, Julieta, Jeroen, Wytse, Seirgei, Jochem, Léon, John, Maartje, Maarten, Daan, Chris, Marnix, Alexander, Bas, Julia and Vedran) thank you for your support during especially the last two years in Twente. My collega's in Eindhoven (Qingliang, Przemyslaw, Miruna, Alberto, George, Azee, Perry, Chris, Guillaume, Pei, Veronika, Stéphan Rui, Bo, Xu, Katrin and Katerina) thank you for the warm welcome every time I visited Eindhoven.

Besides work, relaxation is very important. One of the ways to do this, I have found in the electronic timekeeping during swimming meetings. Ed, Berry, Kees-Jan, Hans, Chris, Bas, Johan and Maike thank you that I may assist you during these swim meetings from World championships and National championships to the lowest level swim meets and making these swim meets a success and more important, let me enjoy the weekends.

Maike, although you may not like this, you deserve your own paragraph, since you are not just only be a team member at the electronic timekeeping, but you become much more in the last couple of years. Without your support and your ability to relativate,

I would not have survived the last three year. Gerrit, Ursula and Sanne thank you for accepting me into the family.

Hans thank you for joining me from the summer of 2007 in Enschede, introducing to the swimming club in Enschede and all dinners together. The last of words of thanks are to my parents. Without your support, I would not made it to the highest level of education.

Oss, 1 February 2015

*Ariën de Korte*

# Contents

<b>1</b>	<b>Introduction</b>	<b>1</b>
1.1	Cement . . . . .	1
1.2	Calcium sulphates . . . . .	4
1.3	World market of calcium sulphates and cements . . . . .	9
1.4	Missing Knowledge . . . . .	9
1.5	Cellular automata . . . . .	13
1.6	CEMHYD3D: a 3D computer-based hydration model . . . . .	14
1.7	The research approach . . . . .	20
1.8	Outline of this thesis . . . . .	23
<b>2</b>	<b>Packing of digitized particles</b>	<b>25</b>
2.1	Introduction . . . . .	25
2.2	Packing Theory . . . . .	25
2.2.1	Regular packing . . . . .	26
2.2.2	Irregular/random packing . . . . .	27
2.3	Methods for characterising packings . . . . .	29
2.3.1	Contact number / coordination number . . . . .	30
2.3.2	Radial distance function . . . . .	30
2.3.3	Bond orientation order . . . . .	31
2.3.4	Translational order metric . . . . .	32
2.3.5	Particle shape . . . . .	32
2.4	Simulations . . . . .	35
2.4.1	Digitized particles . . . . .	35
2.4.2	Regular packing with digitized particles . . . . .	35
2.4.3	Random packing results . . . . .	42
2.5	Conclusions . . . . .	52
<b>3</b>	<b>Reaction kinetics</b>	<b>59</b>
3.1	Introduction . . . . .	59
3.2	Chemical reaction kinetics . . . . .	60
3.2.1	Transition point . . . . .	61
3.2.2	Chemical reaction controlled . . . . .	64
3.2.3	Diffusion controlled . . . . .	65
3.2.4	Hybrid model . . . . .	67
3.3	Simulation results and analysis . . . . .	69
3.3.1	Shrinking particle size case . . . . .	69
3.3.2	Constant particle size case . . . . .	74

3.3.3	Varying particle size case . . . . .	74
3.4	Coupling cellular automata and reaction kinetics . . . . .	74
3.4.1	Shrinking core case . . . . .	74
3.4.2	Constant and varying particle size case . . . . .	79
3.5	Conclusions . . . . .	83
<b>4</b>	<b>Multi-cycle and multi-scale modelling</b>	<b>85</b>
4.1	Introduction . . . . .	85
4.2	Multi-cycle modelling . . . . .	85
4.2.1	Dissolution . . . . .	86
4.2.2	Diffusion . . . . .	86
4.2.3	Nucleation . . . . .	87
4.2.4	Cycles correction . . . . .	87
4.3	Multi-scale modelling . . . . .	88
4.3.1	Modification of the hydration system . . . . .	88
4.3.2	Diffusion layer . . . . .	90
4.3.3	Combined multi-scale and multi-cycle modelling . . . . .	91
4.4	Simulation results . . . . .	93
4.4.1	Multi-cycle . . . . .	93
4.4.2	Multi-scale by voxel splitting . . . . .	93
4.4.3	Muli-scale by particle rescaling . . . . .	96
4.4.4	Combined multi-cycle and multi-scale . . . . .	99
4.5	Conclusions . . . . .	100
<b>5</b>	<b>Ultrasonic sound speed analysis</b>	<b>101</b>
5.1	Introduction . . . . .	101
5.2	Sound velocity of materials . . . . .	101
5.2.1	Introduction . . . . .	103
5.2.2	Sound velocity of a slurry . . . . .	103
5.2.3	Sound velocity of porous solid . . . . .	104
5.3	Theory hydration of calcium sulphates . . . . .	107
5.3.1	Dissolution . . . . .	108
5.3.2	Diffusion . . . . .	109
5.3.3	Crystallization . . . . .	109
5.3.4	Induction time . . . . .	111
5.4	Paste model for hydrating hemihydrate . . . . .	113
5.5	Hydration models . . . . .	114
5.5.1	Relation between hydration degree and sound velocity . . . . .	114
5.5.2	Relation between hydration degree and time . . . . .	115
5.6	Experiments . . . . .	116
5.6.1	Materials . . . . .	116
5.6.2	Measurements . . . . .	117
5.7	Applying the volumetric models to sound velocity measurements . . . . .	118
5.7.1	Sound velocity through a slurry . . . . .	118
5.7.2	Sound velocity of solid: bulk-modulus based approach . . . . .	121
5.7.3	Sound velocity of solid: non-porous velocity based approach . . . . .	122

5.7.4	Conclusions . . . . .	122
5.8	Analysis of measurements using the hydration model . . . . .	122
5.8.1	Analysis . . . . .	122
5.8.2	Conclusions . . . . .	125
5.9	Alternative point of view . . . . .	125
5.10	Conclusions . . . . .	127
<b>6</b>	<b>Thermal conductivity of gypsum exposed to fire</b>	<b>129</b>
6.1	Introduction . . . . .	129
6.2	Thermodynamic system . . . . .	131
6.3	Calculation of properties . . . . .	132
6.4	Thermal conductivity of two phase systems . . . . .	134
6.5	Theory versus experimental data . . . . .	141
6.6	Three phase system . . . . .	145
6.7	Application to thermal conductivity at elevated temperature . . . . .	150
6.7.1	Decomposition reactions . . . . .	150
6.7.2	Model compared to experimental data. . . . .	155
6.7.3	Influence composition and moisture content . . . . .	155
6.8	Summary/Conclusion . . . . .	160
<b>7</b>	<b>Stabilization/solidification</b>	<b>161</b>
7.1	Introduction . . . . .	161
7.2	Materials and methods . . . . .	166
7.2.1	Materials . . . . .	166
7.2.2	Test methods . . . . .	167
7.3	Previous research . . . . .	170
7.3.1	The use of (contaminated) soil for the production concrete blocks .	171
7.3.2	The influence of contaminants on immobilisation . . . . .	172
7.3.3	Possible binder combinations . . . . .	172
7.3.4	Required binder amount . . . . .	173
7.3.5	The composition of the binder . . . . .	175
7.4	Exploratory tests . . . . .	176
7.5	Mortar experiments . . . . .	179
7.5.1	Water demand . . . . .	179
7.5.2	Mortar cubes . . . . .	184
7.5.3	Additional experiment . . . . .	185
7.6	Analysis of the water demand . . . . .	186
7.6.1	Spread-flow analysis . . . . .	186
7.6.2	Void Fraction . . . . .	187
7.6.3	Particle packing theory . . . . .	188
7.7	Concrete mix results . . . . .	189
7.7.1	Tests on fresh concrete . . . . .	191
7.7.2	Results on hardened concrete . . . . .	191
7.8	Financial analysis . . . . .	193
7.9	Conclusions . . . . .	196
7.9.1	Main experiment . . . . .	196

7.9.2	Additional experiment . . . . .	197
<b>8</b>	<b>Conclusions, recommendations and social relevance</b>	<b>199</b>
8.1	Conclusions . . . . .	199
8.2	Recommendations . . . . .	202
8.3	Social relevance . . . . .	203
	<b>Bibliography</b>	<b>205</b>
	<b>Appendix A Physical properties</b>	<b>227</b>
	<b>Appendix B Thermal properties</b>	<b>229</b>
	<b>Appendix C Properties of Calciumsulfate</b>	<b>231</b>
	<b>Appendix D Analysis derivation multi-cycle</b>	<b>237</b>
	<b>List of symbols</b>	<b>239</b>
	<b>Summary</b>	<b>243</b>
	<b>Samenvatting</b>	<b>247</b>
	<b>Curriculum Vitea</b>	<b>253</b>

## Introduction

This thesis focuses on materials containing cement and calcium sulphates. Concrete is the first material which comes into mind when thinking about these materials. It is not that strange, since concrete was already in use by the ancient Romans, Greeks and Egyptians. The oldest concrete discovered so far is in southern Israel, and dates from approximately 7000 BC (Illston and Domone, 2001). A concrete mixture consists out of a binder (i.e. cement, calcium sulphates, slag and fly-ashes), water, aggregates and admixtures. Several types of concrete exists, for instance self-compacting, earth-moist, high strength and foam concrete. Each of these concretes have their own characteristics. But research on concrete is not outdated, when one sees the number of journal articles on concrete which is published every year. This is mainly caused by the introduction of new materials in concrete and the addition of functions such as air-purification. In the Netherlands around 15 million m<sup>3</sup> of concrete is produced each year (Cement en Betoncentrum, 2013).

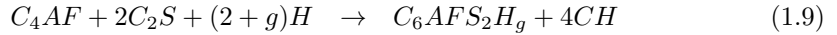
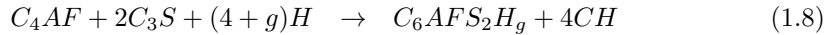
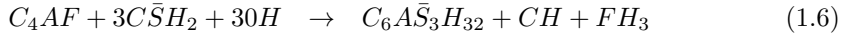
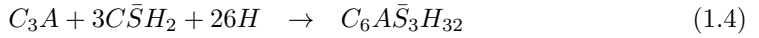
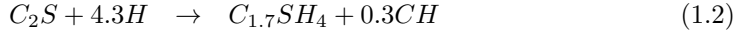
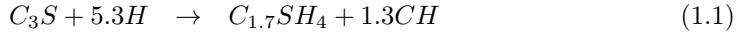
### 1.1 Cement

Cement is one of the essential components of concrete. Different kinds of cements exist, according to the European cement standard EN-197, one can distinguish Portland cement (CEM I), Portland composite cement (CEM II), slag cement (CEM III), Pozzolanic cements (CEM IV) and composite cements (CEM V). In the Netherlands, about 50-55% of the cement used is slag cement and about 40% is Portlandcement (Cement en Betoncentrum, 2013). The contribution of slag cement in the Netherlands is relatively high compared to other countries. Slag cement is a mixture of blast furnace slag (BFS) and Portland cement. Three categories of slag cement are distinguished based on the blast furnace slag content, namely CEM III/A 36 - 65 % BFS, CEM III/B 66 - 80 % BFS and CEM III/C 81 - 95 % BFS. Slag is a by-product of the pig iron production. For the production of Portland cement in Netherlands, a mixture of marl and clay is used. Marl is a natural limestone with high lime (CaCO<sub>3</sub>) content. The marl is dried and it is grinded together with silica, aluminium oxide and iron oxide. This grinded mixture is than burned in a 180 metre long rotating furnace at temperatures up to 1450 °C. Due to this heat, the raw materials react together forming new chemical compounds, which is called sintering. The sintered material (clinker) is cooled down quickly and has comparable properties to a burned natural stone type, Portlandstone, from England. The clinker is than grinded to a cement, to which often small amounts of calcium sulphate anhydrite or dihydrate (gypsum) are added to control the binding time (Blaazer et al., 2006).

The main chemical components of Portland cement are calcium oxide (CaO) and silicon dioxide or silica (SiO<sub>2</sub>). The burning or clinkering of chalk and clay results in Portland

clinker, which consists of four main chemical substances or clinker compounds, Alite ((CaO)<sub>3</sub>SiO<sub>2</sub>), Belite ((CaO)<sub>2</sub>SiO<sub>2</sub>), Ferrite ((CaO)<sub>4</sub>Al<sub>2</sub>O<sub>3</sub>Fe<sub>2</sub>O<sub>3</sub>) and Aluminate ((CaO)<sub>3</sub>Al<sub>2</sub>O<sub>3</sub>). In cement chemistry, abbreviations have been introduced in which C = CaO, S = SiO<sub>2</sub>, A = Al<sub>2</sub>O<sub>3</sub>, F = Fe<sub>2</sub>O<sub>3</sub>, H = H<sub>2</sub>O and  $\bar{S}$  = SO<sub>3</sub>. In this thesis, therefore the four cement clinker are written as C<sub>3</sub>S, C<sub>2</sub>S, C<sub>3</sub>A and C<sub>4</sub>AF (Taylor, 1997).

The main reactions of these cement clinker phases are



Within the cement hydration period, four phases can be distinguished (Hewlett, 1998) (Figure 1.1), namely:

1. Pre-induction period. In these first minutes after mixing with water, the alkali sulphates dissolve completely and the calcium sulphate dissolves until saturation. Therefore the pore solutions will contain K<sup>+</sup>, Na<sup>+</sup>, Ca<sup>2+</sup> and SO<sub>4</sub><sup>2-</sup> ions. C<sub>3</sub>A dissolves and reacts with Ca<sup>2+</sup> and SO<sub>4</sub><sup>2-</sup> in the pore water solution, resulting in the formation of ettringite.
2. Induction or dormant period. After the pre-induction period the overall hydration rate slows down for a period of a few hours (about ~ 3 hours).
3. Acceleration period. During this period, usually between 3-12 hours after mixing, the hydration accelerates again and the hydration rate is controlled by the nucleation and growth of the hydration products. A strong heat evolution will accompany this nucleation and growth of the hydration products.
4. Post-acceleration period. After the acceleration period, the hydration rate will slow down gradually and the hydration rate will become diffusion controlled.

Table 1.1: Physical properties of cement clinker compounds.

Property	C <sub>3</sub> S	C <sub>2</sub> S	C <sub>3</sub> A	C <sub>4</sub> AF
Density [kg/m <sup>3</sup> ]	3120	3326	3060	3730
Molar volume [cm <sup>3</sup> /mol]	73.18	51.79	88.30	128.3
Molar mass [g/mol]	228.32	172.25	270.2	477.0
Formation heat [kJ/mol]	-2927.82	-2311.6	-3587.8	-5090.0
Crystal size [ $\mu$ m]	<150	5-40	1 - 60	
Crystal shape	Hexagonal	$\beta$ -polymorph	Irregular to lath-like	Dendritic, prismatic and massive

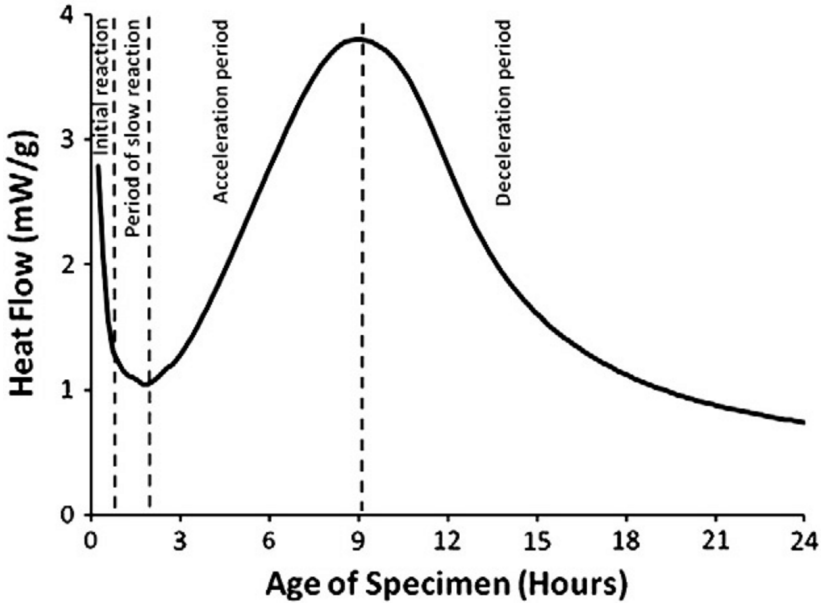
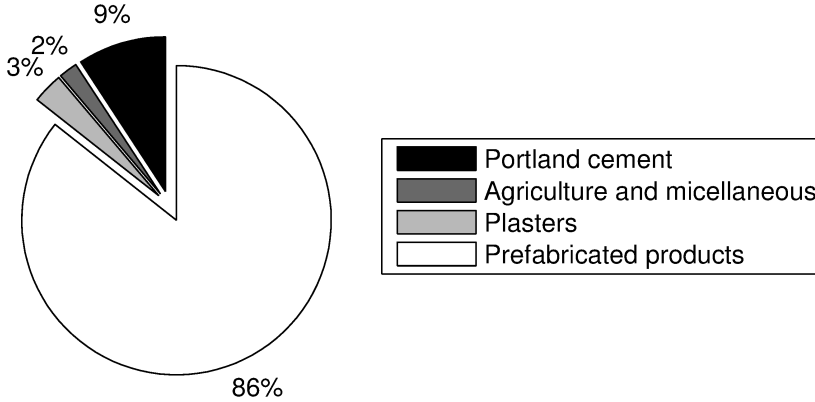


Figure 1.1: Stages of cement hydration (Bullard et al., 2011).

## 1.2 Calcium sulphates

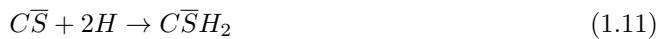
Calcium sulphates are the other binders considered in this thesis. They are used as binder for building materials, mainly for plastering and plasterboard/wallboards. They can also be applied for anhydrite floors. Furthermore, they are added to cement in order to avoid a so-called flash set, which caused a rapid heat evolution, decrease of plasticity and poor strength development (Taylor, 1997), see Reactions (1.3), (1.6) and (1.7). Crangle provide an overview of the purposes for which calcium sulphates are used in the United States (Figure 1.2). One can notice from this overview that 86% of all calcium sulphate is used in the United States for prefabricated products, which are besides other products mainly gypsum plasterboards. In contrast, Roskill Information Services Ltd. (2009) gives an different numbers for the purpose of calcium sulphates. In their report, they point that cement manufactures accounted for up to 60 % of worldwide gypsum composition, while plaster products, including plasterboards, account for approximately 30% of all consumption. Crangle (2012) gives an estimated world production capacity for gypsum plasterboard in 2010 exceeding 17 billion square meter per year at more than 250 plants worldwide. The United states, Asia and Western Europe each accounted for about 20% of this capacity (Crangle, 2012).

The  $\text{CaSO}_4$ -system is characterized by five solid phases, of which four phases are present at room temperature; calcium sulfate dihydrate (gypsum), calcium sulfate hemihydrate, soluble calcium sulphate anhydrite III and insoluble calcium sulphate anhydrite II. The fifth phase is calcium sulphate anhydrite I, which is only chemically stable at temperatures above 1180 °C (Wirsching, 2005). Table 1.2 shows the properties of calcium sulphate according to the Gips-datenbuch (Bundesverband der Gipsindustrie e.V., 2003).



**Figure 1.2:** Gypsum use in United States in 2010 (Crangle et al., 2010).

Table 1.3 lists the thermal properties according to Bénard et al. (1956). Figure 1.3 shows the solubility diagram for the calcium sulphate phases. One can notice that the transition temperature according to diagram between gypsum and hemihydrate is around  $100^{\circ}$  C for solutions (Posnjak, 1938). Calcium sulphate hemihydrate occurs in two different forms,  $\alpha$  and  $\beta$ . The  $\alpha$ -hemihydrate is characterized by its compact, well-formed, transparent, large primary particles. The  $\beta$ -hemihydrate has flaxy, rugged secondary particle made up of extremely small crystals (Wirsching, 2005). The structural difference between both forms is due to their different preparation methods. The  $\alpha$ -hemihydrate is produced by auto-claving of dihydrate, while  $\beta$ -hemihydrate is produced by heating of dihydrate. Their differences in structure have influence on their hydration heats as well as their practical application. The main hydration and dehydration reactions in calcium sulphate systems are:



and



, respectively. Calcium sulphates around the world commonly used in building sector are coming from two main sources. Traditionally natural gypsums were used. In the last two decades, more and more the so called flue gas desulpharization (FGD) gypsum is used. Natural gypsum is a sedimental rock and development due to the evaporation of sea water in shallow seas. The gypsum present in the seawater forms small crystals upon the evaporation, which sink down (sedimenting) towards the bottom of shallow sea. This

**Table 1.2:** Physical properties of the calcium sulphate phases (Bundesverband der Gipsindustrie e.V., 2003).

Chemical form	CaSO <sub>4</sub> ·2H <sub>2</sub> O	CaSO <sub>4</sub> ·0.5H <sub>2</sub> O	CaSO <sub>4</sub> III	CaSO <sub>4</sub> II
Description	Calcium sulphate dihydrate Natural gypsum	Calcium sulphate hemihydrate β-hemihydrate β-gypsum stucco α-hemihydrate α-gypsum plaster of paris α-form β-form	Anhydrite III	Anhydrite II
Further names			Soluble anhydrite	Insoluble anhydrite
Forms			α-AIII β-A III	A II-s (soluble) A II-u (insoluble) A II-E
Water of crystal, % wt	20.92	6.21	0.00	0.00
Density (g/cm <sup>3</sup> )	2.31	α:2.757 β: 2.619	2.580	2.93 2.97
Mole mass	172.17	145.15	136.14	136.14
Lattice symmetry	Monoclinic	Monoclinic	Orthorhombic	Orthorhombic
Space group	I 2/a	I 121	C 222	Amma
Hardness Mohs	2			3.5
Water solubility at 20 °C (g/l)	2.05	α: 6.7 β: 8.8	α: 6.7 β: 8.8	2.7
Stability	< 40 °C	metastable	metastable	40 - 1180 °C
Laboratory conditions		β: 45- 200 °C in dry air α: > 45 °C in water vapour atmosphere	50 °C vacuum RH	200 - 1180 °
Production temperature		α: 80-180 °C wet β: 120-180 °C dry	α: 110 °C wet β: 290 °C dry	300-900 °C A II-s: 300 - 500 °C A II-u: 300 -500 °C A II-E: > 700 °C

**Table 1.3:** Thermal properties of the calcium sulphate phases (Bénard et al., 1956).

Chemical form	CaSO <sub>4</sub> ·2H <sub>2</sub> O	CaSO <sub>4</sub> ·0.5H <sub>2</sub> O	CaSO <sub>4</sub> III	CaSO <sub>4</sub> II
$\Delta H_{298}$ kJ/mole	-1796.9	$\beta$ -1574.1 $\alpha$ -1576.2	$\beta$ -1488.6 $\alpha$ -1409.3	-1433.6
Enthalpy kJ/mole	-2022.5	$\beta$ -1853.8 $\alpha$ -1436.2	$\beta$ -1292.7 $\alpha$ -1297.1	-1318.8
Entropy S <sub>298</sub> J/(K mole)	192.6	$\beta$ 134.4 $\alpha$ 130.6	108.4	106.8
Specific heat C <sub>p</sub> J/(K mole)	186.3	$\beta$ 123.9 $\alpha$ 119.7	98.6	99.4

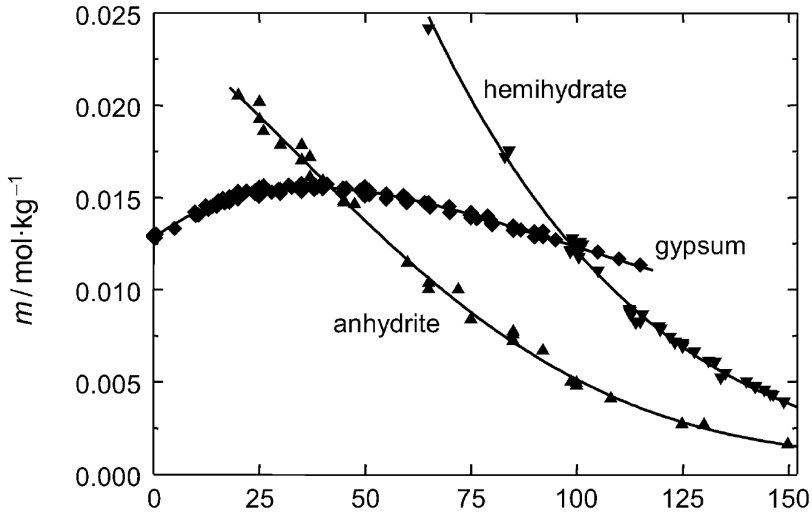


**Figure 1.3:** Solubility of calcium sulphate phases.(Charola et al., 2007).

process even nowadays takes place around the world.

Natural gypsum and anhydrite can be found in Europe mainly in Germany, England, France and Poland (Bundesverband der Gipsindustrie e.V., 2003). The most famous location is located near Paris, France.  $\beta$ -hemihydrate is sometimes referred to as plaster of Paris, which is referring back to this basin. Gypsum- and anhydrite-rock have quite different structures all over Europe (Bundesverband der Gipsindustrie e.V., 2003). The color of gypsum rock is white, but it can differ due to the presence of natural contaminations, like clay, calcium carbonate and iron oxide. The content of gypsum in the sedimentary rock varies from 75% to 95%, the rest being clay and chalk (Eurogypsum, 2011).

FGD gypsum is obtained from the desulphurization of gases in coal-fired power stations. The combustion of sulphurous fossil fuels such as hard coal, lignite (and fuel oil) produces sulphur dioxide ( $\text{SO}_2$ ) which, escapes into the atmosphere with the flue gases, when no further actions are undertaken (Eurogypsum, 2011). Since sulphur dioxide is one of the causes of acid rain and air quality problems, the West-German government enacted in 1983 a law to protect the quality of the air which made it compulsory for fossil-fuel power plants to be fitted with flue gas desulphurisation (FGD) facilities (Eurogypsum, 2011). Due to the state of art desulphurization methods, the FGD gypsum produced in Europe can be directly used as raw material in the gypsum industry (Hamm et al., 2004). The use of FGD-gypsum is strongly increased after 1993, when FGD-gypsum was not longer considered as a waste, since it was removed from the European waste catalogues and the OECD lists for transfrontier movement of wastes. This simplified transportation of FGD gypsum within Europe and led to an increase of the use of FGD-gypsum within Europe (Hamm et al., 2004).

Currently 80% of total synthetic gypsum (including FGD gypsum) used worldwide, is for the production of plasterboard (Crangle et al., 2010). The main reason for this is the

good properties of FGD-gypsum as well as their positive effect on the production. This is caused by the high degree of purity, the low water demand in the mixer slurry and the low board weights. Therefore it can be used best for plasterboard production (Hamm et al., 2004).

FGD-gypsum, which is produced as industrial byproduct, is not the only source of secondary gypsum. Other sources of gypsum are for example phosphor-gypsum and fluoro-anhydrite. But these forms are on the waste list of OECD and need refinement before they can be used. Therefore they are too expensive to be used compared to the natural and FGD-gypsum (Wirsching, 2005).

### 1.3 World market of calcium sulphates and cements

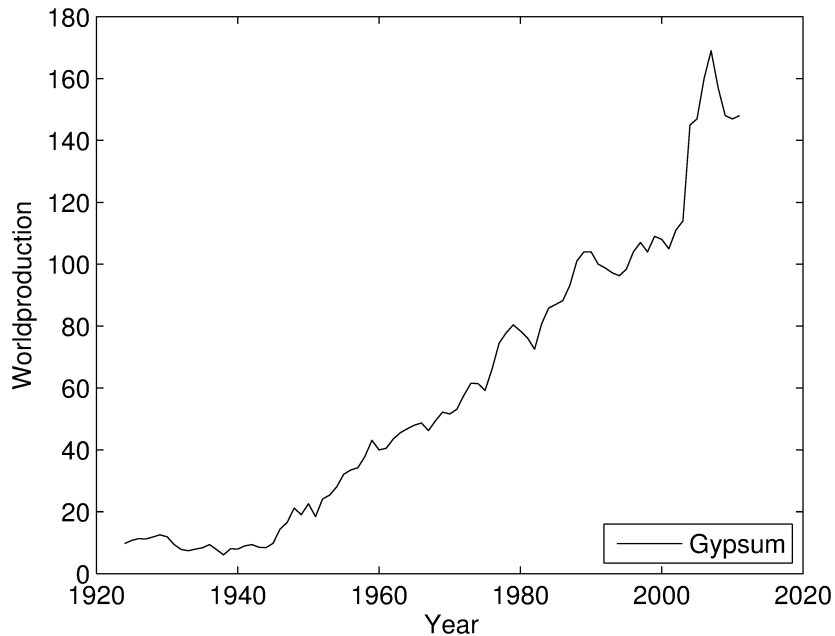
The global extraction of (natural) gypsum and anhydrite increased from about 42 Mt in 1960 to a peak of around 112Mt in 1999 with an average annual growth rate of around 2.6%. US Geological Survey estimated the total world production in 2008 at 159 Mt (Crangle et al., 2010). According to Eurogypsum, 14.8 Mt of FGD-gypsum was produced in 2006 within Europe (Eurogypsum, 2011). The production of FGD-gypsum increased from 4.9 Mt in 1996 to 6.3 Mt in 2000. The production of FGD-gypsum in 2008 in the US was 9.7 Mt (Crangle et al., 2010).

Van Oss (2012) gives an estimation of the world production of cement in 2011 of 3.6 Gt, which is produced in more than 150 countries. China is by far the world's leading producer, with an output of almost 2.1 Gt, which is 58% of the world total. Top five producing countries (China, India, United States, Brazil, Turkey) combined account for 70% of the total world output.

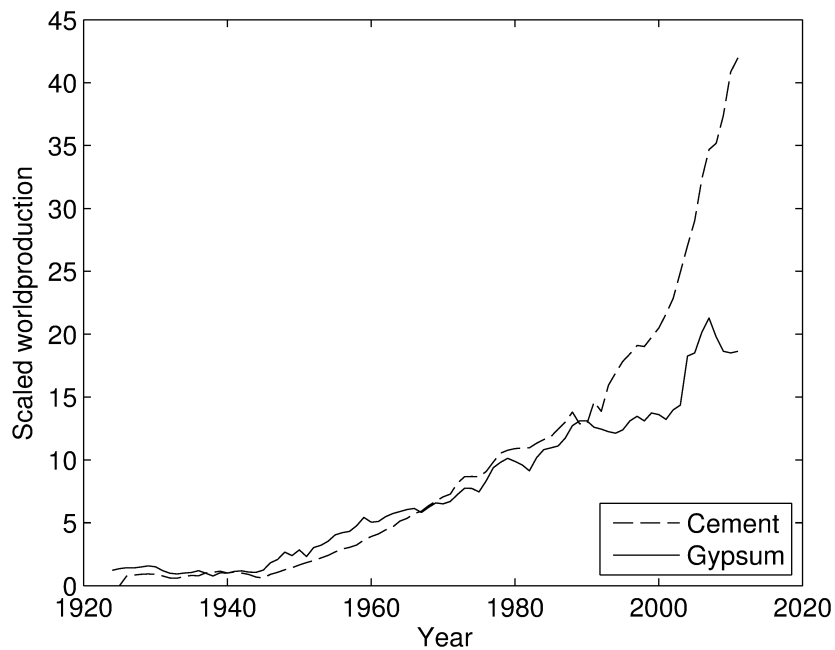
Figure 1.4 shows the world production of gypsum and comparison to the amount of cement produced worldwide according to Founie (2006). As can be noticed from the figure, the growth of the gypsum production is slower than the production of cement in the same period. Furthermore the gypsum production is decreasing in the last year, while the cement production is still increasing. Table 1.4 shows the main producing countries of gypsum in the world.

### 1.4 Missing Knowledge

When one wants to study the thermal behaviour of gypsum plasterboards during fire/heating, the first step is the modelling of thermal conductivity at room temperature. The modelling of the thermal conductivity of materials is complicated for porous media, which consist of different phases. Kaviany (1995) points out that the heat conduction through a fully saturated matrix depends on the thermal conductivity of each phase and the structure of the matrix. Two-phase systems are described earlier in literature (Maxwell 1873; Miller 1969; Zehner and Schlunder 1970, Hadley 1986). These systems usually are a saturated porous solid material. When studying building materials, there is often moisture present and therefore there are three phases (solid, liquid and gas) present and the models from literature are not longer adequate. A possibility to create the microstructure for thermal conductivity study is provided by hydration models, such as CEMHYD3D, which produce a microstructure as output. The CEMHYD3D model is chosen in this thesis because it is believed to be one of the most advanced, well-known and



(a)



(b)

**Figure 1.4:** (a) World production of gypsum in Mt (b) World production cement and gypsum presented as indexed based on the production of 1940 (Crangle, 2012; Van Oss, 2012).

**Table 1.4:** World production of gypsum in kTon (Crangle, 2012).

	2008	2009	2010	2011	2012
United States	14400	9400	8840	8900	9900
Algeria	1670	1700	1700	1650	1650
Argentina	1200	1300	1360	1340	1200
Australia	4000	3500	3500	3500	3000
Austria	1000	1000			
Brazil	2100	1920	2350	2750	2800
Canada	5740	3540	2717	2560	2200
China	46000	45000	47000	48000	48000
Egypt	2000	2500	2400	2400	
France	4800	2300	2300	2300	2300
Germany	1900	1898	1822	2020	2050
India	2550	2600	2650	2700	2750
Iran	12000	13000	13000	13000	14000
Italy	5400	4130	4130	4130	4100
Japan	5800	5750	5700	5600	5700
Mexico	5140	5760	3560	3840	3850
Poland	1580	1500	1300	1200	1200
Russia	2300	2900	2900	3000	3100
Saudi Arabia	2300	2100	2100	2100	2300
Spain	11500	11500	11500	11500	11500
Thailand	8000	8500	8500	9900	10000
Turkey	3000	3100	3200	3200	3000
United Kingdom	1700	1700	1700	1700	1700
Other Countries	12700	11400	12500	14500	14900
World total rounded	159000	148000	149000	149000	150000

most widely-used computer hydration model (Bishnoi and Scrivener, 2009; Van Breugel, 2004). Currently CEMHYD3D is suitable for the hydration of Portland cement, blast furnace slag cement and fly-ash (Chen, 2007).

For the production of gypsum plasterboards, calcium sulphate hemihydrates is the main ingredient. Although hemihydrate is often added to cement (also in CEMHYD3D), the model is not able to handle calcium sulphates as main ingredient and calcium sulphate dihydrate as final product. Another complication for the modelling of the hydration of calcium sulphate hemihydrate, is the extreme short hydration time of these binders compared to cements. The current version of CEMHYD3D is not suitable, since the number of cycles for full hydration is extremely limited, which causes the hydration curves to be too coarse. Therefore it should be necessary to have shorter cycles, which needs to be included to the model.

For the validation of CEMHYD3D, hydration curves are needed. Because the speed of hydration of hemihydrates is more difficult to measure the hydration curve and the different processes which take place. For the measurement of the hydration of cement and concrete, in the last decade ultrasonic sound velocity measurements have been applied successfully (Reinhardt and Grosse 2004, De Belie et al. 2005, Robeyst et al. 2008). The ultrasonic sound velocity measurement has as an advantage that it is continuous (Ylmén et al., 2009) and that it provides information on microstructure development and related properties (Reinhardt et al., 1999). Due to these advantages, ultrasonic sound measurement is interesting for providing the necessary hydration curves.

Furthermore, the combination of ultrasonic measurements and volumetric composition has not been studied for hemihydrates yet, so far only studies are reporting cement paste and mortar, and also here these models were never combined to an overall volumetric composition model for cement, such as the model of Powers and Brownyard (Brouwers, 2004a,b, 2005, 2011) as well as hemihydrate (Brouwers, 2012).

Another improvement to CEMHYD3D, which is interesting to include is smaller elements (voxels in this thesis). As pointed out by Chen and Brouwers (2008), the physical properties of a hydrating microstructure are limited by the smallest element-size available in the system, the so-called system resolution. Due to increasing computational power, resolutions of  $0.2\ \mu\text{m}$  are possible. Previously the outcomes of CEMHYD3D were resolution-dependent (Garboczi and Bentz, 2001). Chen and Brouwers (2008) have incorporated the diffusion layer system of Van Breugel (1997) into the CEMHYD3D-model to overcome this problem, but there is still improvement possible.

One of the main challenges, when using cellular automata models, such as CEMHYD3D, is the linkage of the cycles to time. The relation between cycles (in cellular automata models) and time (general kinetic models and real world) is often not direct. The reaction kinetics is usually analyzed using numerical and analytical models. Although Bentz (1995) applied the Knudsen model in order to get this relation, for further improvement of cellular automata reaction models, it would be useful to have a rigorous link between the (mathematical) chemical reaction models, like chemical reaction (shrinking core) model and the cellular automata approach to study the dissolution of particles. Reactions in cement/calcium sulphate systems often follow the shrinking core model.

As input for the hydration model, an initial microstructure needs to be created by (loose) packing of particles in a volume, where each particle is composed of so-called voxels (Figure 1.5). The packing of disks and spheres, both uniform and graded sizes, was been

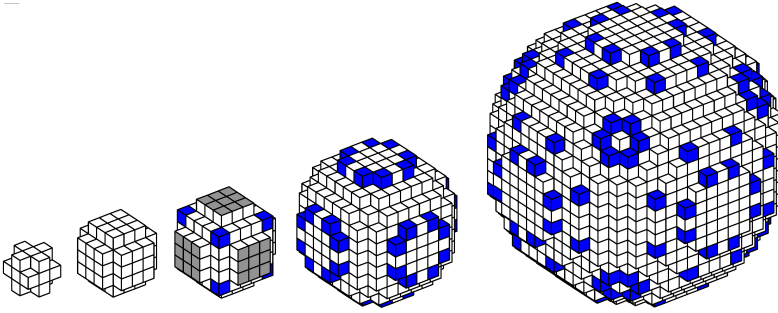


**Figure 1.5:** Digitized particles with a sizes of 3, 5, 7, 11 and 21 voxels (the top-surfaces in gray, which are used for the computation of the digitized roundness in Chapter 2) (the voxel that are removed from the 7 and 11 and 21 particles during shape modification are indicated in black in print and blue digitally).

described in great detail in literature (Lubachevsky and Stillinger 1990, Torquato 2002, Brouwers 2006). Besides these ideal disks and spheres also spheroids and irregular particles are studied (Wouterse, 2008). In this thesis, the interest is on the application of cellular automata. For the study of hydration in cellular automata systems, digitized particles are used. Jia and coworkers (Jia and Williams 2001, Jia et al. 2002, 2007) have also performed simulations using digitized particles. Their research is mainly focused on packing of particles of arbitrary shapes mostly in 2D, while for the study of hydration three dimensional particles are of interest.

The second step is for the calculation of the thermal conductivity of gypsum plasterboard during fire/heating is knowledge on the thermal chemical and physical response of the gypsum plasterboard to elevated temperatures. Up to recently, this response was only studied experimentally (Mehaffey et al., 1994) and modeled by finite element on meso-level (Axenenko and Thorpe, 1996; Thomas, 2002). Micro-structural modeling would provide the possibility to include the chemical decomposition reaction in more detail compared to meso-level modeling and the possibility to model the micro-structure, where meso-level only provides the average void fraction in the gypsum plasterboard. Both possibilities are of interest for the calculation of the thermal conductivity, since composition and (micro)structure have an influence on this property.

## 1.5 Cellular automata

Cellular automata (CA) were first proposed by Ulam (1952, 1976) and Von Neumann (1966), based on ideas of Zuse (Lipkowitz et al., 2001). The first full comprehensive description of cellular automata was made by Wolfram (1983a). Cellular automata are 'simple mathematical idealizations of complex systems in physics, chemistry and engineering' (Wolfram, 1983a). They consist of a lattice of discrete identical sites, each site taking on a finite set of integer values. The values of the sites evolve in discrete time steps according to deterministic rules that specify the value of each site in terms of the values of neighbouring sites (Wolfram, 1983b). Cellular automata may thus be considered as

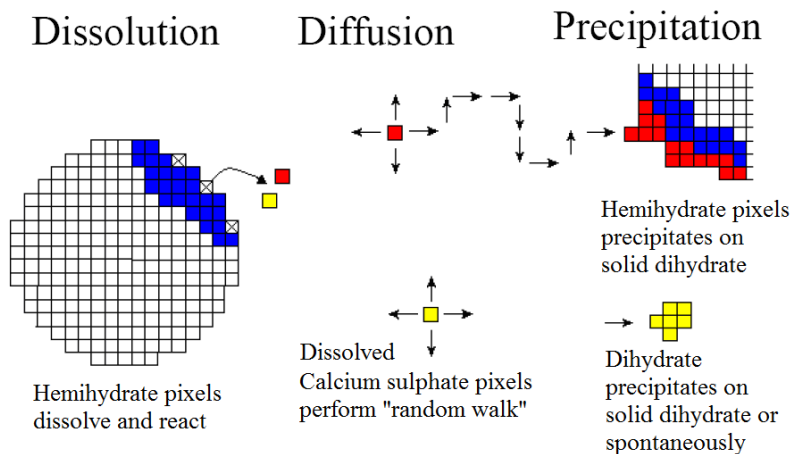


**Figure 1.6:** Main reaction mechanism CEMHYD3D (modified from Bentz and Garboczi (1992) and Van Eijk (2001)).

discrete idealization of the partial differential equations often used to describe natural systems' (Wolfram, 1983a, 1984). The system consisting of triangles, squares, hexagons or other shapes cell in a one (1D), two (2D) or three-dimensional (3D) grid/array. The 2D square cells are used mostly in the last 50 years (Lipkowitz et al., 2001). The first use of grids for study micro-structure of metals was done by Rosenhain (1916). Often the cellular automaton systems apply periodic boundaries, which mean that a cell moving off the system at the edge, reappears from the opposite edge to the grid, in order to avoid wall side effects.

According to Kier et al. (2005) and Lipkowitz et al. (2001), cellular automata are not restricted only to the use of deterministic rules, since probabilistic rules are used extensively for studying real physical and chemical systems. Kier et al. (2005) point out that CA-models have the following four components;

- A grid composed of cells.
- A set of ingredients.
- A set of local rules governing the behaviours of the ingredients.
- Specified initial conditions.

## 1.6 CEMHYD3D: a 3D computer-based hydration model

Hydration models are used to reduce the number of the real tests needed to optimize a mix design with gypsum and cement. Examples of these hydration models are CEMHYD3D (Bentz, 1995), HYMOSTRUC (Van Breugel, 1997), the Navi and Pignat model (Navi and Pignat, 1996) and  $\mu\text{ic}$  (Bishnoi and Scrivener, 2009). These models are able to represent the physical properties and present reaction mechanism during hydration. Table 1.5 shows the most important features of the different hydration models. The CEMHYD3D

is chosen in this thesis because it is believed to be one of the most advanced, well-known and most widely-used computer hydration models (Van Breugel 2004, Bishnoi and Scrivener 2009).

The computer model CEMHYD3D is a cellular automata based model (Section 1.5) that was originally developed by Bentz and Garboczi (1991) to represent the hydration process of Portland cement in two dimensions. Later on, the model was later extended to a 3D computer model and other cementitious materials, like fly-ash and silica fume, as reactants were included (Bentz, 1997). The original version of the model was not suitable for personal computers. Van Eijk (2001) has calibrated the model with two Dutch cements CEM I 32.5R and 52.5R, and introduced pore water chemistry. Chen (2007) and Chen et al. (2007) have introduced slag blended cement into the hydration model including the new phases and their reactions as well as the difference in reactivity between cement and slag material. Furthermore, additional improvements were done in order to overcome some side effects of changing system resolution. At last mineral shrinkage compensating mixtures were designed by Chen (2007) and Chen and Brouwers (2008) based on simulations and real tests. Smilauer (2005) studied the elastic properties of hydrating cement paste by applying elastic homogenization methods on the microstructures provided by CEMHYD3D. Koster (2007) uses CEMHYD3D for the simulation of 3D moisture transport through and moisture absorption by capillary-porous building materials. Newest developments introduced by NIST can be found in the work of Bentz (2000, 2005, 2006). The CEMHYD3D-model usually represent the microstructure of hydrating cement by using a  $100 \cdot 100 \cdot 100$  box with  $10^6$  voxels of size  $1 \cdot 1 \cdot 1$ . Other resolutions are possible to use, although larger system sizes and smaller voxel sizes represent the microstructure more accurately, the computing time needed for these system and voxel sizes is remarkably higher. According to Smilauer and Bittnar (2006), the reasonable microstructure size lies in the range of 20-50  $\mu\text{m}$  and a microstructure edge size above 100  $\mu\text{m}$  has been found to bring no significant accuracy in the hydration model predictions. Garboczi and Bentz (2001) point out that 0.2  $\mu\text{m}$  resolution is accurate enough for simulation of cement hydration, which is close to the minimum particle size of cements and calcium sulphates (Hunger and Brouwers, 2009). Therefore in this chapter a microstructure of  $100 \times 100 \times 100 \mu\text{m}^3$  is used while a system resolution down to 0.2  $\mu\text{m}$  is tested.

Each voxel in the microstructure represents a chemical substance either fresh binder or hydrated material. The initial microstructure thus consists of cement particles and water, where each particle consists of a number of voxels. The particles are created by placing voxels in an approximately spherical shape called "digitized particle" within the box. A 1- $\mu\text{m}$  particle in CEMHYD3D is represented by 1 voxel when the system resolution is 1  $\mu\text{m}$ , while in a system of 0.33  $\mu\text{m}$  resolution it is represented by 19 voxels with size of 0.33  $\mu\text{m}$ . An example for the digitized particle of size 1, 3, 5, 7, 11 and 21 voxels is shown in Figure 1.5, which contain 1, 19, 81, 179, 739 and 4945 voxels, respectively (Van Eijk, 2001).

The first step of the simulation is the creation of an initial microstructure, which is representing the fresh paste. Therefore the particle size distribution and the chemical composition of the binder is taking into account. Based on the chemical composition, the (cement clinker) compounds are assigned randomly to the (solid) voxels. This results in a homogeneous phase distribution throughout the microstructure. The second step of the simulation is the performance of the chemical reactions of clinker phases and dihydrate

**Table 1.5:** Properties of the different 3D cement hydration models (Modified from Ye (2003)).

	CEMHYD3D	Navi's model	DuCom	HYMOSTRUC	$\mu\text{ic}$	HydratiCA
Particle size distribution	Yes (1-40 $\mu\text{m}$ )	Yes (6-60 $\mu\text{m}$ )	No (Mono-sized grains)	Yes (0-90 $\mu\text{m}$ )	Yes	Yes
Composition of cement	C <sub>3</sub> S, C <sub>2</sub> S, C <sub>3</sub> A, C <sub>4</sub> AF, Gypsum	C <sub>3</sub> S	C <sub>3</sub> S	C <sub>3</sub> S, C <sub>2</sub> S	C <sub>3</sub> S, C <sub>2</sub> S, C <sub>3</sub> A, C <sub>4</sub> AF, Gypsum	C <sub>3</sub> S, C <sub>2</sub> S, C <sub>3</sub> A, C <sub>4</sub> AF, Gypsum
Type of cement	OPC, Slag and fly-ash cement	-	OPC, Medium heat, High belite cement	OPC, (slag cement)	OPC	OPC
Mix proportion	Yes	-	Yes	Yes	Yes	Yes
Kinetics	No	Yes	Yes	Yes	Yes	Yes
Mineral	Filler	Mono-sized filler	Filler	Filler	Filler	Filler
Pore scale	Capillary pore	Capillary pore	Statistic pore and capillary pore	Capillary pore	Capillary pore	Capillary pore
Model	Discrete	Continuous	Continuous	Continuous	Continuous	Discrete

Table 1.6: Properties of phases used in CEMHYD3D (Van Eijk, 2001).

Name	Density (g/cm <sup>3</sup> )	Molar volume $\omega$ (cm <sup>3</sup> /mol)	Molar mass M (g/mol)	Heat of formation (kJ/mol)	Dissolution probability $P_{D,1}$ (-)	Nucleation probability $P_{N,1}$ (-)	Maximum number of nucleation sites $i_{max,1}$ (-)
C <sub>3</sub> S	3.21	71	228	-2,928	0.027		
C <sub>2</sub> S	3.28	52	171	-2,312	0.005		
C <sub>3</sub> A	3.03	89.1	270	-3,588	0.027		
C <sub>4</sub> AF	3.73	128	477	-5,090	0.003		
C $\bar{S}$ H <sub>2</sub>	2.32	74.2	172	-2,023	0.0017	0.01	90 000
C $\bar{S}$ H <sub>0.5</sub>	2.73	53.2	145	-1,575	0.005		
C $\bar{S}$	2.61	52.2	136	-1,425	0.001		
C <sub>1.7</sub> SH <sub>4.0</sub>	2.12	108	229	-3,283		0.01	100 000
C <sub>1.1</sub> SH <sub>3.9</sub>	1.69	101.8	172	-2,299		0.01	100 000
CH	2.24	33.1	74	-986		0.01	20 000
C <sub>6</sub> A $\bar{S}$ <sub>3</sub> H <sub>32</sub>	1.7	735	1250	-17,539			
C <sub>4</sub> A $\bar{S}$ H <sub>12</sub>	1.99	313	623	-8,778			
C <sub>3</sub> AH <sub>6</sub>	2.52	150	378	-5,548			
C <sub>4</sub> AH <sub>13</sub>	2.04	273	560	-8,318	0.0167	0.002	10 000
FH <sub>3</sub>	3	69.8	209	-824		0.2	2 500
MH	2.39	24	58	-924		0.6	2 500
S	2.2	27	59	-908			
H	1	18	18	-286			

(Eqs. (1.1)-(1.12) by using the cellular automation and random walk algorithms. The disadvantage of using a box is the presence of wall-effects. In order to eliminate these effects, periodic boundaries are applied within CEMHYD3D (Bentz, 1997).

Reaction of the initial microstructure is simulated by using discrete cycles. Each cycle consists of three processes: dissolution, diffusion and reaction, which are performed in serie (Figure 1.6). The dissolution step is performed by checking each voxel in the box, for its ability to dissolve. This ability is a complicated function of the temperature, extent of prior reaction, concentration of dissolved sulphates, and a couple of other dependencies. During the induction-time of the cement, some cement clinker phases are assumed not to be soluble. Whether a voxel is actually dissolving during a certain cycle depends on the dissolution probability. The dissolution probability is defined by Bentz and Garboczi (1992) as the likelihood of each phase to dissolve. Therefore a random number is generated which needs to be less than the dissolution probability. The probability for the different (chemical) phases of the binder (Table 1.6) differs in order to model the different dissolution rates of these cement phases. The model corrects for the volume changes during reaction by adding one or more diffusing voxels. Due to the discrete behaviour of cellular automata the volume stoichiometry of the reactions is preserved statistically.

In the original version of CEMHYD3D only phase-boundary-reaction (chemical reaction controlled) was considered. According to Chen (2007), the diffusion layer is needed in order to correct for the effect of the system resolution. He incorporated the diffusion layer into the CEMHYD3D-model, based on the work done by Van Breugel (1995b). Van Breugel (1995b) showed that the reaction rate is constant for phase-boundary reaction and decreasing for diffusion controlled circumstances. The transition point between both mechanism is defined by layer thickness  $\delta_{tr}$ . This is shown in Figure 1.7. Both mechanisms and the transition layer have been incorporated by Chen (2007) and Chen and Brouwers (2008). The dissolution probability is a complicated function depending on temperature, reaction degree, sulphate concentration and other parameters. For readability here for the description of dissolution probability function  $P_{D,1}$  is used.  $P_{D,1}$  includes the earlier mentioned parameters. The dissolution probability for the phase-boundary reaction reads;

$$P_{D,1} = P_{D,0} \quad for \quad \delta \leq \delta_{tr} \quad (1.15)$$

and the dissolution probability for the diffusion controlled part, based on Chen (2007) and Chen and Brouwers (2008), reads;

$$P_{D,1} = P_{D,0} \frac{\delta_{tr}}{\delta} \quad for \quad \delta > \delta_{tr} \quad (1.16)$$

with  $P_{D,0}$  the basic dissolution chance function (here presented as an constant value, but in fact a complicated function),  $\delta$  the layer thickness and  $\delta_{tr}$  the theoretical transition layer thickness. According to Van Breugel (1995b), the transition layer thickness for low heat cement equals 2 - 4  $\mu\text{m}$  and for fast hydrating cements 3 - 6  $\mu\text{m}$ . In CEMHYD3D a  $\delta_{tr}$  of 2  $\mu\text{m}$  is chosen (Chen, 2007; Chen and Brouwers, 2008).

The microstructure is updated after each reaction cycle. Reaction related properties, i.e. the reaction degree, are calculated after each cycle. The overall reaction degree of

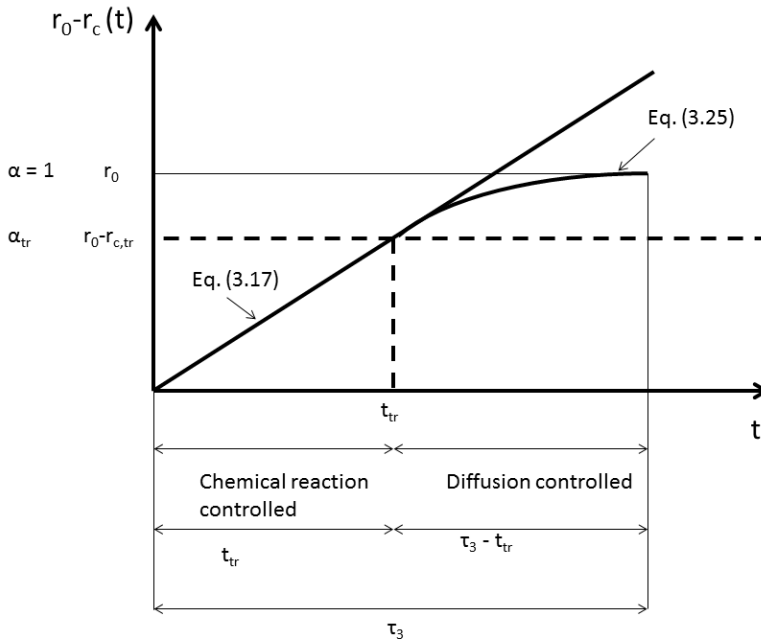


**Figure 1.7:** The relationship between basic rate factor, diffusion coefficient and transition point ( $t_{tr}$ ,  $r_{c,tr}$ ) (modified from Van Breugel (1995a)).

the binder is calculated on volume basis by dividing remaining binder voxels by the total numbers of initial binder voxels. This can be converted into the degree on a mass basis by using the specific densities of the different phases.

The CEMHYD3D-model operates based on cycles rather than time and no direct relation between both existed originally. Bentz (1997) introduced the calculation of the time from the cycles based on Knudsen model. The calculation within the Knudsen model is based on maturity approach with parabolic kinetics (Knudsen, 1984). The maturity approach is mathematical dispersion model, in which the reaction rate determines the reaction time. The reaction rate ( $\alpha$ ) is influenced by particle size distribution and chemical composition and has a close relation with the shrinking-core model, except that it takes in account the differences in particle sizes.

## 1.7 The research approach

The Objective of this thesis is formulated as follows:

*'This research aims to further extend the existing insights of micro-structural development of cement/gypsum-based materials during the hydration, usage and fire using cellular automata, experiments and mathematical models in order to further understand and optimize these cement/gypsum-based products'.*

In order to reach this objective, six targets are defined. The targets are:

- The creation of random packed structures using mono-sized digitized particles using a cellular automata system.
- Researching the applicability of cellular automata for the study of dissolution of particles.
- Improving the CEMHYD3D (cement) hydration computermodel by the introduction of multi-cycle and multi-scale modelling.
- Obtaining insights into the hydration of hemihydrate using ultrasonic sound measurements and relating this information to existing hydration models from literature.
- The prediction of the thermal conductivity of gypsum plasterboards at room and elevated temperatures.
- The usage of a cement/gypsum based binder to stabilisate and solidificate contaminations from polluted soil.

As stated in the objective, three methods are used in this thesis, namely cellular automata, experiments and mathematical models. All these methods have their advantages and disadvantages. Table 1.7 shows which parts of the research make use of the different methods. Furthermore it shows which materials are utilized during the research.

**Table 1.7:** Overview of the used research methods/tools, the level of interest and materials within this thesis.

Subject	Methods	Level	Materials	
2	Cellular automata	Micro	General	Physics
3	Reaction kinetics	Micro	General	Chemistry
4	Multicycle and Multiscale modelling	Micro	OPC	Chemistry
5	Ultrasonic sound speed	Micro	Gypsum	Physics
6	Thermal conductivity	Micro	Gypsum plasterboard	Physics
7	Stabilisation	Macro	Gypsum, Cement, Quicklime	Chemistry

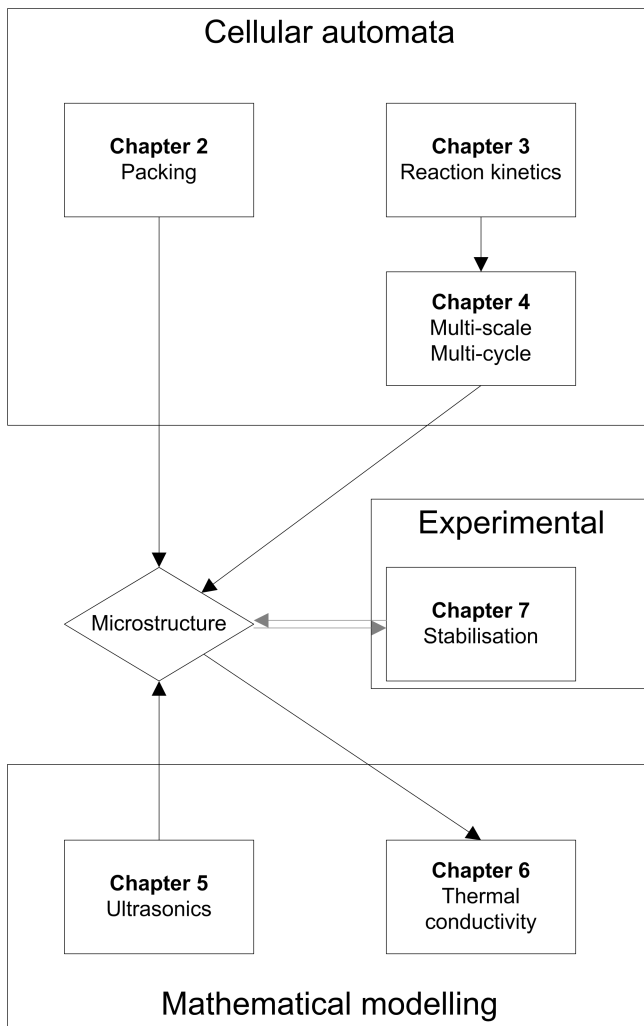


**Figure 1.8:** Research design.

## 1.8 Outline of this thesis

Figure 1.8 shows the main structure of this thesis. The central point of interest is the microstructure. Chapters 2, 3, 4 and 5 all deal with the microstructure. Chapter 6, on the other hand, uses a microstructure for the calculation of the thermal conductivity. Chapter 7 is using the microstructure, both as in- and output, for the design of stabilised products. Another important link between the Chapters 2, 3 and 4 is the application of digitized particles as representation of real particles in the cellular automata systems, which is a simulation technique and is described in detail in this thesis. Furthermore, Chapters 3, 4 and 5 all study (hydration) reactions. Reactions are also involved in Chapter 6, in particular dehydration reactions, when studying the thermal conductivity at elevated temperatures. In this case, the reactions change the microstructure and therefore the thermal conductivity.

Chapter 2 focuses on the regular and random packing of digitized particles using a cellular automata model. The packing of particles leads to an initial microstructure, which can be used in other parts of this thesis. The packing study, using 3D cellular automata systems, of digitized particles and a routine based on the Lubachevsky and Stillinger (1990) algorithm, this chapter shows that the random close packing of digitized particles is comparable to spheres, when taking into account the digitized roundness and Wadell's sphericity of these particles. Furthermore the obtained packing fractions are clearly related to the size ratio (box/particle size).

Chapters 3 and 4 attempt to extend the current knowledge on hydration modelling of cement / gypsum-based materials using the cellular automata hydration model CEMHYD3D. Therefore it uses the same digitized particles as in Chapter 2, although in Chapter 3 the interest lies in dilute systems rather than the dense packed systems studied in the foregoing chapter. Chapter 3 is focussing on the fundamental knowledge of reaction kinetics. Two assumptions are distinguished in literature, reactions are either surface- or diffusion-controlled. Both cases are studied and relations between these general reaction kinetics and the cellular automata approach are derived. This study results in an improvement of the dissolution routine deployed by CEMHYD3D and an unique relation between cycles and time based on kinetic and cellular automata parameters.

Using this modification, Chapter 4 focuses on multi-cycle and multi-time hydration modelling of  $C_3S$  and Portland-cement. In case of multi-scale the particles are divided in smaller elements, while in case of multi-time the size of time-steps taken by the model are reduced. These modifications enable the study of the hydration of calcium sulphate, which have relative short reaction time compared with cement, using CEMHYD3D, which was originally developed to study the hydration of cement-based materials. Since calcium sulphates, compared to cements, tend to have a smaller particle size and their time span for 'full' hydration is significant shorter. These modifications prove to be successful.

Simulation of reactions is the central point in Chapters 3 and 4. Chapter 5 uses a slightly different approach towards reactions. This chapter deals with the monitoring of the reaction during experiments, and the reaction of calcium sulphate hemihydrate towards gypsum is used as a vehicle for this study. The hydration of hemihydrate to gypsum and cement is usually studied by IR, SEM and Vicat techniques. Because the speed of hemihydrate hydration, it is more difficult to measure the hydration curve and the dif-

ferent processes which take place. For the measurement of the hydration of cement in the last decade ultrasonic sound velocity measurements have been applied successfully (Reinhardt and Grosse 2004, De Belie et al. 2005, Robeyst et al. 2008). In chapter 5 the ultrasonic sound measurements are used for the study of the hydration of hemihydrate to gypsum. The first step is to describe the sound velocity of the fresh slurry and the hardened product based on theoretical equations given by literature. The next step is to relate the sound speed to the hydration degree in between these points and to relate the hydration rate to time. This is done by the use of the hydration volume model of Brouwers (2012), the hydration model of Schiller (1974) and relation between speed and hydration degree given by Smith (2002).

Whereas in Chapter 5, sound velocity as physical property during the reaction of hemihydrate is described, Chapter 6 focuses on the calculation of a physical property (here thermal conductivity) of the hardened product (gypsum plasterboard) at room temperature and at elevated temperatures. This last case includes the reactions which are involved in thermal decomposition of the product. For this computation, a gypsum plasterboard is assumed to be a three-phase system, since it consists of a solid phase and a water/air mixture in the voids. The first part of the chapter assesses the feasibility the different (two-phase) models/equations presented in literature. It is found during this assessment that the thermal conductivity equation of Zehner and Schlünder (1972) gives the best results. The next step is the determination of the influence of moisture on the thermal conductivity of the gypsum plasterboard. Regression analysis points out that the moisture content depends only on the gypsum content. A value of 2.8% m/m absorbed water on the mass of gypsum is found. This moisture influences the thermal conductivity at ambient temperature only. The last step is the computation of the thermal conductivity at elevated temperature. Therefore a simple dehydration reaction model describing the changes in volume and chemical content based on temperature is used. A close fit between the computed and experimental values is found.

Chapter 7 focuses on the combined application of calcium sulphate hemihydrate, slag cement and quicklime to immobilise (stabilization / solidification) two contaminated soils by producing non-constructive concrete blocks. The first studied soil is heavily contaminated humus-rich soil and the second soil is a lightly contaminated humus-poor sand soil. Both soils were extracted from locations in the Netherlands and are common in the Netherlands. Besides the binder combination of slag cement with hemihydrate, the combination of slag cement with quicklime is studied. The advantage of the use of calcium sulphates is the possible formation of ettringite. Ettringite can fill the pores between the soil particles and so decrease the porosity and permeability. A lower porosity will result in a lower level of leaching. It is shown that the application of hemihydrate is most suitable for the humus rich soil, because of this high early strength. Furthermore it is shown that instead of increasing the binder content to overcome the negative effect of humus, replacement of half of the soil by primary 0-2 sand is more feasible, because it increases the compressive strength and reduces the capillary absorption and therefore the leaching of heavy metals.

## Packing of digitized particles\*

### 2.1 Introduction

This chapter focuses on the packing of digitized particles. Packing can be simply explained as the (regular or random) placement of particles in a container. An important parameter in the study of packing is the so-called packing fraction ( $f$ ), which can be calculated using

$$f = \frac{V_s}{V_T} = 1 - \varphi \quad (2.1)$$

with  $V_s$  the volume of the solid,  $V_T$  the total volume of the container and  $\varphi$  the void fraction. Packing is important with material science, since it is closely related to the microstructure, other physical properties (e.g. permeability, thermal conductivity) and durability (e.g. chloride penetration). Furthermore packing within concrete mixtures have for instance influence on the compressive strength. In this chapter packing of digitized particles is studied.

Packing of disks and spheres, both uniform and graded sizes, has been described in great detail in literature (Lubachevsky and Stillinger, 1990; Torquato, 2002; Brouwers, 2006). Besides these ideal disks and spheres also spheroids and irregular particles are studied (Wouterse, 2008). Within this chapter, the packing is studied from the perspective of digitized particles. The digitized particles are representing spherical particles in 'cubic' cellular automata system and are composed of voxels (cubic pixels) (Figure 1.5). The properties of the digitized particles are presented in Table 2.1. The background of cellular automata is described in Section 1.5. During the packing experiments these particles are placed in a confined geometry, here a cubic box with rib size  $L_{\text{box}}$ . Both the size of particle ( $d$ ) and box ( $L_{\text{box}}$ ) are expressed in the basic voxel size.

Jia and coworkers (Jia et al., 2007, 2002; Jia and Williams, 2001) have also performed simulations using digitized particles. Their research mainly focused on packing of particles of arbitrary shapes mostly in 2D, while the current research focus on regularly shaped particles in three dimensions. Furthermore in the current research, the influence of shape on the state of random close packing (RCP) is studied thoroughly.

### 2.2 Packing Theory

When studying packings, one can distinguish two types; ordered and disordered systems (Torquato, 2002), sometimes also referred to as regular and random systems. In the ordered systems the spheres/disks are positioned according to a crystal lattice, while in the disordered systems they are orientated in a random way.

---

\*Parts of this chapter were published elsewhere (De Korte and Brouwers, 2013b)

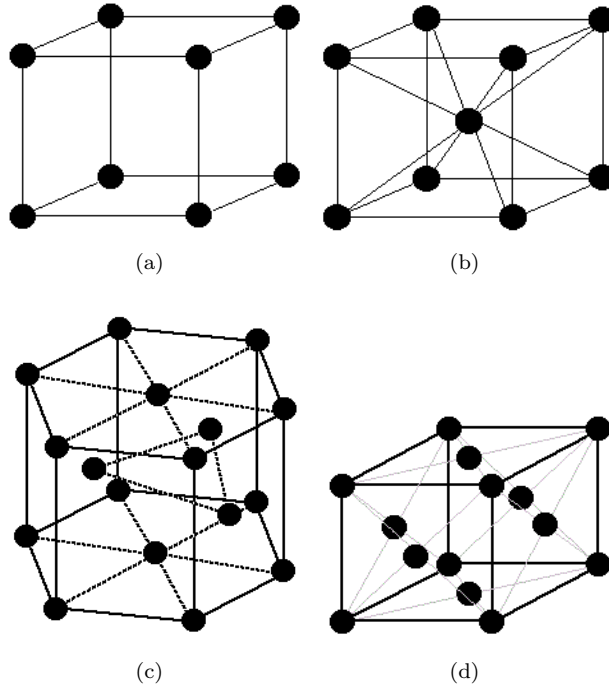


**Figure 2.1:** Unit cell of (a) simple cubic, (b) body centred cubic, (c) hexagonal close packed and (d) face centred cubic packing lattice.

Besides these different systems, an important parameter is the distinction in research of overlapping and hard spheres. In case of overlapping particles, the particles are allowed to overlap, while in case hard or impenetrable particles no overlap is allowed. In the present research hard particles are studied, since cement and gypsum particles can be considered as such.

### 2.2.1 Regular packing

Regular packing is for instance common within metals. Three crystal structures are found for most of the common metals; face-centred cubic, body-centred cubic and hexagonal close packed (Callister, 1996). A face-centred cubic crystal structure has an unit cell geometry, with atoms located at each of the corners and the centres of all the cube faces and cube edge length of  $4r\sqrt{2}$  with  $r$  the radius of particles. The body-centred cubic crystal structure has a cubic unit cell with atoms located at all eight corners and a single atom at the cube centre and its cube edge length equals  $4r/\sqrt{3}$ . The hexagonal close-packed crystal structure has a hexagonal unit cell. Its top and bottom faces consist of six atoms that form regular hexagons and surround a single atom in the centre. Table 2.1 and Figure 2.1 show the different regular packing situations for 3D systems (Torquato, 2002).

**Table 2.1:** Packing fraction ( $f$ ) and contact number  $\langle c \rangle$  of the different regular packings (Hilbert and Cohn-Vossen, 1999; Torquato and Stillinger, 2010).

Packing		$f$	$\langle c \rangle$
Tetrahedral		$\frac{\pi\sqrt{3}}{16} (\sim 0.34)$	4
Random Loose Packing	RLP	0.44	
Simple cubic	SC	$\frac{\pi}{6} (\sim 0.52)$	6
Random close packing	RCP	0.644	
Body centred cubic	BCC	$\frac{\pi\sqrt{3}}{8} (\sim 0.68)$	8
Hexagonal close packing	HCP	$\frac{\pi}{3\sqrt{2}} (\sim 0.74)$	12
Face centred cubic	FCC	$\frac{\pi}{3\sqrt{2}} (\sim 0.74)$	12

### 2.2.2 Irregular/random packing

The most dense irregular packing is the random close packing (RCP). Torquato et al. (2000) points out that this RCP-state concept is ill-defined and thus should be abandoned in favour of a more precise alternative. Their statement makes sense if one compares the found values by computer simulation in literature. For example, Jodrey and Tory (1985) achieves a packing between 0.642 and 0.649 by using a popular rate-dependent densification algorithm, Tobochnik and Chapin (1988) give 0.68 by using a Monte Carlo scheme, a differential-equation densification scheme by Zinchenko (1994) produces  $\sim 0.64$ , and a 'drop and roll' procedure by Visscher and Bolsterli (1972) yields  $\sim 0.60$  (Torquato and Stillinger, 2010). Instead of random packing, Torquato et al. (2000) prefers to use the concept of jamming, which is the amount of mechanical stability of collection of particles. Three categories of jamming were distinguished. The local jamming in which each particle in the packing is locally trapped by its neighbours and it cannot be translated while fixing the position of all other particles. The second category is collective jamming, in which any jammed configuration is collectively jammed if no subset of particles can simultaneously be displaced so that its members move out of contact with one another and with the remainder set. The third and last category is strict jamming in which any collectively jammed configuration that disallows all uniform volume-nonincreasing strains of the system boundary. Torquato (2002) uses the maximum random jammed (MRJ) instead of RCP (random closed packed). The MRJ is the point most disordered state at which still the jamming constraints (of one the three jamming categories) are met (Torquato and Stillinger, 2010). Methods for determining the ordering are described in Section 2.3.

In literature, several different packings algorithm are described and studied. The random sequential addition method places randomly, irreversibly and sequentially non-overlapping objects into a volume. The objects placed by this procedure are forever "frozen", so no movement of objects is allowed (Widom, 1966).

Lubachevsky and Stillinger (1990) describe two types of packing constructions, which allow movement, the "sequential" and the "concurrent" method. The sequential method typically begins with a small "seed", a fixed arrangement of particles, which then grows by addition of further particles one by one according to placement rules until a large aggregate has been formed. The algorithm used for placing particles in contact with those already present can either be deterministic or stochastic. The maximum packing us-

ing the random sequential addition (RSA) method found by Lubachevsky and Stillinger (1990) for 2D was 0.547 and for 3D 0.385 for spheres taking into account non-overlapping condition. The main disadvantage of random sequential addition methods is that as the number of spheres increases it becomes increasingly hard to add additional spheres. Furthermore, in general the obtained packing of the system is low, because the particles are not jammed (Wouterse, 2008). Sherwood (1997) has performed research to the RSA-packing of spheroids and found that when the particles are slightly non-spherical, the packing is maximal. This is the case for both both prolate ( $l/d \sim 1.4$ ) and oblate ( $l/d \sim 0.7$ ) spheroids, which reach a packing of 0.411 and 0.406 respectively.

Bennett (1972) developed a method, which partially overcomes this low state of jamming. The method starts with a suitable seed cluster on which then additional spheres are placed one at a time. The next sphere is placed in hard contact with three spheres below. The spheres remain static after placement. This leads to packing fractions between 0.60 and 0.63 and an average number of contacts of 6.0. Adams and Matheson (1972) further improved the method of Bennett (1972). Adams and Matheson (1972) add the next sphere at the tetrahedral site nearest to the origin instead of a randomly chosen tetrahedral site. They point out that each triplet of established points can give two sites for the addition of next spheres.

The concurrent methods have the entire collection of particles present from the start of the simulation and these methods utilize some appropriate procedure for arranging them into the final jammed configuration. Four categories can be identified: molecular dynamics, overlap elimination, energy minimization and contact network based (Wouterse, 2008). There are two possible ways of performing the simulations of packing. The first method is the Monte Carlo method, in which one can simulate a complex system by creating possible states of the system. This is done by successive random displacement of particles. Monte Carlo method is often used when studying rare events. Tobochnik and Chapin (1988) found a packing fraction of 0.68 using a Monte Carlo scheme. Zinchenko (1994) developed a isotropic kinetics-independent algorithm based on the Monte Carlo method. The algorithm forms a contact network at an early stage and retain contacts maximally throughout densification. Packing fractions obtained using this algorithm are between 0.628 and 0.637 for different number of particles, which corresponds to the experimental value for RCP. Williams and Philipse (2003) applied a mechanical contraction algorithm using Monte Carlo techniques as mathematic system. Mechanical contraction is based on the idea of density quenching of a system without any thermal fluctuations. Therefore a dilute equilibrium fluid of particles is prepared in a cubic cell with periodic boundary conditions. This fluid is the initial configuration of the system, which is then squashed to obtain an amorphous packing. Williams and Philipse (2003) have applied this method on both spheres and spherocylinders. For spheres they found a value of 0.631.

The second method is the molecular dynamics method. In this method the system is simulated by calculating the forces that each particle experiences and then integrating these forces to obtain new particle positions. Therefore the molecular dynamics is suitable for the study of time-dependent phenomena. An example of a molecular dynamics system is the Lubachevsky and Stillinger algorithm (Lubachevsky and Stillinger, 1990), which yields a packing fraction of 0.64 for the faster particle growth rates and close to 0.74 for the slowest growth rates (Torquato and Stillinger, 2010).

The Lubachevsky and Stillinger algorithm have been the main algorithm used in the last two decades to generate a wide spectrum of dense jammed sphere packings. Its event-driven packing protocols with growing particle has the disadvantage that it do not guarantee jamming of the final packing configuration (Torquato and Jiao, 2010). Therefore Torquato and Jiao (2010) introduced an new algorithm, the so-called Torquato-Jiao (TJ) algorithm. The TJ algorithm is an sequential-linear-programming solution of the adaptive-shrinking cell (ASC) optimization problem. Torquato and Jiao (2009) define the ASC problem as the problem of generating dense packings of nonoverlapping polyhedra with the deformation and compression/expansion of the cell boundary subject to periodic boundary conditions as an optimization problem. The TJ-algorithm always leads to jammed packings with a wider range of densities and degree of disorder than packings produced by the LS algorithm. Another advantage is that TJ-algorithm is computationally very efficient. Using the TJ-algorithm, Torquato and Jiao (2010) found an random packing (MRJ) of 0.640 and densest jammed packing of 0.741 for spheres.

Three different generation configuration algorithms based on local packing rules can be distinguished. The first method is the caging method. This method starts with placing a central sphere  $S$  at the origin and subsequently added neighbouring spheres to  $S$  at random fixed positions until  $S$  is caged. A particle is caged when its movement is fully blocked by randomly placed particles. The added neighbour spheres in the first coordination shell are in turn caged by more spheres, which are added randomly and form the second shell. The process continues with next shells. The second method is the parking method (Mansfield et al., 1996), in which the addition of spheres to central sphere continues until no space is available for addition of additional spheres. Then the same procedure is executed for the particles in the first shell (which are particle parked on the central sphere). The number of spheres parked on the central sphere equals to parking number. This number describes the maximum number of hard spherical particles that one can place randomly on a central particle. The third local algorithm is the drop and roll method, which is inspired on the work of Visscher and Bolsterli (1972). The first coordination shell is created as in the parking model, but the next shells are formed by dropping a sphere on the cluster from a random direction and then rolling it over the cluster surface until it contacts at least three spheres. This process is repeated for a fixed number of spheres.

Scott (1960) performed experiments in order to determ the random loose and random close packing of spheres. He found by extrapolating the values of measurements with small spherical flasks a value of 0.634 for the random close packing and 0.591 for random loose packing. Scott and Kilgour (1969) have extended the earlier experiment of Scott (1960) with more cylinders and the use of mechanical vibration techniques. After analyzing the experiments, Scott and Kilgour (1969) came to a value of 0.6366 for random close packing.

## 2.3 Methods for characterising packings

This section describes several methods for assessing the structure of packed system and determines the degree of ordering in the system. These methods are commonly used and describes by other researchers (Steinhardt et al., 1983; Torquato, 2002; Wouterse, 2008). Later on they will be applied for the packing of digitized particles.

### 2.3.1 Contact number / coordination number

The contact or coordination number gives an indication of the structure. This parameter determines the average number of contact of a particle by its neighbours, and gives an indication for the local-ordering. The contact number is defined as

$$\langle c \rangle = \frac{N_{con}}{N} = \frac{\langle C \rangle}{2} \quad (2.2)$$

With  $N_{con}$  the number of contacts in the packed system,  $N$  the number of particles,  $\langle C \rangle$  the average number of contacts per particle. The maximum number of contacts equals 12 according to Newton and 13 according to Gregory, as proved by Coxeter in 1962 (Mansfield et al., 1996) the corrected maximum contact number is 12. The coordination number for face-centred cubic and hexagonal close packed is equal 12 and therefore equal to the maximum value found by Newton. The body centred cubic has a coordination number of 8, while the simple cubic has a coordination number of 6 (Torquato and Stillinger, 2010).

For random packings, the coordination number per particle will differ from particle to particle, while the coordination number of regular packing is constant value across the microstructure. Although the variations among structures in random packing, there are some descriptive value which give an indication on the ordering of the system. The number, which plays a important role, is the so-called parking number  $\langle z \rangle$  (Mansfield et al., 1996). This number describes the maximum number of hard spherical particles that one can place randomly on a central particle. For equal sized spheres, this number equals 8.7 and in more general for hard spheres;

$$\langle z \rangle = K_p \left( \frac{r_1}{r_2} + 1 \right)^2 \quad (2.3)$$

With  $K_p = 2.187$  and  $r_1/r_2$  the sphere ratio (Mansfield et al., 1996). Another number is the caging number  $\langle \gamma_c \rangle$ , which is defined as the average maximum number of randomly placed particles required to block all movement of a central particle. The caging number of equally sized random packed spheres equals 4.71 (Philipse, 2003).

When assessing the number of contacts in a system, the random sequential additional (RSA) method will lead to an average number of contacts equal to 6.0, while the concurrent method either lead to 4.5, 5.83 or 6.14 contacts per particle. For the RCP also no conclusive answer can be found in literature. Mason (1968) reported a contactnumber of 5 using Scott's packing algorithm and data.

### 2.3.2 Radial distance function

The radial distribution function (RDF,  $g_2(r)$ ) is the probability function of finding a particle at a distance  $r$  from another particle normalized by the mean particle density. The RDF is defined as

$$g_2(r) = \frac{n(r)}{\rho \cdot 4\pi \cdot r^2 \cdot \Delta r} \quad (2.4)$$

With  $n(r)$  is the number of particles in a shell  $\Delta r$  at distance  $r$  and  $\rho$  is the average particle number density. The global  $g_2(r)$  can be obtained by calculating the  $g(r)$  for every particle and then be normalized such that it decays to unity for large  $r$  (Wouterse, 2008). Torquato (2002) gives  $g_2(r)$  as

$$g_2(r) = \frac{n_k(r)}{M \cdot N \cdot v_1(r)} \cdot \left( \frac{r^d}{\left(r + \frac{\Delta r}{2}\right)^d - \left(r - \frac{\Delta r}{2}\right)^d} \right) \quad (2.5)$$

With  $n_k$  the number of pairs of particles at distance  $r$ ,  $M$  the total number of configurations and  $N$  the total number of particles.

According to Rintoul and Torquato (1996) a peak in  $g_2(r)$  appears  $\sqrt{2}$  for fcc-lattice, but the absence of a peak is no proof of a disordered system. Aste (2005) points out that the presence of peaks around  $r/d \sim \sqrt{3}$  and  $r/d \sim 2$  are a clear indication that the system is organized or at least local patterns of crystallization are present. Aste (2005) points out that the peaks in the  $g_2(r)$ -graphs are dependent on local configurations. The peak around  $r/d \sim \sqrt{3}$  can be explained by placing the centres of four spheres on the vertices of two in-plane equilateral triangles (with edge length  $d$ ) which share an edge. But also by a configuration of five spheres placed on the vertices of two tetrahedra which share a common face. The  $r/d \sim 2$  peak can be explained by placing three or more spheres which are lying along a (rather) straight line. Radial distribution function for random packing will show a clear peak at  $r/d = 1$ , but further clear peaks will be absent. This does not implicate that the RDF remains on a constant value, since some deviations will be present, because of local jamming.

### 2.3.3 Bond orientation order

Steinhardt et al. (1981, 1983) define a measure for the assessment of bond orientation order in a packed system as

$$Q_{lm}(\vec{r}) \equiv Y_{lm}(\Theta(\vec{r}), \phi(\vec{r})) \quad (2.6)$$

Where the  $Y_{lm}$  are spherical harmonics and  $\Theta(\vec{r})$  and  $\phi(\vec{r})$  are the polar angles of the bond measured with respect to some reference coordination system. Since  $Q_{lm}$  is influenced by the choice of the reference system, normally the normalized  $Q_l$  is used, which reads

$$Q_l = \sqrt{\frac{4\pi}{2l+1} \sum_{m=-l}^l |\bar{Q}_{lm}|^2} \quad (2.7)$$

$Q_4$  and  $Q_6$  are often used.  $Q_4$  give a measure for the cubic symmetry and  $Q_6$  for the icosahedrally orientation of a system. The bond orientation order of a system for the different crystal lattices can be express by  $Q$ , reading;

$$Q = \frac{Q_6}{Q_6^{fcc}} \quad (2.8)$$

With  $Q_6^{\text{fcc}}$  the value of  $Q_6$  for fcc-lattice (0.575).  $Q$  is unity for fcc-based lattices.  $Q$  scales between 0 for complete disorder and 1 for perfect fcc ordering. Truskett et al. (2000) have related the other ordered packings to the  $Q$  and found  $Q = 0.615$  for simple cubic,  $Q = 0.844$  for hexagonal close packed and  $Q = 0.889$  for body centred cubic. The RCP-state has no fixed bond orientation order, since this state is disordered. Therefore the  $Q$  will be below the value for simple cubic, which can also be concluded from the results given by Kansal et al. (2002).

### 2.3.4 Translational order metric

Torquato et al. (2000) defines a simple translational order metric  $T$ , which measures the degree of spatial ordering, relative to the perfect FCC lattice at the same volume fraction. The equation for  $T$  reads

$$T = \left| \frac{\sum_{i=1}^{N_c} (n_i - n_i^{\text{ideal}})}{\sum_{i=1}^{N_c} (n_i^{\text{FCC}} - n_i^{\text{ideal}})} \right| \quad (2.9)$$

With  $n_i$  the average occupation number for the shell of a width  $\delta$  centred at a distance from a reference sphere that equals the  $i$ th nearest-neighbor separation for the open FCC lattice at that density. Moreover,  $a$  is the first nearest-neighbor distance for that FCC lattice, and  $N_c$  is the total number of shells. Similarly,  $n_i^{\text{ideal}}$  and  $n_i^{\text{FCC}}$  are the corresponding shell occupation numbers for an ideal gas (spatially uncorrelated spheres) and the open FCC-lattice. Note that  $T = 0$  corresponds to an ideal gas (perfect randomness) and  $T = 1$  to perfect FCC spatial ordering. For the RCP-state no fixed translational order metric exists, since this packing state is disordered, while  $T$  describes the degree of ordering. Nevertheless, based on results from Kansal et al. (2002) a translational order metric of around 0.2 seems reasonable for the RCP-state.

Gao and Kilfoil (2004) and Errington et al. (2003) show that the translational order metric is related to the radial distribution function in the following way

$$T = \frac{1}{r_c - d} \int_d^{r_c} |g_2(r) - 1| dr \quad (2.10)$$

With  $d$  the diameter of the particle and  $r_c$  the cut-off distance that ensures integration over an equal number of coordinate shells. In the current chapter the cut-off distance of half the box is used.  $g_2(r)$  is unity for an ideal gas and therefore  $g_2(r) - 1$  provides a measure of the deviation of the structure from that of an ideal gas.

### 2.3.5 Particle shape

Barrett (1980) distinguishes three parameters to describe the shape of a particle; form, roundness and surface texture, based on literature review of numerical methods to describe these parameters. Most of these methods are not suitable for digitized particles, which are regularly shaped and have equal dimensions in three perpendiculars, like spheres. For instance the flatness as defined by Wentworth (1922) reads

$$flatness = \frac{L \cdot S}{2 \cdot I} \quad (2.11)$$

with L the length of the long axis, I the length of intermediate axis and S the length of the short axis. For both spheres and digitized particles studied here, the flatness equals unity. Wadell (1932) gives a indices for the sphericity of the particle, which is defined as

$$\psi = \sqrt[3]{\frac{V_p}{V_{cs}}} \quad (2.12)$$

Whereby  $V_p$  and  $V_{cs}$  are the particle volume and the volume of circumscribing sphere, respectively. Lees (1964) uses a slightly different definition of sphericity, being the ratio of the surface area of a sphere having the same volume as the particle to the actual surface area of the particle. Lees (1964) defines roundness as the ratio between the radius of curvature of a projection on the silhouetted outline of a particle and the radius of curvature of the maximum inscribed circle in the silhouette in the same plane. Lees points out that the roundness method is unable to differentiate between truly angular corners of different angles, since the radius of curvature of a circle fitted an angular corner is independent of the size of the angle. Furthermore, circles of identical radius can be fitted into corners of widely different angle which are rounded off to a different extent, assigning identical roundness values to forms of clearly different angularity. Furthermore using this definition of roundness, the roundness of a cube and sphere will be both unity, since the radius of curvation equals the radius of maximum inscribed circle. Lees (1964) introduced therefore degree of angularity as a distinct concept, since angularity is clearly not just the absence of roundness. The equation of Lees for angularity in two dimensions reads

$$Ang_{2D} = \sum (180^\circ - a) \frac{x}{r} \quad (2.13)$$

and for 3D

$$Ang_{3D} = \sum_{i=1}^3 Ang_{2D,i} \quad (2.14)$$

with a as the measured angle, x the distance of the tip of the corner from the centre of the maximum inscribed circle and r the radius of the maximum enveloping circle (Figure 2.2). The 3D-angularity is the summation of the angularity in the three perpendicular directions. A disadvantage of this method is that when the number of corners increases the angularity increases. The angularity is between zero for particles with no angles (i.e. spheres) and infinity for particle with a large number of angles.

The definition for roundness as given by Lees (1964) cannot be applied for particle with squared angles, and this method is designed for assessing 2D projections of particles. Hence, in the present chapter a different approach is proposed for non spherical digitized

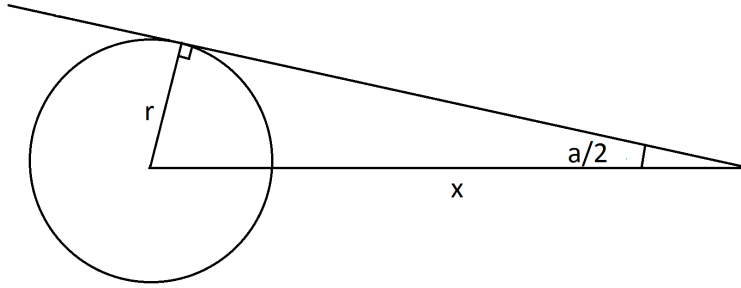


**Figure 2.2:** Example of the calculation of angularity (Lees, 1964).

particles which possess squared corners, symmetrical dimensions in respect to the  $x$ ,  $y$ ,  $z$  axis and flat top-surfaces (Figure 1.5). Hence, the following equation for the digitized roundness is proposed

$$\epsilon = \frac{A_p - 6A_t}{A_p} \quad (2.15)$$

With  $A_p$  the total surface area of the digitized particle (Figure 1.5) and  $A_t$  the surface area of one of the top-surfaces. The top-surfaces are defined as the surfaces of the digitized particle, laying perpendicular to the three main directions at  $x = r$ ,  $y = r$  or  $z = r$ . In Figure 1.5 the top-surfaces of the  $d = 7$  particle are presented in grey as an example. The digitized roundness is unity for a perfect sphere and zero for a cube.

When comparing the two methods, two main differences can be noticed. The first difference is that the angularity presented by Lees (1964) is a property based on 2D projections of a particle, while the here introduced digitized roundness accounts for its true 3D features. The second main difference is the scale used for both methods. The digitized roundness is a number between zero (cube) and unity (sphere), while the angularity is a number in between 0 and infinity.

Furthermore the particle shape can be described using the shape factor (Taylor, 1997) which reads

$$F = \frac{d \cdot A_p}{V_p} \quad (2.16)$$

with  $d$  the particle size,  $A_p$  the surface area of the particle and  $V_p$  the volume of the particle. Table 2.2 shows the shape factor  $F$ , Wadell's sphericity  $\psi$  and digitized roundness  $\epsilon$  of the digitized particles used in this research. From this table, one can notice that the shape factor  $F$  for  $d = 7$  and  $d = 11$  is much lower than for the other particles, which partially explains the differences visible in Figure 2.3.

## 2.4 Simulations

This section first describes the digitized particles including their properties. These digitized particles are applied in both regular (Section 2.4.2) and random (Section 2.4.3) packing simulations. Whereas the regular packing is based on unit cells and known crystal lattices, for the random packing two packing algorithms are applied. The first packing simulation model was based on CEMHYD3D (Bentz, 1995; Chen, 2007; Van Eijk, 2001). It will appear that another packing algorithm is required for the packing of mono-sized digitized particles and therefore an algorithm based on Lubachevsky and Stillinger (1990) is applied.

### 2.4.1 Digitized particles

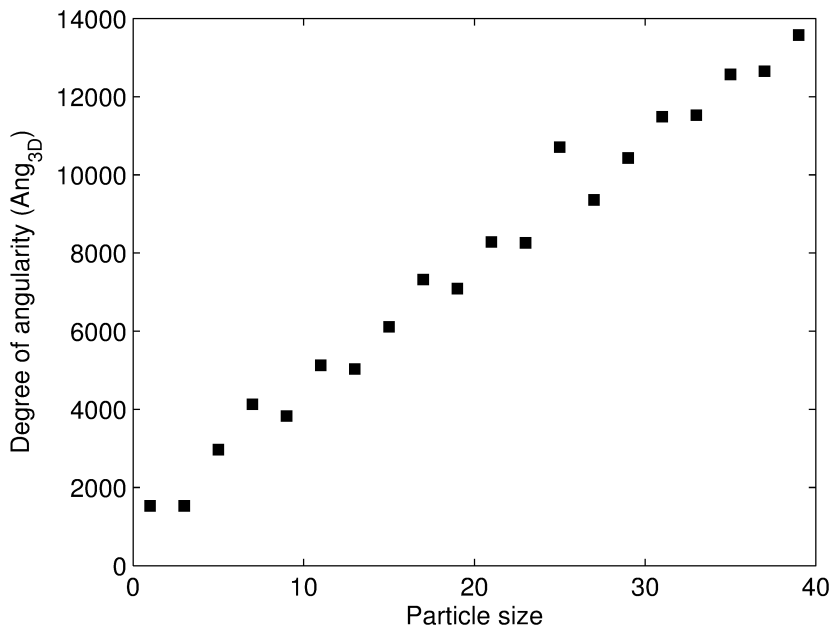
For this research we use digitized particles instead of 'real' spheres. Therefore one should pay attention to the difference between 'real' spheres and 'digitized' particle, since they differ in volume and surface area. Table 2.2 shows the properties of both spheres and digitized particles. As can be seen in the table, the difference in volume between both is small for particles with a size of more than 7 voxels ( $d \geq 7$ ). Therefore within the present research only particles with a size of 7 voxels or more are used.

From Figure 2.3(a) and Table 2.2, one can notice that the angularity increases with increasing size. This is caused by the increasing the number of corners at larger diameters. Furthermore the angularity increases, while the shape resembles a sphere better based on visual inspection of the digitized particles. Therefore Ang3D is not a suitable parameter. Table 2.2 and Figures 2.3(b) show the digitized roundness, introduced in the previous section, and Wadell sphericity for different digitized particles. One can notice that the digitized particle comes closer to unity (sphere) with increasing size. Therefore both the digitized roundness and Wadell sphericity seems to be a suitable measure to describe the particle shape of digitized particles.

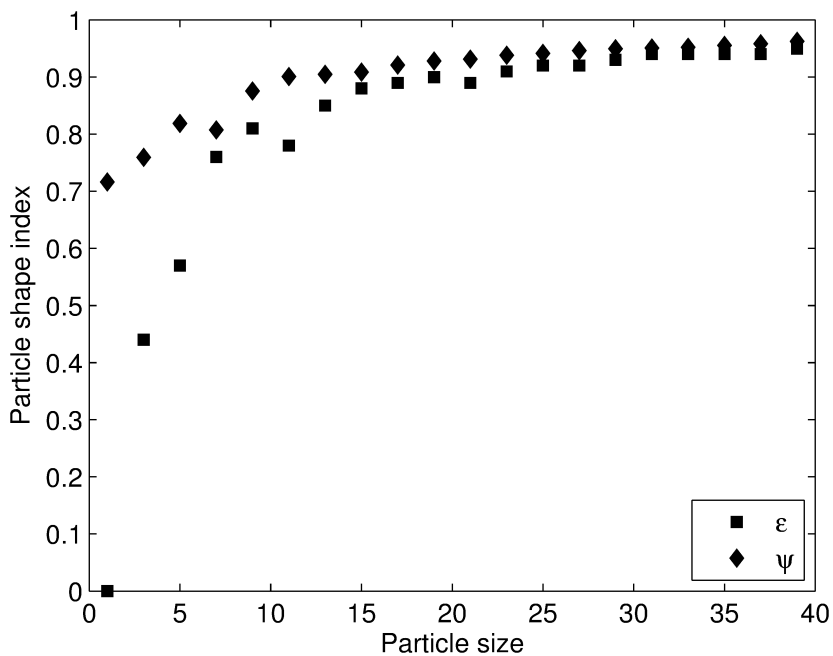
### 2.4.2 Regular packing with digitized particles

In Section 2.2, several regular packings were described. Based on Table 2.1, one can notice that the face-centred cubic and hexagonal close packing are the densest regular packings for spheres. In this section, the different packing structures are studied for digitized particles and compared with values for spheres. One should be aware that due to the difference between spheres and digitized particle, different packing orientations compared to spheres can be result in the highest packing for digitized particles. Furthermore the packing fractions for the fcc and hcp lattice can differ for digitized particles, while these lattices provide same value for spheres.

For the study of the regular system is necessary to distinguish between the different crystal systems. Table 2.3 shows the different crystal systems including their axial relationships and inter-axial angles. Within this research we focus on the cubic, tetragonal orthorhombic and hexagonal systems. The differences between these crystal systems are the dimensions (a, b, c) of the unit cell, the smallest element which is repeated and the angles between the axes ( $\alpha$ ,  $\beta$  and  $\gamma$ ). Whereas the cubic crystal system provides the smallest unit cell for monosized spheres, other crystal systems provide the smallest unit cell for digitized particles. Table 2.4 and Figure 2.4(a)-2.4(d) show the packing for different voxel sizes using the different crystal structures (Table 2.1) and crystal systems



(a)



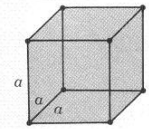
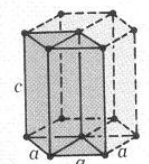
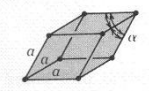
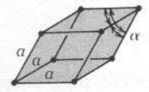
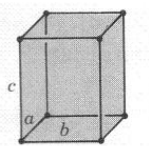
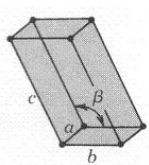
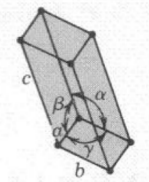
(b)

**Figure 2.3:** (a) Angularity of digitized particles (Eq. 2.14), (b) the digitized roundness ( $\epsilon$ ) (Eq. 2.15) and Wadell sphericity ( $\psi$ ) (Eq. 2.12) of the digitized particles.

Table 2.2: Volume and surface of spheres and digitized particles (Van Eijk, 2001).

Size d $\mu\text{m}$	Digitized particle			Digitized particle / sphere ratio			Roundness	
	Volume V $\mu\text{m}^3$	Surface S $\mu\text{m}^2$	Shape factor F	$\psi$ Eq. (2.12)	Ang <sub>3D</sub> Eq. (2.14)	$\epsilon$ Eq. (2.15)	Angularity	Roundness
1	1	6	6.00	1.00	0.716	1527	0.00	0.00
3	19	54	8.53	1.42	0.760	1527	0.44	0.44
5	81	126	7.78	1.30	0.819	2969	0.57	0.57
7	179	222	8.68	1.45	0.807	4131	0.76	0.76
9	389	414	9.58	1.60	0.876	3828	0.81	0.81
11	739	582	8.66	1.44	0.901	5124	0.78	0.78
13	1189	822	8.99	1.50	0.905	5031	0.85	0.85
15	1791	1062	8.89	1.48	0.909	6110	0.88	0.88
17	2553	1350	8.99	1.50	0.921	7322	0.89	0.89
19	3695	1758	9.04	1.51	0.928	7090	0.90	0.90
21	4945	2094	8.89	1.48	0.931	8281	0.89	0.89
23	6403	2526	9.07	1.51	0.938	8262	0.91	0.91
25	8217	2934	8.93	1.49	0.942	10707	0.92	0.92
27	10395	3462	8.99	1.50	0.946	9362	0.92	0.92
29	12893	3990	8.97	1.50	0.949	10432	0.93	0.93
31	15515	4494	8.98	1.50	0.951	11492	0.94	0.94
33	18853	5166	9.04	1.51	0.952	11528	0.94	0.94
35	22575	5838	9.05	1.51	0.956	12571	0.94	0.94
37	26745	6510	9.01	1.50	0.958	12564	0.94	0.94
39	31103	7206	9.04	1.51	0.963	13582	0.95	0.95

**Table 2.3:** Lattice parameter relations and unit cell geometries for crystal systems (Callister, 1996).

Crystal system	Axial Relationships	Interaxial Angles	Unit Cell Geometry
Cubic	$a = b = c$	$\alpha = \beta = \gamma = 90^\circ\text{C}$	
Hexagonal	$a = b \neq c$	$\alpha = \beta = 90^\circ\text{C}, \gamma = 120^\circ\text{C}$	
Tetragonal	$a = b \neq c$	$\alpha = \beta = \gamma = 90^\circ\text{C}$	
Rhombohedral	$a = b = c$	$\alpha = \beta = \gamma \neq 90^\circ\text{C}$	
Orthorhombic	$a \neq b \neq c$	$\alpha = \beta = \gamma = 90^\circ\text{C}$	
Monoclinic	$a \neq b \neq c$	$\alpha = \gamma = 90^\circ\text{C} \neq \beta$	
Triclinic	$a \neq b \neq c$	$\alpha \neq \beta \neq \gamma \neq 90^\circ\text{C}$	

**Table 2.4:** Theoretical most dense packing of digitized particles (bc = body-centred, fc = face-centred).

Size	Cubic			Hexagonal	Tetragonal		Orthohombic	
	scc	bcc	fcc	hcp	bc	fc	bc	fc
1	1							
3	0.704	0.594			0.594			
5	0.648	0.75			0.75		0.75	
7	0.522	0.358	0.716	0.556	0.559	0.895	0.559	0.895
9	0.534	0.778	0.567	0.463	0.778	0.662	0.778	0.662
11	0.555	0.539	0.722	0.658	0.733	0.825	0.733	0.825
13	0.541	0.581	0.595	0.713	0.674	0.702	0.674	0.702
15	0.531	0.614	0.673	0.708	0.777	0.757	0.777	0.757
17	0.520	0.638	0.581	0.692	0.716	0.724	0.716	0.785
19	0.539	0.694	0.673	0.700	0.711	0.725	0.711	0.692
21	0.534	0.563	0.733	0.681	0.681	0.785	0.681	0.746
23	0.526	0.729	0.652	0.683	0.741	0.692	0.741	0.692
25	0.526	0.609	0.704	0.698	0.715	0.746	0.715	0.746
27	0.528	0.634	0.65	0.682	0.698	0.693	0.698	0.693
29	0.529	0.656	0.696	0.699	0.716	0.731	0.716	0.731
31	0.521	0.665	0.729	0.702	0.721	0.763	0.721	0.763
33	0.525	0.687	0.682	0.682	0.709	0.712	0.709	0.712
35	0.527	0.609	0.722	0.698	0.697	0.752	0.717	0.752
37	0.528	0.628	0.679	0.705	0.712	0.706	0.732	0.706
39	0.524	0.639	0.708	0.683	0.72	0.735	0.72	0.735

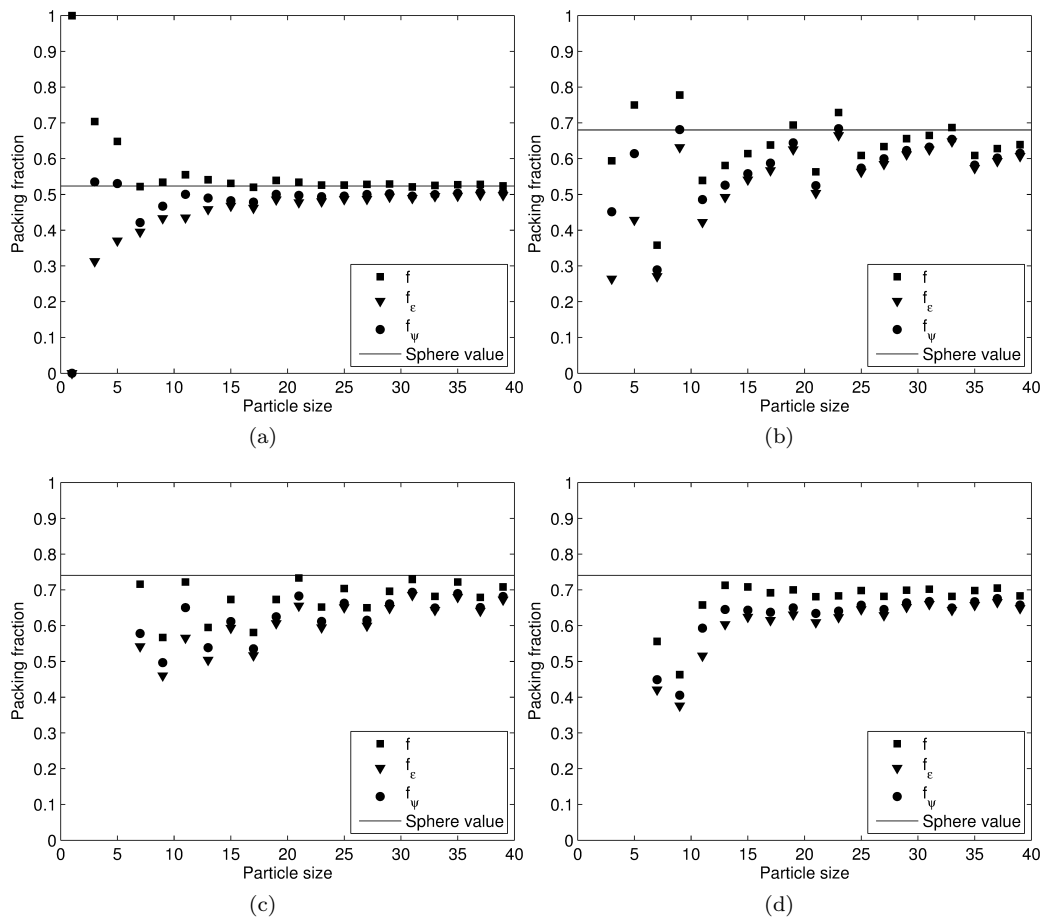


**Figure 2.4:** Regular packings of digitized particles (a) simple cubic (b) body centred cubic (c) face centred cubic and (d) hexagonal close packed. The straight lines indicate the packing fraction of spheres.

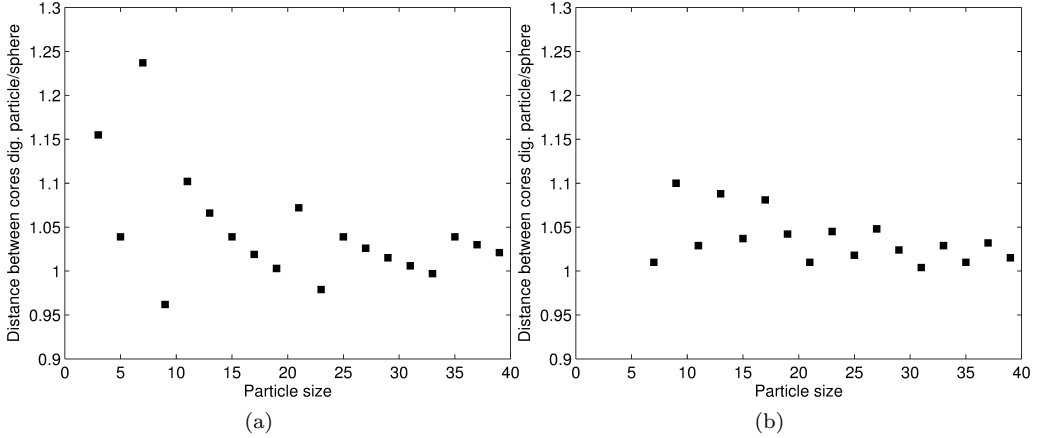


**Figure 2.5:** The ratio of distance of cores of (a) bcc, (b) fcc packing of digitized particles versus their sphere pendant.

(Table 2.3). Furthermore Figures 2.4(a)-2.4(d) present the product of the packing fraction with the digitized roundness. This modification does not improve the results found. One can notice from Table 2.4 and Figure 2.4 that the lowest regular packing fraction is derived for the simple cubic system (Fig. 2.4(a)) and that this value is comparable to the value for spheres. The value for body centred cubic are in general lower than the sphere pendant ( $\sim 0.68$ ), especially for  $d = 11$  (voxels) and  $d = 21$  (Fig. 2.4(b)). The distance between the digitized particles differs from sphere pendant (Fig. 2.5(a)). Particles of  $d = 11$  and  $d = 21$  have a higher distance between particles compared to the unit cell sphere pendant, while  $d = 9$ ,  $d = 23$  and  $d = 33$  have a relative distance smaller than unity. The determined contact numbers are equal to sphere pendants, except for  $d = 7$ ,  $d = 11$ ,  $d = 15$ ,  $d = 21$ ,  $d = 25$ ,  $d = 35$  and  $d = 39$ , which are equal to 0. This means that the centered particle is rattling in between the other particles.

The derived value for the face centred cubic lattice gives the most dispersed results. The packing values for digitized particles are considerably lower for  $d = 9$ , 13 and 17, equal to sphere pendant ( $\sim 0.74$ ) for  $d = 11$ , 21 and 31 and slightly lower for all other sizes (Fig. 2.4(c)). The distance between digitized particles (Fig. 2.5(b)) is higher than those of spheres. This result in a lower packing fraction ( $f$ ) for the digitized particles compared to the sphere pendant. If one assesses the trend in the found particle distance, one can notice that the distance for  $d = 11$  and  $d = 21$  is clearly different compared to the other diameters. For all diameters a contact number of 12 has been found during analysis, which is equal to the sphere pendant.

Besides the cubic crystal systems also the other crystal systems have been studied in order to assess the possible dense packing structures. During the analysis of the values for hexagonal close packing for digitized particles, one can notice from Figure 2.4(d) that for sizes smaller than 13 the obtained value is considerably lower than the sphere case ( $\sim 0.74$ ). For  $d \geq 13$  the value is between 0.68 and 0.71, which is lower than hcp of spheres. When analysing the hcp structures, one can notice that the distance between the digi-

tized particles within the layers is between 0.98 and 1.08 times the sphere pendant. The angle between the particles within the layers is around  $60^\circ$ , which is equal to the sphere packing. The distance between the layers is higher than for spheres except for  $d = 21$ , which is lower. When determining the contact number of the produced regular packings with digitized particles, a contact number of 12 is found, except for  $d = 9$  (14) and  $d = 31$  (10). This contact number corresponds to the sphere value.

One can notice from Table 2.4 that the values for the tetragonal and orthorhombic crystal systems are in general the same. The main reason for this is the condition that the digitized particle is in the centre of either the body or the face, and the fact that the digitized system requires that the coordinates of the centre of digitized particle to be an integer. These conditions often lead the fact that at least two sides to be equal. From Table 2.4, it can be concluded that the face centred tetragonal and orthorhombic systems have a higher packing fraction than the comparable body centred systems except for  $d = 9, 13$  and  $23$ . The contact number of orthombic and tetragonal face centred equals 14 for  $d = 7, 10$  for  $d = 13, d = 15$  and  $d = 17, 8$  for  $d = 13$  and 12 for all other diameters. The body-centred tetragonal systems have a contact number of 12 except for  $d = 5$  and  $d = 9$ , which have a contact number of 14.

The maximum theoretical packing fraction for digitized systems of monosized particles of different diameters is in general comparable to the maximum packing fraction of monosized spheres. The maximum packing fraction is 0.895 for  $d = 7$  followed by 0.825 for  $d = 11, 0.785$  for  $d = 21$  and 0.778 for  $d = 9$ . The lowest maximum packing fraction found is 0.698 for  $d = 27$ . The differences in the maximum packing fraction are caused by the possibilities for interlocking of the digitized particles at a certain size.

### 2.4.3 Random packing results

#### Packing routine

Bentz (1995) model generates an initial microstructure by placing digitized particles in the 3D box at random locations from largest to smallest particle size with periodic boundaries (Van Eijk, 2001). This model has been developed for the creation of the initial microstructure using graded particles rather than monosized particles. Using this module for uniform particle sizes, a packing fraction up to 0.379 was found for  $d = 13$  and  $L_{\text{box}} = 100$ . This is close to RSA (random sequential addition) of 0.385 as found by Williams and Philipse (2003). The found value is far below the random close packing (RCP) of 0.634 (Song et al., 2008). The packing resulting from the makecem-module is not surprising, since the found packing is line with expectations based on the algorithm. Since this original model was developed to create a starting microstructure for cement hydration and is not aimed to acquire close packings of monosized particles, a new packing routine has been developed. The used routine is comparable to the sequential methods as described by Lubachevsky and Stillinger (1990), which obtained a packing fraction of 0.634 for monosized spheres. This value is compatible with random close packing (RCP) values from experiments (Scott, 1960; Scott and Kilgour, 1969).

Within the new routine, particles are placed randomly in a box, after placing a new particle all other particles are moved. The movement of the particles and speed of addition of particles is described by two parameters. The first parameter governs the number of moves (over a distance of 1 voxel in x, y or z direction) that each particle

**Table 2.5:** Parameters of the used packing simulation model.

Parameter	Explanation
2D/3D	Dimensions of the matrix (2D is disk, 3D is sphere packing)
Boundary condition	0. No boundaries 1. Boundaries on all sides of the box. 2. Only bottom boundary 3. Limited movement over the bottom of the box 4. Modified x boundaries
$L_{\text{box}}$	The size of the box (in voxels) in which the disks/spheres are placed.
$n_t$	The maximum number of attempts to move a disk/sphere
$n_m$	The number of moves of disk/sphere in each placing round
$r$	Radius of disk/sphere (in voxels)

attempts to make during a movement cycle ( $n_t$ ). The second parameter is the number of movement cycles ( $n_m$ ). Furthermore different boundary conditions can be applied, which each have a certain limitation on moves over the boundaries of the box (Table 5). These boundary conditions range from periodic boundary conditions on all sides to the limitation of particle movement across the boundaries of the box (the faces of the cubic box). During this research, a combination of both boundaries was applied. The movement through the top and bottom surface of the box was limited, will applying periodic boundaries on the other sides. Table 2.5 shows the used parameters of the packing algorithm.

### Influence input-parameters

This subsection focuses on the influence of boundary conditions and the amount of particle movement on the acquired packing fraction. The outcomes of these tests will be used to determine the suitable input parameters for the extensive set of simulations, which will be reported in Section 2.4.3.

The effect of the boundary conditions is studied using particles with diameter  $d = 13$  in boxes of 200, 300 and 400 voxels ( $L_{\text{box}} = 200, 300$  and  $400$ ), respectively. Table 2.5 shows the different boundary conditions which can be applied on the simulation, which range from full periodic boundaries to a fixed bottom of the box. Figure 2.6 shows the results from these tests. One can notice that the packing fraction is highest for boundary condition 2, which used an impenetrable bottom of the box and periodic condition on the other sides. The lowest packing fraction is found for boundary condition 0, which use periodic boundary on all sides.

The effect of variation the number of moves of the particles has been studied using a  $L_{\text{box}} = 300$  and  $d = 13$ , using boundary condition 2. Figures 2.7(a) shows the influence of the amount of motions on the packing fraction. One can notice that number of moves has a clear influence on the packing fraction and that packing fraction goes to an asymptote for an increasing number of moves. For  $n_m > 20$  the obtained packing fraction is in the same range. Furthermore it can be noticed from Figure 2.7(a) that the number of tries

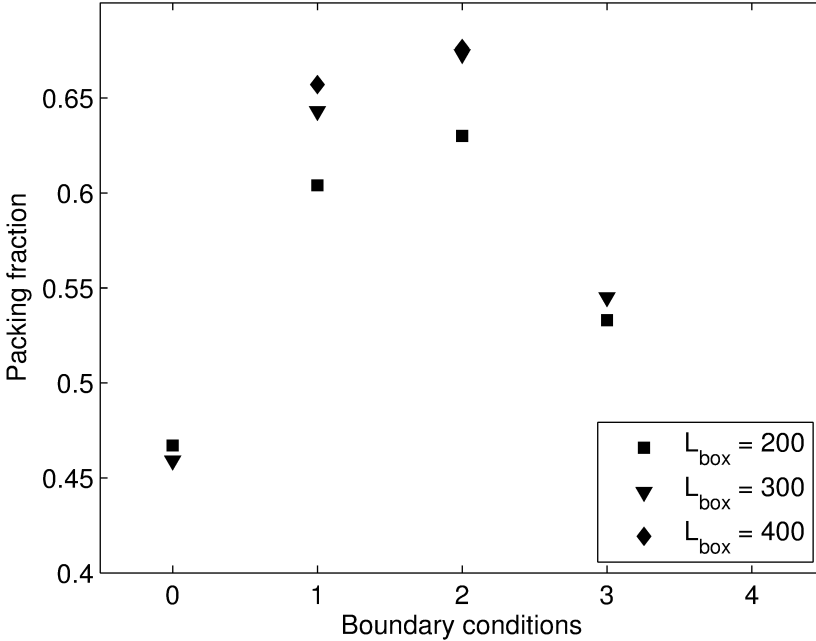
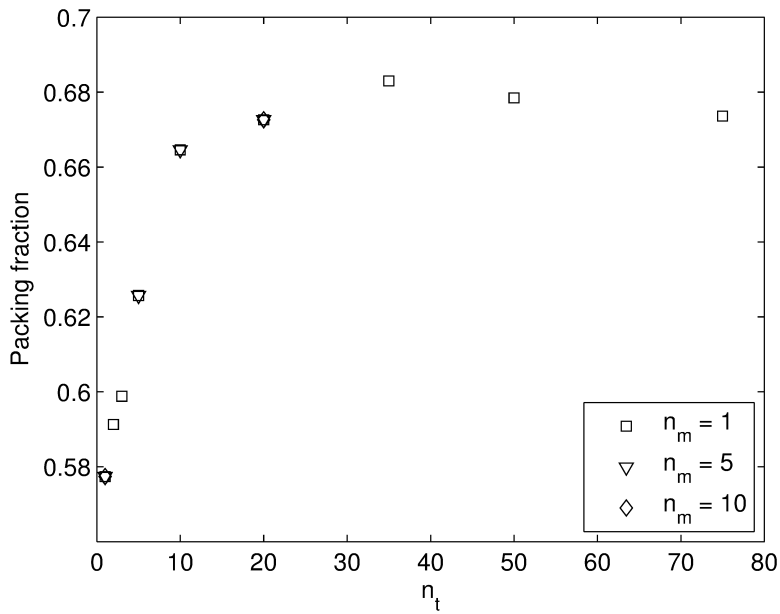


**Figure 2.6:** Packing fraction using different boundary conditions ( $n_t = 10$  and  $n_m = 20$ ) for three boxes ( $L_{\text{box}} = 200, 300$  and  $400$  voxels) and particle with  $d = 13$ .

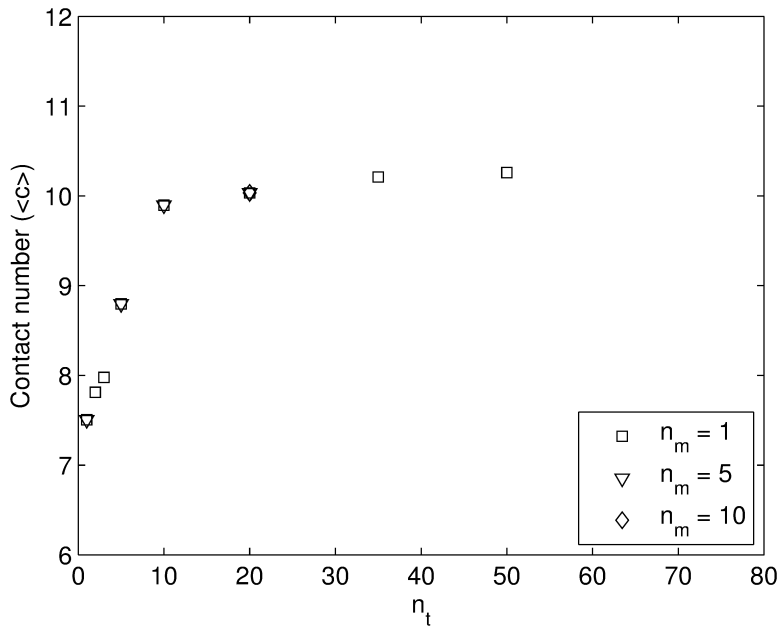
has no effect on the obtained packing fraction. The number of moves can be compared to the amount of shaking of the box. It is known from experiments that the packing increases with increase of vibration of the box (Scott, 1960; Scott and Kilgour, 1969). Furthermore, Torquato and Stillinger (2010) found that the fastest growth rates generated the most disordered sphere packings (with  $f = 0.64$ ), but that by slowing the growth rates larger packing fractions could be continuously achieved up to the densest value ( $f = \pi/\sqrt{18} \sim 0.74$ ). Due to the increase of the motion of the particles, the particles have more time to settle and therefore the growth rate is low. Therefore the present results are compatible with those of Torquato and Stillinger (2010). Figure 2.7(b) show the influence of the particle motion on the contact numbers. One can notice that the contact numbers increase with increasing motion.

### Simulation results

All further simulations were performed using boundary condition 2 (limitation of the movement through bottom of the box, while applying periodic boundaries on all other faces of the box),  $n_t = 10$  and  $n_m = 20$ . Figure 2.8 show the results of these simulations. One can notice that there is a clear relation between size ratio  $l$  and the packing fraction  $f(l)$ , a similar trend can be observed as by Desmond and Weeks (2009). One can see that  $f(l)$  tends to a limiting value for the higher size ratios  $l$ , higher than the RCP value for spheres (0.64), particularly for  $d = 7$ ,  $d = 11$  and  $d = 21$  particles. Jia and Williams



(a)



(b)

**Figure 2.7:** The effect of movement on the random packing fraction (a) for different  $n_t$  and (b) relation between  $n_t$  and contact number for  $L_{\text{box}} = 300$  voxels and  $d = 13$ .

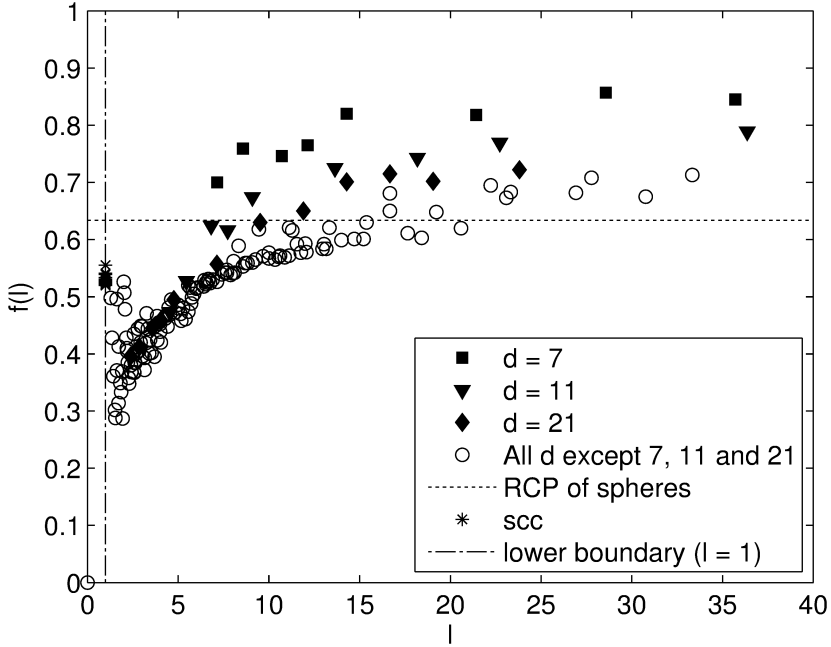


**Figure 2.8:** Relation between size ratio  $l$  ( $L_{\text{box}}/d$ ) and random packing fraction ( $n_t = 10$ ,  $n_m = 20$ , boundary-condition 2).

(2001) found a similar result when packing identical circles in their 2D-system DigiPac. They found a value of 0.875, which is in between the value for random packings (0.82) and crystals (0.91), which according to these authors indicates that the generated structure contains crystal domains. During preliminary tests in 2D during our research we have found a comparable value of 0.877 for  $L_{\text{box}} = 350$  and  $d = 11$ . Caulkin et al. (2006) investigated packing of mono-sized spheres, binary and ternary mixed beds both experimental and using DigiPac using cylindrical containers and found a maximum packing fraction of 0.599 for mono-sized spheres. The main difference with this research is the absence of periodic boundaries and the shape of the container.

Furthermore, from Figure 2.8 one can observe a raise in the found packing fractions close to  $l = 1$ , which is caused by the finite size effect as observed by McGeary (1961) during experiments and described in Desmond and Weeks (2009).

The data presented in Figure 2.8 is obtained using cubic boxes with equal dimensions in the three directions. Figure 2.9 shows the effect of changing the height of the box for different dimensions of a square bottom and  $d = 13$ . Figure 2.9 shows the data scaled to the maximum packing fraction obtained for a particular bottom size ratio  $h$  ( $H_{\text{box}}/d$ ). As one can notice the height of the box ( $H_{\text{box}}$ ) has an influence on the packing density. Furthermore a raise in the packing fraction can be observed close to  $h = 1$ , comparable to the effect at  $l = 1$  and which can be explained by the work of Desmond and Weeks (2009) as well as McGeary (1961).

Besides the packing fraction to assess the packing, other parameters are also available,

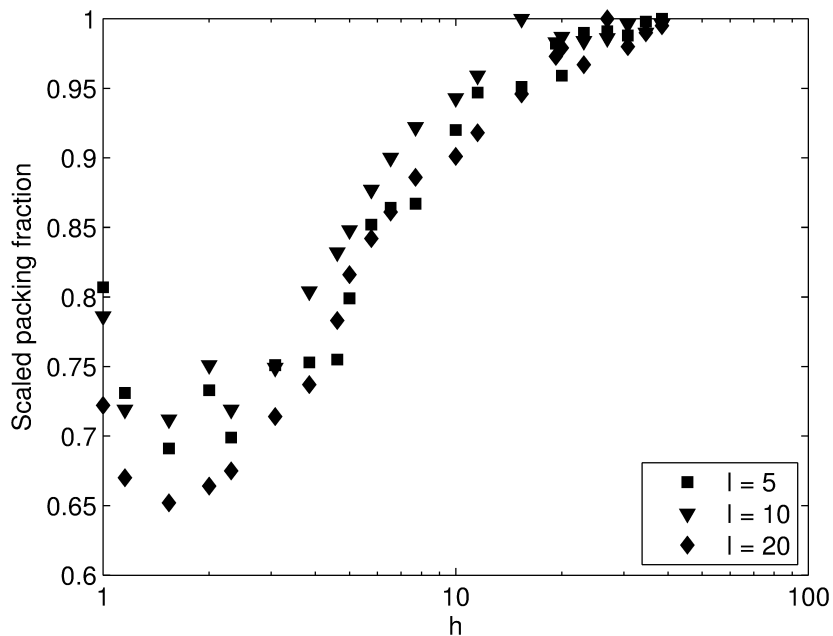


**Figure 2.9:** Relation between height ratio  $h$  ( $H_{\text{box}}/d$ ) and the scaled random packing fraction for different size ratios of the box bottom ( $L_{\text{box}}/d$ ) ( $n_t = 10$ ,  $n_m = 20$ ,  $d = 13$ , boundary-condition 2) (scaling of the packing fraction by the maximum packing fraction of a certain  $l$ ).

such as the contact number and translational order metric (Section 2.3). Figure 2.10 shows the average contact number for several of the performed 3D-simulations. From the results, one can notice a linear trend between aspect-ratio ( $l$ ) and contact number ( $\langle C \rangle$ ) (Figure 2.10(a)). Furthermore the contact number is linearly related with the packing (Figure 2.10(b)). This linear trend is almost equal to the linear trend found by Aste (2005), who used a cylindrical container for his simulations, while in this research a cubic container is used. For some simulations with high packing, the contact number is higher than the caging number, which could indicate some ordering in the system. Furthermore one can notice contact numbers higher than 12, which is higher than one should expect from theory. These extreme values are all caused by particles with  $d = 7$ , most probably due to their particle shape.

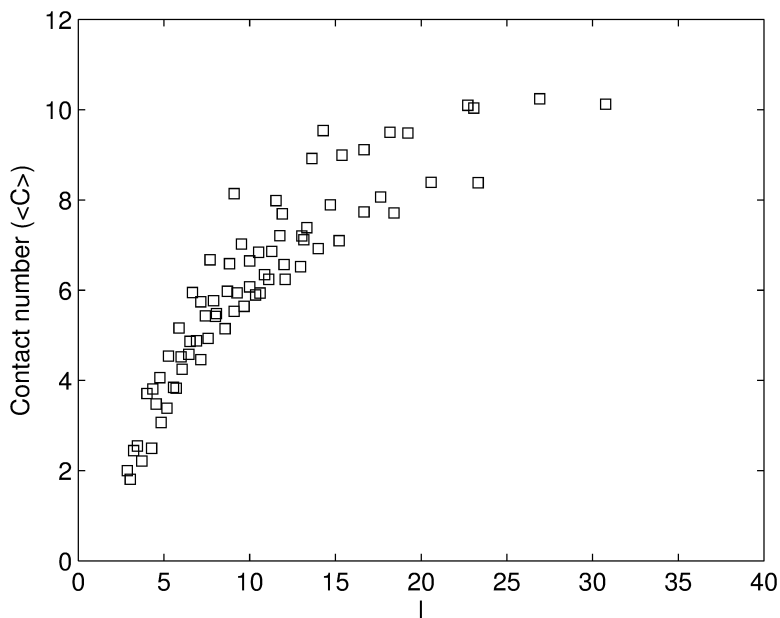
When assessing the  $g_2(r)$ -graph, one can notice that the first peak lies at a value smaller than unity. This is caused by the digitized particle, since the cores of spheres can lay at a distance less than the diameter of the spheres. This is caused by interlocking of the particles. Figure 2.11 shows the minimal and maximum distance between the cores of digitized particles which are in contact with each other. Within the  $g_2(r)$ -graphs also some small peaks are visible, but it is not clear if their size is sufficiently significant to indicate ordering. Furthermore, the absence of these peaks would not prove that a disordered system is generated.

As already noticed in Figure 2.8, all particle sizes tend to a random packing fraction larger than 0.64, the RCP value of spheres. The effect was most pronounced for  $d = 11$  and  $d = 21$ . One possible explanation is the angularity of these digitized particle (Section 2.4.1).

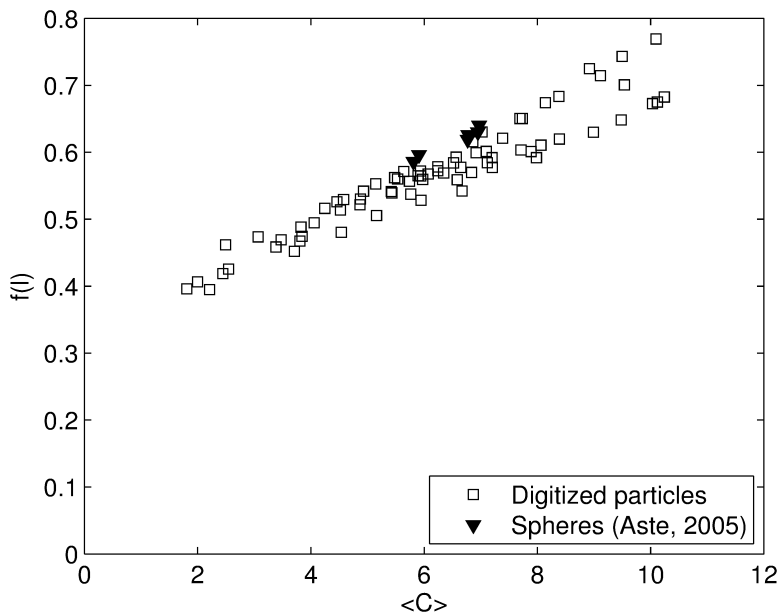
In order to derive a correction factor, the digitized roundness and Wadell sphericity are combined with the computed packing results. Figure 2.12(a) and 2.12(b) shows the result of multiplying the packing fractions with the digitized roundness and Wadell sphericity, respectively. One can notice that the results for  $d = 7$ ,  $d = 11$  and  $d = 21$  become more in line with the results of the other diameters, but are still higher than those of the other particles. Furthermore both modifications result in a packing fraction for all digitized particles that are below the random close packing value of spheres. Although these corrections bring the packing results in line with the RCP-value of spheres, the packing of particles with  $d = 7$ ,  $d = 11$  and  $d = 21$  are still behaving differently from the other sizes.

A possible solution to bring  $d = 7$ ,  $d = 11$  and  $d = 21$  in line with the other sizes is to modify the particle shape of  $d = 7$ ,  $d = 11$  and  $d = 21$ . The particles are namely shaped using a routine that determines if a voxel within the box is part of the digitized particle (Bentz, 1995). A voxel is part of digitized particle in case the distance from the centre of the voxel to the centre of the digitized particle is smaller than half the size of the digitized particle. With the reduction of the diameter by 0.05, the particle shape already alters. The volume of the modified particles decreases compared to the original, while the total particle surface remains equal. In Figure 1.5 the removed voxels are colored black/blue. The volume decrease in case of  $d = 11$  is 48 voxels, which means the removal of 8 voxels in each 6 (top)sides. For  $d = 21$  besides 8 voxels in each 6 (top)sides, another 96 voxels were removed from the outer layer.

The angularity of the modified particles is equal to original particle, while the digital roundness increased. For 11 and 21 particle the roundness changes from 0.78 and 0.87 to



(a)



(b)

**Figure 2.10:** The relation between contact number  $\langle C \rangle$  of random packing and (a) size ratio  $l$  ( $L_{\text{box}}/d$ ) and (b) packing fraction  $f(l)$  (for  $n_t = 10$ ,  $n_m = 20$ , boundary-condition 2).

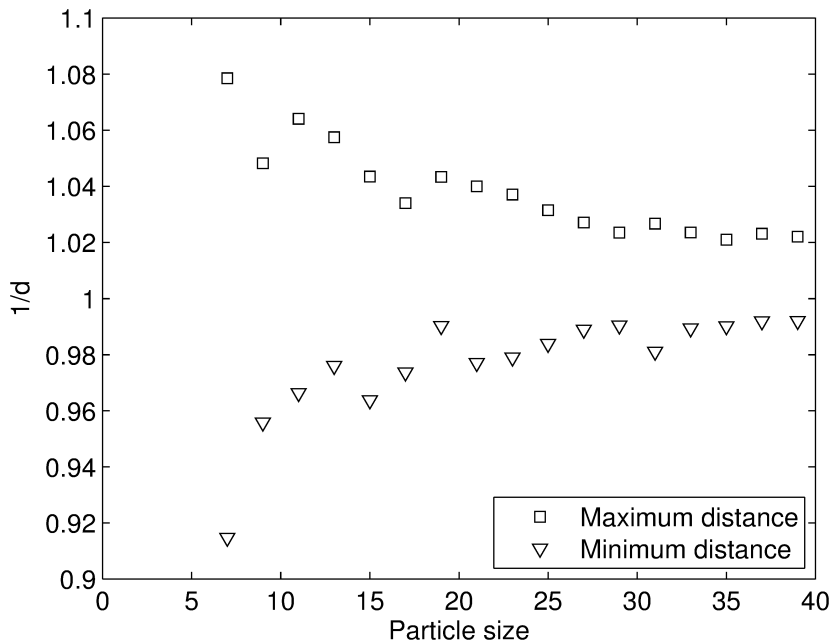
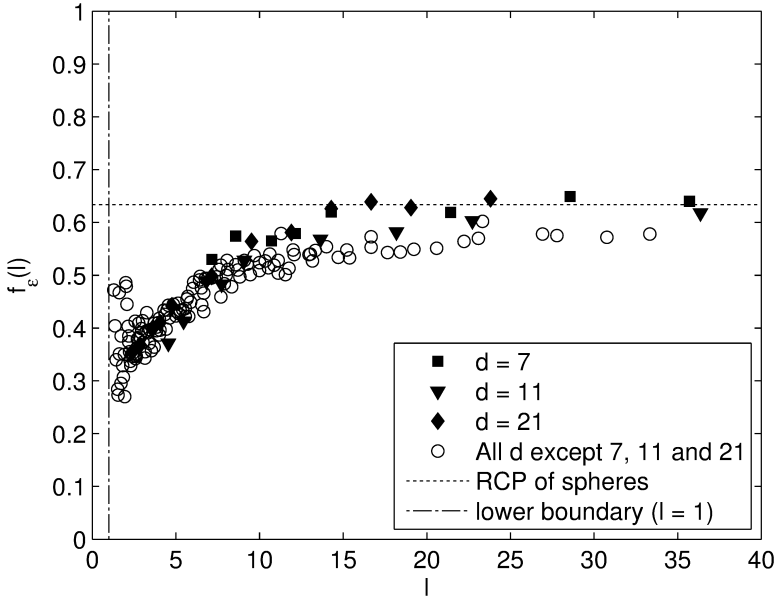


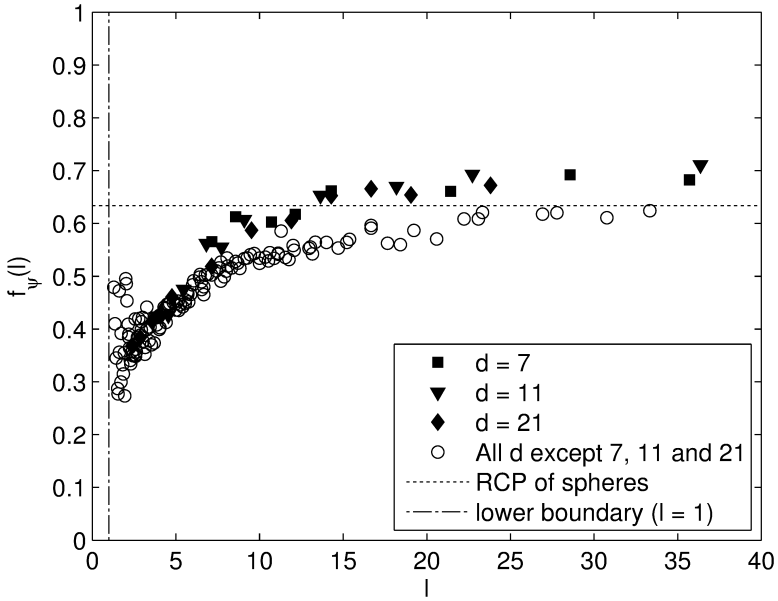
**Figure 2.11:** The minimum and maximum distance between the cores of two particles which are in contact with each other scaled by their particle size for the different (digitized) particle sizes.

**Table 2.6:** Properties of original and modified digitized particles of  $d = 7$ ,  $d = 11$  and  $d = 21$ .

Size (d)	Original			Modified		
	7	11	21	7	11	21
Surface (S)	222	582	2094	222	582	2094
Volume (V)	179	739	4945	171	691	4801
Shape factor (F)	8.68	8.66	8.89	9.09	9.26	9.16
Digitized particle/sphere ratio	1.45	1.44	1.48	1.51	1.54	1.53
Angularity ( $\text{Ang}_{2D}$ )	1377	1708	2760	1377	1708	2760
Digitized roundness ( $\epsilon$ )	0.76	0.78	0.89	0.76	0.87	0.92
Wadell sphericity	0.81	0.90	0.93	0.84	0.88	0.93



(a)



(b)

**Figure 2.12:** (a) The relation between size ratio  $l$  ( $L_{\text{box}}/d$ ) and the product of packing fraction and digitized roundness ( $f_\varepsilon(l)$ ) and (b) the relation between size ratio  $l$  and the product of the packing fraction and the Wadell sphericity ( $f_\psi(l)$ ) (for  $n_t = 10$ ,  $n_m = 20$ , boundary-condition 2).

0.89 and 0.92, respectively (Table 2.7), while it remains at 0.76 for  $d = 7$ . So the digital roundness of the modified particles are now more in line with those of the other particle sizes (Table 2.6). Figure 11a shows the simulation results for the product of the packing fraction and digitized roundness using the modified particles of  $d = 7$ ,  $d = 11$  and  $d = 21$ , together with the other unmodified particles. When comparing Figure 2.13(a) with Figure 2.12(a) one can notice that the results of the digitized (modified) particles are now closer to the other particle sizes, and only very slightly higher than the other sizes. Scott (1960) used the relation between the reciprocal size ratio ( $1/h$ ) and the packing fraction to determine the theoretical random close packing. Figure 2.14 shows the results of performing this kind of analysis on packing results of digitized particles. From the figures one can notice that the maximum packing fraction goes to 0.61 for product with the digitized roundness (Figure 2.14(a)) and to 0.63 for the product with the Wadell sphericity (Figure 2.14(b)) based on the derived trendlines. The found value of the product of packing fraction and Wadell sphericity is close to the RCP-value of spheres. Figure 2.15 shows the translational order (T) (Kansal et al., 2002) results for  $L_{\text{box}}/d \geq 5$ . The results for  $L_{\text{box}}/d \leq 5$  are less reliable since the number of particle relations is too limited for a sound statistical analysis and wall effects play an important role (Desmond and Weeks, 2009; McGeary, 1961; Suzuki et al., 2008). Two outliers can be observed in Figure 2.15, these are outliers caused by particles of  $d = 21$  in a box with  $L_{\text{box}} = 300$  and  $l_{\text{box}} = 350$ .

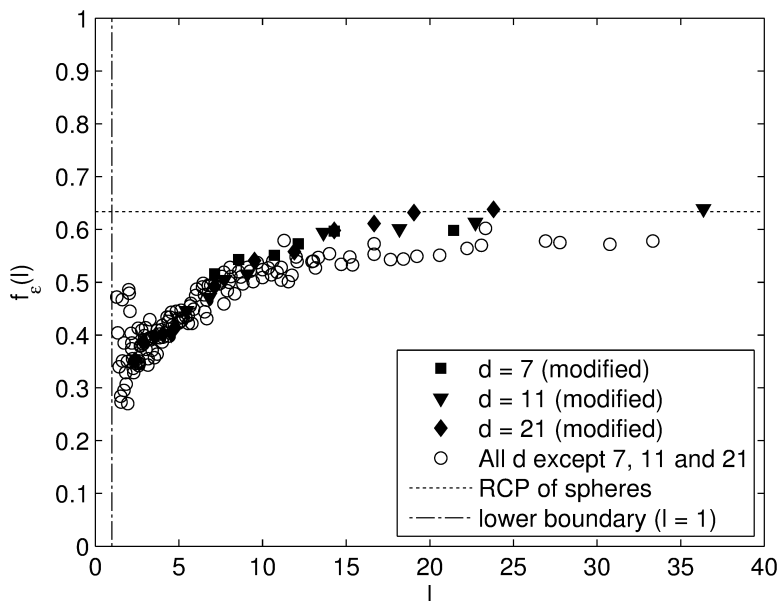
From this figure, one can notice a negative correlation between packing fraction and translational order metric, which is opposite to the relation shown by Kansal et al. (2002), Torquato et al. (2000) and Torquato (2002). Kansal et al. (2002) created the lower packing fractions by removing spheres from an fcc lattice leaving the other spheres on existing position and therefore the structure will not change. While in the present research the lower packing fractions are caused by the properties of digitized particles. Torquato et al. (2000) and Torquato (2002) determined the translational order metric for random packing of spheres also using the Lubachevsky and Stillinger algorithm, and a positive correlation between packing fraction and translational order metric was obtained.

The derived translational order metric from the simulations is in the same range as found by Kansal et al. (2002), Torquato et al. (2000) and Torquato (2002), which could indicate that the generated (particle) arrangements are random indeed. Especially since Torquato et al. (2000) and Torquato (2002) showed that the translational order metric of crystalline systems is higher than 0.4 and in the present research the translational order metric is lower for high values of  $h$  (Figure 2.15). Figure 2.16 shows an example of a packed structure created using the applied packing routine with bottom dimensions of  $50 \times 50$  ( $L_{\text{box}} \times L_{\text{box}}$ ) and a height of 100 ( $H_{\text{box}}$ ).

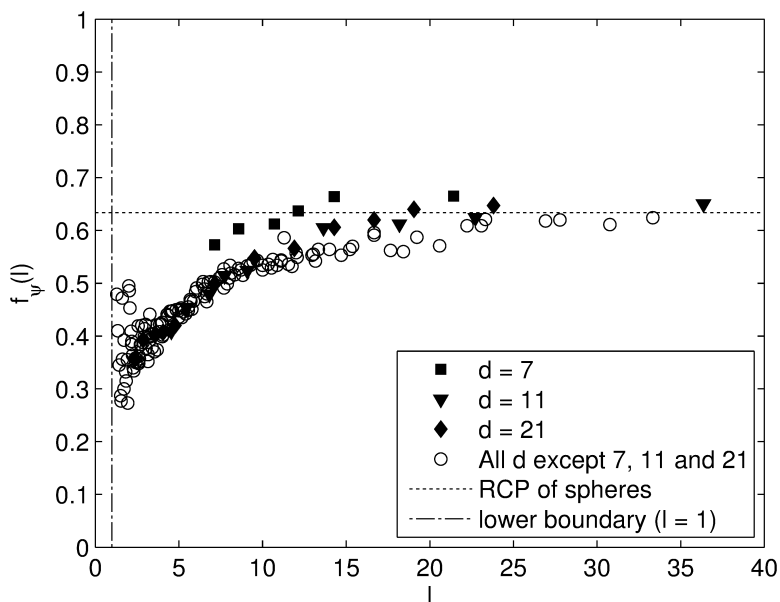
## 2.5 Conclusions

The current research has focussed on the regular and random packing of digitized particles as used in 3D cellular automata based models, such as the CEMHYD3D cement hydration model. The main findings of the research are

- The densest regular packing with digitized particle is obtained with a face centred tetragonal or orthorhombic crystal structure while face centred cubic or hexagonal

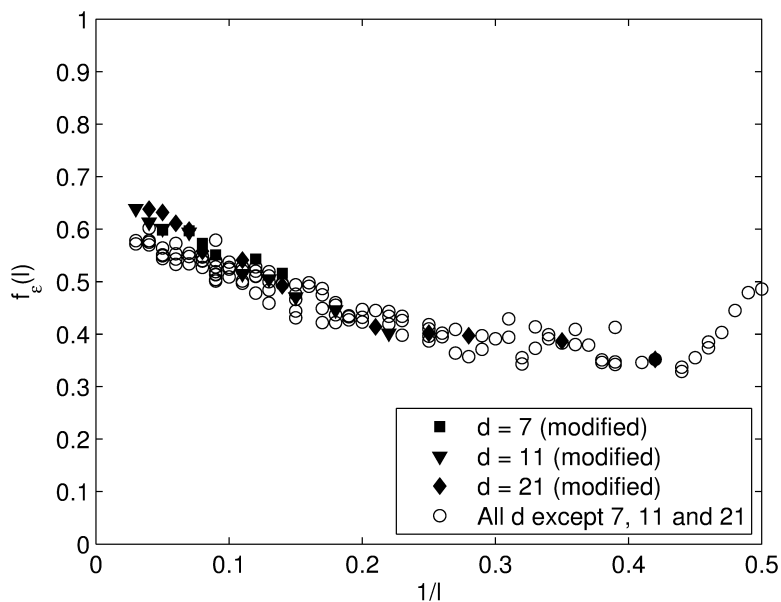


(a)

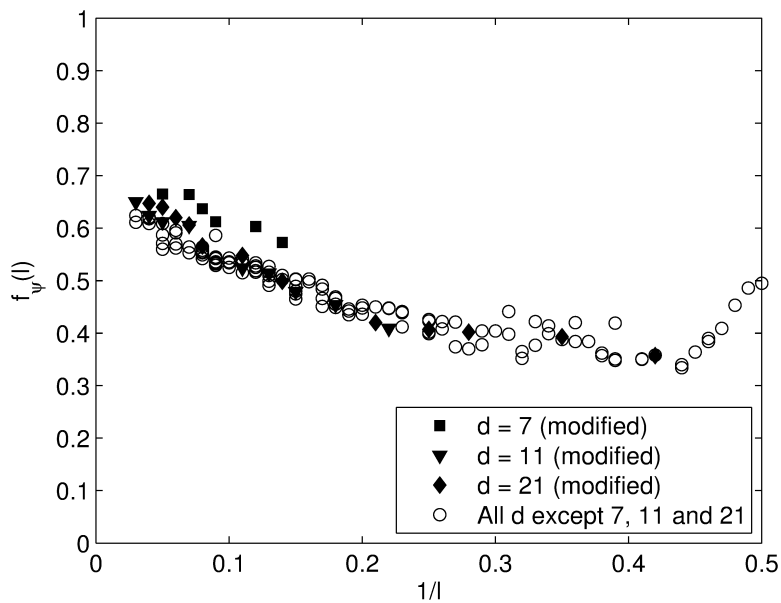


(b)

**Figure 2.13:** The relation between size ratio  $l$  ( $L_{\text{box}}/d$ ) and (a) product of packing fraction and digitized roundness and (b) the product of packing fraction ( $f_\epsilon(h)$ ) and Wadell sphericity ( $f_\psi(h)$ ) using the modified  $d = 11$  and  $d = 21$  particles ( $n_t = 10$ ,  $n_m = 20$ , boundary-condition 2).

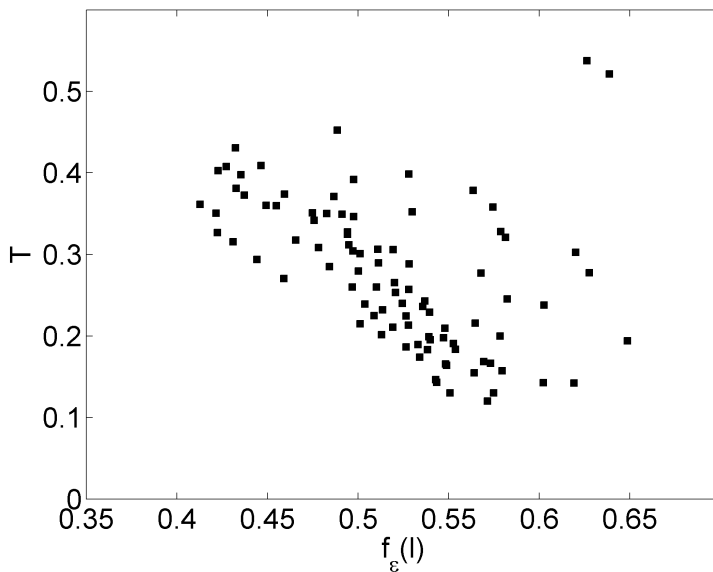


(a)

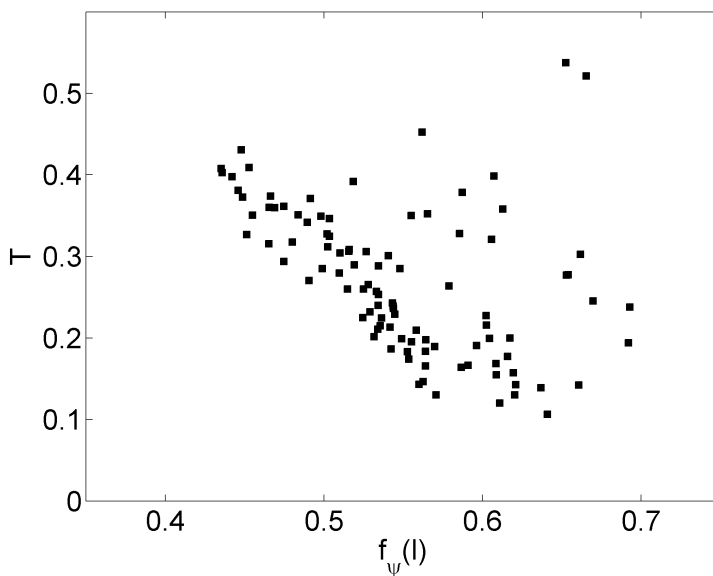


(b)

**Figure 2.14:** The relation between reciprocal size ratio ( $1/l = d/L_{\text{box}}$ ) and (a) the product of packing fraction and digitized roundness ( $f_\epsilon(l)$ ) and (b) the product of packing fraction and Wadell sphericity ( $f_\psi(l)$ ).



(a)



(b)

**Figure 2.15:** The translational order metric ( $T$ ) of the simulations versus (a) the product of packing fraction and digitized roundness ( $f_\varepsilon(h)$ ) and (b) the product of packing fraction and Wadell sphericity ( $f_\psi(h)$ ) for  $L_{\text{box}}/d \leq 5$ .

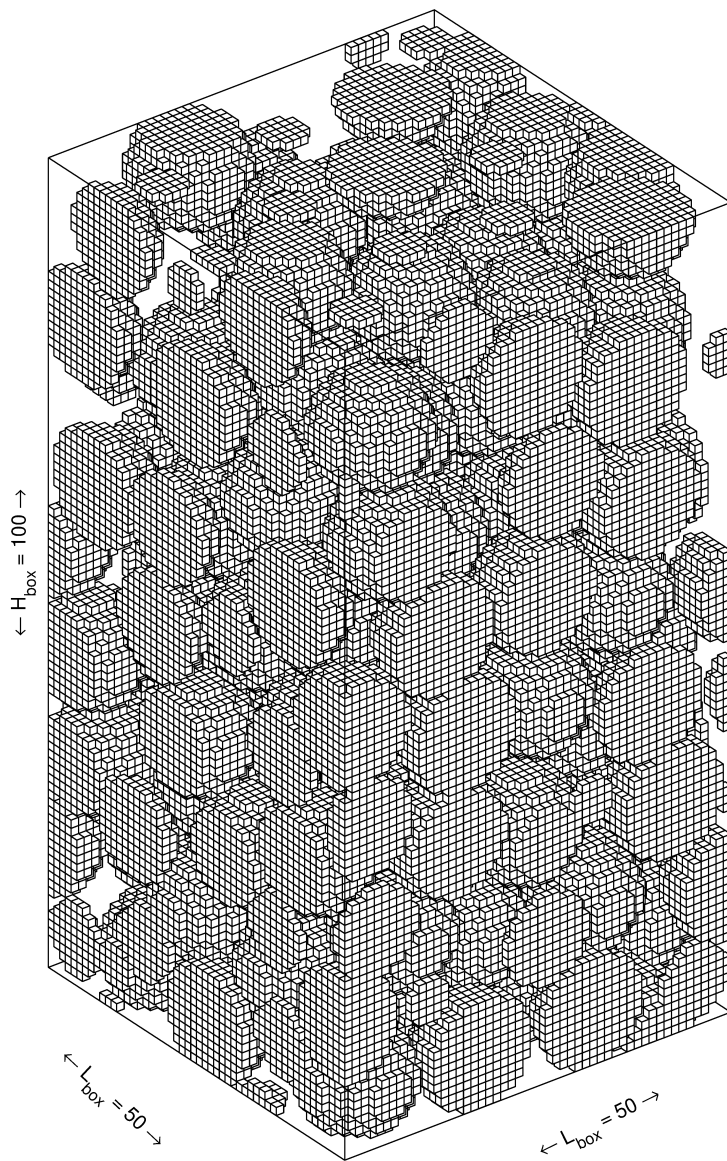


**Figure 2.16:** Example of the structure of packed bed created using the packing routine for box dimensions 50 x 50 x 100.

close-packed crystal structure provide the densest packing for spheres

- The original packing model within CEMHYD3D (Bentz et al., 1995) is not suitable for research of (random close) packing of mono-sized digitized particles, since the found packing fractions are close to the random sequential addition value of spheres. A new model, similar to Lubachevsky and Stillinger (1990) algorithm, has been introduced in this chapter. The found packing fractions during simulations are clearly related to the size ratio  $l$  ( $L_{\text{box}}/d$ ) for all particle sizes except for  $d = 7$  (voxels),  $d = 11$  and  $d = 21$ , which results in higher packing fractions. Furthermore the packing fraction is influenced by the amount of movement during placement of the particles.
- The digital roundness was been introduced in order to describe the particle shape of the digitized particles. This was not possible by existing methods, since these methods are mostly based on 2D-projection and irregularly shaped particles, while the digitized particles are regularly shaped and have equal dimensions in three main-directions. Using the digitized roundness and Wadell's sphericity, the packing results obtained during simulation could be explained. The product of Wadell sphericity (Wadell, 1933) and packing fraction approaches the random close packing fraction of spheres ( $\sim 0.63$ ) for the higher size ratios  $l$  ( $L_{\text{box}}/d$ ), as also shown by using the analysis of Scott (1960).
- New particle shapes for  $d = 7$ ,  $d = 11$  and  $d = 21$  have been introduced in order to overcome the outliers noticed during simulations. The modified particle shapes have a digitized roundness which shows a closer fit with value of the other particle sizes and the packing fraction is reduced compared to the packing fraction of the original particle shape used in CEMHYD3D.



## Reaction kinetics\*

### 3.1 Introduction

Chemical reactions have been studied for decades. Levenspiel (1984, 1999) and Szekely et al. (1976), among others, describe the progression of chemical reactions based on the particle geometry. From the described reactions, the chemical reaction controlled shrinking core model is the most simple reaction (Levenspiel, 1984). This reaction is relevant for particles and used for instance to describe the burning of carbon in air. The reaction kinetics is usually analyzed using numerical and analytical models. Besides these models also other methods have become available such as cellular automata (CA). The background is described in Section 1.5.

Cellular automata are already commonly used for the modeling of chemical systems (Chopard and Droz, 2005; Kier et al., 2005). Cellular automata systems are among others applied for studying biology, cement reaction, population growth, computability theory, mathematics, physics, complexity science, theoretical biology and microstructure modelling. Kier et al. (1999) uses cellular automata to describe the percolation within chemical systems.

Furthermore Kier and co-authors described a broad range of chemical systems and processes in which the cellular automata approach can be applied, ranging from aqueous systems (water), dissociation of organic acid in solutions and bond interactions (Cheng and Kier, 1995; Kier, 2000, 2007; Kier and Cheng, 1994a,b, 1995; Kier et al., 1998; Testa et al., 2002). Berryman and Franceschetti (1989) described the simulation of diffusion controlled reaction kinetics using cellular automata. Kier and Cheng (1995) presented a cellular automata model for dissolution. Goetz and Seetharaman (1998) used cellular automata to describe the static recrystallization kinetics with homogeneous and heterogeneous nucleation. Liu et al. (1996) and Raghavan and Sahay (2007, 2009) simulated grain growth using cellular automata. Dab et al. (1990) used a cellular-automaton for reactive systems containing particles.

Zahedi Sohi and Khoshandam (2012) used 2D cellular automata to describe non-catalytic gas-solid reactions of pellets consisting out of agglomerated grains with diffusion through a porous product layer and reaction on the surface of grains. In their work the cells were the grains and the conversion per cell was considered. This chapter considers spheres in 3D which consists of several cells, being either product, reactant or void.

Kier and Seybold and their co-authors (Hollingsworth et al., 2004; Kier et al., 2000; Kier and Seybold, 2009; Lipkowitz et al., 2001; Neuforth et al., 2000; Seybold et al., 1997) did research to the application of cellular automaton systems to describe chemical reac-

---

\*Parts of this chapter are published by Chemical Engineering Journal (De Korte and Brouwers, 2013a) and submitted to Modelling and Simulation in Materials Science and Engineering (De Korte and Brouwers, 2015)

tions. Their work describes first and second order reactions as well thermodynamically controlled reactions (Neuforth et al., 2000) and is closely related to this study. Their research on first and second order reactions is based on the concentration of the reactant, while in this research the shape is taking in account as well as the specific surface of the dissolving particle. Hence, this chapter considers the reaction as surface-based rather than volume-based.

A rigorous link between the (mathematical) chemical reaction models, like chemical reaction (shrinking core) model and the cellular automata approach to study the dissolution of particle has, to the author's knowledge, not been achieved yet. This relation between general reaction kinetical models and cellular automata is of interest for the further improvement of cellular automata reaction models, as for example the cement hydration model CEMHYD3D. Since reaction often follow the shrinking core model, cellular automata models need to be able to model these reactions. The relation between cycles (in cellular automata models) and time (general kinetic models and real world) is often not direct. The here described (hybrid) model provides a direct relation between these parameters.

## 3.2 Chemical reaction kinetics

Within the chemical reaction kinetics literature, two main reaction model families are distinguished the progressive-conversion model (PCM) and the shrinking unreacted core model (SCM). Within the progressive-conversion model (sometimes referred to as the zone reaction model (Ishida and Wen, 1971)), the solid reactant is converted continuously and progressively throughout the particle, while within the shrinking core model, the reactions take place on the outer skin of the particle and the zone of reaction is moving into the solid leaving behind completely converted material and inert solids. The main assumption within the shrinking core model is that the zone of reaction is narrowly confined to the interface between the unreacted solid and the product, when the chemical reaction is very rapid and the diffusion of the fluids sufficiently low, for instance due to a low void fraction of the unreacted material (Braun et al., 2000). If on the other hand the solid contains enough voids so that the fluid reactants can diffuse freely into the interior of the solid, the reactions between fluid and solid may be regarded as occurring homogeneously throughout the entire solid, this is described using the progressive conversion model (Braun et al., 2000).

Levenspiel (1999) points out that in practice in most cases the shrinking core model approximates real particles more closely than the progressive conversion model does, as shown in a wide variety of situations. But in fact the PCM and SCM describe the two limiting cases of the reality and a combination of both models should be applied (Braun et al., 2000). Several authors developed a more general model for solid-gas reactions, which takes into account these two phases of reaction (Ishida and Wen, 1971; Ishida et al., 1971). They presented the shrinking unreacted core model as a special case of the progressive conversion model.

Yagi and Kunii (1961a,b,c) distinguish five steps to occur during reaction succession;

- Diffusion of gaseous reactant A through the film surrounding the particle to the surface of the solid.

- Penetration and diffusion of A through the blanket of ash to the surface of the unreacted core.
- Reaction of gaseous A with solid at this reaction surface.
- Diffusion of gaseous products through the ash back to the exterior surface of the solid.
- Diffusion of gaseous products through the gas film back into the main body of fluid.

Based on these reaction steps three resistances to reaction can be distinguished namely, film diffusion, ash diffusion and reaction controlled (surface area controlled). The highest resistance forms the rate-controlling step. An important parameter in the use of the shrinking core model is the assumption of unchanging or changing particle size, since this determines the available reaction surface.

### 3.2.1 Transition point

This chapter deals with a hybrid system which starts chemical reaction controlled (CRC) until a ash/product layer of certain thickness (the so-called  $\delta_{tr}$ ) is formed and becomes diffusion controlled after this so called transition point. In order to arrive at this 'hybrid' system, some intermediated steps are made. In the first step the chemical reaction controlled system/stage is studied solely in Section 3.2.2. In Section 3.2.3 the diffusion controlled stage is studied. In Section 3.2.4, both stages are combined to one 'hybrid' model.

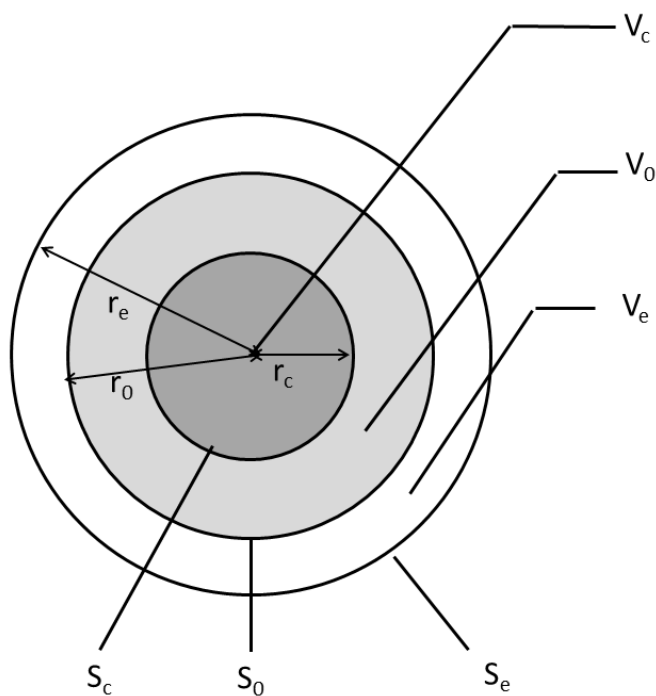
Figure 1.7 provides a graphical overview of the studied (hybrid) system. Besides the thickness of ash/product layer, the transition point can be described by the time needed to reach this point  $t_{tr}$ , the radius of the unreacted core  $r_c$  and the reaction degree  $\alpha_{tr}$ . In the CRC model, the formed reaction products does not play a role, since it is surface controlled. Here, the model transfers into the diffusion controlled model. For this model, the reaction product is relevant and therefore considered here.

Figure 3.1 shows a graphical representation of a particle with ash layer formation. The model assumes that the reaction rate at any instance is given by its rate of diffusion to the reaction surface. The volume including ash layer reads

$$V_e = V_c + v(V_0 - V_c) \quad (3.1)$$

where  $V_0$  is the volume of the initial particle with radius  $r_0$ ,  $V_C$  the volume of the shrinking core (with radius  $r_c$ ),  $V_e$  is the volume of the particle including ash layer (with radius  $r_e$ ) and  $v$  constitutes the volume increase ratio associated with the reaction ( $V_e/V_0$ ). Based on this volume relationship, the radius of varying particle including ash layer can be derived and reads

$$r_e^3 = vr_0^3 + (1 - v)r_0^3 \quad (3.2)$$



**Figure 3.1:** Graphical representation of the ash diffusion system with  $V_0$  is the volume of the initial particle with radius  $r_0$  and surface  $S_0$ ,  $V_c$  the volume of the shrinking core (with radius  $r_c$  and surface  $S_c$ ),  $V_e$  is the volume of the particle including ash layer (with radius  $r_e$  and surface  $S_e$ ).

The reaction degree can be described based on the volume of the unreacted core ( $V_c$ ) and initial volume of the particle ( $V_0$ ). The equation for the reaction degree reads

$$\alpha = 1 - \frac{V_c}{V_0} = 1 - \left(\frac{r_c}{r_0}\right)^3 \quad (3.3)$$

with  $r_c$  being the radius of the shrinking core and  $r_0$  the initial radius of the particle. The transition point, between the chemical reaction controlled and diffusion controlled phase with the reaction, can be described by several parameters, such as time, reaction degree, radius of shrinking core and product/ash layer thickness. Taking the layer thickness ( $\delta_{tr}$ ) and radius of the unreacted core ( $r_{c,tr}$ ) as a starting point, the corresponding reaction degree ( $\alpha_{tr}$ ) at the transition point reads

$$\alpha_{tr} = 1 - \left(\frac{r_{c,tr}}{r_0}\right)^3 \quad (3.4)$$

Furthermore the (external) radius of particle including product/ash layer at the transition point can be described either on the volume increase ratio  $v$  or the transition layer thickness  $\delta_{tr}$ ;

$$r_{e,tr} = \sqrt[3]{vr_0^3 + (1-v)r_{c,tr}^3} \quad (3.5)$$

$$r_{e,tr} = r_{c,tr} + \delta_{tr} \quad (3.6)$$

The transition layer in a cellular automata system has a minimal thickness of one voxel. This is inherent to the cellular automata approach, in which the reaction is simulated using discrete voxels. In the cellular automata approach it is possible to use layer thickness of more one voxel, but layer thickness smaller than unity is impossible due to discrete manner of the cellular automata approach. Besides the discrete case, one can also derive the corresponding radius of the unreacted core for the (continuous) mathematical case by solving Eqs. (3.5) and (3.6). The combination of these equations leads to the following implicit equation;

$$r_{c,tr} = \sqrt[3]{vr_0^3 + (1-v)r_{c,tr}^3} - \delta_{tr} \quad (3.7)$$

The value for  $r_{c,tr}$  can be approached using the following equation;

$$r_{c,tr} = r_0 - \frac{\delta_{tr}}{v} \quad (3.8)$$

The corresponding reaction degree ( $\alpha_{tr}$ ) for this approximated radius reads

$$\alpha_{tr} = 1 - \left(1 - \frac{\delta_{tr}}{vr_0}\right)^3 \quad (3.9)$$

For the discrete case, as the case in the cellular automata models, the formed layer needs to equal an integer and  $\alpha_{tr}$  is in general higher than that of the (continuous) mathematical case (Figure 3.2).

The following Sections 3.2.2 and 3.2.3 address the chemical reaction controlled and diffusion controlled stage respectively, while Section 3.2.4 combines both stages to a single (hybrid) model.

### 3.2.2 Chemical reaction controlled

In the present subsection, the surface-controlled system is studied. Both Levenspiel (1984, 1999) and Szekely et al. (1976) call this system chemical reaction controlled (CRC). The progress of the reaction within the reaction controlled model is unaffected by the presence of any ash/product layer, therefore the reaction rate is proportional to the available surface of the unreacted core.

$$\frac{1}{S_c} \frac{dV_c}{dt} = k_1 \quad (3.10)$$

with  $k_1$  being the first-order rate constant for the surface reaction,  $S_c$  the surface area of unreacted core and  $V_c$  as the unreacted core volume. Using the standard equations for the volume ( $4/3\pi r_c^3$ ) and surface ( $4\pi r_c^2$ ) dependence on the radius of unreacted core ( $r_c$ ), Eq. (3.10) can be rewritten to

$$\frac{dr_c}{dt} = k_1 \quad (3.11)$$

Eq. (3.11) can be integrated and applying

$$r_c(t=0) = r_0 \quad (3.12)$$

results in

$$t = \frac{1}{k_1}(r_0 - r_c) \quad (3.13)$$

The time  $\tau_1$  required for complete conversion, i.e. when  $r_c = 0$ , reads

$$\tau_1 = \frac{r_0}{k_1} \quad (3.14)$$

The decrease in radius or increase in fraction conversion of the particle in terms of  $\tau_1$  is obtained by combining Eqs. (3.13) and (3.14)

$$\frac{t}{\tau_1} = 1 - \frac{r_c}{r_0} \quad (3.15)$$

This can be rewritten based on the reaction degree, which is described by the volume of unreacted core ( $V_c$ ) and the initial volume of the particle ( $V_0$ ).

$$\alpha = 1 - \frac{V_c}{V_0} = 1 - \left(\frac{r_c}{r_0}\right)^3 \quad (3.16)$$

Eqs. (3.15) and (3.16) can be combined to a general equation for the reaction controlled system, which reads

$$\frac{t}{\tau_1} = 1 - (1 - \alpha)^{1/3} \quad (3.17)$$

In Section 3.2.1 the transition point was introduced. The time needed for reaching the transition point  $t_{tr}$  can be described using the chemical reaction controlled model (Eq. (3.17)), reads

$$t_{tr} = \left(1 - \frac{r_{c,tr}}{r_0}\right) \tau_1 = \left(1 - (1 - \alpha_{tr})^{1/3}\right) \tau_1 \quad (3.18)$$

One can notice that for  $\alpha_{tr} = 1$ ,  $t_{tr}$  equals  $\tau_1$ , which means that the conversion is completely chemical reaction controlled.

### 3.2.3 Diffusion controlled

As a first step only the diffusion model is considered. The chemical reaction controlled model assumes that the formed ash/product, if any, does not limit the reaction speed. The formed ash/product, however in practice, can reduce the reaction rate. The ash-layer model deals with this resistance to reaction. Šesták and Berggren (1971) mention two three-dimensional transport process models, namely the Jander model (Jander, 1927) and the Ginstling and Brounshtein model (Ginstling and Brounshtein, 1950). The Jander model assumes a spherical reactant surface and flat product layer, while the Ginstling-Brounshtein model assumes a spherical reactant surface as well as spherical product layer. Carter (1961) points out that there are some major simplifications in the Jander model. The Jander equation assumes a plane surface which is only valid when the ratio of inner and outer radius of the ash layer is close to unity, so for small values of  $\alpha$ . Brown (1989) points out that the Jander model cannot account for the decrease in interfacial area between the reactant and the reaction product as reaction proceeds. Considering these limitations of the Jander model here the model of Ginstling and Brounshtein (1950) is used.

The equations of Ginstling and Brounshtein (1950) have also been used by Levenspiel (1984, 1999) to describe the reaction of a shrinking core with an ash layer, where the total size of the particle (reacted and unreacted) is constant. The model assumes that the reaction rate at any moment in time is given by its rate of diffusion to the reaction surface

$$-\frac{dV_c}{dt} = S_e Q \quad (3.19)$$

with  $Q$  being the flux of  $S_e$  through the exterior surface of a particle. The rate of diffusion depends on the effective diffusion coefficient ( $D_e$ ) and the concentration ( $C_e$ ) present on the reaction surface and reads;

$$Q = D_e \frac{dC}{dr} \quad (3.20)$$

Combining Eqs. (3.5), (3.19) and (3.20), using  $A_e = 4 \cdot \pi \cdot r_e^2$  and integrating by applying  $C = 0$  for  $r_c$ ,  $C = C_e$  for  $r = r_e$  leads to

$$-\frac{dV_c}{dt} = 4\pi D_e C_e \left( r_c - (v \cdot r_0^3 + (1-v) \cdot r_c^3)^{1/3} \right) \quad (3.21)$$

Using  $V_c = 4/3 \cdot \pi \cdot r_c^3$ , separating of the variables  $r_c$  and  $t$  leads to

$$\frac{dr_c}{dt} = \frac{D_e C_e (r_c - (v \cdot r_0^3 + (1-v) \cdot r_c^3)^{1/3})}{r_c^2} \quad (3.22)$$

integrating Eq. (3.22), applying  $r_c(t=0)=r_0$  and combining with Eq. (3.3) leads to

$$\frac{k_2 t}{r_0^2} = \frac{v - (v + (1-v)(1-\alpha))^{2/3}}{v-1} - (1-\alpha)^{2/3} \quad (3.23)$$

with  $\alpha$  the reaction degree and  $k_2$  the kinetic constant. The kinetic parameter  $k_2$  describes the effective diffusion coefficient ( $D_e$ ) and the concentration of the solution at the reaction surface ( $C_e$ ). For the complete conversion of a particle,  $r_c = 0$ , the total reaction time ( $\tau_2$ ) required equals

$$\tau_2 = \frac{v - v^{2/3}}{v-1} \cdot \frac{r_0^2}{2k_2} \quad (3.24)$$

So, the dimensionless equation for this system reads

$$\frac{t}{\tau_2} = \left( \frac{v - (v + (1-v)(1-\alpha))^{2/3}}{v-1} - (1-\alpha)^{2/3} \right) \cdot \left[ \frac{v-1}{v-v^{2/3}} \right] \quad (3.25)$$

This equation is also given by Szekely et al. (1976) for diffusion controlled reaction of particles with changing size. In case of  $v = 1$ , Eq. (3.25) turns into the ash diffusion equation of Levenspiel (1999), using the L'Hôpital's rule. This ash diffusion equation of Levenspiel reads;

$$\frac{3t}{\tau_2} = 1 - 3(1 - \alpha)^{2/3} + 2(1 - \alpha) \quad (3.26)$$

### 3.2.4 Hybrid model

The model in the previous subsection is applicable when during the whole conversion (i.e.  $0 \leq \alpha \leq 1$ ), the diffusion controlled model is applicable. But in cellular automata systems, the process starts with chemical reaction controlled, and after the formation of a layer thickness  $\delta_{tr}$ , diffusion controlled kinetics prevails. So, for  $0 \leq \alpha \leq \alpha_{tr}$ , CRC from Section 3.2.2 prevails and for  $\alpha_{tr} \leq \alpha \leq 1$ , diffusion (Section 3.2.3) is governing the reaction speed. The time corresponding to  $\alpha_{tr}$  is called  $t_{tr}$ .

Figure 1.7 shows a graphical representation of the studied system. As one can notice the total reaction time  $\tau_3$  consists of two parts. The first part of the reaction is chemical reaction controlled. This part is valid until a transition thickness  $\alpha_{tr}$  is reached. The time required for this stage is given by Eq. (3.18).

The second part of the reaction is diffusion controlled. To determine the time needed for this phase, Eq. (3.21) needs to be integrated with applying  $r_c = r_{c,tr}$  for  $t = t_{tr}$ . After integration and simplification, this leads to;

$$(t - t_{tr}) \frac{k_2}{r_0^2} = -\frac{(v + (1 - v)(1 - \alpha))^{2/3}}{v - 1} - (1 - \alpha)^{2/3} + \frac{(v + (1 - v)(1 - \alpha_{tr}))^{2/3}}{v - 1} + (1 - \alpha_{tr})^{2/3} \quad (3.27)$$

One can notice the resemblance of Eq. (3.27) to Eq. (3.23). In case of  $\alpha_{tr} = 1$ , Eq. (3.27) equals 0, which means that the chemical reaction controlled since the diffusion part is zero. In case of  $\alpha_{tr} = 0$  and  $t_{tr} = 0$ , Eq. (3.27) transfers into Eq. (3.23). In fact Eq. (3.27) is just the difference between the outcomes for  $t_{tr}$  and  $t$  of Eq. (3.23). For  $v = 1$ , Eq (3.27) becomes;

$$(t - t_{tr}) \frac{k_2}{r_0^2} = 3(1 - \alpha_{tr})^{2/3} - 3(1 - \alpha)^{2/3} + 2(\alpha_{tr} - \alpha) \quad (3.28)$$

By using Eq. (3.18) for the transition time and by substituting  $\alpha = 1$  into Eq. (3.27) for the diffusion controlled stage, the time  $\tau_3$  needed for full reaction ( $\alpha = 1$ ) reads;

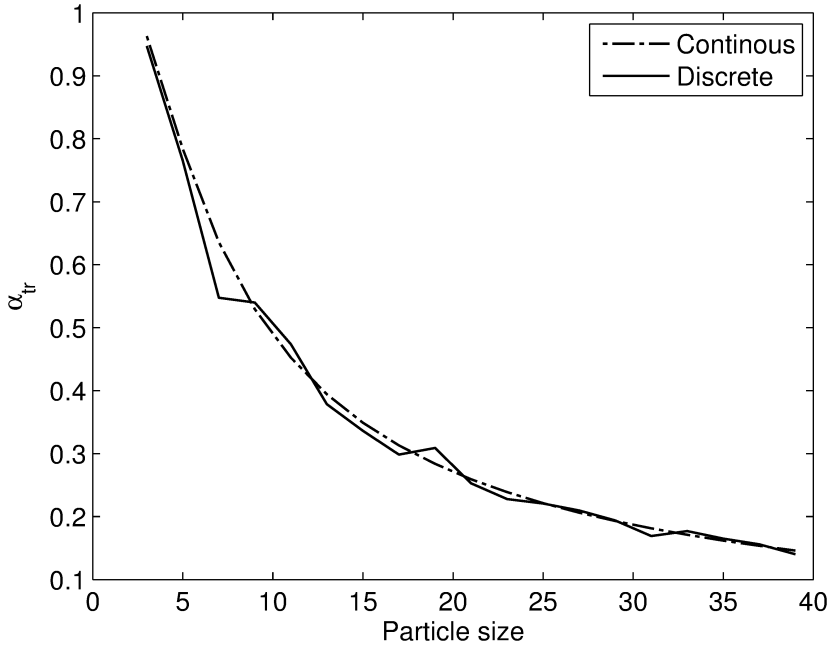


**Figure 3.2:** The reaction degree ( $\alpha_{tr}$ ) corresponding to transition point of chemical reaction controlled to diffusion controlled calculated for continuous and discrete (only integers allowed) situation.

$$\tau_3 = -\frac{v^{2/3} + (v + (1 - v)(1 - \alpha_{tr}))^{2/3} + (v - 1)(1 - \alpha_{tr})^{2/3}}{v - v^{2/3}} \tau_2 + \left(1 - (1 - \alpha_{tr})^{1/3}\right) \tau_1 \quad (3.29)$$

For  $\alpha_{tr} = 0$  (i.e. the system is fully diffusion controlled),  $\tau_3$  is equal to  $\tau_2$  and for  $\alpha_{tr} = 1$  (i.e. the system is complete chemical reaction controlled),  $\tau_3$  is equal to  $\tau_1$ , as would be expected.

In case of  $v = 1$  and using the L'Hôpital's rule, Eq. (3.30) can be rewritten as

$$\tau_3 = \left(3(1 - \alpha_{tr})^{2/3} - 2(1 - \alpha_{tr})\right) \tau_2 + \left(1 - (1 - \alpha_{tr})^{1/3}\right) \tau_1 \quad (3.30)$$

for  $\alpha_{tr} = 0$  (i.e. the system is fully diffusion controlled),  $\tau_3$  is equal to  $3/\tau_2$  and for  $\alpha_{tr} = 1$ ,  $\tau_3$  is equal to  $\tau_1$ .

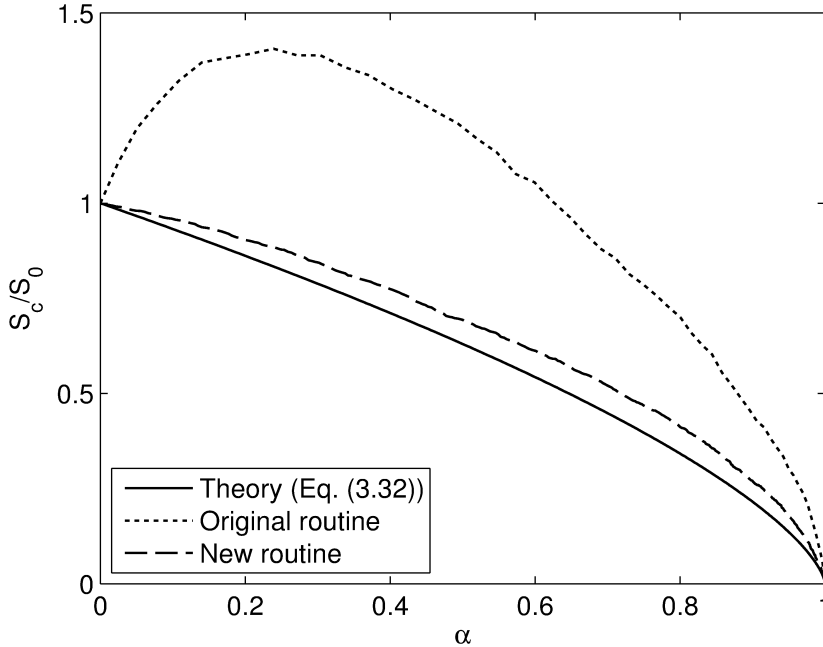


**Figure 3.3:** The available reactive surface during reaction in CEMHYD3D using the original and new dissolution routine compared to the theoretical surface (Eq. (3.32)) according to chemical reaction controlled model of Levenspiel (1999).

### 3.3 Simulation results and analysis

#### 3.3.1 Shrinking particle size case

Using simulations, the cycle in a certain  $\alpha$  is reached has been determined for a dissolution probability ( $P_1$ ) of 0.003 to 0.09 with steps of 0.003 and diameter ( $d$ ) of 7, 13, 21, 25 and 35. The particle shape has been modified in the same way as done in Chapter 2. This modification improves sphericity and roundness of the digitized particles, which approaches a spherical shape better. Analysis of the simulation data shows that the reaction rate depends on the available surface area of the reactant. Based on the description in the previous section, the chemical reaction controlled (CRC) model is most appropriate to describe a chemical system without precipitation of reaction products and the existence of a diffusion layer.

However when assessing the available surface area within CEMHYD3D during reaction, as shown in Figure 3.3, one can notice an increase in available surface area rather than a decrease, as would be expected. This surface increase is caused by the dissolution of voxels from the middle of the flat top surface of the particles (indicated in gray in Figure 1.5), rather than the edge of the flat top surfaces. This results in a loss of the spherical shape and the creation of additional (reactive) surface area. Figure 3.5 shows the cross-section of 35 particle during dissolution. From this figure, one can indeed conclude that the spherical shape is lost and that holes seems to be formed in the cross-section.

Therefore a new routine has been added to the dissolution module of CEMHYD3D.

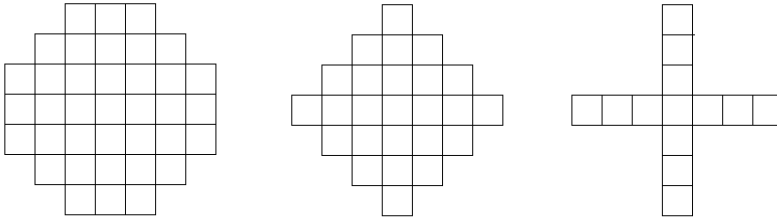


**Figure 3.4:** A example of 2D-particle with the same perimeter and radius but with different surface area.

Within this routine the determination whether a voxels dissolves or not (the probability part) is done in the regular way as done in CEMHYD3D. In case the voxels will dissolve, the position of the voxels is checked. When the number of surfaces of the particular voxel exposed to the pore solution is three or higher the voxel will dissolve immediately. Otherwise the edge of the particle is searched and a voxel at this edge will dissolve instead. Figure 3.4 shows three particles in 2D with the same perimeter but with different surfaces. For 3D comparable images can be produced. Due to the way the dissolution module is programmed it is always searching for the outer pixels (it is so programmed that an increase of the external surface is prohibited). Figure 3.3 shows the dissolution of particle of size 35 using both the original and the new routine. As one can notice the particle in the original routine dissolves faster than in the new routine. This is caused by higher reactive surface area, which leads to an increase of reaction speed in the system. Furthermore, a particle dissolving using the new routine retains its spherical shape (Figure 3.6).

Figure 3.3 also shows the result of applying the new routine at the dissolution of a 35-voxel particle. As can be noticed the surface-decrease during reaction is much closer to the theoretical surface decrease for a shrinking core. The theoretical dependence of the specific surface area on the reaction degree reads as

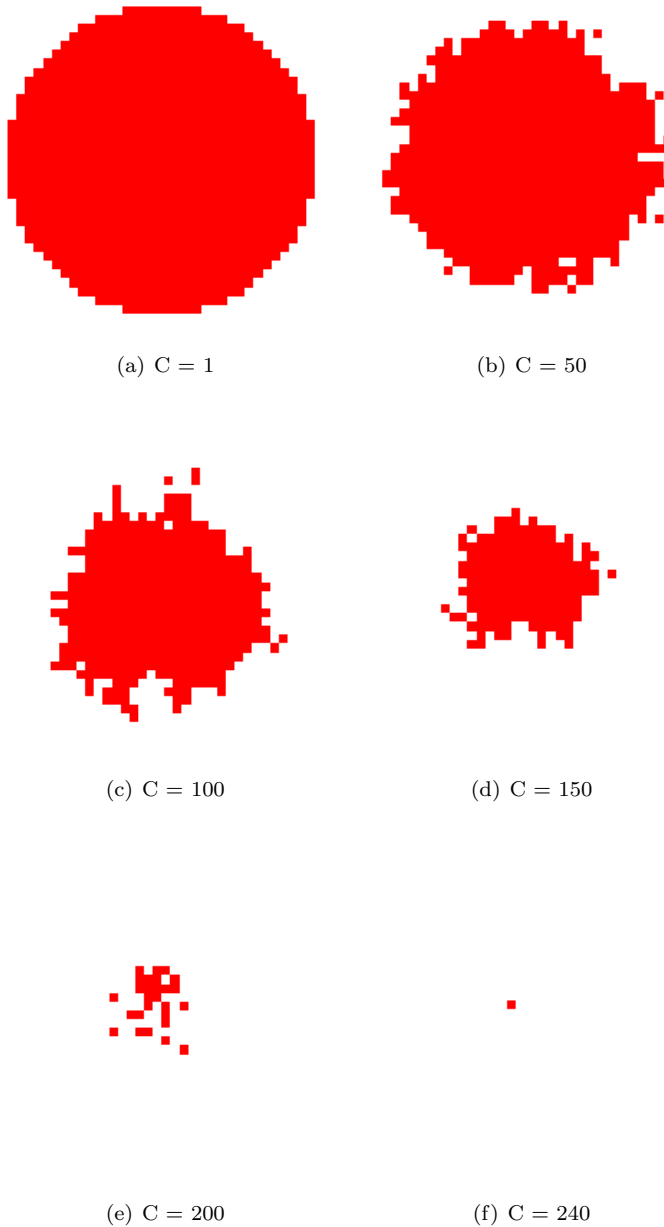
$$\frac{S_c}{S_0} = \left(\frac{r_c}{r_0}\right)^2 \quad (3.31)$$

with  $S_0$  the initial surface of the digitized particle. Combining Eqs. (3.16) and (3.31), this results into

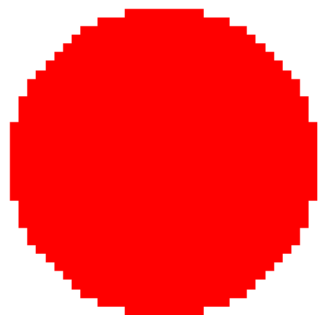
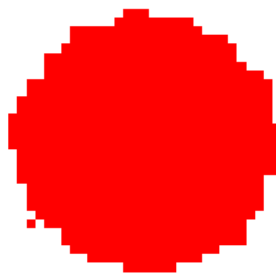
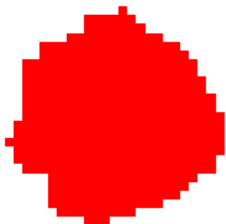
$$S_c = (1 - \alpha)^{2/3} S_0 \quad (3.32)$$

Based on Figure 3.3, one can notice that the surface area of the dissolving particles is slightly higher than one should expect based on these general models. According to this models a relation between available reactive surface area and reaction degree should exist.

Figure 3.7 shows the results of the different particle radius for  $P_1 = 0.021$ . The reaction



**Figure 3.5:** Example of dissolving particle using the original routine and the developing shape during its dissolution (in red the unreacted voxels), with  $C$  the cycle number.

(a)  $C = 1$ (b)  $C = 100$ (c)  $C = 200$ (d)  $C = 300$ (e)  $C = 400$ (f)  $C = 500$ 

**Figure 3.6:** Example of dissolving particle using the new routine and the developing shape during its dissolution (in red the unreacted voxels), with  $C$  the cycle number.

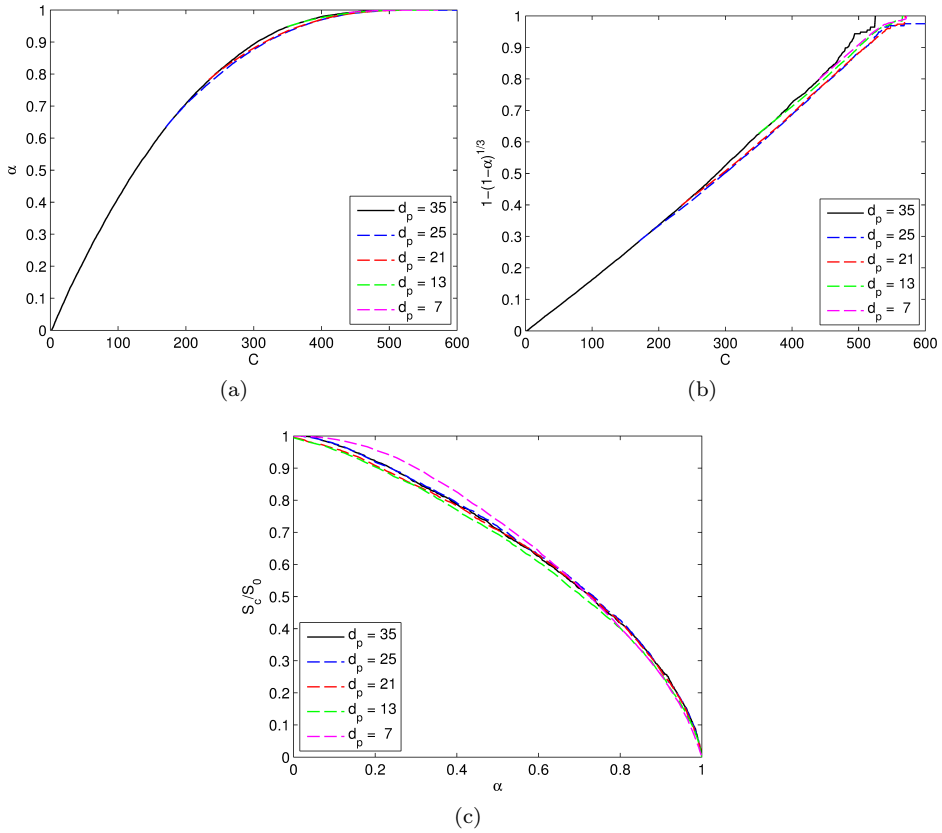


**Figure 3.7:** Partial reaction of different particle sizes ( $d_p$ ) for  $P_0 = 0.021$  (a) relation between cycles ( $C$ ) and reaction degree ( $\alpha$ ), (b) the relation between cycles and chemical reaction model and (c) the relation between reaction degree and surface fraction of unreacted core ( $S_c/S_0$ ).

degree of smaller particles ( $d_p < 35$ ) has been recalculated so their starting point corresponds to moment that a 35 particle reach the same volume and the curves have been scaled. This enables a direct comparison of the curves. From this figure one can notice that the reaction rate indeed depends on the particle size.

### 3.3.2 Constant particle size case

Figure 3.8 shows the reaction of a 35 particle using the new reaction routine described in Section 3.3.1. One can notice from this figure that the particle indeed keeps the same shape (as  $v = 1$ ) and that no cavity is formed between the ash/product-layer and the unreacted shrinking core.

Figure 3.9 shows the surface area of the (shrinking) core during the reaction compared to the theoretical surface area (Eqs. (3.32)). One can notice that the surface area of simulation is slightly higher than the theoretical curve, and that the difference between the curves is comparable to Figure 3.3.

### 3.3.3 Varying particle size case

In the previous section, a system with  $v = 1$  was evaluated. In this case the reactant has transformed into the product without any change in the volume of the solid during the process. In practice often a change in volume during reaction occurs ( $v \neq 1$ ). In this section a system with  $v = 1.7$  is used as example, which means that the volume of the product ( $V_e - V_c$ ) is 1.7 times the reacted volume of the reactant ( $V_0 - V_c$ ) (Figure 1.7). In the original version of CEMHYD3D of Bentz (1995), the additional product formed during reaction was randomly distributed through the microstructure, although with a slight favor for placing in contact with a solid. Figure 3.10 shows the reaction of a 35 particle including the formation of additional product. One can notice from Figure 3.10, that some voxels appear to be unconnected to the core, but in fact they are connected to the particle. This appearance of loose voxels is caused by the 2D representation which is a cut-through with a thickness of only 1 voxel.

For the testing of the general reaction equations, it is necessary that the additional product voxels are placed on the surface of the 'digitized sphere'. Therefore a routine is added, which searches a spot on the surface suitable placement/precipitation of this additional product voxel. Figure 3.10 shows the slice through of a dissolving particle with the unreacted core in red and the formed reaction product in blue. One can notice that the spherical shape of the reactant and the hydration product is maintained during the reaction.

## 3.4 Coupling cellular automata and reaction kinetics

### 3.4.1 Shrinking core case

Since the resemblance between the reaction curves obtained from the CEMHYD3D and the reaction controlled curves as, in this section a correlation between simulations and theoretical model is researched. Therefore a linear regression between cycle number ( $C - 2$ ) and  $(1 - (1 - \alpha)^{1/3})$  is tested, since according to the chemical reaction controlled model a linear relation between time and  $(1 - (1 - \alpha)^{1/3})$  exists and linear relation between cycle

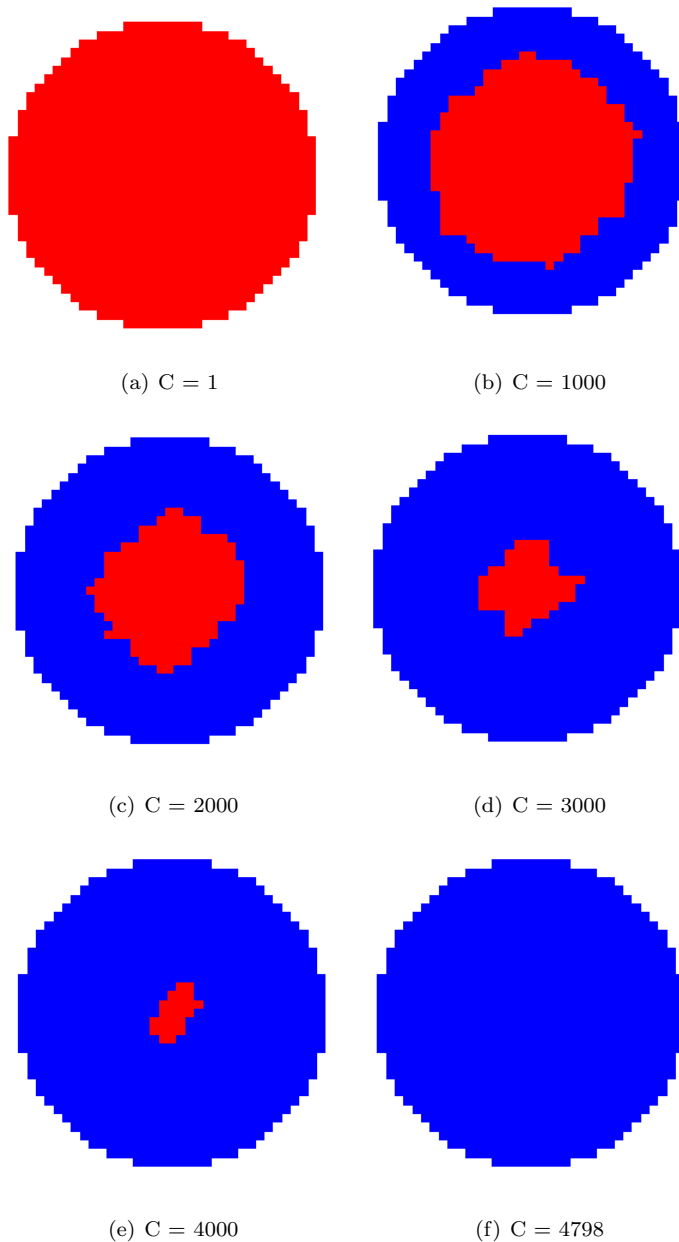


**Figure 3.8:** Example of dissolving particle and the developing shape during its dissolution in case of  $\nu = 1$  (in red the unreacted voxels and blue the formed hydration product), with  $C$  the cycle number.

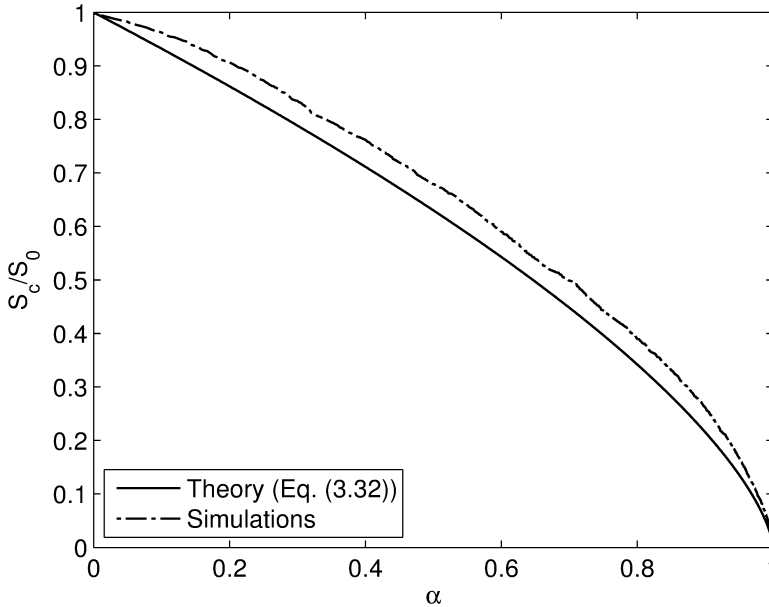


**Figure 3.9:** The surface area of the shrinking core during reaction in CEMHYD3D compared to the theoretical surface according to the ash diffusion controlled model of Levenspiel (1999), given as Eq. (3.32).

and time is assumed here. The relation with  $C - 2$  rather with  $C$  is used because the reaction within CEMHYD3D always start not earlier than cycle 2, as described earlier in this thesis. Figure 3.11 shows the simulation of three reaction curves scaled both on the  $x$ - and  $y$ -axis. As one can notice the scaled curves are similar and can be described with the following equation;

$$\left(1 - (1 - \alpha)^{1/3}\right) = \beta_1 \frac{(C - 2) \cdot P_0}{r_p} \quad (3.33)$$

with  $\beta_1$  the relation constant for CRC,  $r_p$  the radius of particle size in voxels and  $P_0$  the dissolution probability. Note that here  $\alpha$  is based on the volume of reacted voxels in the cellular automata system. Using the fitting toolbox of Matlab the  $\beta_1$  has been determined for all reaction curves with  $d = 7, 13, 21, 25, 35$  and  $P_0 = 0.003$  to  $0.09$  for  $0.05 < \alpha < 0.9$ . Table 3.1 shows the statistical data on found values of  $\beta_1$ . A mean ( $\beta_1$ ) of 1.420 was found with a standard deviation ( $\sigma$ ) of 0.057, i.e. a coefficient of variation of 0.039, which is a satisfactory outcome. When determining the  $\beta_1$  of ten simulations with the same initial microstructure,  $P_0 = 0.003$  and  $d = 35$ , also a standard deviation ( $\sigma$ ) of 0.015 is found. This statistical variation for identical systems is inherent to cellular automata and constitutes already 25% of the variation found for  $\beta_1$  of the whole range of diameters and probabilities. The other statistical data on these simulations can be found in Table 3.1(b).

Figure 3.11 shows the results from the model compared to the (original) simulation

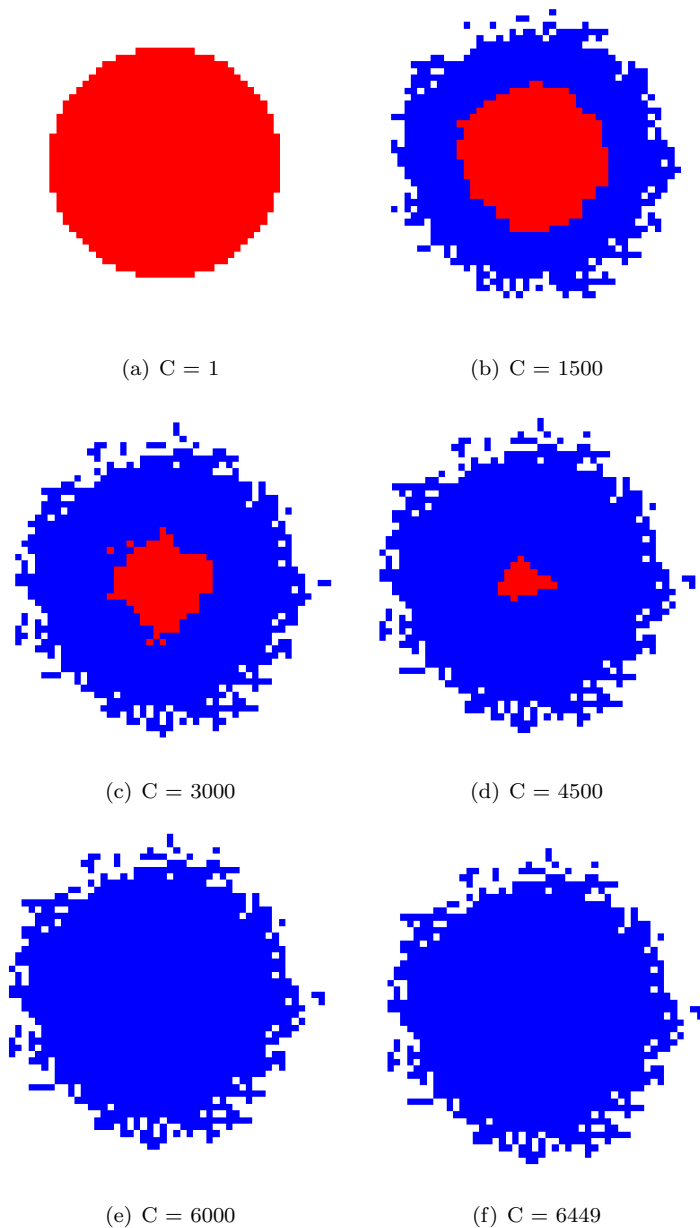


**Figure 3.10:** Example of dissolving particle and the developing shape during its dissolution in case of  $v = 1.7$  (in red the unreacted voxels and blue the formed hydration product).

**Table 3.1:** (a) Statistical information on the derived values of  $\beta_1$  for  $d = 7, 13, 21, 25$  and  $35$  and  $P_0 = 0.003$  to  $0.099$  for the shrinking core case (b) statistical information on derived values of  $\beta_1$  for 10 simulations with  $d = 35$  and  $P_0 = 0.003$  and  $d = 35$  and  $P_0 = 0.021$ .

(a)		(b)		
Parameter	Value	Parameter	$P_0 = 0.003$	$P_0 = 0.021$
Average	1.420	Average	1.465	1.437
Median	1.423	Median	1.467	1.437
Standard deviation ( $\sigma$ )	0.057	Standard deviation ( $\sigma$ )	0.013	0.012
Variance ( $\sigma^2$ )	0.003	Variance ( $\sigma^2$ )	0.000	0.000
Coefficient of variation	0.039	Coefficient of variation	0.009	0.008

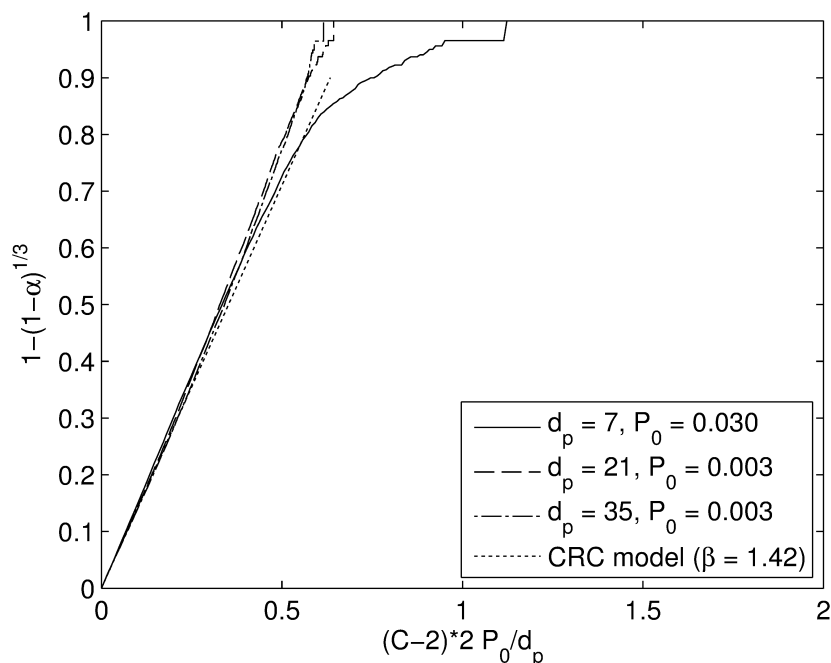


**Figure 3.11:** The relation between  $(C-2) 2P_0/d_p$  and  $1 - (1 - \alpha)^{1/3}$  (with  $\beta_1 = 1.420$ ) for three simulations and the reaction controlled processes given by Levenspiel (1999).

curves for three different cases. From Figure 3.11, one can notice that the assumption for linearity is valid for  $1 - (1 - \alpha)^{1/3} < 0.9$ , especially for slow reaction curves. This range of applicability corresponds to a reaction degree of 0.999. From the reaction curves (Figure 3.11), one can notice that the model is sufficiently accurate to describe the reaction curve produced using CEMHYD3D.

In order to derive a mathematical correlation between the chemical reaction controlled model and the cellular automata simulations, Eqs. (3.14) and (3.17) can be combined rewritten as

$$\left(1 - (1 - \alpha)^{1/3}\right) = \frac{t \cdot k_1}{r_0} \quad (3.34)$$

Combining Eqs. (3.33) and (3.34), the following relation between time and cycles is derived

$$t = \beta_1 \frac{P_0 r_0}{k_1 r_p} \cdot (C - 2) \quad (3.35)$$

Hence, a universal and linear relation is established between cellular automata cycles ( $C$ ) and digital particle size ( $d_p$ ) and dissolution probability ( $P_0$ ) on the one hand, and time for given initial sphere size of a reacting particle  $r_0$  and reaction constant  $k_1$ . So, a direct relation is obtained between cellular automata parameters and the governing parameters of chemically controlled reaction systems. Furthermore, it can be seen that the  $P_0$  and digitized particle size scale proportionally.

### 3.4.2 Constant and varying particle size case

In this section a relation between time and cycles is derived for the hybrid model, so both surface and diffusion controlled reactions. Before the transition point, the relation only depends on the chemical reaction model and the relation is equal to the unique relation derived in Section 3.4.1. From the transition point onwards, it can be assumed that the reaction time is the summation of the time needed to reach the transition point using the chemical reaction controlled model and time needed to reach a certain reaction degree from the transition point onwards.

The time to reach a certain  $\alpha$  during the diffusion controlled phase from the transition point ( $t_{tr}$ ) onwards can be calculated using Eq. (3.27). Analogue to Eqs. (3.33) instead of time, this point can also be described based on cycles and reads;

$$(C - C_{tr}) \frac{k_2}{r_0^2} = - \frac{(v + (1 - v)(1 - \alpha))^{2/3}}{v - 1} - (1 - \alpha)^{2/3} \frac{(v + (1 - v)(1 - \alpha_{tr}))^{2/3}}{v - 1} - (1 - \alpha_{tr})^{2/3} \quad (3.36)$$

Based on this the following relation for the diffusion controlled phase can be derived

**Table 3.2:** The derived values of  $\beta_1$  for  $d = 7, 13, 21, 25$  and  $35$  and different values of  $v$  for the chemical reaction controlled phase up to  $\alpha_{tr}$ .

$v$	$\beta_1$
0	1.360
1	1.314
1.05	1.313
1.35	1.314
1.7	1.310
2.5	1.313
3.4	1.313
4.25	1.315
5.1	1.315
5.95	1.314
6.8	1.314

$$t - t_{tr} = \beta_2 (C - C_{tr}) \frac{P_0 r_0^2}{k_2 r_p^2} \quad (3.37)$$

with  $\beta_2$  the relation constant for the diffusion controlled phase. The time needed to reach the transition point ( $t_{tr}$ ) according to Eq. (3.35) and for  $C = C_{tr}$  reads

$$t_{tr} = \beta_1 (C_{tr} - 2) \frac{P_0 r_0}{k_1 r_p} \quad (3.38)$$

Combining Eqs. (3.37) and (3.38), the total time becomes

$$t = \beta_1 (C_{tr} - 2) \frac{P_0 r_0}{k_1 r_p} + \beta_2 (C - C_{tr}) \frac{P_0 r_0^2}{k_2 r_p^2} \quad (3.39)$$

With  $\beta_1$  and  $\beta_2$  being the relation constants for the chemical reaction controlled and diffusion controlled systems, respectively,  $k_1$  and  $k_2$  the kinetic parameters of the chemical reaction controlled and diffusion controlled systems, respectively,  $r_p$  the radius of the particle in voxels,  $r_0$  the initial size of a reacting particle and  $P_0$  the reaction probability according to cellular automata model.

The relation constant  $\beta_1$  for the chemical reaction controlled phase can be derived using Eq. (3.33) for  $\alpha \leq \alpha_{tr}$ . A value of 1.42 for  $\beta_1$  was found in Section 3.4.1 for  $0.05 < \alpha < 0.9$ . The same relation is tested here for  $0.05 < \alpha < \alpha_{tr}$  with  $\alpha_{tr}$  being the transition reaction degree as defined in the previous section. For the  $v \geq 1$  system, a value of 1.31 was found (Table 3.2). These values are lower than the value for  $v = 0$ . For the same range ( $0.05 < \alpha < \alpha_{tr}$ ), the  $v = 0$  case leads to a  $\beta_1$  value of 1.36. During derivation of the  $\beta_1$ -values for all cases high  $R^2$ -values were obtained (the minimum  $R^2$  was 0.996).

In order to derive the relation constant for the diffusion controlled phase  $\beta_2$ , the following relation equation based on Eq. (3.26) for constant particle size is used;

**Table 3.3:** (a) Statistical information on the derived values of  $\beta_2$  for  $d = 13, 21, 25$  and  $35$  and  $P_0 = 0.003$  to  $0.099$  in the constant particle size case ( $v = 1$ ) (b) statistical information on derived values of  $\beta_2$  for 10 simulations with  $d = 35$  and  $P_0 = 0.003$  and  $d = 35$  and  $P_0 = 0.021$ .

(a)		(b)		
Parameter	Value		$P_0 = 0.003$	$P_0 = 0.0217$
Mean	4.817	Mean	4.741	4.732
Median	4.800	Median	4.725	4.735
Standard deviation	0.094	Standard deviation	0.053	0.040
Variation	0.009	Variation	0.003	0.002
Coefficient of variation	0.020	Coefficient of variation	0.011	0.009

**Table 3.4:** The derived values of  $\beta_2$  for different values of  $v$  in the diffusion controlled phase.

$v$	$\beta_2$
1	4.817
1.05	4.848
1.35	5.018
1.7	5.171
2.5	5.360
3.4	5.480
4.25	5.552
5.1	5.585
5.95	5.627
6.8	5.637

$$3(1 - \alpha_{tr})^{2/3} - 3(1 - \alpha)^{2/3} + 2(\alpha_{tr} - \alpha) = \beta_2 (C - C_{tr}) \frac{P_0}{r_p^2} \quad (3.40)$$

with  $\beta_2$  being the relation constant,  $C_{tr}$  the cycle in which the (discrete) transition reaction degree  $\alpha_{tr}$  is reached,  $r_p$  the radius of particle size in voxels and  $P_1$  the reaction probability. Table 3.3(a) shows the results of determining the relation based on the ash layer model of Levenspiel (Eq. (3.26)) for the reaction degree between  $\alpha_{tr}$  and 0.9 for  $d = 13, 21, 25$  and  $35$ . During the determination of the relation constant, an coefficient of variation of 0.02 was found, which is half of the coefficient of variation found for the chemical reaction controlled model for shrinking particles (0.04).

Table 3.3(b) shows the results of determining the  $\beta_2$  of 10 simulations with the same initial microstructure containing a 35 particles with two  $P_0$ , namely 0.003 and 0.0217. The coefficient of variation as presented in Table 3.3(b) is below 0.010. This value is an indication for the intrinsic variation of the CEMHYD3D model. The variation of a single particle size within all models is comparable to this intrinsic variation and therefore this variation is intrinsic to the chosen simulation method (e.g. cellular automata).

Analogue to the analysis for the constant particle size case, the varying particle size

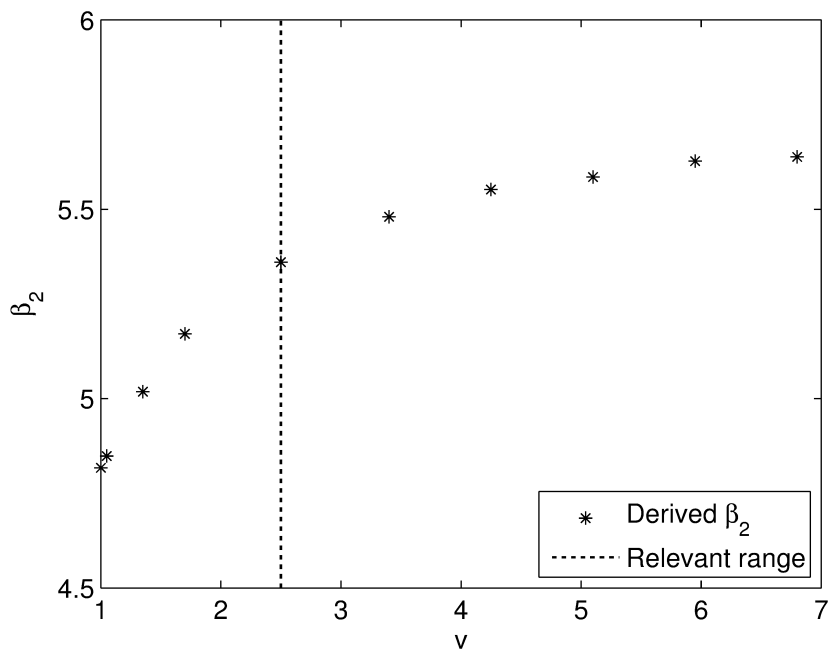


**Figure 3.12:** A graphical representation of the derived values of  $\beta_2$  for different values of  $\nu$  in the diffusion controlled phase and marked area representing the relevant range of  $\nu$  for the reaction of the four main cement clinker phases with water.

**Table 3.5:** (a) Statistical information on the derived values of  $\beta_2$  for  $d = 7, 13, 21, 25$  and  $35$  and  $P_1 = 0.003$  to  $0.099$  in the varying particle size case ( $v \neq 1$ ) (b) statistical information on derived values of  $\beta$  for 10 simulations with  $d = 35$  and  $P_1 = 0.003$  and  $d = 35$  and  $P_1 = 0.021$ .

(a)		(b)		
Parameter	Value	Parameter	$P_1 = 0.003$	$P_1 = 0.217$
Mean	5.171	Mean	5.121	5.170
Median	5.175	Median	5.121	5.170
Standard deviation	0.079	Standard deviation	0.051	0.046
Variation	0.006	Variation	0.003	0.002
Coefficient of variation	0.015	Coefficient of variation	0.010	0.009

case ( $v > 1$ ) be analyzed (with the relation equation based on Eq. (3.25) instead of Eq. (3.26)). The particles in these systems grow due to the fact that more volume of product is formed than the volume of reactant that is disappeared.

Table 3.5(a) shows the results of the combined model with single relation parameter  $\beta_2$  for  $v = 1.7$  (as example) using 165 simulation runs (with each curve the  $R^2 \geq 0.994$ ). It can be noticed from this table that the coefficient of variation is around 1.5%. The coefficient of variation, when performing ten simulation runs with the same initial microstructure is around 1.0 % (Table 3.5(b)).

Table 3.4 and Figure 3.12 show the results of the same analysis for more ash/reactant ratios ( $v$ ). As one can notice from Figure 3.12, that  $\beta_2$  depends on  $v$ . Based on the theory, a constant value for  $\beta_2$  would be expected. Nevertheless the deviation of  $\beta_2$  is 10.7 % for the relevant range of  $v$  between 1 and 2.5, so for - mean-  $\beta_2 = 5.1$  the maximum error is about 5 %. Larger values of  $v$  are hardly found in practice. For cement reactions, for instance the minimum and maximum volume expansions of the reaction of the four (main) cement clinkers phases with water are 1.69 and 2.27.

### 3.5 Conclusions

Cellular automata is a suitable technique to model chemical reactions/systems (Chopard and Droz, 2005; Fraser, 1987; Kier et al., 2005; Ramkrishna and Amundson, 2004; Van der Weeën et al., 2011; Zygourakis and Sandmann, 1988). The disadvantage is the absence of a link between time and cycles, which is the time-based parameter in cellular automata. This chapter intends to provide an unique direct relation between time and cycles for diffusion controlled systems. This is of interest, since in many reactions, a layer of reaction products is formed on the unreacted core, rendering the reaction diffusion rather than surface controlled. The studied system starts as surface controlled, until a certain reaction product layer thickness is reached. From this point of time, the diffusion controlled mechanism can be the rate determining reaction mechanism.

As cellular automata tool, CEMHYD3D was employed. In order to derive this relation a major improvement/modification was introduced. This modification introduced the preference of the system to dissolve voxels on the outside of the particles rather than the middle of the top-surfaces of the particles. In this way a spherical shape is maintained

(in both the chemical controlled and diffusion controlled phase), which could not be maintained in the original version of the dissolution routine.

Using these modification, it is proven that a cellular automata approach is suitable to simulate the chemical reaction controlled model for the shrinking core case. Based on 165 simulations using a wide variation of dissolution probabilities ( $P_0$ ) and particle diameters ( $d_p$ ) a general and original linear relation between cycles and time was derived (Eq. (3.35)). The derived model can describe the reaction sufficiently accurate up to a reaction degree of 99.9%.

Furthermore, it is shown using the results of simulations, that the cellular automata approach (applying the (earlier developed) modified dissolution routine) can adequately describe the constant ( $v = 1$ ) and varying ( $v \neq 1$ ) particle size case using a diffusion (ash layer) controlled model in both cases for a reaction degree larger than the transfer reaction degree ( $\alpha_{tr}$ ). The threshold reaction degree is the reaction degree at which a diffusion layer of 1 voxel is formed. A hybrid reaction model based on chemical reaction controlled and (ash) diffusion controlled model have been introduced in order to cope with the existence of the transition reaction degree.

In the present analysis, the cellular automata parameters are mathematically related to the kinetic parameters of the CRC and ash diffusion model, only using the relation constants  $\beta_1$  and  $\beta_2$ , respectively. This is achieved by computing the mathematical relation between the cellular automata simulations and the chemical reaction models for 132 different simulations with varying particle sizes and reaction probabilities. A value of 1.31 was found for the relation constant  $\beta_1$ , while a relation between the product/reactant ratio  $v$  and the relation constant ( $\beta_2$ ) is found for  $v \geq 1$  from threshold reaction degree onwards. The coefficient of variation for 132 simulations is around 2 %. It should be noticed that typical cellular automata simulations have already an intrinsic coefficient of variation of 1.0 % owing to their statistical nature, since it depends on probabilities for transitions.

This relation is tested from the threshold reaction degree  $\alpha_{tr}$  (so the transition point between chemical reaction and diffusion controlled) onwards. Since the full conversion time is of interest, a hybrid model is introduced here, which combines the chemical reaction controlled and diffusion controlled phase. Using this hybrid model, a unique relation between time and cycles based on the parameters of cellular automata (particle size and reaction probability) and chemical models is derived (Eq. (3.39)).

## Multi-cycle and multi-scale modelling \*

### 4.1 Introduction

This chapter intends to improve the predictions of the CEMHYD3D model (Section 1.6) for different system resolution (different scales) by further modification of the dissolution and nucleation probability and the number of diffusion steps within the model. As pointed out by Chen and Brouwers (2008), the physical properties of a hydrating microstructure are limited by the smallest element-size available in the system, the so-called system resolution. Besides the representation of the properties, the system resolution also influences the needed computation power and time needed to run a simulation. In this chapter it is shown that resolutions of  $0.2 \mu\text{m}$  nowadays are possible due to increased computations power, while in the original version of CEMHYD3D the used resolution is  $1 \mu\text{m}$ . The use of lower resolutions leads to problem that the amount of hydrated cement per cycle decreases when the system resolution increases (Garboczi and Bentz, 2001) and therefore the predictions of the models significantly depend on the system resolution. Garboczi and Bentz (2001) discuss the required resolution needed and concluded that  $0.2 \mu\text{m}$  is sufficient, which is close to the smallest particle size in cement and calcium sulphates (Hunger and Brouwers, 2009). Chen and Brouwers (2008) have incorporated the diffusion layer system of Van Breugel (1997) into the CEMHYD3D-model.

Besides the multi-scale modelling, this chapter also pays attention to multi-cycle modeling. Multi-cycle modelling enables to zoom in and out into hydration process with regard to time. This is needed for instance when one wishes to study the hydration of calcium sulphate hemihydrates, which have a extreme short hydration time compared to cements, or when one wishes to study the long-term reaction behaviour of cementitious materials, when the reaction rate becomes extremely slow. Both modifications will lead to modifications in the modelling of the hydration process, which consists of dissolution, diffusion and nucleation stage of the process.

### 4.2 Multi-cycle modelling

In this section, the option of multi-cycle modelling is introduced. The idea behind multi-cycle is the variation of the length of the time steps in the model. Figure 4.1 shows the principle of multi-cycle modelling. In this section the term reference cycle will be used to describe a cycle within the original model. In order to describe this variation, the multi-cycle factor  $k$  is introduced. A higher multi-cycle factor  $k$  results in  $k$  smaller time steps during hydration and therefore resulting in  $k$  time more cycles to achieve a same

---

\*Parts of this chapter were published elsewhere (Brouwers and de Korte, 2014; De Korte, 2008; De Korte and Brouwers, 2009a)

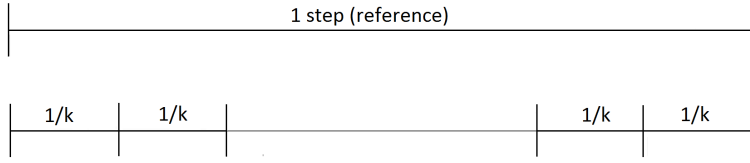


**Figure 4.1:** Schematic representation of the reference cycle and the multi-cycle cycle ( $k < 1$ ).

degree of hydration. Hence, for a reference cycle holds that  $k = 1$ .

This is necessary, because the hydration of some reactants, e.g. hemihydrate, may be much faster compared with the hydration of the cement clinkers. The complete hydration of hemihydrate takes place within half an hour, while full cement hydration takes a much longer time. Multi-cycle modelling introduces two major adaptations to the model: the modification of the reaction kinetics and a correction of the calculation of the reaction time.

Within CEMHYD3D the kinetics are mainly regulated by the dissolution and nucleation probabilities and the number of diffusion steps. Due to smaller time step at a larger  $k$ -factor, the number of particles that dissolve, diffuse and nucleate is smaller. Therefore these probabilities need to be smaller. In this section, the modification of the reaction kinetics is described. In this chapter the reference system refers to the system with system resolution of  $1 \mu\text{m}$  and without any multi-scale (nor multi-cycle) modifications.

#### 4.2.1 Dissolution

The expectation of a voxel-face to dissolve in the reference system during a cycle equals the dissolution probability ( $P_{D,1}$ ). In general, for  $k$  cycles the expectation reads

$$\sum_{i=1}^k i \left[ \binom{k}{i} P_{D,k}^{k-i} (1 - P_{D,k}) \right] = k P_{D,k} \quad (4.1)$$

with  $P_{D,k}$  is the dissolution probability when a cycle is divided into  $k$  new cycles. This probability is equal to the expectation of dissolution in the reference system,  $P_{D,1}$ , when

$$P_{D,k} = \frac{1}{k} P_{D,1} \quad (4.2)$$

with  $k$  is the multi-cycle factor.

#### 4.2.2 Diffusion

As described earlier, in Section 1.6, diffusion is modelled as a series of random walks. In the present model 500 random diffusion steps ( $D_1$ ) are undertaken. After every diffusion

step, there is a possibility for nucleation. The average distance according to literature (Berryman and Franceschetti, 1989; Gardner, 1992; Kier et al., 2005) reads

$$\langle d \rangle = l_0 \cdot \sqrt{D_1} \quad (4.3)$$

with  $\langle d \rangle$  the average distance,  $l_0$  the average step size and  $D_1$  the number of cycles. When it is assumed that a voxel can walk in 1 cycle over a distance  $\langle d \rangle$ , and multi-cycle modelling will not change the speed and step size ( $l_0$ ) of a voxel, then in multi-cycle situation after  $k$  cycles the same distance  $\langle d \rangle$  should be travelled. Therefore the number of diffusion steps ( $D_k$ ) during one new cycle reads;

$$D_k = \frac{1}{k} D_1 \quad (4.4)$$

### 4.2.3 Nucleation

Nucleation is the third reaction mechanism. If  $P_{N,1}$  is the nucleation probability for  $k = 1$  and  $P_{N,k}$  is the nucleation probability for 1 cycle in the situation of  $k$  cycles. Similar to the dissolution probability, the nucleation probability reads;

$$P_{N,k} = \frac{1}{k} P_{N,1} \quad (4.5)$$

### 4.2.4 Cycles correction

The multi-cycle modification influences both the number of cycles and the reaction rate. Since the reaction rate depends on the temperature and the reactions (dissolution and nucleation) in the model directly influence the temperature, no modification is needed here. On the other hand, the number of cycles needs to be modified. The number of cycles in the reference system can be calculated from the number of cycles in the multi-cycle systems. The correction consists of two parts. The first part is the correction for the step size. Instead of 1 cycle in the reference situation,  $k$  cycles are carried out in the multi-cycle situation. The second correction is a correction for the starting point. Instead of starting with cycle 0, the new situation starts with cycle  $2 - 2k$ . So the calculation of cycles in according to the following equation;

$$C_1 = C_k \frac{1}{k} + \left(2 - \frac{2}{k}\right) \quad (4.6)$$

Eq. (4.6) can also be expressed in terms of the new multi-cycle cycles ( $C_k$ ) and reads

$$C_k = k(C_1 - 2) + 2 \quad (4.7)$$

**Table 4.1:** Used versions of the model.

	A	B
Purpose	Simplified model	Full model
Diffusion layer	Impermeable	Yes
Surface precipitation	No	Yes
Spontaneously nucleation	No	Yes
Cement composition	C <sub>3</sub> S	OPC
Particle size distribution	Mono-sized (1 $\mu\text{m}$ )	Poly-dispersed
water-binder ratio	Dilute(12.65)	Normal

### 4.3 Multi-scale modelling

Chen (2007) and Chen and Brouwers (2008) pointed out that the smallest size handled in CEMHYD3D, called the 'system resolution', is an important feature of a digitized model. Particles smaller than the 1  $\mu\text{m}$  voxel size cannot be represented since the model is based on the movement and phase change of each discrete voxel. Furthermore, the system resolution determines the amount of computing time needed for a specific task, a higher system resolution will lead to a longer computational time. Due to better computation possibilities, the use of higher resolutions is possible nowadays. Chen (2007) already presented the simulations with resolutions from 0.5 to 2  $\mu\text{m}$ . In this research the model has been further modified to cope with several different resolutions from 0.2-2  $\mu\text{m}$  (or  $500^3$ - $50^3$  voxels in the system).

Chen (2007) and Chen and Brouwers (2008) indicate that the absence of diffusion controlled reaction mechanism in the original version of CEMHYD3D leads to undesired effects of system resolution on the model predictions. Changing the system resolutions will change the model outcome significantly (Garboczi and Bentz, 2001), which will not be the case in a robust system. Therefore Chen (2007) included diffusion controlled reaction mechanism in the CEMHYD3D-model. The next section will describe the necessary modification needed for the multi-scale modification.

#### 4.3.1 Modification of the hydration system

The initial microstructure at a resolution of 1  $\mu\text{m}$  is created with the Makecem-module of CEMHYD3D, while the microstructure at other (lower) resolutions is created by splitting the voxels in the microstructure into more elements. Figure 4.2(a) shows a voxel at resolution of 1  $\mu\text{m}$ , while Figure 4.2(d) shows the same voxel at resolution of 0.33  $\mu\text{m}$ . The simplest case of 1 voxel particle that is split in a particle containing 8 voxels of size 0.5 is treated as example here (Figure 4.2(b)). The probability that particle consisting of one voxel does not dissolve in one cycle reads

$$1 - P_{D,p1} = (1 - P_{D,1})^6 \quad (4.8)$$

with  $P_{D,1}$  as the dissolution probability of one particle (voxel) face in the reference system, and  $P_{D,p1}$  is the dissolution probability of the entire particle, which has 6 faces (Fig. 4.2(a)). When the particle consists of 8 voxels of size 0.5, each voxel has 3 external

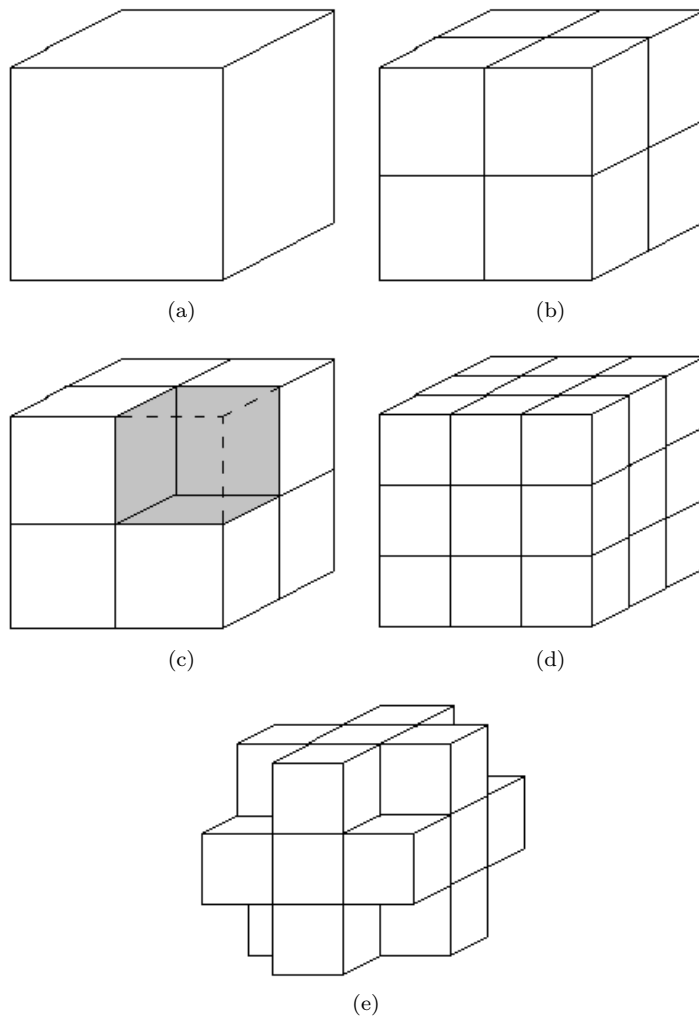


**Figure 4.2:** Schematic presentation of the principles of 4.2(d) splitting and 4.2(e) scaling particles for multi-scale modelling using a 1 voxel size particle 4.2(a). In 4.2(c) the blocked surfaces in case of dissolution in version A of CEMHYD3D are shown in gray.

faces (Fig. 4.2(b)). Hence, the probability one individual voxel will not dissolve follows as

$$1 - P_{D,v2} = (1 - P_{D,2})^3 \quad (4.9)$$

with  $P_{D,2}$  as the dissolution probability of each 0.5 voxel face in the system with double resolution, and  $P_{D,v2}$  is the dissolution probability of each voxel. The probability that none of the 8 voxels dissolves is  $(1 - P_{D,v2})^8$  and that all 8 voxels (i.e. the entire particle) dissolve is  $(P_{D,v2})^8$ . In general, the probability that  $i$  voxels dissolve is  $\binom{8}{i} (1 - P_{D,v2})^{8-i} (P_{D,v2})^i$ . The overall probability for the dissolution of the 8 voxel particle reads:

$$P_{D,p2} = \sum_{i=0}^8 \left[ \binom{8}{i} P_{D,v2}^{8-i} (1 - P_{D,v2})^i \left( \frac{i}{8} \right) \right] = P_{D,v2} \quad (4.10)$$

The 1 voxel and 0.5 voxel systems are congruent when  $P_{D,p2} = P_{D,v2}$  equals  $P_{D,p1}$ , hence yielding as expression

$$P_{D,s} = 1 - (1 - P_{D,1})^s \quad (4.11)$$

with  $s = 2$ , i.e. as the number that governs the split of each voxel. Without further proof it is assumed that the derivation for  $s = 2$ , presented in the foregoing, also holds for other resolution increases, so  $s = 3, 4$ , etc.

### 4.3.2 Diffusion layer

The modification of diffusion controlled system consists of two parts, the modification of the probability and the number of cells forming the layer thickness. It is assumed that the probability changes in the same manner as for the surface-based dissolution (Subsection 4.3.1). When taking into account these needed modifications, the modified equation for the diffusion controlled part reads;

$$P_{D,s} = (1 - (1 - P_{D,0})^s) \frac{\delta_{tr}}{\delta} \quad (4.12)$$

with  $\delta$  the diffusion layer thickness,  $\delta_{tr}$  the transition layer thickness,  $s$  the multi-scale factor. To obtain the same (transition) layer thickness and layer thickness at different resolutions, the number of voxels differ. Figure 4.3 shows a graphical representation of the diffusion layer thickness ( $\delta$ ) at different resolutions. Figure 4.3(a) shows diffusion layer at the reference system ( $s = 1$ ) and 4.3(b) shows the layer at  $s = 2$ . Whereas on the left side the diffusion layer is formed by one voxel, on the right side two voxels are needed. So, the number of voxels to reach a diffusion layer thickness  $\delta$  is proportional to  $s$  and reciprocal to the resolution.

Besides the dissolution probability also the number of diffusion steps and nucleation

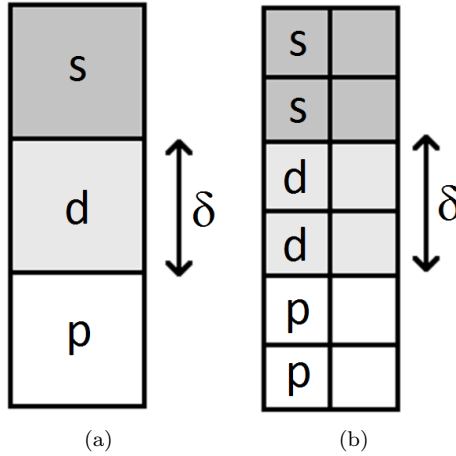


**Figure 4.3:** A graphical representation of the diffusion layer thickness at different resolutions with  $s$  the source (cement) voxel,  $d$  the diffusion layer voxel and  $p$  the void fraction voxel. In the example, (a) the reference system with a diffusion layer of 1 voxel and (b) a  $s = 2$  system, in which the diffusion layer consists of two voxels.

chance need to be adjusted. The average distance that a voxel moves during a random walk needs to be the same at different resolutions. The average distance is given by Eq. (4.3). Assuming that distances at different resolutions needs to be equal and the average step size is equal to  $1/s$ , the following relation between number of diffusion steps then reads

$$D_s = s^2 \cdot D_1 \quad (4.13)$$

with  $D_1$  the original number of steps and  $s$  the multi-scale factor. The modified nucleation probability equation reads

$$P_{N,1} = 1 - (1 - P_{N,0})^s \cdot \left( 1 - e^{-\frac{i_1}{i_{max,1} \cdot s^3}} \right) \quad (4.14)$$

with  $i_1$  is the number of diffusing voxels,  $P_{N,1}$  the nucleation chance without multi-scale and multi-cycle,  $i_{max,1}$  the scale factor for nucleation for the  $1 \mu\text{m}$  reference system, and  $s$  the multi-scale factor. The factor  $s^3$  in Eq. (4.14) can be explained by the fact that the total number of voxels in the system increases by this factor compared to the reference system.

### 4.3.3 Combined multi-scale and multi-cycle modelling

The previous sections describe the modifications for multi-cycle and multi-scale modelling separately. This section addresses the combination of both modifications. In case of

**Table 4.2:** The used particle size distribution for simulations.

Particle size( $\mu\text{m}$ )	Volume fraction (% V/V)
1	0.0
3	0.0
5	10.8
7	20.8
9	14.4
11	10.8
13	8.5
15	6.5
17	5.2
19	4.1
21	3.2
23	2.6
25	2.5
27	2.3
29	2.2
31	2.1
33	1.1
35	1.0
37	1.0
39	0.9

surface-controlled reaction (so no diffusion layer) the equation for the dissolution probability, assuming both modification are not correlated, reads;

$$P_{D,k,s} = 1 - \left(1 - \frac{1}{k}P_{D,1}\right)^s \quad \text{for } \delta \leq \delta_{tr} \quad (4.15)$$

While the equation for diffusion controlled part reads;

$$P_{D,k,s} = \left(1 - \left(1 - \frac{1}{k}P_{D,0}\right)^s\right) \cdot \frac{\Omega}{\delta} \quad \text{for } \delta < \delta_{tr} \quad (4.16)$$

In both cases the number of diffusion steps is equal to

$$D_{k,s} = \frac{1}{k} \cdot s^2 \cdot D_1 \quad (4.17)$$

**Table 4.3:** Chemical composition of the used CCRL-116 cement (Bentz et al., 2002; NIST, 2002).

Cement clinker	Mass fraction (% m/m)
C <sub>3</sub> S	67.08
C <sub>2</sub> S	22.17
C <sub>3</sub> A	7.11
C <sub>4</sub> AF	3.64

## 4.4 Simulation results

### 4.4.1 Multi-cycle

In Section 4.2, the modifications of CEMHYD3D in case of multi-cycle simulations were described. These modifications included the modification of all three main hydration process steps, namely dissolution, diffusion and nucleation. This involved the modification of the dissolution and nucleation probability, the number of random walk diffusion steps as well the correction of the number of cellular automata cycles. In this subsection, all modifications are validated.

For the validation of the multi-cycle modifications, a mixture of Portland cement and water with a water-binder ratio of 1.2 was used. The applied Portland cement was CCRL cement 116 (Bentz et al., 2002; Bullard and Garboczi, 2006; NIST, 2002). Table 4.2 shows the particle size distribution used for the multi-cycle simulations. The clinker composition of the used CCRL-116 cement can be found in Table 4.3. The cellular automata parameters, such as specific density, dissolution and nucleation probabilities of the different cement phases, used for the simulations are presented in Table 1.6.

Figure 4.4 shows the hydration curve for a OPC with diffusion layer for several multi-cycle factors  $k$ . The difference between the dissolution lines is very small, confirming the validity of the newly derived equations for dissolution probability, the number of diffusion steps and nucleation probability, Eqs. (4.2), (4.4) and (4.5), respectively. The figure also shows that the correction of the cycles using Eq. (4.6) is valid.

In Appendix D, three different equations for the multi-cycle modification are tested for mono-sized particle (15  $\mu\text{m}$ ) with extreme high dissolution probability ( $P_{D,0}$ ) of 0.2 in order to enlarge magnify the differences at different multi-cycle factors. Also at this large dissolution probability Eq. (4.2) proves to give very good results.

Furthermore it can be concluded from Figure 4.4, that the multi-cycle modification can be applied both for zooming in and out with regard to cycles/time. This features enables the possibility to study very fast hydrations, like calcium sulphates as well as the study of the long term hydration behaviour of cementitious materials.

### 4.4.2 Multi-scale by voxel splitting

In order to verify the multi-scale model, Eq. (4.11) is tested within version A of CEMHYD3D (see Table 4.1). This version of the system consists of a dilute system with dispersed 1  $\mu\text{m}$  voxels (2.47 %V/V) with a minimum distance of 2  $\mu\text{m}$ , so no diffusion layers nor precipitation of hydration products are considered, and each voxel which dissolves creates leaves behind nonreacting surfaces, keeping the shared surfaces of other voxels insoluble. In Figure 4.2(c), the shared insoluble voxel sites are shown in gray in

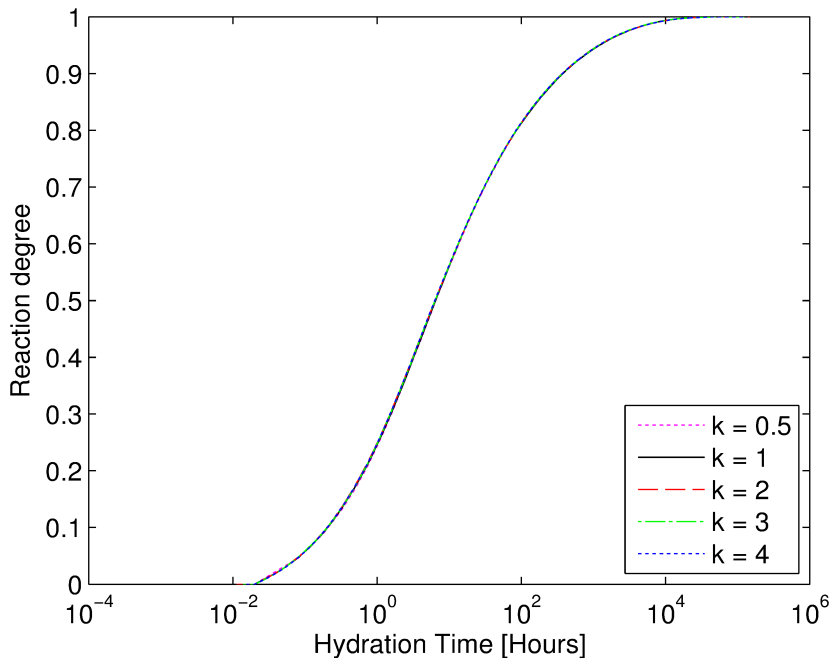
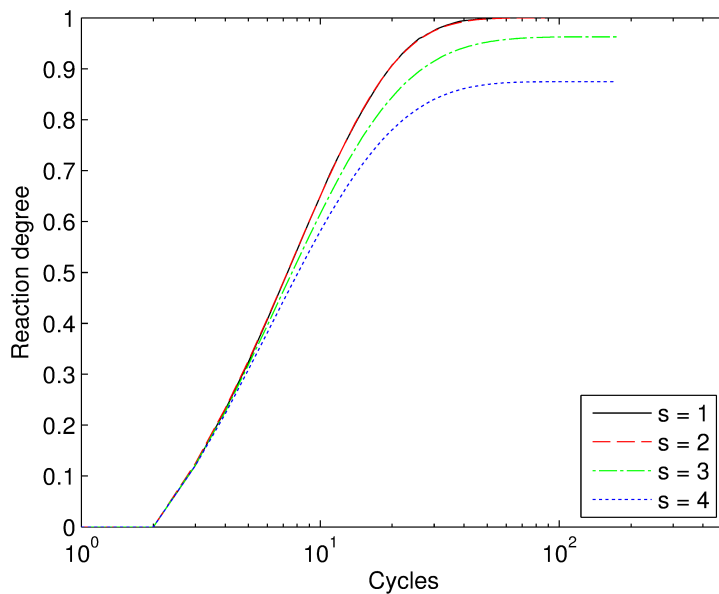


**Figure 4.4:** Multi-cycle simulation of CCRL-116 (Table 4.3) with PSD (Table 4.2) and  $w_{br} = 1.2$ .

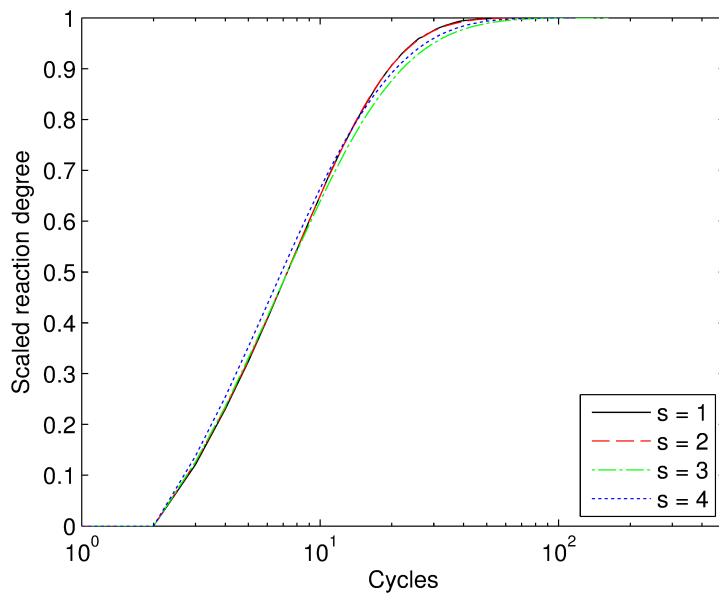
case the top right voxel is dissolved.

Figure 4.5(a) shows the simulation results for this test case. As can be noticed from the figure, the hydration lines for  $s = 1$  and  $s = 2$  are almost identical. Therefore this case is confirming the derivation presented in Subsection 4.3.1. The hydration curves for  $s = 3$  and  $s = 4$  reach a lower final hydration degree, which can be explained by the fact that voxels in the middle of particles are blocked for dissolution by the surrounding particles. The theoretical maximum hydration degree due to blocking of these internal voxels is  $26/27$  ( $\sim 0.963$ ) and  $56/64$  ( $= 0.875$ ) for  $s = 3$  and  $s = 4$ , respectively. When one takes into account the theoretical maximum hydration degree, the hydration curves for  $s = 3$  and  $s = 4$  behave as expected, although some effects of the fact that the outer layer consists of voxels with 1, 2 and 3 surfaces exposed to the pore solution, are visible (Figure 4.5(b)).

Eq. (4.11) has been validated using version A of CEMHYD3D (Table 4.1) for several resolutions. In reality this simplified system does not exist, since dissolution creates additional reaction surfaces and leads to the formation of hydration products through which the cement can diffuse. Here this simplified system (version A) will be extended with the creation of additional reaction surface by not blocking the shared sides of voxels and allowing for the creation of hydration products, which can precipitate on the particle and spontaneously nucleate in the pore solution. The extended cement hydration model (version B) including Eq. (4.12) is used in this section. The new (dissolution) routine, which was introduced in Chapter 3, has been incorporated in this (extended) version



(a)



(b)

**Figure 4.5:** Hydration curves showing the results of applying/validating the derivation of Eq. (4.11) using a dilute system ( $wbr = 12.64$ ) with  $1 \mu\text{m}$  particles (without deposition of reaction products).

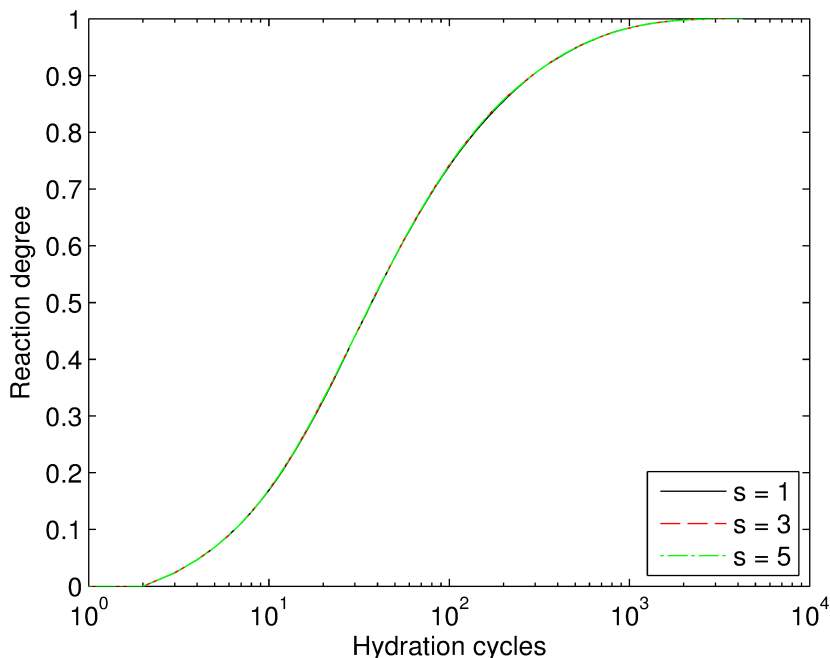


**Figure 4.6:** The results of multi-scale simulations of a OPC-cement (Table 4.3) with full particle size distribution (Table 4.2) and a water-binder ratio of 1.37 using the voxel splitting method.

B of CEMHYD3D. The main difference between the original and the new (dissolution) routine is that the new routine tries to maintain the spherical shape of the particles and therefore its dissolution behaviour is closer to the shrinking core theory, since the creation of additional reactive surface, due to the discrete manner of cellular automata, is partially prohibited.

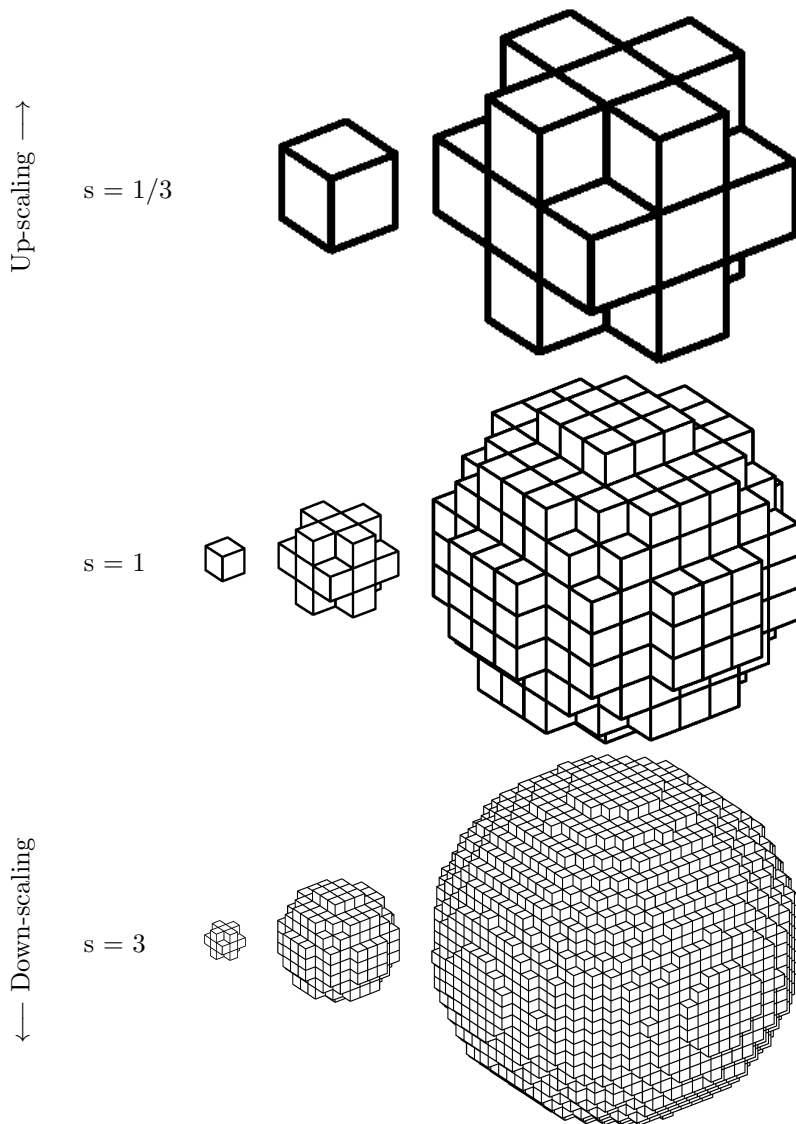
Figure 4.6 shows the reaction degree during hydration of CCRL Portland cement 116 with a water-binder ratio of 1.37. The clinker composition of this cement can be found in Table 4.3 and the used particle size distribution is given in Table 4.2. One can notice from Figure 4.6 that the derived multi-scale modifications (Eqs. (4.11) and (4.12)) can be successfully applied using the splitting method (Figures 4.2(b) and 4.2(d)) for the multi-scale simulation of Portland cement.

#### 4.4.3 Multi-scale by particle rescaling

Another possibility to simulate the hydration at higher resolutions is rescaling instead of splitting of voxels. Table 4.4 shows the principle of both the up and down-scaling for a 1, 3 and 9 particle with a factor of three. With up-scaling, a 3 voxel particle is used to represent a 1  $\mu\text{m}$ -particle in a  $s = 3$  system, a 9 voxel particle is used for 3  $\mu\text{m}$  particle and so on. The difference of down-scaling compared to splitting is that particles are becoming more spherically shaped.

During this simulation, the number of particles of the different sizes is kept the same at

**Table 4.4:** Schematic representation of the principle of up- and down-scaling of 1, 3 and 9 voxel particle (at  $s = 1$ , reference system) with  $s < 1$  for down-scaling and  $s > 1$  for up-scaling.



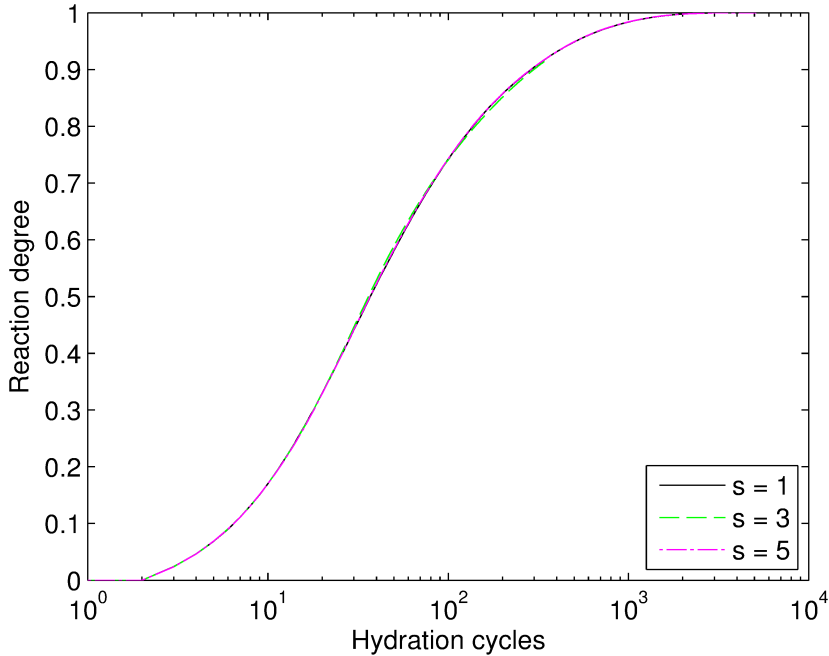


**Figure 4.7:** The results of multi-scale simulations of a OPC-cement (Table 4.3) with full particle size distribution (Table 4.2) and a water-binder ratio of 0.6 using the particle re-scaling method.

different resolutions. This ensures that the particle size distribution remains the same, but it has a slight effect on the volume ratio of the binder. Furthermore scaling down would enable the possibility to use a smaller minimum particle size, which is beyond the scope of this research.

As one can notice from Table 4.4, in case of up-scaling, there is a challenge in order to represent a  $1\ \mu\text{m}$  particle, since no digitized particle is available for this size. A solution for this could be a redesign of the particle size distribution.

Figure 4.7 shows the results of hydration using down-scaling of the CCRL 116 Portland cement with a water-binder ratio of 0.6. Tables 4.2 and 4.3 present the used particle size distribution and the clinker composition of the applied Portland CCRL 116 cement, respectively. Table 1.6 shows the cellular automata parameters, such as specific density and dissolution probability of the different cement phases, which were used during the simulation. The figure reveals that with the current multi-scale model different system resolutions can be successfully transformed into each other. This provides the opportunity to use a larger size range than was available in the original version of CEMHYD3D. For example for  $s = 3$  down-scaling, instead of  $1\ \mu\text{m}$  particle as minimum particle size now  $1/3\ \mu\text{m}$  particles are allowed in the system. This size is actually very close to the smallest particle size found in cements, calcium sulphates, and other cementitious materials (Hunger and Brouwers, 2009).

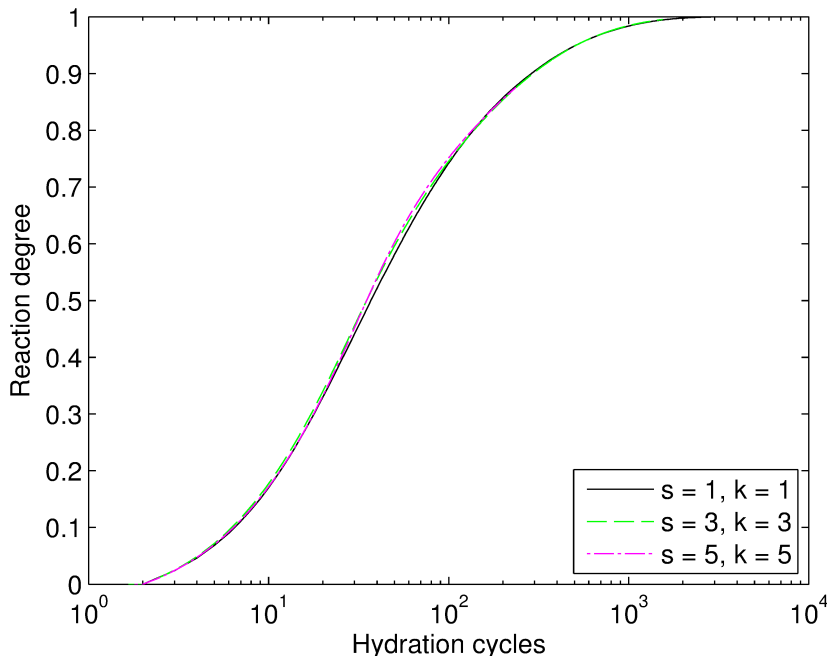


**Figure 4.8:** The results of a combined multi-scale and multi-time simulation of a OPC-cement (Table 4.3) with full particle size distribution (Table 4.2) and a water-binder ratio of 0.60 using the particle re-scaling method.

#### 4.4.4 Combined multi-cycle and multi-scale

In Subsections 4.4.1, 4.4.2 and 4.4.3, the multi-cycle and multi-scale modifications were tested separately. In this subsection, both modifications are applied simultaneously. This is tested using a mixture containing CCRL-116 Portland cement with a water-binder ratio of 0.60. The particle size distribution and clinker composition listed in Tables 4.2 and 4.3, respectively, were used. The used dissolution probabilities and other cellular automata parameters are again taken from Table 1.6.

Figure 4.8 shows the simulation results of the three tested combinations of multi-cycle and multi-scale factors,  $k$  and  $s$ , respectively. The first combination is the so-called reference case, in which  $s = 1$  and  $k = 1$  (e.g. no modifications). The second combination is the 300 system (i.e. a system resolution of  $0.33 \mu\text{m}$ ) with  $1/3$  time steps ( $s = 3$ ,  $k = 3$ ) and the third combination is a 500 system ( $0.2 \mu\text{m}$ ) with  $1/5$  time steps (so  $s = 5$ ,  $k = 5$ ). As one can notice from the figure, there is only a slight deviation between all combinations, but the difference is minor. In other words, both multi-cycle as multi-scale features presented, can be used to model cellular automata systems. These features extend the CEMHYD3D model with the possibility to zoom in and out in both time/cycles as well as particle size range at the same time.

## 4.5 Conclusions

This chapter focuses on the modification/extensions of the CEMHYD3D cement hydration model. The main purpose of these extensions is to be able to study the properties of cementitious materials during hydrating with smaller time-steps (multi-cycle) and at higher resolutions (multi-scale). Therefore the dissolution and nucleation probabilities and the number of diffusion steps from the original model have been modified based on statistical considerations. For the multi-scale modifications, two variants to obtain the microstructure at higher resolutions have been applied, namely voxel splitting and rescaling. The main difference between both methods is the change of the particle shape (see Figure 4.2 and Table 4.4). Using the new version of the CEMHYD3D a system resolution of down to  $0.2 \mu\text{m}$  is possible. Garboczi and Bentz (2001) point out that  $0.2 \mu\text{m}$  is accurate enough for the simulation of cement hydration and is close to the minimum particle size in cement and other binders (Hunger and Brouwers, 2009).

All modifications have been tested for the multi-cycle and multi-scale modification separately, as well as both and the modifications combined, for a system consisting of an OPC cement. All simulations showed good agreements between the results at different resolutions (for both methods) and applying different time-steps. The current models are therefore recommended when one wishes to change the system resolution, cycle-time relation or both.

## Ultrasonic sound speed analysis\*

### 5.1 Introduction

Currently the hydration of hemihydrate to dihydrate and cement is studied by IR, SEM and Vicat techniques. Because the speed of hydration is more difficult to measure the hydration curve and the different processes which take place. For the measurement of the hydration of cement and concrete, in the last decade ultrasonic sound velocity measurements have been applied successfully (De Belie et al., 2005; Reinhardt and Grosse, 2004; Robeyst et al., 2008). This method has the advantage over the more traditional methods, such as the aforementioned Vicat-needle, SEM and IR, that ultrasonic measurements are continuous (Ylmén et al., 2009), and that they provide information about the microstructure development and the related properties like strength development (Robeyst et al., 2008). Especially for hemihydrate hydration, due to the short hydration time, it is difficult to stop the hydration for discontinuous measurements. The ultrasonic sound velocity method used here is developed and patented by the university of Stuttgart (Reinhardt et al., 1999). The combining of ultrasonic measurements and volumetric composition has not been studied for hemihydrates yet, so far only studies are reported concerning cement paste and mortar, and also here these models were never combined to an overall volumetric composition model. Hence, this article will focus on the application of the ultrasonic sound velocity measurement for assessing the hydration curve of hemihydrate to gypsum. Therefore it will be combined with information about the volume fractions of binders and hardened material during hydration and the classic hydration-time relations given by Schiller (1974). The currently used models do not fully combine this information, because they either only focus on the microstructure development (Sayers and Dahlin, 1993) or the effect of additives on the hydration (Reinhardt and Grosse, 2004; Robeyst et al., 2009, 2008). In this chapter a relation is established between ultrasonic speed and microstructure during hydration, from fresh state after mixing until hardened state at fully completed hydration.

### 5.2 Sound velocity of materials

This section describes the sound velocity through materials. Therefore first a short introduction is given about sound velocity through fluid and non-porous material (Section 5.2.1). Afterwards the velocity through slurries (Section 5.2.2) and porous material (Section 5.2.3) are given. These two sections describe the starting and final states during the hydration, respectively.

---

\*Parts of this chapter were published elsewhere (De Korte and Brouwers, 2011)

**Table 5.1:** Relevant physical properties of different materials; sound velocity of water, air and steel according to Lide (2003); sound velocity of gypsum according to Losso and Viveiros (2005); elastic, bulk and shear modulus and Poisson ratio according to Haecker et al. (2005); Meille and Garboczi (2001); Schofield et al. (1997); bulk modulus air Haecker et al. (2005).

	Specific density ( $\text{kg}/\text{m}^3$ )	Sound speed ( $\text{m}/\text{s}$ )	Elastic modulus ( $\text{GPa}$ )	Bulk modulus ( $\text{GPa}$ )	Shear modulus ( $\text{GPa}$ )	Poisson ratio
Water	1000	1497		2.2		
Air		346		0.142		
Steel	7700	5930	170	79.3		
Dihydrate	2310	6800	45.7	42.5-45.7	15.7-17	0.33
Hemihydrate	2619		62.9	52.4	24.2	0.30
Anhydrit	2520		80	54.9	29.3	0.275

### 5.2.1 Introduction

There are two methods to obtain the sound speed of materials. The first method is the use of measured values. Table 5.1 shows the sound speed through some materials as reported in literature. Besides this direct method, there is a second method to acquire the value of sound speed. This indirect method is based on the bulk modulus and density of the material and reads

$$c = \sqrt{\frac{K}{\rho}} \quad (5.1)$$

with  $c$  the sound speed,  $K$  the bulk modulus and  $\rho$  the specific density. This method is suitable for fluids and gases, but is not valid for solid materials. Since solid materials can support both longitudinal and shear waves, the shear modulus besides the bulk modulus influences the sound velocity. Therefore the equation for solids reads

$$c = \sqrt{\frac{K + \frac{4}{3}G}{\rho}} \quad (5.2)$$

where  $K$  and  $G$  are the bulk and shear modulus of the solid, respectively, and  $\rho$  its specific density. Table 5.1 shows the elastic, bulk and shear modulus of several materials, as well as that of water and air. When applying Eqs. (5.1) and (5.2), the results for (non-porous) gypsum are 4289-4448 m/s, and 5019-5210 m/s, respectively. The results of both equations are lower than the experimental value of 6800 m/s provided by Losso and Viveiros (2005). This value is too high according to Sakalli (2011). Eqs. (5.1) and (5.2) tend to underestimate the sound velocity through solids. This is even more true for porous solids, which also contain voids. In Section 5.4 the composition of a hemihydrates-water-gypsum system is addressed, used here for the development of a new model relating sound velocity and compositional properties.

### 5.2.2 Sound velocity of a slurry

This sub-section describes the sound velocity of a slurry, i.e. a suspension, containing entrapped air. Robeyst et al. (2008) presented a model for the ultrasonic velocity through fresh cement mixtures, based on the theoretical model of Harker and Temple (1988) for ultrasonic propagation in colloids. According to these models, the effective wave velocity ( $c_e$ ) in a suspension is given by;

$$c_e^2 = \left[ \left( \varphi_t \frac{1}{K_f} + (1 - \varphi_t) \frac{1}{K_s} \right) \cdot \left( \frac{\rho_f(\rho_s(\rho_t + (1 - \varphi_t)S) + \rho_f S \varphi_t)}{\rho_s \varphi_t^2 + \rho_f(S + \varphi_t(1 - \varphi_t))} \right) \right]^{-1} \quad (5.3)$$

with the subscript  $f$  referring to the fluid,  $s$  to the solid, and  $\varphi_t$  to the fluid volume fractions. The parameter  $S$  generally depends on the size and shape of the particles, the void fraction and the continuous phase viscosity (Austin et al., 1996), but it can be approximated by Eq. (5.4) for spherical particles in a fluid (Gómez Álvarez-Arenas et al., 2002)

$$S = \frac{1}{2} \left( \frac{1 + 2(1 + \varphi_t)}{\varphi_t} \right) \quad (5.4)$$

When also entrapped air is present in the fluid, the compressibility of the continuous phase can be corrected, assuming the air to be uniformly distributed

$$\frac{1}{K_f} = \left( 1 - \frac{c_{air}}{\varphi_t} \right) \frac{1}{K_{water}} + \frac{c_{air}}{\varphi_t} \frac{1}{K_{air}} \quad (5.5)$$

with  $c_{air}$  as the air volume fraction in the voids of the fluid and  $K_{air}$  the bulk modulus of air.

### 5.2.3 Sound velocity of porous solid

The equations from Section 5.2.1 are not directly applicable to a porous materials. Therefore this subsection will describe two ways to calculate the sound velocity through porous material. First the calculation based on the bulk and shear modulus like in Eqs. (5.1) and (5.2) is described. Afterwards the calculations using the theoretical sound velocities of the non-porous materials (as presented in Table 5.1) are described.

#### Bulk modulus based approach

When using the bulk-based approach for the calculation of the sound velocity through porous materials, the bulk modulus, shear modulus and density need to be computed. Analogue to thermal conductivity one could expect the boundaries for a material to be given by the parallel and series arrangement. Hoyos et al. (1994) uses the parallel arrangement, this equation reads

$$K_e^{-1} = (1 - \varphi_t) K_s^{-1} + \varphi_t K_f^{-1} \quad (5.6)$$

with  $K_e$  the effective bulk modulus,  $K_s$  the bulk modulus of solid and  $K_f$  the bulk modulus of the fluid. The series equation reads

$$K_e = (1 - \varphi_t) K_s + \varphi_t K_f \quad (5.7)$$

The series arrangement can be used for the bulk and shear modulus. But using the parallel arrangement the shear modulus ( $G_e$ ) cannot be calculated since fluids do not have a shear modulus. In order to calculate the shear modulus, the relation between the bulk modulus and shear modulus (Landau, 1986) is as follows

$$G_e = \frac{3K(1 - 2\nu)}{2(1 + \nu)} \quad (5.8)$$

with  $\nu$  the Poisson ratio of the solid. Arnold et al. (1996) give the following equation for very porous media ( $\varphi_t > 0.4$ ) with spherical pores

$$K_e = K_s \frac{2(1-2\nu)(1-\varphi_t)}{2(1-\nu)} \quad (5.9)$$

with  $K_s$  and  $\nu$  as the bulk modulus and the Poisson ratio at zero void fraction, respectively. Besides a difference in bulk and shear modulus of a porous material, also the density will be different. The equation for effective density reads

$$\rho_e = (1-\varphi_t)\rho_s + \varphi_t\rho_f \quad (5.10)$$

with  $\rho_s$  and  $\rho_f$  as the density of the solid and the fluid, respectively. Eqs. (5.6)-(5.10) can be used in Eq. (5.1)-(5.2) to calculate the sound velocity of a porous material. Summarizing, the combined equations for parallel arrangement without taking in account the contribution of the shear modulus read

$$c_e = \sqrt{\frac{K_s K_f}{(1-\varphi_t)K_f + \varphi_t K_s} \cdot \frac{1}{(1-\varphi_s)\rho_s + \varphi_t \rho_f}} \quad (5.11)$$

by combination of Eqs. (5.1), (5.6) and (5.10), for the series arrangement without shear modulus contribution, the sound velocity reads

$$c_e = \sqrt{\frac{K_s + \varphi_t(K_f - K_s)}{\rho_s + \varphi_t(\rho_f - \rho_s)}} \quad (5.12)$$

by combination of Eqs. (5.1), (5.7) and (5.10), for the bulk modulus according to Arnold et al. (1996) the sound velocity reads

$$c_e = \sqrt{K_s \frac{(2-\nu)(1-\varphi_t)}{3(1-\nu)} \cdot \frac{1}{(1-\varphi_t)\rho_s + \varphi_t \rho_f}} \quad (5.13)$$

by combination of Eqs. (5.1), (5.9) and (5.10), for the parallel arrangement with shear modulus according to Landau (1986) the sound velocity reads

$$c_e = \sqrt{\frac{K_s K_f}{(1-\varphi_t)K_f + \varphi_t K_s} \cdot \frac{1}{(1-\varphi_t)\rho_s + \varphi_t \rho_f} \cdot \left(1 + \frac{2(1-2\nu)}{1+\nu}\right)} \quad (5.14)$$

by combination of Eqs. (5.2), (5.6), (5.8) and (5.10), for the series arrangement with shear modulus according to Landau (1986), the sound velocity reads

$$c_e = \sqrt{\frac{K_s + \varphi_t(K_f + K_s)}{\rho_s + \varphi_t(\rho_f - \rho_s)} \cdot \left(1 + \frac{2(1-2\nu)}{(1+\nu)}\right)} \quad (5.15)$$

by combination of Eqs. (5.2), (5.7), (5.8) and (5.10), and for the bulk modulus according

to Arnold et al. (1996) with shear modulus according to Landau (1986), the sound velocity reads

$$c_e = \sqrt{K_s \frac{(2-\nu)(1-\varphi_t)}{3(1-\nu)} \cdot \frac{1}{(1-\varphi_t)\rho_s + \varphi_t\rho_f} \cdot \left(1 + \frac{2(1-2\nu)}{(1+\nu)}\right)} \quad (5.16)$$

by combination Eqs. (5.2), (5.8), (5.9) and (5.10) with  $c_e$  as the effective sound speed,  $K_s$  and  $K_f$  the bulk modulus of the solid and the fluid, respectively,  $\nu$  the Poisson ratio,  $\rho_s$  and  $\rho_f$  the specific density of the solid and the fluid, respectively and  $\varphi_t$  the void fraction of the mixture.

### Non-porous velocity based approach

The sound velocity of a porous material can also be calculated directly from the individual sound velocities of the individual phases. Roth et al. (1990) used a simple equation to predict the effective sound speed in a porous medium. This equation reads

$$c_e = c_s(1 - \varphi_t) \quad (5.17)$$

with  $c_s$  the sound speed in the non-porous material and  $\varphi_t$  the void fraction. Dalui et al. (1996) have added an exponent

$$c_e = c_s(1 - \varphi_t)^n \quad (5.18)$$

with exponent  $n$  being an empirical constant. For  $\alpha$ -hemihydrate, Dalui et al. (1996) proposed  $n = 0.84$  and  $c_s = 4571$  m/s. A drawback of these empirical equations is that in the limit of the void fraction approaching unity, a sound velocity of zero is obtained, which is obviously not correct. Therefore, here an additional term is added to Eqs. (5.17) and (5.18) which takes into account the sound velocity of the fluid:

$$c_e = c_s(1 - \varphi_t) + c_f\varphi_t \quad (5.19)$$

and

$$c_e = c_s(1 - \varphi_t)^n + c_f\varphi_t^n \quad (5.20)$$

with  $c_f$  being the sound speed of the fluid. Eqs. (5.17)-(5.20) are based on a parallel arrangement. Another possibility is to use a series arrangement (Ye, 2003), and the equation for this arrangement reads

$$c_e = \frac{c_s c_f}{(1 - \varphi_t)c_f + \varphi_t c_s} \quad (5.21)$$

with  $c_e$  as the effective velocity,  $c_s$  the velocity of the solid phase,  $c_f$  the velocity of the fluid and  $\varphi_t$  the void fraction. Equations (5.11)-(5.21) are applied and validated in Section 5.7.

### 5.3 Theory hydration of calcium sulphates

This section describes the reaction kinetics of the hydration of calcium sulphates. The main reaction is the reaction of calcium sulphate hemihydrate with water to form calcium sulphate dihydrate (gypsum):



This main reaction exists in several variations. For instance, there are two forms of hemihydrate. The production-method of the hemihydrate is the main difference between both forms. These forms differ in reactivity, crystal shape and strength of the hydration products (Lewry and Williamson, 1994). The form normally used for the production of gypsum plasterboards is the  $\beta$ -hemihydrate.

The hydration of hemihydrate can be described using as a through-solution-mechanism (Amathieu and Boistelle, 1988; Gartner et al., 1989; Pommersheim et al., 1985; Solberg and Hansen, 2001). A through-solution-mechanism contains six stages according to Pommersheim et al. (1985), all containing dissolution, diffusion and crystallisation mechanisms, but the one which is rate-determining differs. The first stage starts as soon as the hemihydrate comes into contact with water, the surface layer dissolves and ions are spread through the bulk solution. The hydration degree remains quite low, since hemihydrate is not very soluble. Since no gypsum nuclei of sufficient size are formed, the precipitation of dihydrate is low and therefore the dissolution of hemihydrate is reduced, this stage is called the induction time and is further described in Section 5.3.4. During the third stage, the nucleating embryos achieve the critical size and the crystallisation of dihydrate starts. Since the total surface area of dihydrate is small and the supersaturation remains high, the dissolution of hemihydrate is limited. This results in a low rate of hydration. Within this third stage the crystallisation of dihydrate is the rate controlling step. During the accelerator period (stage 4) the maximum hydration rate can be found. During this stage the hemihydrate and dihydrate particles are about the same size. As the hemihydrate particles become smaller and the supersaturation of the solution becomes low, the hydration rate drops. During this fifth stage (post-acceleratory period) the dissolution of hemihydrate becomes the rate-determining step. The final stage of the hydration is diffusion controlled since the solidifying mass restricts access of ions to and from hydrate surfaces.

Two theories for the hydration can be distinguished: crystalloids (le Chatelier, 1919; Schiller, 1962) and colloids (Budnikoff, 1927) theories (Maeda, 1927). The crystalloid-model assumes a equilibrium between the hemihydrate and the solution (Amathieu and Boistelle, 1988). In the colloid model hemihydrate is assumed to be covered by some intermediate calcium sulphate hydrates, forming a gel. The transformation kinetics of this gel would control the crystallisation of calcium sulphates. Birdi (1997) gives the

following definition of a colloid system, a system representing a multi-phase (heterogeneous) system, in which at least one of the phases exists in the form of very small particles: typically smaller than 1  $\mu\text{m}$ , but still much larger than the molecules. Such particles are involved in phenomena such as Brownian motion, diffusion and osmosis. In the early 20<sup>th</sup> century the equilibrium model had most followers, while since 70's and 80's more researchers preferred the colloids theory. Maeda (1927) points out that the theories are complementary and not antagonistic. This is also concluded by Triollier and Guillhot (1976), who concluded that crystalloids mechanism was not the only mechanism presented during hydration.

### 5.3.1 Dissolution

Dissolution is the mechanism in which the crystal lattice breaks down into individual ions, atoms or molecules. The amount that will dissolve depends among others on the surface area and the dissolution product of the salt ( $K_s$ ). The amount of solid salt and dissolved salt in a solution is assumed to be in equilibrium. The solution product of alpha-hemihydrate is  $10^{-3.73} \text{ mol}^{2.5} \text{ l}^{-2.5}$ , while the solution product of dihydrate is  $10^{-4.52} \text{ mol}^4 \text{ l}^{-4}$ . A solution saturated with respect to hemihydrate is supersaturated with respect to dihydrate. Owing to the supersaturation of dihydrate, dihydrate will precipitate. The rate of saturation of a solution depends on the concentrations of hemihydrate dissolved in a liquid and the activity of the ions:

$$K_s = a \{Ca^{2+}\} \cdot a \{SO_4^{2+}\} \cdot a \{H_2O\}^{0.5} = 10^{-3.73} \quad (5.23)$$

in which  $K_s$  is the solution product of hemihydrate.

According to Amathieu and Boistelle (1988) the dissolution of hemihydrate is extremely fast and not only result in free  $Ca^{2+}$  and  $SO_4^{2-}$  ions, but in soluble complexes such as  $CaOH^+$  and  $HSO_4^-$ . The concentrations of  $CaOH^+$  and  $HSO_4^-$  are negligible in comparison to the concentrations of  $Ca^{2+}$  and  $SO_4^{2-}$  and the present mass of  $CaSO_4 \cdot xH_2O$ . In practice the dissolution of hemihydrate results in maximum 60.6 mmol  $Ca^{2+}/l$ , 60.6 mmol  $SO_4^{2-}/l$  or 8.8 g  $\beta$ -hemihydrate/l water, which precipitates in maximum 10.4 g dihydrate.

According to Niemann (2005), there are more chemicals involved in a  $Ca-SO_4-H_2O$  system. Niemann (2005) also includes the ions resulting from the dissolution of  $NaCl$  as background ions in the system. Brandt and Bosbach (2001) give data about the dissolution rate compared to the amount of hemihydrate crystals present in deionized water. For 100%  $\beta$ -hemihydrate they found a dissolution rate of  $9.5 \cdot 10^{-5} \text{ mol}/(\text{m}^2 \text{ s})$ .

The dissolution of hemihydrate is controlled by an interfacial process at low density replaced by a process controlled by volume diffusion at high density (Amathieu and Boistelle, 1988). In case of the production of gypsum plasterboards, the system has a high density, so the process is volume diffusion controlled (Christoffersen and Christoffersen, 1976; Liu and Nancollas, 1971).

Besides the influence of the concentration of calcium sulphate on the hydration process, also the pH of the solution plays a role. The dissolution rate of  $CaCO_3$  is pH-dependent, while  $CaSO_4$  is pH-independent for  $\text{pH} > 3$ , while the dissolution rate of calcium carbonate for instance is not influenced by pH (Sudmalis and Sheikholeslami, 2000).

### 5.3.2 Diffusion

Diffusion is a spontaneous process, which can be considered as the outcome of a random walk. The mechanism of diffusion is the Brownian motion, whereby a molecule makes a random walk about a central location since by kinetic theory the mean velocity of a voxel is zero when it is not subject to any external forces. Due to collisions with neighbouring molecules the motion of the particle is characterized by a mean free path which tends to limit the molecule. But since there is no potential field acting to restore a molecule to its original position, it is free to move through the fluid, in which it is located. Diffusion is closely related with the second law of thermodynamics, since it increase the entropy and decrease the Gibbs free energy of a mix. These random walks result in the net movement of molecules from an area of high concentration to an area of low concentration in a fluid (either liquid or gas). Therefore the net diffusion is proportional to the concentration gradient and is in the direction of the lowest concentration.

### 5.3.3 Crystallization

According to Mullin (1972), three different models exist for crystallization, namely

- Surface energy model
- Diffusion model
- Adsorption layer model

The surface energy theories are based on the fact that the shape a growing crystal assumes is that which has the minimum surface energy. This theory is based on the work of both Gibbs and Curie at the end of 19<sup>th</sup> century. The theory is not often used nowadays although it is still valid. The diffusion theory presumes that material is deposited continuously on the crystal face at a rate proportional to the difference in concentration between the point of deposition and the bulk of the solution. This theory was first introduced by Noyes and Whitney (1897).

The third model was suggested by Volmer (1922). He suggested that crystal growth was a discontinuous process, taking place by adsorption, layer by layer, on the crystal surface. Volmer's theory is based on thermodynamic reasoning. When units of the crystallizing substance arrive at the crystal face they are not immediately integrated into the lattice. They lose one degree of freedom but they are still free to migrate over the crystal face (surface diffusion). According to Mullin (1972), adsorption layers play an important role in secondary nucleation and precipitation.

Precipitation involves many individual steps and kinetic processes (Söhnel and Garside, 1992). The most important steps are primary nucleation, growth and secondary nucleation. These steps have a certain overlap. Sudmalis and Sheikholeslami (2000) use a slightly different definition and point out that the crystallization process when be simplified consists of three main steps: nucleation, growth and recrystallisation. In reality these steps are not fully separated, but there is a great deal of overlap like by the separation used by Söhnel and Garside (1992). This crystallisation process becomes even more complicated in case of the co-presence of salts in a solution. Schierholtz (1958) points that several parameters influence the crystallisation of calcium sulphate dihydrate, namely supersaturation, crystal surface area, pH and presence of accelerators and retarders. An

increase of available surface area of dihydrate for nucleation will lead to increase of the reaction speed Ridge et al. (1972). An increase of the pH will lead to longer induction time and lower reaction rate. Brandt and Bosbach (2001) give the following equation for the dihydrate crystal growth;

$$R = k(\beta - 1)^2 \quad (5.24)$$

With R as the growth rate,  $\beta$  the supersaturation, k the reaction constant ( $3.78 \cdot 10^{-6}$  mol/(m<sup>2</sup>s)). They also found an activation energy of 40 kJ/mol for the dihydrate growth. The key variable within the precipitation process is the supersaturation (Brandt and Bosbach, 2001; Söhnel and Garside, 1992). The degree of supersaturation of dihydrate can be calculated with

$$\beta = \frac{a \{Ca^{2+}\} \cdot a \{SO_4^{2+}\} \cdot a \{H_2O\}^2}{K_s} \quad (5.25)$$

A solution saturated with respect to hemihydrate is supersaturated with respect to dihydrate. But the condition of supersaturation is not sufficient for a system to begin crystallizing (Chong and Sheikholeslami, 2001; Mullin, 1972). Before crystals can grow a number of minute solid objects must exist. These minute solid objects are called seeds, embryos or nuclei. A stable nuclei is necessary for the growth into crystals of visible size. A stable nuclei is a particle larger than the critical size formed in a supersaturated or supercooled system.

Different forms of nucleation exist (Söhnel and Garside, 1992). The main difference between primary and secondary nucleation is the presence of any crystal from the chemical that is crystallizing. Two types of primary nucleation are known; homogeneous and heterogeneous. Homogeneous nucleation is the formation of the solid phase when no solid phase exists. At heterogeneous nucleation, only foreign solid phases exist. Secondary nucleation is a mechanism by which formation of the solid phase is initiated by the presence of the solid phase of the crystallizing material itself (Söhnel and Garside, 1992) (Figure 5.1).

The hydration of hemihydrate to dihydrate can be categorized as heterogeneous and secondary nucleation (Amathieu and Boistelle, 1988). The dihydrate is formed by heterogeneous nucleation onto hemihydrate particles. But in a later phase of the hydration the dihydrate nucleates on the present dihydrate particles, which is secondary nucleation. In the classic theory of nucleation, homogeneous nucleation is described based on the work of Gibbs and in terms of Gibbs free energy. Heterogeneous nucleation has a lower critical Gibbs energy compared to homogeneous nucleation (Sudmalis and Sheikholeslami, 2000). Although the secondary nucleation rate will decrease with an increase in the seed size or in the number of seeds of a given size (Mullin, 1972).

The crystal growth of dihydrate has normally a needle form. The crystal form of the dihydrate crystal depends on the concentration of calcium sulphates present, but also on the presence of for instance citric acids. Plate-like crystals are formed at an initial concentration of less than 0.270 mol CaSO<sub>4</sub> /l (36.8 g/l), while needles are formed at concentrations of more than 0.4 mol CaSO<sub>4</sub> /l (54.46 g/l). Citric acids can be used

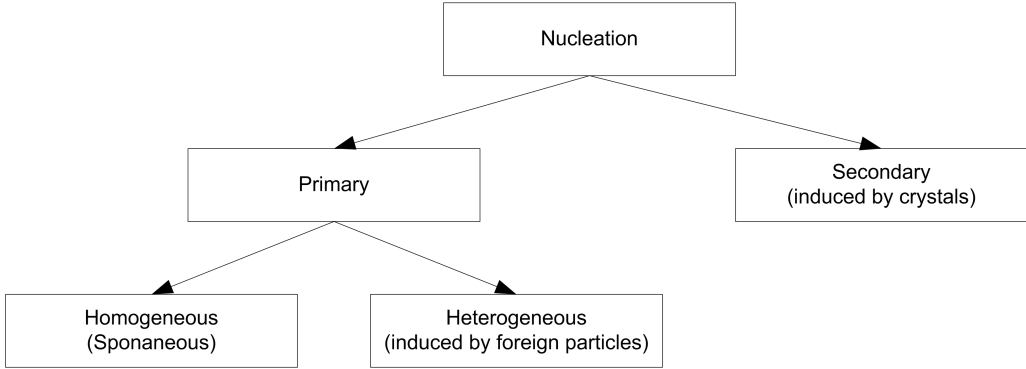


**Figure 5.1:** Different forms of nucleation based on Söhnel and Garside (1992).

to change the crystal shape and delay the hydration of dihydrate (Söhnel and Garside, 1992). The citric acid can be used for crystal shape engineering. The needle formation can be described by spiral growth theory. This theory is based on a particular mode of dislocation of the crystalline, the screw dislocation. A screw dislocation forms when the atoms are displaced along a dislocation line, rather than at right angles to it as in the case of the edge dislocation. The attachment of growth units to the face of the dislocation results in the development of a spiral growth pattern over the crystal face (Mullin, 1972). This growth looks like it 'is growing up a spiral staircase'. Complex spirals often develop, especially when several dislocations grow together. The curvature of the spiral cannot exceed a certain maximum value. This is determined by the critical radius for a two-dimensional nuclei's under conditions of supersaturation in the medium in which the crystal is growing (Mullin, 1972).

#### 5.3.4 Induction time

Brandt and Bosbach (2001) point out that an induction time is present during hydration due to the time needed for homogeneous nucleation of dihydrate. Klepetsanis et al. (1999) shows that the dependence of the induction time on the supersaturation and temperature based on literature-research and own experiments. Based on Schierholtz (1958) the pH should be added to this list. Singh and Middendorf (2007) defines the induction time as the time needed to form a nuclei of critical size and they define the critical size as following;

$$r_c = \frac{2\sigma v}{k_b T \ln \beta} \quad (5.26)$$

with  $\sigma$  the surface energy,  $v$  the molecular volume of calcium sulphate dihydrate,  $k_b$  the Boltzmann constant,  $T$  the temperature and  $\beta$  the supersaturation. Amathieu and Boistelle (1988) give the following general equation for the induction time;

$$\ln(t_i) = \frac{f \Omega^2 \gamma^3}{(k_b T)^3 \ln^2 \beta} \quad (5.27)$$

with  $t_i$  the induction time,  $k_b$  the Boltzman constant,  $\Omega$  the volume of crystal molecule,  $\gamma$  the interfacial free energy,  $T$  the absolute temperature,  $\beta$  the supersaturation of calcium sulphate dihydrate,  $N$  the number of nuclei per unit volume,  $f$  the dimensionless shape factor of the crystals. Lancia et al. (1999) found that the induction time is inversely proportional to the nucleation rate, defined as the number of nuclei formed in solution per unit time and volume. They present three equations based on other literature. Packter (1974) gives

$$t_i \sim \left( (C - C_{eq})^{-4} \right) \quad (5.28)$$

with  $C$  the calcium sulphate concentration and  $C_{eq}$  the calcium sulphate solubility. Sarig and Mullin (1982) indicate that the induction time depends on the supersaturation ( $\beta$ ) as

$$t_i \sim \left( (\ln\beta)^{-2} \right) \quad (5.29)$$

Lancia et al. (1999) present, based on He et al. (1994), the following equation;

$$\log(t_i) = A + \frac{F\gamma_s^3 v^2 N_A g}{(2.3R)^3 T^3 (\log\beta)^2} \quad (5.30)$$

with  $F$  the shape factor ( $16/3 \pi$ ),  $\gamma_s$  the surface energy ( $37 \text{ mJ/m}^2$ ),  $N_A$  the Avogadro number,  $R$  the gas constant,  $v$  the molecular volume ( $74.69 \text{ cm}^3/\text{mol}$ ) and  $g$  an correction factor (being unity for homogeneous nucleation and smaller than unity for heterogeneous nucleation). The water quality has a distinguished influence on the induction times and precipitation of calcium sulphates (Sudmalis and Sheikholeslami, 2000). Sudmalis and Sheikholeslami (2000) have done research to crystallisation of calcium carbonate and calcium sulphate in heat exchangers, both for presence of the salts separately and combined. They found that the temperature-effect on the induction time was limited when comparing those at  $60 \text{ }^\circ\text{C}$  and  $70 \text{ }^\circ\text{C}$ , while at  $80 \text{ }^\circ\text{C}$  the induction time is slightly shorter. Unfortunately the results of this study are not fully applicable to the current research, because the temperature-range in the current research is lower and the range where calcium sulphate dihydrate is the less soluble calcium sulphate phase, while in the temperature range of heat exchangers soluble anhydrite is the least soluble calcium sulphate phase. Furthermore, the concentration during the production of plasterboards is much higher than the concentrations used by Sudmalis and Sheikholeslami (2000). Nevertheless some of their observations can be interesting. They observed that the induction period of the mixture of calcium carbonate and calcium sulphate follows the induction time of  $\text{CaCO}_3$ , irrespectively of the solutions temperature and initial Ca concentration. However, the solubility concentration of the mixture follows that  $\text{CaSO}_4$  and again the same trends exists for all operating temperate and initial calcium concentrations. When comparing the dissolution of calcium carbonate and calcium sulphate, their main difference is that dissolution of  $\text{CaCO}_3$  is pH-dependent, while  $\text{CaSO}_4$  is pH-independent for  $\text{pH} > 3$  (Sudmalis and Sheikholeslami, 2000).

**Table 5.2:** Parameters of the paste model for the different calcium sulphate phases (Brouwers, 2012).

Substance	$v_c/v_w$	$w_n/c$	$v_n/v_w$	$v_n w_n/v_w c$	$v_s/v_w c$
$\text{CaSO}_4$ ( $\gamma$ )	0.39	0.265	0.60	0.160	0.106
$\text{CaSO}_4(\text{H}_2\text{O})_{0.5}$ ( $\alpha$ )	0.36	0.186	0.81	0.151	0.035
$\text{CaSO}_4(\text{H}_2\text{O})_{0.5}$ ( $\beta$ )	0.38	0.186	0.71	0.133	0.054

## 5.4 Paste model for hydrating hemihydrate

In this section a paste model for hydration of calcium sulphates is presented. This paste model is subsequently used for the calculation of the volume fractions of solids and voids in the slurry and solid materials. These volume fractions are needed for the calculation of the sound speed through porous media in following sections, since the void fraction influences the bulk and shear modulus as well as the density of the material, and hence the sound speed. The model of Brouwers (2012) is used to describe the volume fractions of binder, hardened product, water and shrinkage before, during and after hydration. This model makes use of the molar mass of the reactant and product as well as the reaction stoichiometry. It can be used for both  $\alpha$ - and  $\beta$ -hemihydrate as well as anhydrite. The volume fractions read

$$\varphi_{hp} = \frac{\alpha \left[ \frac{v_c}{v_w} + \frac{w_n v_n}{v_w c} \right]}{\frac{v_c}{v_w} + \frac{w_0}{c_0}} \quad (5.31)$$

$$\varphi_c = \frac{(1 - \alpha) \left[ \frac{v_c}{v_w} \right]}{\frac{v_c}{v_w} + \frac{w_0}{c_0}} \quad (5.32)$$

$$\varphi_w = \frac{\frac{w_0}{c_0} - \alpha \left[ \frac{w_n}{c} \right]}{\frac{v_c}{v_w} + \frac{w_0}{c_0}} \quad (5.33)$$

$$\varphi_s = \frac{\alpha \left[ 1 - \frac{v_n}{v_w} \right] \frac{w_n}{c}}{\frac{v_c}{v_w} + \frac{w_0}{c_0}} \quad (5.34)$$

with  $\varphi_c$ ,  $\varphi_{hp}$ ,  $\varphi_w$  and  $\varphi_s$  as the volume fractions of binder, hardened product, water and shrinkage respectively, and  $\alpha$  the hydration degree,  $w_n/c$  the mass of nonevaporable water on mass of reacted hemihydrates,  $v_c/v_w$  the specific volume ratio of hemihydrate on water,  $w_n/c_0$  the initial water/binder-ratio and  $v_n/v_w$  the volume ratio of non-evaporable water on water. The values for  $w_n/c$ ,  $v_c/v_w$  and  $v_n/v_w$  can be found in Brouwers (2012) and Table 5.2.

For  $\alpha = 0$ , Eqs. (5.31)-(5.34) give the volume fractions in case of a slurry of hemihydrate and water, while  $\alpha = 1$  describes the case of the fully hydrated (porous) gypsum, so

including its voids. The total void fraction ( $\varphi_t$ ) is the sum of the volume fraction water and volume fraction shrinkage, so the void fraction is equal to

$$\varphi_t = \varphi_w + \varphi_s = \frac{\frac{w_0}{c_0} - \alpha \frac{v_n}{v_w} \frac{w_n}{c}}{\frac{v_c}{v_w} + \frac{w_0}{c_0}} \quad (5.35)$$

The void fraction before mixing corresponds to the volume fraction of the water ( $\alpha = 0$ ) and reads

$$\varphi_t = \frac{\frac{w_0}{c_0}}{\frac{v_c}{v_w} + \frac{w_0}{c_0}} \quad (5.36)$$

For a fully hydrated system ( $\alpha = 1$ ), Eq. (5.35) yields

$$\varphi_t = \frac{\frac{w_0}{c_0} - \frac{v_n}{v_w} \frac{w_n}{c}}{\frac{v_c}{v_w} + \frac{w_0}{c_0}} \quad (5.37)$$

The void fraction of  $\alpha$ -hemihydrate based dihydrate after full hydration ( $\alpha = 1$ ), following Table 5.2, reads

$$\varphi_t = \frac{\frac{w_0}{c_0} - 0.15}{0.36 + \frac{w_0}{c_0}} \quad (5.38)$$

This equation was also introduced already by Schiller (1958), which was also used by other researchers (Dalui et al., 1996; Phani et al., 1986). Brouwers (2012) and Yu and Brouwers (2011) have compared experimental values with the model presented here, in particular Eq. (5.37), for hardened  $\beta$ -hemihydrate ( $\alpha = 1$ ), and found good agreement. Equations (5.32), (5.33) and (5.36) are applicable to the hydration of  $\alpha$ - and  $\beta$ -hemihydrate, for  $0 \leq \alpha \leq 1$ , so not only for fully hydrated binder only. In the next sections they will be applied to a hydrating system, so  $0 < \alpha < 1$ , measured using the ultrasonic velocity.

## 5.5 Hydration models

Section 5.2 addressed the sound velocity of the material in the initial and final state of hydration. But besides these both states, also the process in between is interesting. Therefore first a model for the relation between sound velocity and hydration degree is given. For the study of the hydration the relation to time is essential, therefore hydration degree is related to time by use of analytical hydration models in Section 5.5.2.

### 5.5.1 Relation between hydration degree and sound velocity

Smith (2002) describes the relation between hydration mechanism and ultrasonic measurements in aluminous cement. They provide a correlation between hydration degree and ultrasonic measurements. This correlation reads

$$\alpha = \frac{c_e + c_{sl}}{c_{hp} + c_{sl}} + \alpha_0 \quad (5.39)$$

with  $c_e$  is the measured sound velocity through mix,  $c_{sl}$  is the sound velocity at moment the velocity starts increasing (so, of the slurry),  $c_{hp}$  is the sound velocity when the velocity stops increasing (so, of the hardened product) and  $\alpha_0$  is the hydration degree at moment of  $c_{sl}$  (which is here zero). Eq. (5.39) can be rewritten to

$$c_e = \alpha(c_{hp} - c_{sl}) + c_{sl} \quad (5.40)$$

when it is invoked that at  $\alpha = 0$  corresponds to  $c_e = c_{sl}$  and at  $\alpha = 1$  corresponds to  $c_e = c_{hp}$ .

### 5.5.2 Relation between hydration degree and time

In literature several different analytical hydration models are introduced. Most models are based on the work of either Schiller (1962, 1963, 1965, 1974) or Ridge and Surkevicius (1961, 1966) and Ridge et al. (1962). Hand (1994) has generalized these formulas to;

$$\frac{d\alpha}{dt} = k_0 \cdot \alpha^m \cdot (1 - \alpha)^n \quad (5.41)$$

with  $k_0$  is the initial reaction rate,  $\alpha$  the hydration rate and  $m$  and  $n$  as constants. This equation given no information on starting point of the reaction (i.e. induction time and the reaction degree at  $t = 0$ ). Schiller (1962, 1974) give a value of  $2/3$  for both  $m$  and  $n$ . The value of  $2/3$  is commonly used to relate the mass to the specific surface area of a hemihydrate particle (Hand, 1994). Both Ridge (1964); Ridge et al. (1972) and Schiller (1962, 1974) use the value of  $2/3$  for  $n$  to describe the dissolution of hemihydrate. Schiller and Ridge debate about the correct value of  $m$ , which describe the dihydrate growth. Ridge (1964) assumed a linear relation between surface area and mass of the dihydrate crystals, while Schiller (1962, 1965, 1974) claims that the surface area varies as the  $2/3$  power of the mass. As already pointed out by Hand (1994), the fundamental difference between both researchers is the assumed growth geometry of the needlelike dihydrate crystals. The assumed relation by Ridge (1964) ( $m = 1$ ) is valid in case the crystals only grow in one direction at any time and the used linear relation can roughly approximated the growth in two dimensions. But in case the growth takes place in three dimensions, the assumed relation by Schiller ( $m = 2/3$ ) seems more appropriate. Hand (1994) indicates that the growth in three dimensions is most probably dominant over one dimensional growth, since otherwise the crystal will not acquire a certain thickness. Therefore the relation given by Schiller (1974) is used here.

Schiller (1974) presented a more complex equation in his paper, which has the advantage that it indirectly includes water/binder ratio in the parameters. The equation of Schiller (1974) reads

$$t = K_1 \sqrt[3]{\alpha} + K_2(1 - \sqrt[3]{1 - \alpha}) + K_0 \quad (5.42)$$

in which  $K_0$  equals the induction time ( $t_0$ ). Eq. (5.41) is equal to Eq. (5.42) for  $m = 2/3$ ,

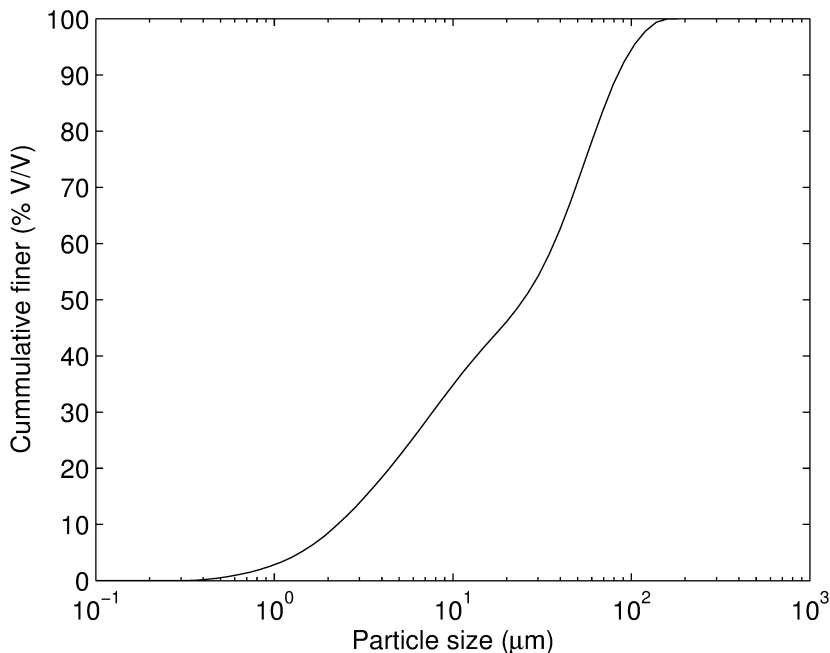


**Figure 5.2:** Particle size distribution of applied hemihydrate.

$n = 2/3$ ,  $K_1 = K_2$ ,  $K_0 = 0$  and  $k_0 = 3/K_1$ . Schiller (1974) emphasizes that  $K_1$  and  $K_2$  have clearly defined physical meanings and are not just fitting parameters. Schiller (1974) shows a number of simulations for the hydration of hemihydrate. In his simulations  $K_1$  is between 21 - 48.3 minutes and  $K_2$  from 11 to 21.6 minutes. Beretka and Van der Touw (1989) used value for  $K_1$  between 37.8 and 43.5 minutes and 15.1 - 30.3 minutes for  $K_2$  for a mixture with a water/binder-ratio of 0.70. Fujii and Kondo (1986) used  $K_1 = 44$  min and  $K_2 = 276$  min for a wbr of 0.40. Although none of these authors specify the type of hemihydrate used, from the hydration time one can assume that it concerned  $\alpha$ -hemihydrate. Singh and Middendorf (2007) point out that the induction period for  $\alpha$ -hemihydrate hydration is shorter than that for  $\beta$ -hemihydrate. But they also point out that  $\beta$ -hemihydrate hydrates faster because of its higher surface area which provides more nucleation sites for the crystallization of gypsum.

## 5.6 Experiments

### 5.6.1 Materials

Within this research  $\beta$ -hemihydrate is used as the binder. The hemihydrate used during the experiments was produced from flue gas desulpharization gypsum, which is commonly used for the production of gypsum plasterboards. The particle size distribution (PSD) is shown in Figure 5.2. The used  $\beta$ -hemihydrate consists of 94.5% pure hemihydrate, 3.9% limestone and 1.6% other compounds Yu (2012). The hemihydrate has a Blaine value of  $3025 \text{ cm}^2/\text{g}$  and a density of  $2619 \text{ kg}/\text{m}^3$ . The Blaine value describes the fineness

**Table 5.3:** An overview of the applied mix designs, their computed void fractions (Eq. (5.38)) based on Brouwers (2012) and the results of the performed ultrasonic measurements by Grosse and Lehmann (2008) on these mix designs.

	Mix design				
	A	B	C	D	E
Water/hemihydrate ratio	0.63	0.8	1.25	1.59	1.59
Accelerator (m/m on hemihydrates)					0.40%
Before hydration					
- Computed void fraction $\varphi_t$ (Eq. (5.38))	0.624	0.678	0.767	0.807	0.807
- Measured sound velocity (m/s)	75	85	134	223	134
After hydration					
- Computed void fraction $\varphi_t$ (Eq. (5.38))	0.493	0.566	0.685	0.740	0.740
- Measured sound velocity (m/s)	2500	2300	2000	3172	1835

of the binder particle (hemihydrate). Hunger and Brouwers (2009) point out that the Blaine test methods are not applicable for powders with higher fineness (i.e. particles  $\leq 10 \mu\text{m}$ ). The hemihydrates used have 50% of the particles smaller than  $10 \mu\text{m}$ , therefore the Blaine value is less suitable. Another method to determine the fineness of powder is the use of specific surface area (SSA). Hunger (2010) showed a method to calculate the specific surface area based on the PSD. Hunger and Brouwers (2009) showed that there is a constant ratio between Blaine value and computed SSA. The Blaine value has to be multiplied by about 1.7 to obtain the SSA. Applied here, the SSA based on the given Blaine value would amount  $5130 \text{ cm}^2/\text{g}$ . The computation of the SSA using the PSD depends on the shape of the particles. For spheres the shape factor equals unity. Using this shape factor, the SSA of the used hemihydrate would be  $4432 \text{ cm}^2/\text{g}$ . However, these powder particles are not spherical, and the amount of specific surface area is higher. To match computed SSA and Blaine value of  $5130 \text{ cm}^2/\text{g}$ , here a shape-factor of 1.16 follows for the applied  $\beta$ -hemihydrate. It noteworthy that Hunger and Brouwers (2009) found shape-factor of 1.18 for  $\alpha$ -hemihydrate.

### 5.6.2 Measurements

The measurements were executed in corporation with the Materialprüfungsanstalt of the University of Stuttgart (Germany). The sound velocity of  $\beta$ -hemihydrate/water mixtures with 4 water/binder ratios is measured during the experiments. The 4 water/binder-ratios (wbr) are 0.63, 0.80, 1.25 and 1.59. Besides these four mixtures also a mixture with wbr of 1.59 with 0.40 % (m/m) accelerator is tested. Table 5.3 shows the mix-designs used during the experiments.

Figure 5.3 shows the measured sound velocity during hydration of the 5 mixtures. The hemihydrate hydration experiments with ultrasonic method were performed using the FreshCon system which was developed at the University of Stuttgart. The measurements are performed in a container, which consists of two polymethacrylate walls and u-shaped rubber foam element in the center, which are tied together by four screws with spacers. The volume of the mold is approximately  $45 \text{ cm}^3$  for the test. The measurements were performed with use of two Panametrics V106, 2.25MHz centre frequency sensors. For the processing of the measuring data during the experiments, in-house developed software

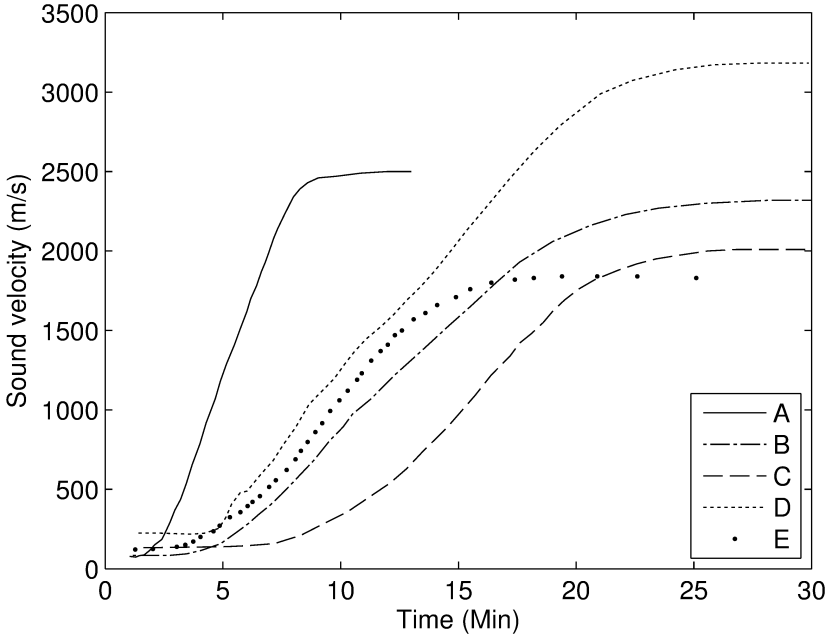


**Figure 5.3:** The measured sound velocity by Grosse and Lehmann (2008) of the mix designs A - E (Table 5.3).

(FRESHCON2) is used. More detailed information about the FreshCon system and the measurement procedure can be found in Reinhardt and Grosse (2004); Reinhardt et al. (1999).

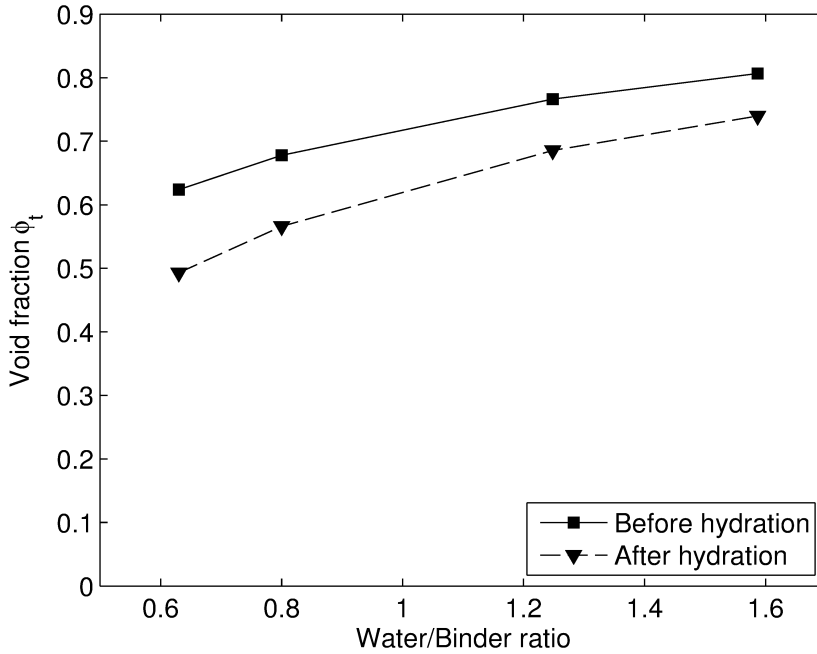
The calculated void fractions of the mixtures in this research, based on the model of Brouwers (2012), are given in Table 5.3 and shown in Figure 5.4.

Table 5.3 also shows the measured ultrasonic velocity by Grosse and Lehmann (2008). Figures 5.5(a) and 5.5(b) are graphic representations of the sound velocity data versus computed void fraction from Table 5.3. It can be noticed from the figures that there is a clear relation between void fraction and velocity as well before as after hydration, so  $\alpha = 0$  and  $\alpha = 1$ , respectively. But the trend is exactly opposite before and after hydration. Before hydration the velocity increases with increasing void fraction (i.e. water content), while the velocity is decreasing with increasing void fraction after hydration. In the next section relations will be established between the volumetric composition (at  $\alpha = 0$  and  $\alpha = 1$ ) and sound velocity.

## 5.7 Applying the volumetric models to sound velocity measurements

### 5.7.1 Sound velocity through a slurry

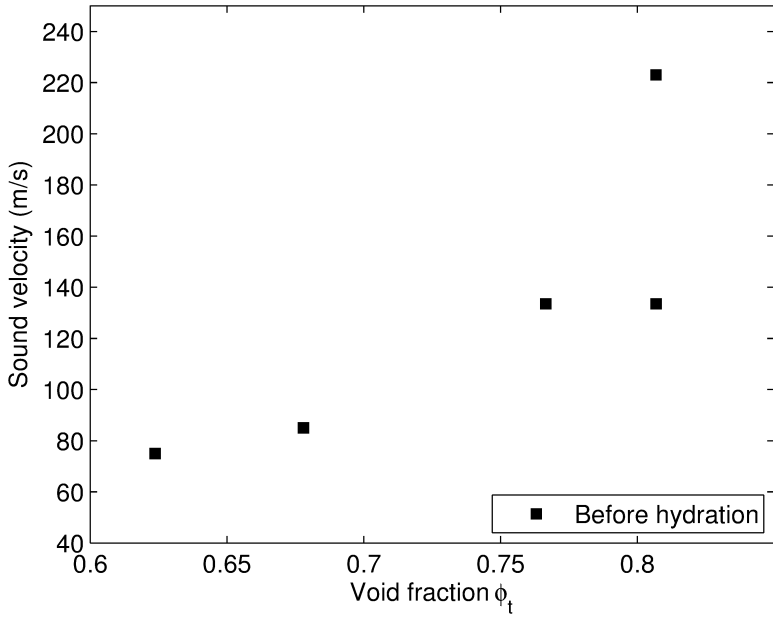
Table 5.4 shows the results of Eq. (5.3) with  $K_s = 52.4$  GPa,  $K_f = 2.2$  GPa (5.1). The calculated sound velocities with Eq. (5.3) are much higher than the measured sound velocity during the experiments. The main reason for this is the overestimation of the



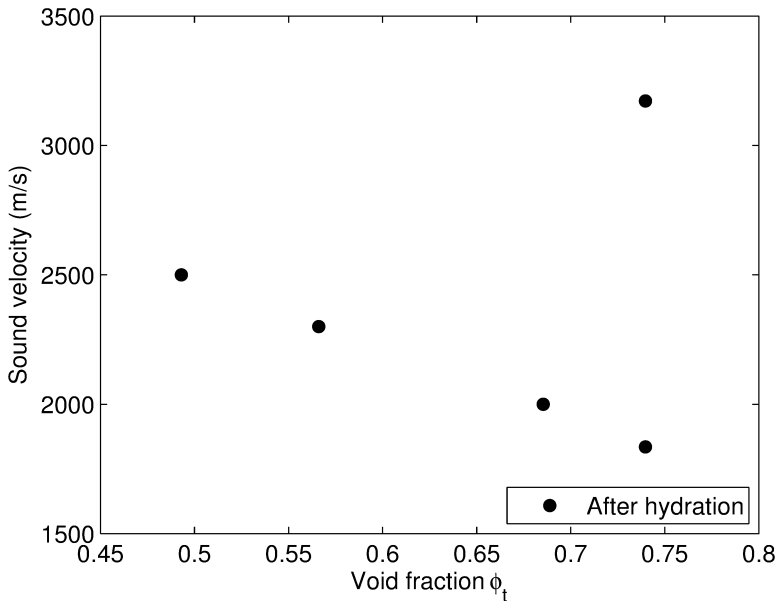
**Figure 5.4:** Relation between water/binder ratio and computed void fraction based on Brouwers (2012) before and after hydration.

**Table 5.4:** Results of the slurry method (Eq. (5.3)) without entrapped air and derived air content with use of the slurry method (Eqs. (5.3)-(5.5)).

	Wbr	Initial Void fraction $\phi_t$	Measured velocity (m/s)	Computed velocity Eq. (5.3)	Derived air content	
					$C_{\text{air}}$	$V_{\text{air}}/V_{\text{HH}}$
A	0.63	0.624	75	1520	1.69 %	2.85 %
B	0.80	0.678	85	1511	1.41 %	3.00 %
C	1.25	0.767	134	1503	0.63 %	2.09 %
D	1.59	0.807	223	1500	0.23 %	0.98 %
E	1.59 <sup>acc</sup>	0.807	134	1500	0.66 %	2.78 %



(a)



(b)

**Figure 5.5:** Void fraction (a) before hydration and (b) after hydration based on the experiments of Grosse and Lehmann (2008).

**Table 5.5:** Results of the bulk modulus based approach (Eqs. (5.11)-(5.16)) and the non-porous velocity based approach (Eqs. (5.17)-(5.21)) with sound velocity (m/s), specific density ( $\text{kg/m}^3$ ), bulk moduli (GPa), shear moduli (GPa), and poisson ratio (-) of gypsum taken from Table 5.1.

	$c_s$ (m/s)	A	B	C	D	E
Water/binder ratio		0.63	0.8	1.25	1.59	1.59
Accelerator						0.40%
Final void fraction		0.493	0.566	0.685	0.74	0.74
Measured		2500	2300	2000	3172	1835
Bulk modulus based approach						
Eq. (5.11)		1597	1545	1491	1476	1476
Eq. (5.12)		3749	3601	3298	3122	3122
Eq. (5.13)		2130	2029	1822	1699	1699
Eq. (5.14)		1963	1899	1833	1815	1815
Eq. (5.15)		4609	4427	4055	3838	3838
Eq. (5.16)		2618	2495	2240	2089	2089
Non-porous velocity based approach						
Eq. (5.17)	6800	3448	2951	2142	1768	1768
Eq. (5.18)	6800	3843	3373	2577	2193	2193
Eq. (5.19)	4571	2584	2267	1732	1474	1474
Eq. (5.19)	6800	4186	3799	3167	2876	2876
Eq. (5.20)	6800	4670	4301	3666	3356	3356
Eq. (5.20)	4571	3410	3195	2822	2637	2637
Eq. (5.21)	6800	2476	2263	1985	1878	1878
Eq. (5.21)	5440	2367	2184	1939	1845	1845
Eq. (5.21)	4571	2271	2114	1899	1814	1814

fluid bulk modulus as described by Robeyst et al. (2008). Therefore the bulk modulus of the fluid is corrected with Eq. (5.5), with the bulk modulus of air 142 kPa and the bulk modulus of water 2.2 GPa (Table 5.1). Based on Eqs 5.3 and 5.5, the air content ( $C_{\text{air}}$ ) of the pore fluid can be derived by mathematical solving these equations. The derived air contents are included in Table 5.4. Further computations reveal that the volume fraction air divided by the volume fraction of the binder in the slurry lies in a very small range (Table 5.4). This could indicate that air entered the slurry on the surface of the hemihydrate particles and a typical value is thus 2.7% (V/V) or 10 ml air per kg hemihydrate. Given the Blaine value of  $3025 \text{ cm}^2/\text{g}$ , this would mean  $3.28 \cdot 10^{-6}$  ml air per  $\text{cm}^2$  hemihydrate surface ( $= 3.28 \cdot 10^{-2} \text{ ml}/\text{m}^2$ ), corresponding to an air layer thickness of 32.8 nm.

### 5.7.2 Sound velocity of solid: bulk-modulus based approach

Table 5.5 shows the results of Eqs. (5.11)-(5.13) with  $K_s = 44 \text{ GPa}$ ,  $K_f = 2.2 \text{ GPa}$  and  $\nu = 0.33$  (Table 5.1). The use of bulk-modulus based on Eq. (5.11) and (5.13) lead to an

underestimation, while Eq. (5.12) leads to an overestimation of the velocity. Table 5.5 also shows the results for Eqs. (5.14)-(5.16). The best estimation of the sound velocity was found using Eq. (5.16). The difference between predicted values for this combination and experimental value becomes slightly larger when the water/binder ratio increases.

### 5.7.3 Sound velocity of solid: non-porous velocity based approach

The results of Eqs. (5.17)-(5.21) are shown in Table 5.5. It can be noticed that the predicted values based on Eq. (5.17) differ from the measured values. Eq. (5.21) results in a too high velocity for all measurements when using the sound speed of 6800 m/s for gypsum (Table 5.1). When using 4571 m/s as sound velocity of gypsum as given by Dalui et al. (1996), the measurements for the first two experiments show good agreement. But the values for the mixtures with higher water/binder ratio (e.g. higher void fraction) are too low. Both Eqs. (5.19) and (5.20) lead to an overestimation compared with the experimental value. The predicted values based on Eq. (5.21) are close to the experimental values for all water/binder ratios. For the lowest water/binder ratios the predictions are too low, while for the higher water/binder ratios the prediction tends to overestimate the velocity. The best results for Eq. (5.21) are found with the solid sound velocity of 6800 m/s.

### 5.7.4 Conclusions

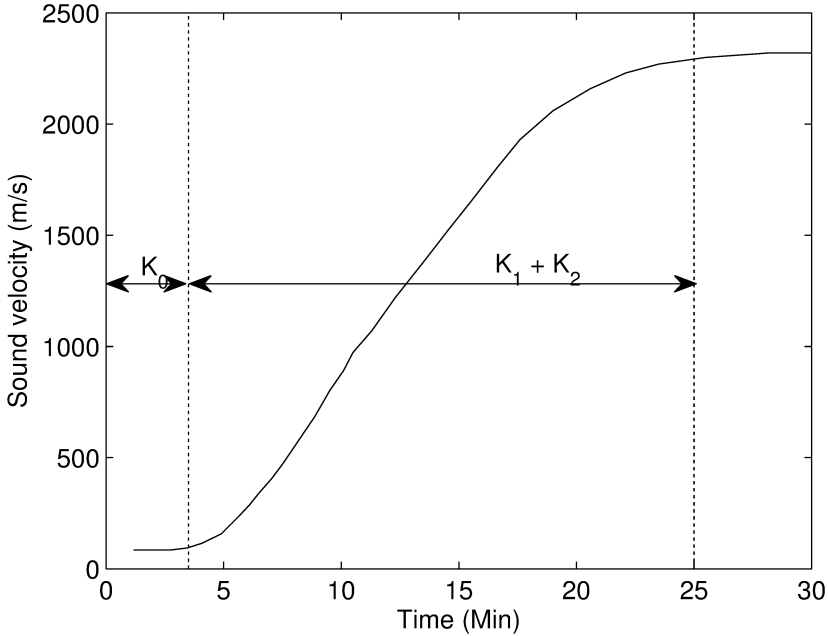
The model given by Robeyst et al. (2008) for predicting the sound velocity of an air-water-solids slurry is compatible with the experiments assuming a constant air content of 2.7% (V/V) based on the volume of hemihydrate. In case of the hardened (porous) material, the closest fit between experimental and predicted value is found by the use of the direct method. The best results were obtained with the series arrangement based on the empirical sound velocity values; Eq. (5.21) with  $c_s = 6800$  m/s and  $c_f = 1497$  m/s. Also the equation of Dalui et al. (1996) (Eq. (5.18)) shows a good agreement for the two lowest void fractions, using with  $c_s = 4571$  m/s and  $n = 0.84$ .

## 5.8 Analysis of measurements using the hydration model

In the previous section the ultrasonic measurements were compared with the prediction based on theoretical equations for initial and final state of the hydration. The next step is to apply the described models from Section 5.5 to the measured hydration curves from Section 5.6.

### 5.8.1 Analysis

The sound velocity graphs contain a serie of characteristic important points. For instance,  $t_{\alpha = 0}$  is the point in time at which the sound velocity starts to increase. The time until this point is called the induction time. The previous section showed that the sound velocity of this point can be best described based with model of Robeyst (Eqs. (5.3)-(5.5)). And  $t_{\alpha = 1}$  is the moment in time at which hydration is completed. The previous section showed that this could be best described by equation given by Ye (Eq. (5.21)). These points can be directly related to the parameters of the Schiller model.  $K_0$  is equal to  $t_{\alpha = 0}$  and  $K_0 + K_1 + K_2$  equals to  $t_{\alpha = 1}$ , see Eq. (5.45).



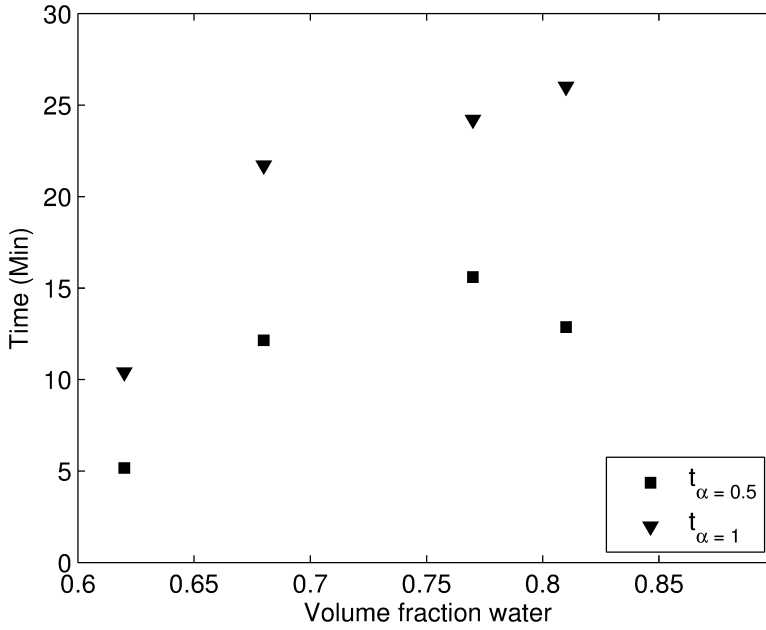
**Figure 5.6:** Determination of  $K_0$  and  $K_1 + K_2$  for experimental results with  $wbr = 0.80$ .

Figure 5.6 shows both points in time for  $wbr = 0.80$ . The exact determination of the value of  $t_{\alpha = 1}$  is challenging, since it requires that the moment of full hydration is clearly visible in the sound velocity graphs. Since this is not really the case, another method is applied here. In this method the time ( $t_{\alpha = 0.5}$ ) needed to perform half of the hydration ( $\alpha = 0.5$ ) is determined. Based on Eq. (5.40), the sound velocity describing half hydration equals the average of the sound velocity of slurry and of hardened product. Table 5.6 and Figure 5.7(a) show the determined values for  $t_{\alpha = 0.5}$ , based on the sound velocity curves. In order to determine the individual values of  $K_0$ ,  $K_1$  and  $K_2$ , the model is fitted to the experimental sound velocity curves taking into account the already determined values for  $t_{\alpha = 0.5}$ . The fitting is performed by using the modified Schiller model (Eq. (5.43)) with  $t_{\alpha = 0.5}$ . This modified model reads

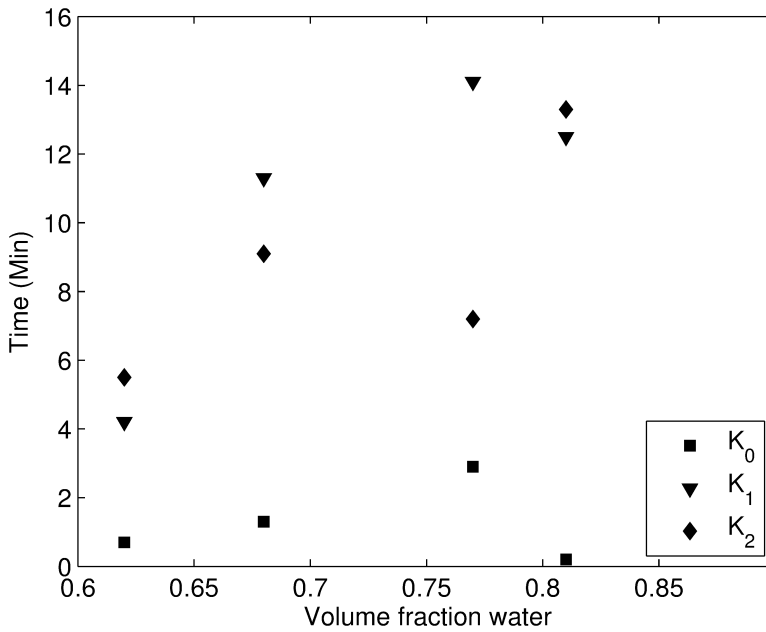
$$\begin{aligned} t_{\alpha=0.5} &= k_1 \sqrt[3]{0.5} + K_2(1 - \sqrt[3]{1-0.5}) + K_0 \\ &= (K_1 - K_2)\sqrt[3]{0.5} + K_2 + K_0 \end{aligned} \quad (5.43)$$

Table 5.6 and Figure 5.7(b) show the results of the fitting. From Figure 5.7(a), one can notice that the total time of hydration ( $t_{\alpha = 1.0}$ ) increased with an increasing volume fraction of water in the mix. Both  $K_1$  and  $K_2$  seem linearly related to the volume fraction water, but these fits are not really conclusive. Ignoring the results of  $wbr = 1.59$ , there is a more clear trend visible. When doing this,  $K_0$  and  $K_1$  are related to the volume fraction water, while  $K_2$  is unrelated to this property.

The current research reveals the presence and magnitude of induction times ( $K_0$  or  $t_{\alpha = 0}$ ),



(a)



(b)

**Figure 5.7:** (a) Determined values of  $t_{\alpha = 0.5}$  and  $t_{\alpha = 1}$  ( $K_0 + K_1 + K_2$ ) versus initial volume fraction of water. (b) Derived values of  $K_0$   $t_{\alpha = 0}$ ,  $K_1$  and  $K_2$  by fitting of the experimental and simulated sound velocity curves without accelerator.

**Table 5.6:** Determined value for  $t_\alpha = 0.5$  and derived values for  $K_1$  and  $K_2$  by fitting with  $\varphi_{w,\alpha=0}$  the initial calculated water fraction and  $\varphi_\alpha = 1$  the final calculated void fraction (<sup>acc</sup> stands for 0.40 % m/m accelerator added).

Mix	wbr	$\varphi_{w,\alpha=0}$	$\varphi_\alpha = 1$	$t_\alpha = 0.5$	$K_0$	$K_1$	$K_2$	$t_\alpha = 1$
A	0.65	0.62	0.38	5.16	0.7	4.2	5.5	10.4
B	0.8	0.68	0.32	12.14	1.3	11.3	9.1	21.7
C	1.25	0.77	0.23	15.60	2.9	14.1	7.2	24.2
D	1.59	0.81	0.19	12.86	0.2	12.5	13.3	26.0
E	1.59 <sup>acc</sup>	0.81	0.19	9.52	2.2	6.1	12.0	20.3

while Schiller (1974) neglects the induction time when applying his model. When comparing the derived value of  $K_1$  and  $K_2$  with the values given by Schiller (1974) and Beretka and Van der Touw (1989), one can notice that here the values for  $K_1$  and  $K_2$  are lower. The lower values compared to literature (Beretka and Van der Touw, 1989; Fujii and Kondo, 1986; Schiller, 1974) can be explained by fact that these values were most probably determined for  $\alpha$ -hemihydrate. While  $\beta$ -hemihydrate hydrates faster because of its larger surface area, which provides more nucleation sites for the crystallization of dihydrate (Singh and Middendorf, 2007). The nucleation of gypsum is, according to the model of Schiller, governed by  $K_1$ . Literature does not provide additional information describing the effect of water/binder-ratio on  $K_1$  and  $K_2$ , neither for  $\alpha$ - nor  $\beta$ -hemihydrate. A research on the hydration of calcium aluminate cement using the Schiller model by Smith (2002) showed a relation between  $K_1$  and water/binder ratio, while the value of  $K_2$  was constant within small water/binder ratio range. The current research shows partly the same positive relation between  $K_1$  and water/binder-ratio, particularly if the measurement with water/binder ratio of 1.59 is omitted. Furthermore, also here a relatively constant value of  $K_2$  is observed.

### 5.8.2 Conclusions

It is shown that the relation between hydration degree and sound velocity as given by Smith (2002) is applicable for the hydration of hemihydrate. Within this model the equations of Robeyst et al. (2008) and Ye et al. (2003) can be used to describe the sound velocity at the start and end, respectively, of the hydration process. Furthermore the hydration model of Schiller is applied on the ultrasonic sound velocity measurements. A fitting of the Schiller (1974) model to the experimental results has been performed using the  $t_{\alpha=0.5}$ -method. The analysis of the results showed that  $K_0$  and  $K_1$  are linearly dependent on the water/binder ratio, while  $K_2$  is unrelated to the water/binder ratio.  $K_0$ ,  $K_1$  and  $K_2$  describe the induction time, the dihydrate growth and the hemihydrates dissolution, respectively. Furthermore it is noticed that the induction time ( $t_{\alpha=0}$  or  $K_0$ ) is linearly related to the volume fraction water, and therefore directly related to the water/binder ratio.

## 5.9 Alternative point of view

In the previous sections the sound speed through porous media was predicted based on the calculated void fraction. In this section, the void fraction and density are calculated

**Table 5.7:** Derived void fractions based on measured sound velocity and Eqs. (5.44) and (5.45).

Mix	Calculated final void fraction (Brouwers, 2012)	Prediction void fraction		
		Eq. (5.44)	Eq. (5.44)	Eq. (5.45)
		$c_s = 6800 \text{ m/s}$	$c_s = 4571 \text{ m/s}$	
A	0.493	0.696	0.512	0.485
B	0.566	0.724	0.558	0.552
C	0.685	0.767	0.626	0.677
D	0.740	0.596	0.352	0.323
E	0.740	0.789	0.662	0.764

based on the measured sound velocity through a porous hardened material. Eqs. (5.18) and (5.21) can be rewritten as

$$\varphi_t = 1 - \left( \frac{c_e}{c_s} \right)^{\frac{1}{n}} = 1 - \left( \frac{c_e}{c_s} \right)^{\frac{1}{n}} \quad (5.44)$$

or

$$\varphi_t = \left( \frac{c_f c_s}{c_e} - c_f \right) \cdot \frac{1}{c_s - c_f} \quad (5.45)$$

respectively, with  $c_e$  is the measured sound velocity during experiments (Table 5.3),  $c_s$  the sound velocity through non-porous material and  $c_f$  the sound velocity through the fluid in the pores (Table 5.1). Table 5.7 shows the derived void fractions for gypsum based on Eqs. (5.44) and (5.45) using the experimental values from Section 5.6.2.

The results of Eq. (5.44) show that better results are obtained with a sound velocity of 4571 m/s compared to solid sound velocity of 6800 m/s. This finding is in line with Section 5.6, which also showed better results with a solid sound velocity of 4571 m/s. The results show a very close fit between the derived void fraction from Eq. (5.45) and the void fractions from model of Brouwers (2012), governed by the water/binder ratio. The difference between model and derived value are limited except for a water/binder ratio of 1.59 without accelerator. The derived void fraction could be useful for deriving the density of materials in-situ. The equation for the apparent density based on the (derived) void fraction reads

$$\rho_e = \varphi_t \rho_f + (1 - \varphi_t) \rho_s \quad (5.46)$$

with  $\rho_e$  as the apparent density,  $\varphi_t$  the void fraction,  $\rho_f$  and  $\rho_s$  the specific density of the fluid, and the solid, respectively. When combining Eq. (5.46) with Eqs. (5.44) and (5.45), one can obtain the following equations for the effective density of the material based on the measured effective sound velocity

$$\rho_e = \rho_f + (\rho_s - \rho_f) \cdot \left( \frac{c_e}{c_s} \right)^{\frac{1}{0.84}} \quad (5.47)$$

and

$$\rho_e = \rho_s - \frac{\rho_s - \rho_f}{c_s - c_e} \cdot \left( \frac{c_f c_s}{c_e} - c_f \right) \quad (5.48)$$

respectively. Summarizing based on the measured sound velocity both void fraction and apparent density can be predicted.

## 5.10 Conclusions

In the present chapter three situations were distinguished; slurry (starting situation), hardened product (end situation) and material during hydration (situation in between slurry and hardened product). The following main finding with regard to these situations were found

- The model of Robeyst et al. (2008) for the sound velocity of a slurry showed a good agreement with the experimental values, when taking into account an air content of 2.7% (V/V) on applied hemi-hydrate (or 10 ml air / kg hemihydrate).
- A very good agreement for porous hardened materials was found between the experimental and theoretical values with the series arrangement according to Ye et al. (2003) (Eq. (5.21)) with  $c_s = 6800$  m/s for dihydrate.
- The ultrasonic sound velocity through the hydrating material, which is related to the hydration curve, can be described by using the combination of the hydration model of Schiller (1974) and the relation between hydration degree and sound velocity given by Smith (2002).

Furthermore the analysis of the results of the fitting with the Schiller model showed that the parameters  $K_0$  (induction time) and  $K_1$  (gypsum growth) are positively linearly related to the water/binder ratio (wbr). The parameter  $K_2$  (dissolution of hemihydrate) is unrelated to the volume fraction water.



## Thermal conductivity of gypsum exposed to fire\*

### 6.1 Introduction

The exposure of a structural material, such as steel, to high temperature reduces its strength and rigidity and may lead to structural collapse, when the critical temperature is reached (Pignatta e Silva, 2005). Two methods are commonly used to protect the steel namely the insulation and capacitive method (Milke et al., 2001). The insulation method consists of attaching insulating material to the external surface of the board. One of the possible insulation materials is gypsum plasterboard. The capacitive method is based on the principle of using the heat capacity of a protective material to absorb heat. Gypsum uses mainly the insulation method, because it conducts heat slowly, but it will also absorb some of the heat of the fire by its volumetric enthalpy. Gypsum plasterboards therefore increase the time until the structural members reach the critical temperature. The most important property governing the heat transfer is the thermal diffusion. The thermal diffusivity provided here, can serve as an input for the energy transport models which are used in moisture transfer models (Ang and Wang, 2009; Erich et al., 2008; Gawin et al., 2003; Pignatta e Silva, 2005) and fire simulation models (Ang and Wang, 2009; Belmiloudi and Le Meur, 2005; Craft et al., 2008; Gerlich et al., 1996; Manzello et al., 2007; Takeda, 2003). Section 6.2 gives some background of underlying thermodynamic system.

The thermal diffusivity ( $td$ ) depends on the density ( $\rho$ ), specific heat ( $C_p$ ) and thermal conductivity ( $\lambda$ ) and reads

$$td = \frac{\lambda}{C_p \rho} \quad (6.1)$$

The density and specific heat can be calculated based on the mass-composition of the board, which is showed in Section 6.3. The thermal conductivity is more difficult to calculate since it is directional property. This chapter will focus on the considering of local microstructure system rather than the overall moisture and heat transfer model.

The thermal conductivity of materials is more complicated for porous media, which consist of different phases. Kaviany (1995) points out that the heat conduction through fully saturated matrix depends on the structure of the matrix and the thermal conductivity of each phase. The same principle applies for any heterogeneous material. One of the most difficult aspects of the analysis of heat conduction through a porous medium is the structural modelling. This is because the representative elementary volumes are three-dimensional and have complicated structures that vary greatly among different porous media. Since the thermal conductivity of the solid phase is generally larger than that of the fluid, the manner in which the solid is interconnected influences the conduction.

---

\*Parts of this chapter were published elsewhere De Korte and Brouwers (2010)

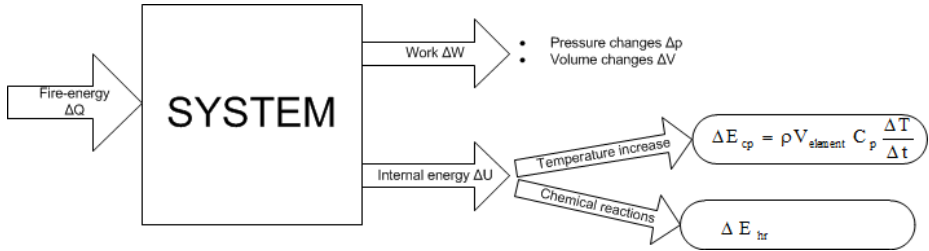


**Figure 6.1:** Thermodynamic system.

Furthermore, a plasterboard consists of a solid phase and water/air mix in the voids. The thermal conductivity of the voids depends strongly on the amount of moisture (absorbed water) in the voids, since the thermal conductivity of water is 23 times the thermal conductivity of air. Within this chapter a gypsum plasterboard is assumed to be a three-phase system. The calculation of the thermal conductivity of this system is divided in a number of steps.

The first step (Sections 6.4 and 6.5) is the calculation of the thermal conductivity of two different two-phase porous systems. The first system consists of the solid material and air as the pore fluid, whereas the second system consists of the solid material and liquid water as the pore fluid. Based on the thermal conductivities of these two systems, the thermal conductivity of the porous medium with moistened air as the void fluid can be computed. This concept is applied to various types of gypsum/limestone plasterboards. The models are validated by comparing the results of the models with experiments (Section 6.6). Based on these results and models conclusions are drawn in regard to the amount of absorbed water.

Finally the concept of thermal conductivity is applied on gypsum plasterboards under fire (Section 6.7). When gypsum plasterboard is exposed to fire, the density / void fraction, the structure, the moisture content and the composition of the board will change, due to decomposition reactions in the core of the board. These properties influence the thermal conductivity of the boards. The thermal conductivity of the individual solid phases also varies with temperature. The variation of thermal conductivity over certain temperature ranges can be neglected for some materials, but may be significant for others. The thermal conductivity temperature dependence of the considered solids is however limited (Çengel, 2007). Therefore in this research the thermal conductivity of the solid phases is assumed to be constant, but the thermal conductivity of the composited material (e.g. the gypsum plasterboard) will change due to the changes in the void fraction and composition of the material. The assumption of constant thermal conductivity is permissible since the thermal conductivity are experimentally measured at room temperature. The experimental results of plasterboards are compared with the results from simulations based on the developed model. Based on these results, conclusions are drawn in regard to the applicability of the proposed thermal conductivity model during fire.

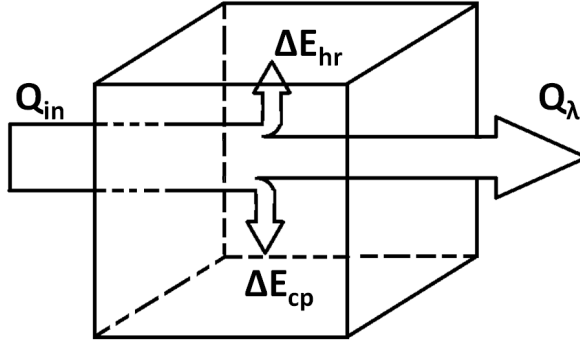


Figure 6.2: Thermodynamic system modified from Çengel (2007).

## 6.2 Thermodynamic system

The thermal response of building materials to fire can be considered as a thermodynamic system. Three thermodynamic heat flows can be distinguished in any thermodynamic system, namely net heat delivered to the system  $\Delta Q$ , work performed by the system  $\Delta W$  and the change of the internal energy  $\Delta U$  (Çengel, 2007). According to the first thermodynamic law, the energy in a closed system is constant. This means that no energy can be created or destroyed, but in all processes energy can be transferred from one form in another. Therefore three thermodynamic heat flows can be described according to the following equation;

$$\Delta Q = \Delta U + \Delta W \quad (6.2)$$

The net delivered heat  $\Delta Q$  is the heat delivered to system  $Q_{in}$  minus the heat which is conducted through the material  $Q_{\lambda}$ .

$$\Delta Q = Q_{in} - Q_{\lambda} \quad (6.3)$$

The equation for the conducted heat through slab reads;

$$Q_{\lambda} = \lambda A \frac{\Delta T}{x} \quad (6.4)$$

with  $\lambda$  the thermal conductivity,  $A$  the exposed surface,  $\Delta T$  the temperature difference over the thickness of the slab and  $x$  the thickness of the slab.

The change of internal energy of a system can be separated in two parts the energy absorbed by the system by temperature increase ( $\Delta E_{cp}$ ) and energy absorbed by the system by chemical reactions ( $\Delta E_{hr}$ ). The amount of energy needed for temperature increase of a material can be described based on the specific heat of the material and the temperature increase according to the following equation;

$$\Delta E_{cp} = \rho V C_p \Delta T \quad (6.5)$$

with  $\rho$  the specific density of the material,  $V$  the volume,  $C_p$  the specific heat and  $\Delta T$  the temperature increase. The energy needed for the chemical reactions can be described using;

$$\Delta E_{hr} = \sum_i \Delta H_r \delta_{i,0} \alpha_i \quad (6.6)$$

with  $\Delta H_r$  the energy needed to perform the decomposition reaction,  $\delta_{i,0}$  the initial volume fraction of the  $i^{\text{th}}$  chemical component of the material and  $\alpha_i$  the reaction degree. The reaction energy can be calculated based on the so-called formation heat of a chemical ( $\Delta H_f(T)$ ), this formation heat is temperature dependent. In general the reaction heat is the formation heat of the reactants minus the formation heat of products. When this reaction heat is negative a reaction is endothermic and will absorb energy from the systems. A positive reaction heat will add energy to the system and is called exothermic. The here studied decomposition reactions absorb heat from the system and are endothermic.

### 6.3 Calculation of properties

In the previous section, the main equations in the thermodynamic system were given. As one can notice these equations depend on the density and enthalpy (the sum of the specific heat and energy needed for the chemical (decomposition) reactions). The first relevant property is the effective density. The effective density of a material is given by the following equation

$$\rho_e = \sum \varphi_i \rho_i \quad (6.7)$$

With  $\rho_i$  the density of substance  $i$  and  $\varphi_i$  the volume fraction of substance  $i$ . The volumetric enthalpy ( $\Delta H_0(T)$ ) is the total energy needed to heating up the material up to certain temperature. The equations for the volumetric enthalpy reads;

$$\Delta H_0(T) = \Delta H_{f,0}(273) + \int C_p dT + \Delta H_r \quad (6.8)$$

with  $\Delta H_{f,0}$  the sum of formation heat of the chemical substances at 273 °C (Table 1.6),  $C_p$  the specific heat of the chemical substances,  $T$  the temperature and  $\Delta H_r$  the reaction heat of the decomposition reactions. Figure 6.3 shows a overview of the volumic enthalpy founded by Thomas (2002) in literature (Andersson and Gram, 1987; Harmathy, 1970; Mehaffey et al., 1994) and the volumetric curve used by Thomas (2002) in his paper.

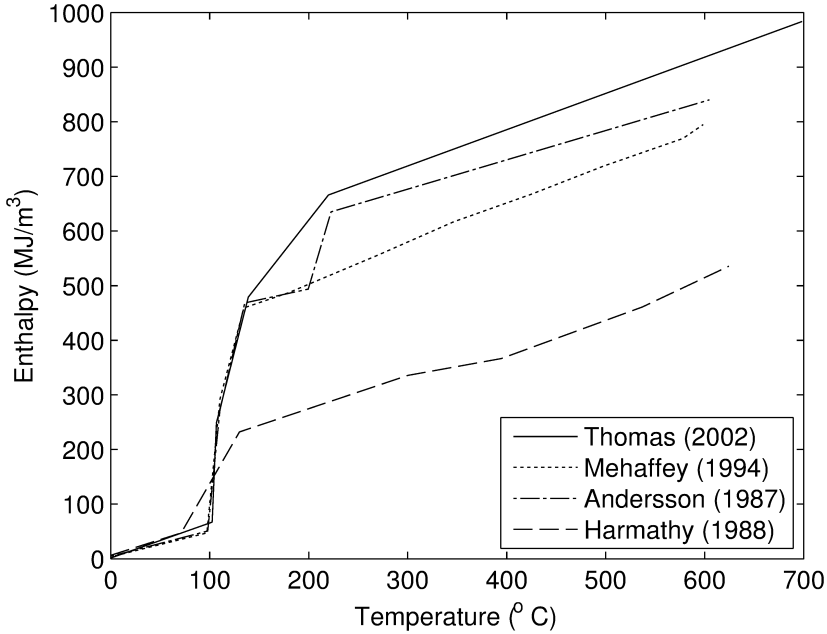


**Figure 6.3:** Enthalpy curves for gypsum plasterboard (Thomas, 2002).

In order to calculate the enthalpy, the specific heat is needed. The specific heat of a material defined as the amount of energy necessary to heat one kilogram of material one degree Celsius. Therefore the equation for specific heat reads

$$C_p = \left( \frac{\Delta H}{m \cdot \Delta T} \right)_p \quad (6.9)$$

With  $\Delta H$  the amount of energy,  $m$  the mass and  $\Delta T$  the temperature increase. When reactions take place this will influence the amount of energy needed for the heating up of the material. This apparent specific heat of composite material like plasterboard can be computed with the following equation (Mehaffey et al., 1994);

$$C_p(T) = \sum \frac{\delta_i}{\rho_i} C_{p,i}(T) + \frac{\Delta H_r}{\Delta T} \quad (6.10)$$

With  $C_{p,i}$  the specific heat of mineral  $i$  and  $\Delta H_r$  the reaction heat. Thomas (2002) has made a comparison of specific heat values obtained from different researchers (Andersson and Gram, 1987; Harmathy, 1970; Mehaffey et al., 1994; Sultan, 1996). The results are presented in Figure 6.4. As one can notice, some differences exist in their findings, which are caused by their different assumptions.

These properties, are often assumed to be constant over temperature. But this is a simplification, since they are actually temperature and pressure dependent. Table 6.2 shows the temperature dependence for dihydrate and anhydrite (Raju and Atkinson,

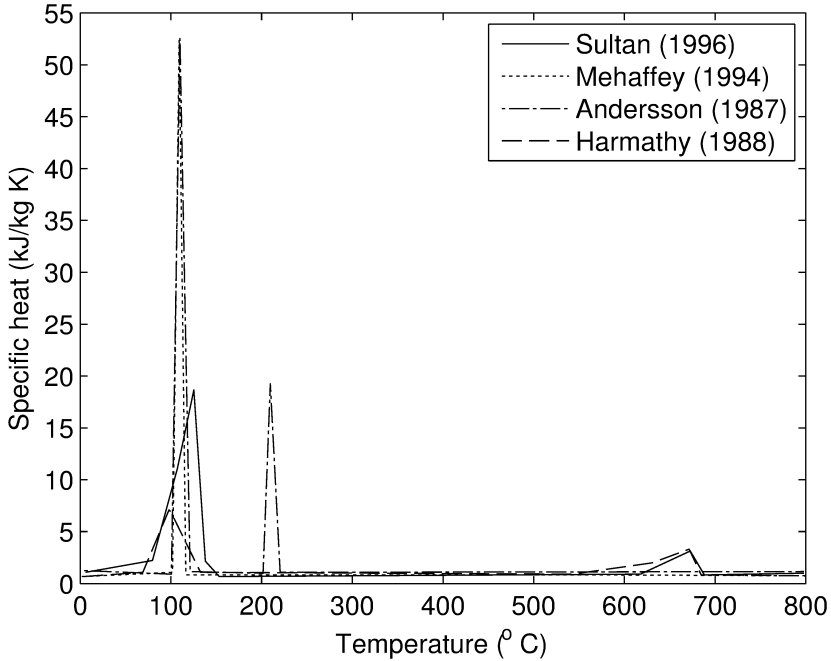


**Figure 6.4:** Comparison of specific heat values from different researchers (Thomas, 2002).

$$\begin{array}{l}
 \hline
 C_p = A + BT + C/T^2 \\
 \Delta H^0 = AT + \frac{BT^2}{2} - \frac{C}{T} + I_h \qquad \Delta H_f^0 = C_p \cdot T \\
 \Delta S^0 = A \ln T + BT - \frac{C}{2T^2} + I_s \qquad \Delta S^0 = \frac{C_p}{T} dT \\
 -G^0 = AT \ln T + \frac{BT^2}{2} + \frac{C}{2T} - I_h - IgT \qquad \Delta G^0 = \Delta H - T\Delta S \\
 \hline
 \end{array}$$

**Table 6.1:** Equations of the calculation of thermal properties (Raju and Atkinson, 1990).

1990). Besides heat capacity also enthalpy, entropy and free Gibbs energy are temperature dependent. The equations from Table 6.1 and the numbers in Table 6.2 describe the temperature dependences of the thermodynamic properties of some other chemicals.

## 6.4 Thermal conductivity of two phase systems

For two-phase systems, several equations have been suggested during the last two centuries. Côté and Konrad (2009) point out that heat conduction through a two-phase porous media depends on the thermal conductivity as well as the structure of the solid matrix. In terms of thermal behaviour, the structure of the solid matrix determines the contact resistance and the continuity of the solid phase (Kaviany, 1995). Hamilton and Crosser (1962) showed theoretically that the thermal conductivity of particle packings decrease with increasing sphericity of particles in case of rubber-saturated porous material. This effect was also noticed by Johansen (1975) and Côté and Konrad (2005) in air-saturated geomaterials where the thermal conductivity of natural particle packing

	A	B	$10^{-6} C$	$I_h$	$I_g$	$I_s$
	J/(mol K)	J/(mol K <sup>2</sup> )	(J K)/mol	J/mol	J/(mol K)	J/(mol K)
CaSO <sub>4</sub>	70.21	0.09874	0.0	-1459 593	876.13	-322.75
CaSO <sub>4</sub> · $\frac{1}{2}$ H <sub>2</sub> O	70.97	0.16329				
CaSO <sub>4</sub> ·2H <sub>2</sub> O	91.38	0.31798	0.0	-2064 398	1461.01	-421.33
H <sub>2</sub> O (l)	47.65	0.05824	0.9188	-299 545	494.72	-213.80
Ca(OH) <sub>2</sub>	79.77	0.04518	0			
CaO	41.83	0.02025	-4.51·10 <sup>5</sup>			
CO <sub>2</sub>	44.21	0.00878	-8.61·10 <sup>5</sup>			
CaCO <sub>3</sub>	104.49	0.02192	-2.59·10 <sup>6</sup>			
MgCO <sub>3</sub>						
H <sub>2</sub> O (g)	30.54	0.01029				

**Table 6.2:** Coefficients of thermodynamical equations of Table 6.1 (Raju and Atkinson, 1990).

(rounded/sub-rounded particles) were systematically lower than those of crushed particle packings (angular/sub-angular particles). A possible reason for this effect could be found in the smaller contact areas among the spherical particles compared to the more angular particles. Since the amount of contact area is related to the possible amount of solid-solid conductivity, assuming that the thermal conductivity of the solid is higher than the thermal conductivity of the fluid (liquid or gas).

The most simple calculation methods for the conduction of two-phase media are the serie and parallel arrangements (Torquato, 2002). Both arrangements assume a very simple structure (Figure 6.6). The effective thermal conductivity  $\lambda_e$  assuming the parallel arrangement reads;

$$\lambda_e = \varphi\lambda_f + (1 - \varphi)\lambda_s \quad (6.11)$$

and assuming the serie arrangement reads

$$\lambda_e = \frac{\lambda_f\lambda_s}{\varphi\lambda_f + (1 - \varphi)\lambda_s} \quad (6.12)$$

with  $\lambda_e$  is the effective thermal conductivity of porous medium,  $\lambda_f$  is the thermal conductivity of the pore fluid,  $\lambda_s$  is the thermal conductivity of the solid phase,  $\varphi$  is the void fraction of the porous medium. Porous materials are in fact a large combination of parallel and serie arrangements. Since these thermal networks are complicated, there has been a search for more general equations/methods to describe the thermal conductivity of porous media. The Maxwell equations can be used for this. They were introduced by Maxwell (1873), and there are two limits distinguished: the so-called upper and lower bound. The lower bound describes the dilute suspension of particles and reads

$$\lambda_e = \lambda_f \left( \frac{2\varphi + (3 - 2\varphi)\lambda_s/\lambda_f}{3 - \varphi + \varphi\lambda_s/\lambda_f} \right) \quad (6.13)$$

The upper bound is a solid body containing dilute inclusion of fluid and reads

$$\lambda_e = \lambda_s \left( 1 + \frac{3\varphi(1 - \lambda_s/\lambda_f)}{(1 - \varphi) + \lambda_s/\lambda_f(2 + \varphi)} \right) \quad (6.14)$$

Both limits neglect the exact particle shapes within the microstructure. There are also methods, which take into account both the thermal conductivity of the different phases as well as the specific particle shape. For example Miller (1969) introduced a more complicated equation for the upper and lower bound, including a correction for cell shape (G). The cell shape factor G is between 1/9 for spherical and 1/3 for plate cell shape. The Miller equations for the lower and upper bound read:

$$\lambda_e = \lambda_f [1 + (1 - \varphi)(\kappa - 1)] \cdot \left( 1 - \frac{(1 - \varphi)(\kappa - 1)^2\varphi}{3 \cdot [1 + (1 - \varphi)(\kappa - 1)] \cdot [1 + ((1 - \varphi) + 3(2\varphi - 1)G)(\kappa - 1)]} \right) \quad (6.15)$$

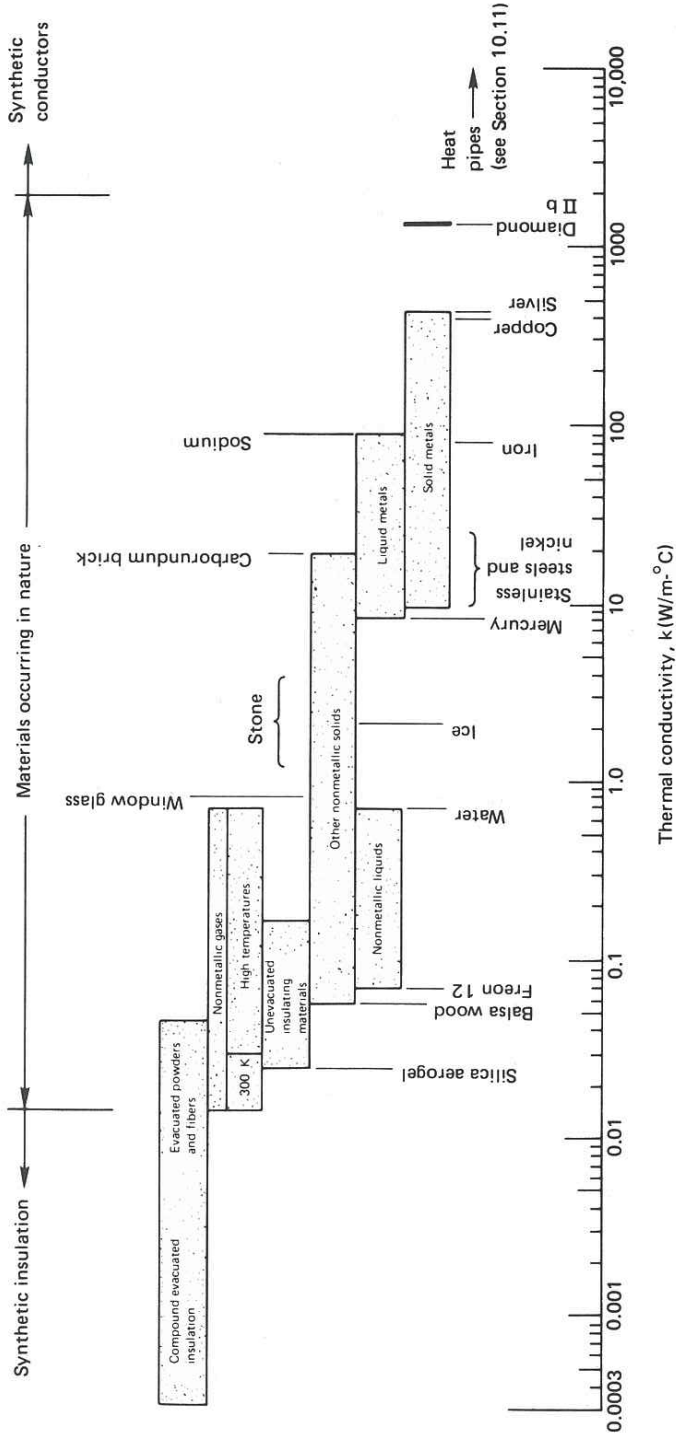
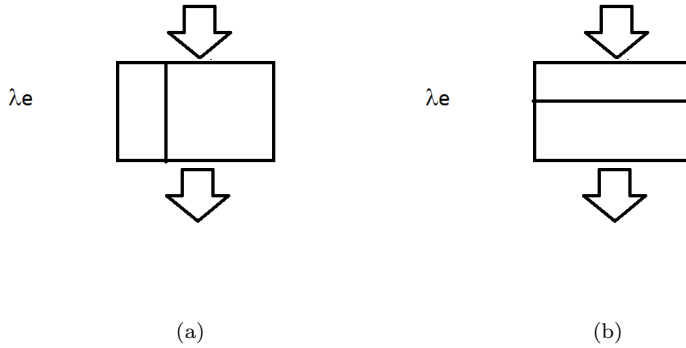


Figure 6.5: The approximate ranges of thermal conductivity of various substances (Lienhard, 1987).



**Figure 6.6:** The (a) parallel and (b) serie arrangements of (thermal) conductivity.

and

$$\lambda_e = \lambda_s \left[ \kappa - (1 - \varphi)(\kappa - 1) - \frac{\frac{3}{4}(\kappa - 1)^2(1 - \varphi)\varphi}{1 + \kappa + 3(1 - 2\varphi)(\kappa - 1)G} \right]^{-1} \tag{6.16}$$

respectively. The thermal conductivity will be between the upper and lower bound, since the porous material is neither a dilute fluid nor a dilute solid. Hadley (1986) introduced therefore the ‘weighted average Maxwell equation’. This equation combines an expression describing the conduction through a contiguous solid (the upper Maxwell formula, Eq. (6.14)) with one describing a suspension of particles. The part for the suspension of particle approaches the lower Maxwell formula (Eq. (6.13)) when the limit of void fraction tends to unity. This is a valid assumption when assuming that solid spheres are to far apart to interact under the lower Maxwell equation. This weighted average Maxwell equation reads:

$$\lambda_e = \lambda_f \cdot \left( (1 - \alpha_0) \left( \frac{f_0\varphi + \kappa(1 - f_0\varphi)}{1 - \varphi(1 - f_0) + \kappa\varphi(1 - f_0)} \right) + \alpha_0 \left( \frac{2\kappa^2(1 - \varphi) + (1 + 2\varphi)\kappa}{(2 + \varphi)\kappa + 1 - \varphi} \right) \right) \tag{6.17}$$

with

$$\kappa = \frac{\lambda_s}{\lambda_f} \tag{6.18}$$

with  $f_0$  is the mixture factor and  $\alpha_0$  degree of consolidation. The degree of consolidation reads

$${}^{10}\log(\alpha_0) = -4.898\varphi \qquad \text{for } 0 \leq \varphi < 0.0827$$

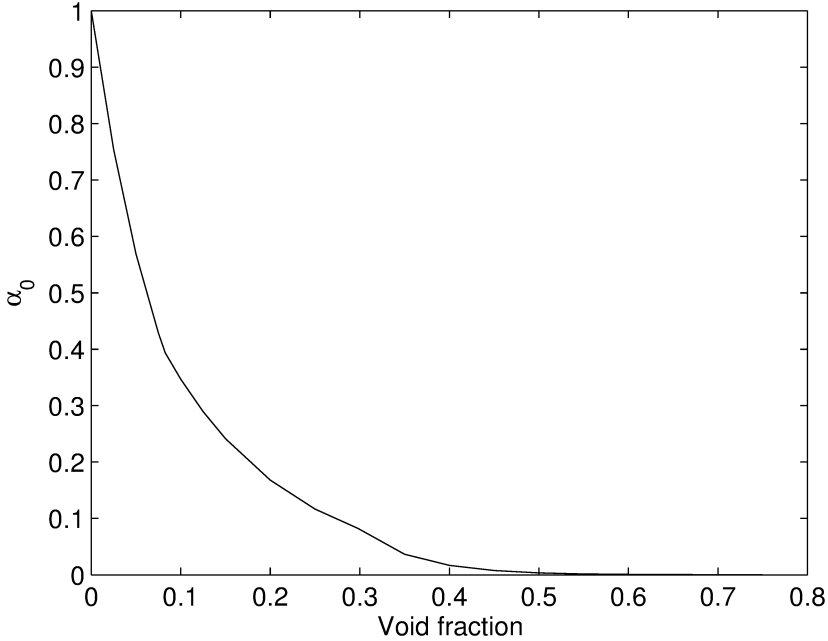


**Figure 6.7:** Degree of consolidation ( $\alpha_0$ ) used for the weighted average Maxwell equation (Eq. (6.19)) versus void fraction.

$${}^{10}\log(\alpha_0) = -0.405 - 3.154(\varphi - 0.0827) \quad \text{for } 0.0827 \leq \varphi < 0.298 \quad (6.19)$$

$${}^{10}\log(\alpha_0) = -1.084 - 6.778(\varphi - 0.298) \quad \text{for } 0.298 \leq \varphi < 0.580$$

Figure 6.7 shows the values of  $\alpha_0$  versus  $\varphi$  for this equation. From Figure 6.7 it follows that the degree of consolidation tends to zero when the void fraction tends to unity. For  $\varphi = 0.58$ ,  $\alpha_0$  equals 0.001 and since gypsum plasterboards have normally a void fraction bigger than 0.6,  $\alpha_0$  can be assumed to be zero. Therefore Eq. (6.18) can be represented by

$$\lambda_e = \lambda_f \left( \frac{f_0 \varphi + \kappa(1 - f_0 \varphi)}{1 - \varphi(1 - f_0) + \kappa \varphi(1 - f_0)} \right) \quad (6.20)$$

with  $f_0$  as mixture factor. When the mixture factor is equal to  $2/3$ , it corresponds to the lower Maxwell equation (Eq. (6.13)). When mixture factor is equal to  $2\chi/(2\chi+1)$ , Eq. (6.20) is equal to the upper Maxwell limit (Eq. (6.14)). Therefore the value of  $f_0$  should be between  $2/3$  and  $2\chi/(2\chi+1)$ . Hadley (1986) points out that the value of  $f_0$  is

**Table 6.3:** The sphericity ( $\psi$ ) of different particle shapes used to describe the interconnection of particles for the thermal conductivity (Hamilton and Crosser, 1962).

Particle Shape	Shape factor ( $\psi$ )
Sphere	1.0
5:1 cylinder	0.68
10:1 cylinder	0.57
Parallel pipes	0.62

increasing with  $(1 - \varphi)$  starting at  $2/3$ . Unfortunately there is no proper functional form yet. Hadley (1986) introduced a linear function for  $f_0$  of the void fraction, reading;

$$f_0 = 0.8 + 0.1\varphi \quad (6.21)$$

This linear function does not fit with the upper and lower limit for  $f_0$ , which were set by Hadley (1986). Therefore, here a linear function is proposed that is located between the upper and lower limit for  $f_0$ ;

$$f_0 = \frac{2}{3} + \varphi \left( \frac{2\kappa}{2\kappa + 1} - \frac{2}{3} \right) \quad (6.22)$$

Another equation for  $f_0$  was proposed by Verma et al. (1991)

$$\ln f_0 = - \left( \frac{\psi^3}{\kappa} \right)^{\frac{1}{3}} \quad (6.23)$$

In which  $\psi$  is the sphericity of the particles in the matrix. The sphericity of a sphere equals unity and is smaller than unity for non-spherical shapes. Hamilton and Crosser (1962) gave the sphericity of different particle shapes. Table 6.3 shows the sphericity of the different particle shapes. The sphericity is determined based on the surface area of the particle ( $A_p$ ) and surface of sphere ( $A_{sph}$ ) with same volume as the particle and the equation reads;

$$\psi = \frac{A_{sph}}{A_p} \quad (6.24)$$

The microstructure of the core of plasterboard is characterized by needle-like structure. The needle-like structure could be modelled as long cylinders. According to Hamilton and Crosser (1962) (Table 6.3), a sphericity of 0.555 corresponds with long cylinder shape. Eq. (6.22) yields between  $2/3$  and 0.877 for void fraction ( $\varphi$ ) of 0.65 and Eq. (6.23) equals 0.859 for  $\kappa = 48.3$  (air-gypsum system) with  $\psi = 0.555$ . While Eq. (6.22) yields between 0.667 and 0.758 for  $\varphi = 0.65$ , and Eq. (6.23) equals 0.648 for  $\kappa = 2.09$  (water-gypsum system) with  $\psi = 0.555$ .

Another possibility is to describe the thermal conductivity with method of Zehner and

**Table 6.4:** The shape factor (C) for different particle shapes used to describe the interconnection of particles within the thermal conductivity equations (Zehner and Schlünder, 1972).

Particle Shape	Shape factor (C)
Sphere	1.25
Broken Particle	1.40
Cylinder and tubes	2.50
Cementitious material	5.00

Schlünder (1972). Zehner and Schlünder, like Miller (1969) and Verma et al. (1991), take into account the shape of the particles and therefore their surface connectivity. The equation of Zehner and Schlünder reads

$$\lambda_e = \lambda_f \left(1 - \sqrt{1 - \varphi}\right) + \lambda_f \sqrt{1 - \varphi} A \quad (6.25)$$

with

$$A = \frac{2}{N} \left( \frac{B}{N^2} \frac{\kappa - 1}{\kappa} \ln \left( \frac{\kappa}{B} \right) - \frac{B + 1}{2} - \frac{B - 1}{N} \right)$$

$$N = 1 - \frac{B}{\kappa}$$

$$B = C \left( \frac{1 - \varphi}{\varphi} \right)^{\frac{10}{9}}$$

and with  $\kappa$  following from Eq. (6.18). The factor C depends on the shape of the particle. The different values for this factor are presented in Table 6.4. These values are for particles which can be freely move in/through the matrix. In the case of a gypsum core there are a high number of so-called solid-phase bridges. This higher connectivity leads to a higher conductivity compared to a system with the same void fraction but with lower connectivity. For such systems with high number of solid-phase bridges, a C-value of 5 is proposed (Zehner and Schlünder, 1970).

## 6.5 Theory versus experimental data

This section describes the experimental data on thermal conductivity of gypsum plasterboards found in literature, which are used to compare with the calculation results obtained by presented equations. This experimental data is often found together with a description of the apparent density and chemical composition. Both these parameters are important in order to predict the thermal conductivity of plasterboards. The density

**Table 6.5:** Experimental values of apparent density ( $\rho_a$ ), chemical composition (%m mass percentage) and thermal conductivity ( $\lambda$ ) of gypsum plasterboards at room temperature as described in literature (W = Wullschleger and Ghazi Wakili (2008), A = Ang and Wang (2004), M = Mehaffey et al. (1994), S = Sultan (1996), G = Ghazi Wakili and Hugi (2009)).

	$\rho_a$ (kg/m <sup>3</sup> )	%m <sub>C<math>\bar{S}</math>H<sub>2</sub></sub> (kg/kg)	%m <sub>CC</sub> (kg/kg)	%m <sub>MC</sub> (kg/kg)	$\lambda$ (W/(m K))
W	810	81	9.5		0.28
A	836				
M1	732				0.25
M2	648				0.24
S	698				0.25
G1	735	80.9	12.3		0.28
G2	840	62.2	32.3		0.30
G3	740	76.5	4.2	4.7	0.23
G4	870	98			0.32

is important because it is closely related to the void fraction of plasterboards. As can be seen in the previous section, the void fraction is one of the main parameters for the calculation of the thermal conductivity. The chemical composition of gypsum plasterboards influences the thermal conductivity of the solid phase within the board.

Table 6.5 shows values which are presented in literature. It should be noted that most articles on the thermal properties of gypsum plasterboard tend to use the data of Mehaffey et al. (1994) or Sultan (1996). Both Ghazi Wakili and Hugi (2009) and Wullschleger and Ghazi Wakili (2008) performed additional experiments and also determined the chemical composition of the gypsum-plasterboard based on the thermal decomposition peaks. The presence of calcium carbonate is confirmed by Maksoud and Ashour (1981) and Oates (2005), who point out that calcium carbonate is used by the production of FGD-gypsum. For the production of the plasterboards partly FGD-gypsum is used, which explains the presence of calcium carbonate in plasterboards.

The experimental data is compared with the equations of the previous section. For this comparison the thermal conductivity of the solid needs to be known. Since the solid phase of gypsum plasterboards consist of several phases, the thermal conductivity of the solid phases has to be calculated. There are different calculation methods available for thermal conductivity of the composite solid. Clauser and Huenges (1995) mentioned the following three equations for this calculation

$$\lambda_s = \sum_{i=1}^n \delta_i \lambda_i \quad (6.26)$$

$$\lambda_s = \frac{1}{\sum_{i=1}^n \frac{\delta_i}{\lambda_i}} \quad (6.27)$$

**Table 6.6:** Thermal conductivities and specific density of the used substances.

Substance	Thermal conductivity (W/(m K))	Specific density (kg/m <sup>3</sup> )
<i>CaSO<sub>4</sub> · 2H<sub>2</sub>O</i>	1.255	2310
<i>CaCO<sub>3</sub></i>	3.58	2720
<i>MgCO<sub>3</sub></i>	5.83	2990
Liquid water	0.60	1000
Air (dry)	0.026	1.3

$$\lambda_s = \prod_{i=1}^n \lambda_i^{\delta_i} \quad (6.28)$$

with  $\lambda_i$  is the thermal conductivity of  $i^{\text{th}}$  solid phase and  $\delta_i$  the volume fraction of  $i^{\text{th}}$  solid phase. The summation of the volume fractions ( $\delta_i$ ) equals unity. All three methods provide a thermal conductivity of the solid phase based on average of the available solid phases while taking into account the volume fraction of the phases. Eq. (6.26) is the arithmetic average. This average assumes that the volume fractions are in parallel and Eq. (6.11) is special case of Eq. (6.26) for  $n = 2$ . Eq. (6.27) is the harmonic average, which assumes a serie arrangement of the ingredients. Eq. (6.12) is a special case of Eq. (6.27) for  $n = 2$ . Eq. (6.28) is the geometric mean method, which seems more realistic. The geometric method cannot be linked to a clear defined physical model, as is the case for the arithmetic and harmonic average. The geometric mean is a type of average, which indicates the central tendency or typical value of a set of numbers, and is often used for exponential data. Côté and Konrad (2005) use the third method for their calculation of the thermal conductivity of dry soil.

All three methods are used for the calculation of the thermal conductivity of the complete solid phase based on the thermal conductivity of the individual phases. All three methods use the volume-based composition. In order to get the volume-based composition from the mass-based composition, the specific densities of the different solid phases need to be known. The thermal conductivities and specific densities of the individual substances used are presented in Table 6.6.

Figure 6.8 shows the effects on the solid thermal conductivity, when replacing gypsum by calcium carbonate. Table 6.7 shows the results of the thermal conductivity of the solid phase of plasterboards based on Eqs. (6.26)-(6.28), the chemical composition from Table 6.5 and properties from Table 6.6. It can be noticed from Table 6.7 that the three equations for the calculation of the thermal conductivity of the solid based on the chemical composition of the solid phase result in large differences. The difference can be up to 33% between the arithmetic and harmonic method. In general the harmonic method will deliver the lowest value, while the highest value is obtained with the arithmetic method. The geometric method leads to a value in between. Since the microstructure of porous medium is also in between the serie and parallel arrangement and usually a combination of these extreme cases, it seems the most realistic model for the calculation of the solid thermal conductivity. According to Clauser and Huenges (1995) both the arithmetic and

**Table 6.7:** The results of the calculation of the solid thermal conductivity for the solid phase only based on the three methods mentioned by (Clauser and Huenges, 1995).

	Arithmetic Eq. (6.26)	Harmonic Eq. (6.27)	Geometric Eq. (6.28)
Wullschleger and Ghazi Wakili (2008)	1.47	1.33	1.38
Mehaffey et al. (1994) 1	1.26	1.26	1.26
Mehaffey et al. (1994) 2	1.26	1.26	1.26
Sultan (1996)	1.26	1.26	1.26
Ghazi Wakili and Hugi (2009) 1	1.52	1.36	1.42
Ghazi Wakili and Hugi (2009) 2	1.97	1.57	1.72
Ghazi Wakili and Hugi (2009) 3	1.56	1.34	1.40
Ghazi Wakili and Hugi (2009) 4	1.26	1.26	1.26

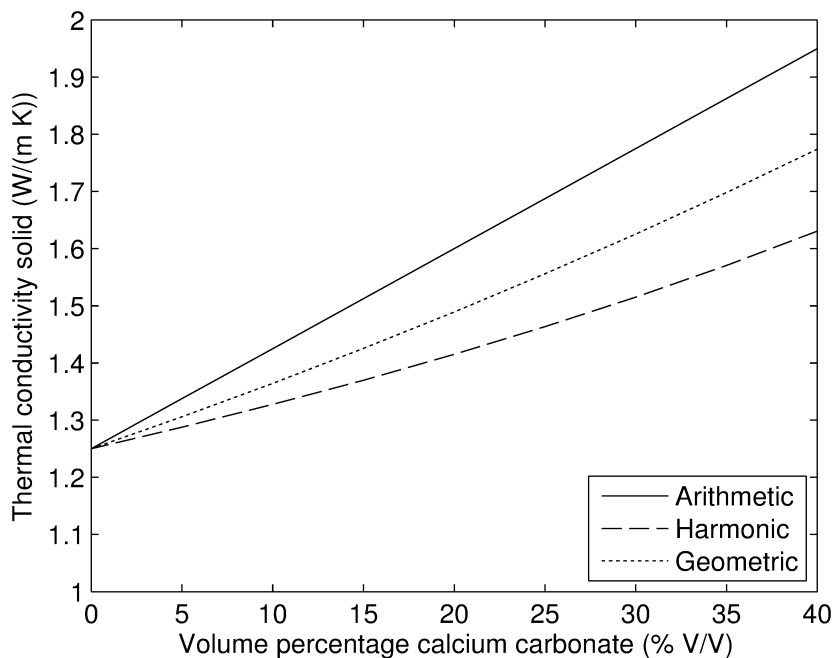


**Figure 6.8:** Thermal conductivity of gypsum and calcium carbonate compounds for three mixing/calculation equations (Eqs. (6.26)-(6.28)).

harmonic method have the disadvantage of describing the special cases and therefore are given the upper and lower boundaries. They point out that geometric method is quite successful in predicting the thermal conductivity in many cases. Furthermore the geometric method was also recommended by Côté and Konrad (2005).

Next, the two-phase conductivities are computed based on the expressions from Section 6.4 and the calculated solid thermal conductivities from Table 6.7. The results of these computations are presented in Table 6.8 and Figure 6.9. From Table 6.8 and Figure 6.9 it could be concluded that the measured value is between upper and the lower bound of the Maxwell. The upper Miller limit is in some cases larger than measured value. The weighted average Maxwell, the equation of Hadley and the equation of Zehner and Schlunder are all smaller than the measured value. A good agreement was obtained with weighted average Maxwell, and with Zehner and Schlunder with  $C = 5$ .

The calculation method for the solid has a influence on the results. The highest thermal conductivity is obtained with the arithmetic and lowest with harmonic method. The obtained geometric value is in between. These findings are in line with the findings based on only the thermal conductivity of the solid phase.

The obtained value from the equations of both Hadley (1986) and Zehner and Schlunder (1972) are too low compared to the results obtained from experiments. This could be the result of the current assumption that the voids are filled with dry air, while in reality the fluid in the voids is usually moistured. Building materials, like gypsum plasterboards, are porous media in which moisture transfer occurs in both the vapor/gas and liquid phase. Bouguerra (1999) points out that the thermal conductivity is strongly influenced by the moisture content migrating through porous material. Since the thermal conductivity of water vapour is similar to the thermal conductivity of air, there will be no clear difference. But the thermal conductivity of liquid water is 23 times the thermal conductivity of air which will lead to clear difference. The next section will focus on the effect of moisture on the thermal conductivity of the gypsum plasterboards.

## 6.6 Three phase system

The considered three phase system consists of a solid porous medium with a mixture of a liquid (water) and a gas (dry air) in the voids. Somerton et al. (1974) have derived the following equation for porous medium filled by a mixture of two fluids

$$\lambda_e = \lambda_g + \sqrt{s_l} (\lambda_l - \lambda_g) \quad (6.29)$$

here  $\lambda_g$  is the effective thermal conductivity of the porous medium filled with dry air,  $\lambda_l$  is the effective thermal conductivity of the porous medium filled with water and  $s_l$  the volume-based saturation rate of fluid in the voids. Both  $\lambda_g$  and  $\lambda_l$  can be calculated with the equations for two-phase effective conductivity given in Section 6.4, with  $\lambda_{\text{air}}$  and  $\lambda_{\text{water}}$  as the  $\lambda_f$  respectively.

Here, the method proposed by Somerton et al. (1974) is used to derive the amount of water needed to comply with the thermal conductivity as measured in the literature. During this derivation the effect of the moisture on apparent (wet) density needs to be taken into account. The apparent density consists of the dry density and the effect of

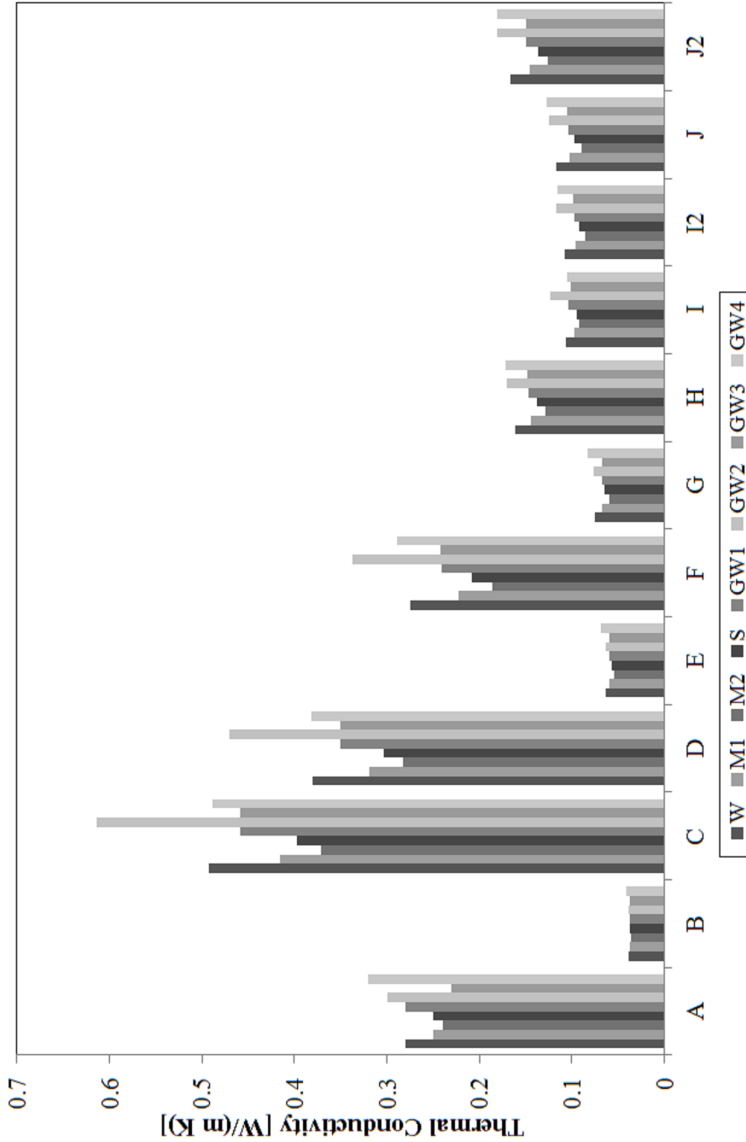


**Figure 6-9:** Thermal conductivity at ambient temperature for the different plasterboards with A the measured values and B-J2 the computed values. (A) Measured; (B) Serie; (C) Parallel; (D) Maxwell Upper bound; (E) Maxwell Lower bound; (F) Miller Upper bound; (G) Miller Lower bound; (H) Weighted Average Maxwell; (I) Hadley (Eq. (4)) with Eq. (6) for  $f_0$ ; I2: Hadley (Eq. (4)) with Eq. (7) for  $f_0$ ; (J) Zehner and Schlunder (Eq. (9)) with  $C=2.5$ ; (J2) Zehner and Schlunder (Eq. (9)) with  $C=5.0$ .

**Table 6.8:** Results of different theoretical equations from literature for the dry thermal conductivity ( $\lambda_{meas}$  = the experimental measured thermal conductivity, W = Wullschlegler and Ghazi Wakili (2008), M =Mehaffey et al. (1994), S = Sultan (1996), GW = Ghazi Wakili and Hugi (2009)).

Board	$\lambda_{meas}$	A	B	C	D	E	F	G	H	I	I2	J	J2
W	0.28	Eq. (6.26)	0.039	0.517	0.398	0.064	0.287	0.076	0.164	0.118	0.110	0.119	0.171
W	0.28	Eq. (6.27)	0.039	0.477	0.368	0.064	0.267	0.075	0.160	0.116	0.107	0.116	0.165
W	0.28	Eq. (6.28)	0.039	0.493	0.381	0.064	0.275	0.075	0.161	0.107	0.108	0.117	0.167
M1	0.25		0.038	0.416	0.319	0.059	0.223	0.068	0.144	0.097	0.096	0.103	0.145
M2	0.24		0.036	0.371	0.282	0.054	0.186	0.060	0.129	0.092	0.085	0.090	0.126
S	0.25		0.037	0.397	0.304	0.057	0.208	0.065	0.138	0.095	0.092	0.097	0.137
GW1	0.28	Eq. (6.26)	0.038	0.492	0.375	0.059	0.257	0.068	0.150	0.105	0.100	0.106	0.152
GW1	0.28	Eq. (6.27)	0.038	0.441	0.337	0.059	0.233	0.067	0.145	0.111	0.097	0.103	0.146
GW1	0.28	Eq. (6.28)	0.038	0.459	0.351	0.059	0.241	0.067	0.147	0.104	0.098	0.104	0.149
GW2	0.30	Eq. (6.26)	0.039	0.695	0.533	0.064	0.379	0.077	0.177	0.127	0.121	0.129	0.189
GW2	0.30	Eq. (6.27)	0.039	0.557	0.429	0.064	0.308	0.076	0.167	0.120	0.113	0.121	0.175
GW2	0.30	Eq. (6.28)	0.039	0.614	0.471	0.064	0.337	0.076	0.171	0.124	0.117	0.125	0.181
GW3	0.23	Eq. (6.26)	0.038	0.505	0.385	0.059	0.264	0.068	0.152	0.103	0.102	0.108	0.154
GW3	0.23	Eq. (6.27)	0.038	0.438	0.335	0.059	0.232	0.068	0.146	0.111	0.097	0.104	0.147
GW3	0.23	Eq. (6.28)	0.038	0.458	0.350	0.059	0.242	0.068	0.148	0.101	0.099	0.105	0.149
GW4	0.32		0.041	0.489	0.382	0.069	0.289	0.083	0.172	0.105	0.116	0.128	0.181

**Table 6.9:** Moisture content (m/m) needed to match the measured thermal conductivity for the three different methods with A the arithmetic method, G the geometric method and H the harmonic method (W = Wullschleger and Ghazi Wakili (2008), M =Mehaffey et al. (1994), S = Sultan (1996), GW = Ghazi Wakili and Hugi (2009)).

	Weighted average method			Zehner and Schlunder		
	A	H	G	A	H	G
W	2.50 %	3.00 %	2.81 %	1.81 %	2.25 %	2.08 %
M1	2.85 %	2.85 %	2.85 %	2.32 %	2.32 %	2.32 %
M2	3.90 %	3.90 %	3.90 %	3.42 %	3.42 %	3.42 %
S	3.51 %	3.51 %	3.51 %	2.95 %	2.95 %	2.95 %
GW1	3.75 %	4.55 %	4.23 %	2.93 %	3.66 %	3.37 %
GW2	1.96 %	3.02 %	2.50 %	2.28 %	2.16 %	1.72 %
GW3	1.22 %	1.64 %	1.49 %	0.92 %	1.32 %	1.78 %
GW4	4.45 %	4.45 %	4.45 %	3.24 %	3.24 %	3.24 %

	Hadley			Miller upper		
	A	H	G	A	H	G
W	2.47 %	2.96 %	2.77 %	0.02 %		
M1	2.58 %	2.58 %	2.57 %	0.15 %	0.15 %	0.15 %
M2	3.20 %	3.20 %	3.20 %	0.86 %	0.86 %	0.86 %
S	3.06 %	3.06 %	3.06 %	0.46 %	0.46 %	0.46 %
GW1	3.34 %	4.11 %	3.81 %	0.07 %	0.55 %	0.32 %
GW2	1.93 %	2.97 %	2.46 %			
GW3	1.01 %	1.42 %	1.28 %			
GW4	4.69 %	4.69 %	4.69 %	0.21 %	0.21 %	0.21 %

moisture on the density. The dry density, is related to the void fraction of the material. So the density, void fraction and moisture content are all interrelated. This relation read

$$\rho_e = \rho_s \cdot (1 - \varphi) + \rho_l \cdot \varphi \cdot s_l \quad (6.30)$$

With  $\rho_e$  the wet (apparent) density of the board,  $\rho_g$  the dry specific solid density,  $\rho_l$  the density of the water,  $\varphi$  the void fraction and  $s_l$  the volume-based saturation rate of void fluid.

Table 6.9 and Figure 6.10 shows the results of the derived moisture content in the voids based on both the Hadley (weighted average Maxwell) and the Zehner & Schlunder equations with the use of the three different equations for the solid phase thermal conductivity. As shown in Table 6.9 the calculation method for the solid thermal conductivity has an influence on the deduced water amount. The introduced water amount is lowest for arithmetic (Eq. (6.26)) and is highest for harmonic method (Eq. (6.27)). This is exactly the opposite to the dry thermal conductivity, where the arithmetic method gives the highest thermal conductivity and the harmonic method the lowest conductivity. This seems logical since there is less water introduced to comply with the measured value.

Furthermore, the values derived from the Zehner and Schlunder equation are lower than the values derived with the Hadley and weighted average Maxwell equations. The sorbed water values following from Hadley, Zehner and Schlunder and weighted average Maxwell equation are all in line with values from literature. Ang and Wang (2009) also give a moisture content of 3% m/m. This value is furthermore mentioned by Thomas (2002), and Belmiloudi and Le Meur (2005). Therefore one can conclude that all three equations are close to the values from literature, with Zehner and Schlunder being closest to the value.

The results from Table 6.9 can be analysed even further to see if there is any parameter explaining the difference between the moisture contents of the different boards. Based on knowledge on the composition of gypsum boards one can derive the following hypotheses

1. The moisture content depends on the total mass of the solid.
2. The moisture content depends on the mass of the gypsum.
3. The moisture content depends on the masses of the gypsum and the limestone.

In order to verify these hypotheses, a regression analysis on the obtained data is performed, to find if there is any relation between the solid composition and the absorbed amount of water. This is done for the all three equations with the use of the three solid thermal conductivity equations in order to check the dependences of the solid thermal conductivity on the effective thermal conductivity.

Table 6.10 and Figure 6.11 show the analysis performed on the results of the three equations and three solid calculation methods. Both hypothesis 1 and 2 gave stable results for all methods. As can be noticed from Table 6.10, negative values for the relation of moisture with calcium carbonate (hypothesis 3) were derived, which is physically impossible. In these cases, the derived moisture values for calcium carbonate are not reliable. The best results are obtained for hypothesis 2, because it delivers the smallest

average error and smallest maximum error with the smallest number of parameters, i.e. implying that limestone does not contain moisture. Furthermore in general the best results were obtained with the geometric method for the calculation of the solid thermal conductivity. The difference between the different solid conductivity calculation methods is around 0.3%. Therefore the influence is limited and all three equations could be used. The regression coefficient for gypsum is in the line with the value found in literature for the sorption and desorption of water. Thomas (2002) for instance gives a moisture content of 3% m/m, a value confirmed by Belmiloudi and Le Meur (2005).

## 6.7 Application to thermal conductivity at elevated temperature

In the previous sections the thermal conductivity at ambient temperatures were analysed. In this section, the developed method is used for the determination of the thermal conductivity during fire, i.e. for elevated temperatures. Therefore first the reactions during fire are described. The second part will address the comparison between literature and calculations.

### 6.7.1 Decomposition reactions

This section will describe the decomposition reactions within gypsum plasterboard during fire. The composition of the plasterboards is described in Section 6.5. The composition of gypsum plasterboard has influence on the thermal conductivity, but also will introduce several different decomposition reactions, which are the result of the decomposition of the different substances in the gypsum plasterboard. Calcium sulphate dihydrate will decompose to calcium sulphate hemihydrate at temperatures above 145°C, while hemihydrate will become anhydrite at temperatures above 200°C. Calcium carbonate will react at 800 degrees Celsius to calcium oxide and carbon dioxide. Calcium sulphate anhydrite dissociates at 1450°C.

Based on the presence of these phases the following reactions can therefore be expected up to 1000°C;



The decomposition reactions are endo-thermal reactions. This is one of the reasons that gypsum plasterboard is used for fire protection, since it can absorb energy of the fire. Table 6.11 summarizes the reaction temperatures which is needed for the reactions. One should notice that the mentioned temperatures are experimental conditions, e.g. by the heating rate, nitrogen or air atmosphere and impurities (Dantas et al., 2007; Elbeyli

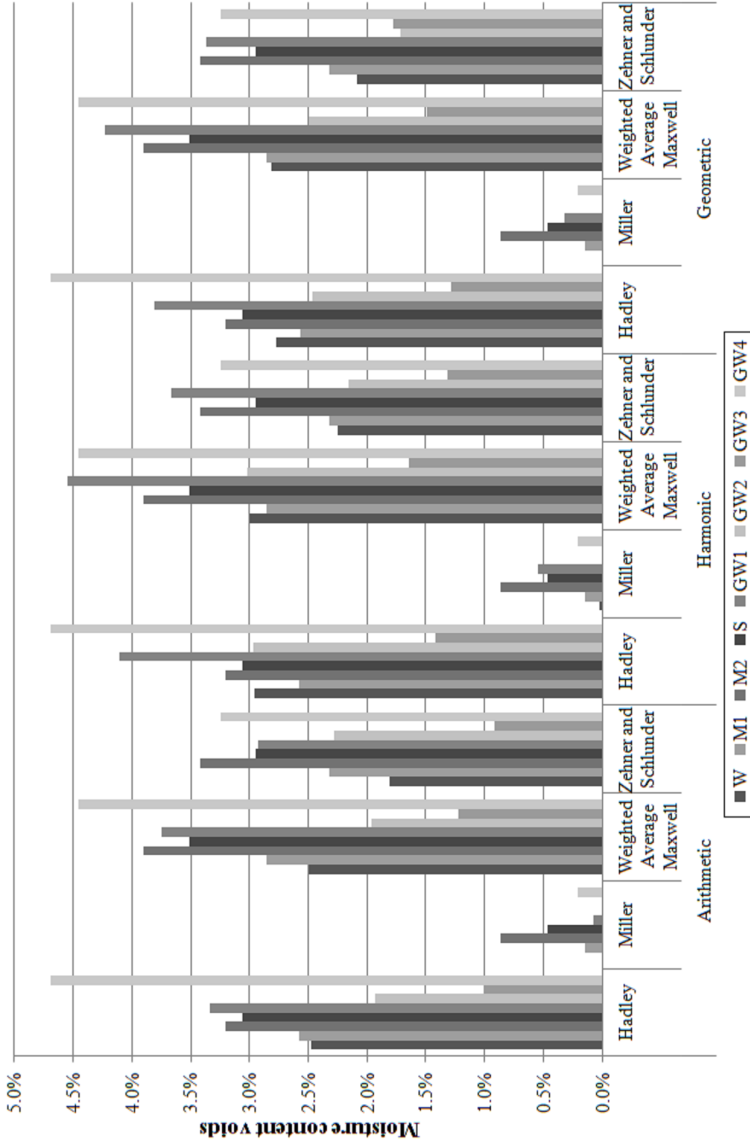
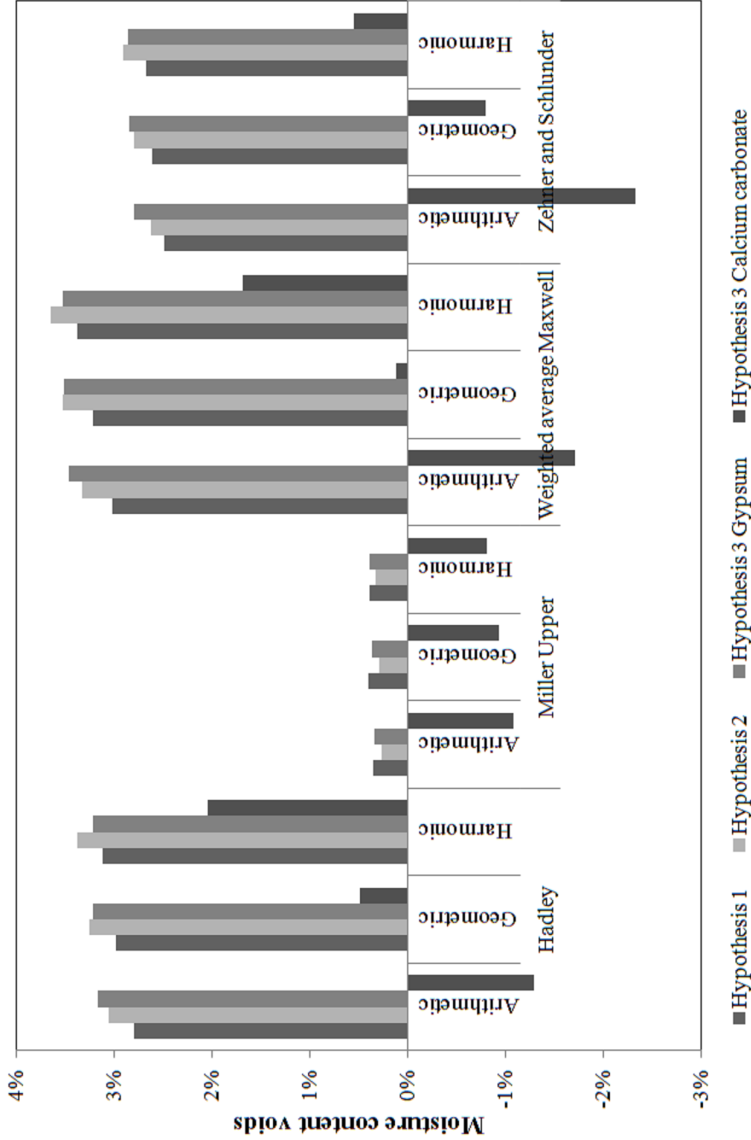


Figure 6.10: Derived moisture content needed to fit the theoretical and experimental values.

**Table 6.10:** Regression analysis of moisture content, in order to investigate its dependence on the chemical composition of the gypsum plasterboards with M being the mass water on mass solid/gypsum/calciumcarbonate, avr the average error and max being the maximum found error (WaM = Weighted average Maxwell, Had = Hadley (1986), Z-S = Zehner and Schlünder (1972) and Mil = Miller (1969) Upper).

Equation	Method	Hypothesis 1			Hypothesis 2			Hypothesis 3			
		$M_{solid}$	avr	max	$M_{gypsum}$	avr	max	$M_{gypsum}$	$M_{carbonate}$	avr	max
WaM (Eq. (6.18))	Arithmetic	3.02%	0.89%	1.80%	3.33%	0.71%	1.76%	3.46%	-1.71%	0.68%	1.70%
WaM (Eq. (6.18))	Geometric	3.22%	0.81%	1.73%	3.52%	0.67%	1.66%	3.51%	0.11%	0.67%	1.66%
WaM (Eq. (6.18))	Harmonic	3.37%	0.74%	1.73%	3.65%	0.73%	1.63%	3.52%	1.68%	0.67%	1.69%
Had (Eq. (6.20))	Arithmetic	2.79%	0.79%	1.91%	3.06%	0.63%	1.73%	3.17%	-1.30%	0.65%	1.69%
Had (Eq. (6.20))	Geometric	2.98%	0.71%	1.71%	3.25%	0.68%	1.64%	3.21%	0.49%	0.65%	1.65%
Had (Eq. (6.20))	Harmonic	3.12%	0.66%	1.70%	3.38%	0.78%	1.61%	3.22%	2.04%	0.66%	1.68%
Z-S (Eq. (6.25))	Arithmetic	2.48%	0.65%	1.56%	2.62%	0.64%	1.42%	2.80%	-2.33%	0.57%	1.34%
Z-S (Eq. (6.25))	Geometric	2.61%	0.64%	0.89%	2.79%	0.56%	1.32%	2.85%	-0.80%	0.55%	1.29%
Z-S (Eq. (6.25))	Harmonic	2.67%	0.65%	1.35%	2.91%	0.56%	1.29%	2.86%	0.55%	0.55%	1.30%
Mil (Eq. (6.16))	Arithmetic	0.35%	0.29%	0.51%	0.26%	0.22%	0.60%	0.34%	-1.09%	0.20%	0.52%
Mil (Eq. (6.16))	Geometric	0.40%	0.28%	0.46%	0.29%	0.22%	0.57%	0.36%	-0.94%	0.20%	0.50%
Mil (Eq. (6.16))	Harmonic	0.38%	0.28%	0.49%	0.32%	0.25%	0.54%	0.38%	-0.81%	0.23%	0.47%



**Figure 6.11:** Results for the three hypotheses. Hypothesis 1; moisture content depends on the total mass of the solid. Hypothesis 2: moisture content depends on the mass of the gypsum and hypothesis 3: the moisture content depends on the masses of the gypsum and the limestone.

**Table 6.11:** Reaction temperatures of the different components according to <sup>a</sup> Thomas (2002) and <sup>b</sup> Ghazi Wakili et al. (2007).

Reaction	Temperature
Eq. (6.31)	100-120 <sup>a</sup> 154 <sup>b</sup>
Eq. (6.32)	210 <sup>a</sup> 174 <sup>b</sup>
Eq. (6.33)	761 <sup>b</sup>

**Table 6.12:** Heat needed for and volume changes during dehydration reactions with  $\Delta H_{f0}$  being the formation heat of substances (kJ/mol),  $\omega$  being the molar volume ( $\text{cm}^3/\text{mol}$ ) and  $\omega_0$  being the molar volume of the reactant ( $\text{cm}^3/\text{mol}$ ) (The negative values are the number of moles of species which react).

	$\text{CaSO}_4 \cdot 2\text{H}_2\text{O}$	$\rightarrow$	$\text{CaSO}_4 \cdot 0.5\text{H}_2\text{O}$	$+$	$1.5\text{H}_2\text{O}$	$\Delta$
$\Delta H_{f0}$	-1 · -2022.6		-1574.6		$1.5 \cdot -286$	= 19.0
$\omega$	-1 · 74.54		53.33		$\frac{3}{2} \cdot 18$	
$\omega/\omega_0$	-1		0.715		0.362	= 0.077
	$\text{CaSO}_4 \cdot 0.5\text{H}_2\text{O}$	$\rightarrow$	$\text{CaSO}_4$	$+$	$0.5\text{H}_2\text{O}$	$\Delta$
$\Delta H_{f0}$	-1 · -1574.6		-1424.6		$0.5 \cdot -286$	= 7.0
$\omega$	-1 · 53.33		53.33		$0.5 \cdot 18$	
$\omega/\omega_0$	-1		1		0.169	= 0.169
	$\text{CaCO}_3$	$\rightarrow$	$\text{CaO}$	$+$	$\text{CO}_2$	$\Delta$
$\Delta H_{f0}$	-1 · 1207.0		-636.0		-393.5	= 450.5
$\omega$	-1 · 37.07		16.76		22160	
$\omega/\omega_0$	-1		0.452		597.8	= 597.3

et al., 2003; Sebbahi et al., 1997). The previously described reactions are a simplification of decomposition system. Wirsching (2005) described the system in more detail.

The dehydration reactions also result in volume changes of the material due to the different specific density of the phases. Table 6.12 show the volume changes of important reactions within a gypsum plasterboard during heating. The first line of these blocks is the reaction. The second line is the volume of the reaction (in  $\text{cm}^3/\text{mol}$ ). The third line gives volume for the reaction of 1  $\text{cm}^3$  of dehydration reactant. This line also reveals the volume expansion on percent base. For instance the dehydration of dihydrate leads to shrinkage of the amount of solids with 28.5%, so an increase of void fraction. The negative values for the amounts in Table 6.12 are the number of moles of species reacting. The assumed reaction temperatures in the model are 145°C for the dihydrate-hemihydrate conversion, 200°C for the hemihydrates-anhydrite conversion and 800°C for the calcium carbonate reaction.

**Table 6.13:** Starting composition of the plasterboard at 20°C for simulation of the thermal conductivity underlying Figure 6.12 and Figure 6.13.

Parameter	Value
Bulk density	732 kg/m <sup>3</sup>
Moisture content	3.0 % m/m gypsum
Composition	90 % gypsum and 10 % calcium carbonate
Gypsum	642 kg/m <sup>3</sup>
Calcium carbonate	71 kg/m <sup>3</sup>
Moisture	19 kg/m <sup>3</sup>

### 6.7.2 Model compared to experimental data.

The thermal conductivities can now be computed as the composition of the system is known for all temperatures. Figure 6.12 shows the comparison of the results of the three-phase system with the experimental results of Mehaffey et al. (1994). The used properties of the gypsum plasterboard of Mehaffey et al. (1994) and other important properties are presented in Table 6.13. Five temperature-ranges can be distinguished in Figure 6.12. At the boundaries of these temperature-ranges the dehydration/decarbonation reactions take place, which will change the chemical composition of gypsum plasterboard. Figure 6.13 shows these changes in the composition during heating. The thermal conductivity is simulated with the Zehner and Schlunder equation with a shape-factor ( $C$ ) of 5 and an initial moisture content of 2.8% on the gypsum mass is used. This is based on the result from Section 6.6. The equation of Zehner and Schlunder is used because it depends on a few parameters only. Furthermore the thermal conductivities of the solid and fluid phases are assumed to be equal to the data in Table 6.5, so the thermal conductivities of the individual solid phases are assumed to be constant, i.e. not a function of temperature. Although in reality the thermal conductivity of the composite will slightly change due to changes in density and composition. Also the thermal expansion of the solids is ignored. Upon heating, the solids expand, which reduces the void fraction and the occurrence of complex cracking patterns in case the body is restrained.

Notwithstanding these and other simplifications, it can be seen from Figure 6.12 that the simulated value have a good fit with the experimental value obtained from literature. The raise in thermal conductivity beyond 850°C in the experiments is probably caused by shrinkage cracks in the material. Due to cracks the air flows through the cracks more easily, and hence increasing the apparent thermal conductivity. This system change is not dealt with by the present model.

### 6.7.3 Influence composition and moisture content

This section deals with the effective thermal properties at elevated temperatures with a special focus on the influence of composition and moisture content. All materials in this section have a bulk density of 732 kg/m<sup>3</sup> (including moisture at room temperature). Figure 6.14-6.16 show the specific heat, volumetric enthalpy and thermal conductivity, respectively. Figures 6.14(a), 6.15(a) and 6.16(a) show the effect of the calcium carbonate content, while Figures 6.14(b), 6.15(b) and 6.16(b) show the effect of the moisture. The presence of calcium carbonate decreases the first peaks in the specific heat slightly

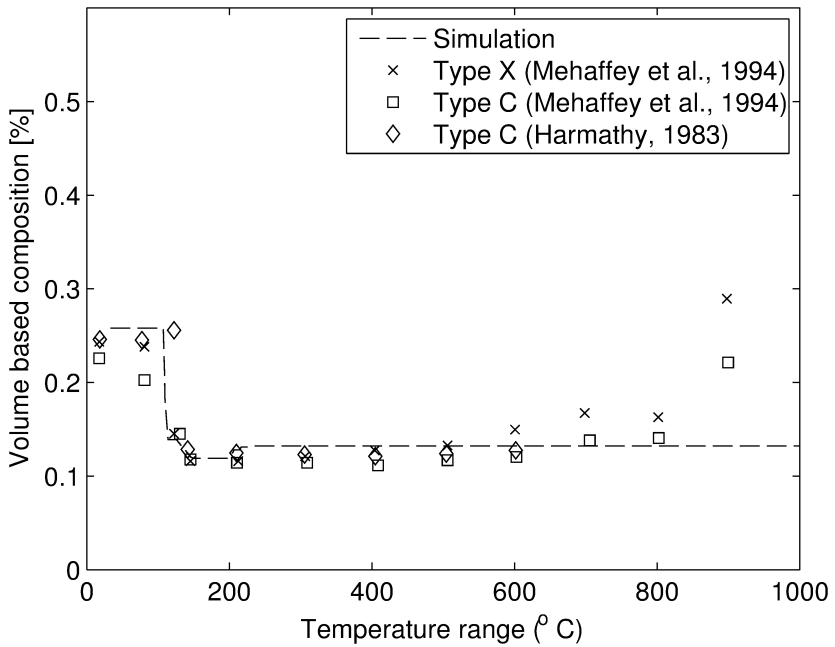


**Figure 6.12:** Simulated thermal conductivity according to the proposed model (thin line) and experimental thermal conductivity (Mehaffey et al., 1994).

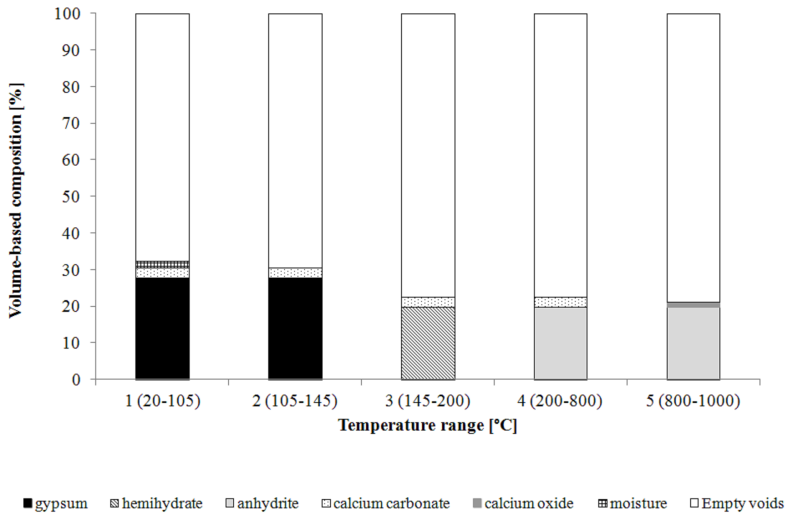


**Figure 6.13:** Graphical representation of the volumetric chemical composition of the gypsum plasterboard during heating.

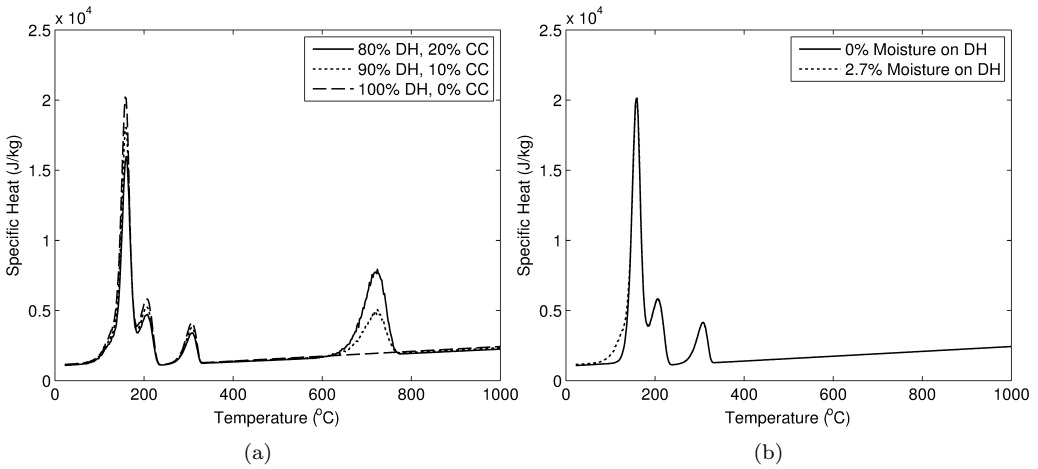


**Figure 6.14:** The effect of (a) mass composition and (b) moisture on the specific heat of the material.

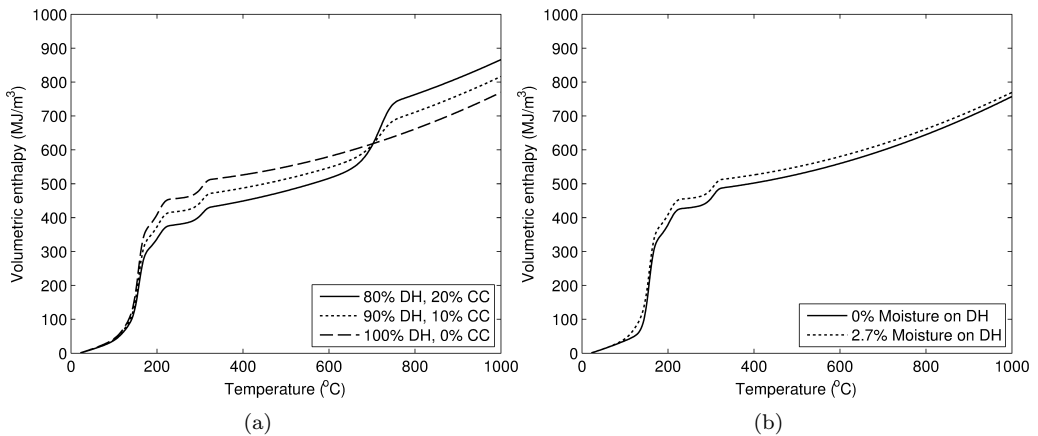


**Figure 6.15:** The effect of (a) mass composition and (b) moisture on the volumetric enthalpy of the material.

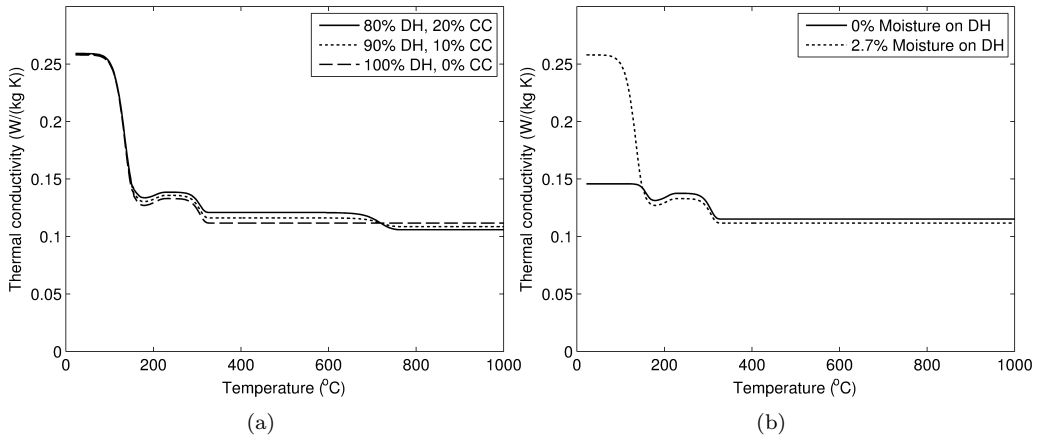


**Figure 6.16:** The effect of (a) mass composition and (b) moisture on the thermal conductivity of the material.

and add an additional peak around 700 °C, which is caused by the degradation of calcium carbonate to calcium oxide and carbon dioxide (Eq. (6.33)) (Figure 6.14(a)).

The influence of the calcium carbonate content on the volumetric enthalpy depends on the temperature range (6.15(a)). Until the degradation temperature of calcium carbonate, the volumetric enthalpy decreases with increasing calcium carbonate content, while above this temperature the volumetric enthalpy increases with increasing content. The explanation is the amount of heat needed for the degradation reaction. Depending on the temperature range one is interested in, the calcium carbonate content needs to be high or low to have the favourable volumetric enthalpy. For instance the fire department will favour to have the optimal properties up to 300 °C and prefers a high volumetric enthalpy and so low calcium carbonate content.

Similar to the volumetric enthalpy, the effect of calcium carbonate on the thermal conductivity (Figure 6.16(a)) depends on the temperature range of interest. Up to 650 °C, the increase of the calcium carbonate content leads to an increase in the thermal conductivity. After 650 °C, the increase of the calcium carbonate content leads to a lower thermal conductivity. The presence of moisture (Figure 6.14(b)) leads to an earlier rise of the specific heat due to the evaporation of water.

The moisture content has a slight influence on the volumetric enthalpy. The presence of moisture will increase the volumetric enthalpy at the earlier phase of heating. As can be noticed from Figure 6.15(b) the difference in volumetric enthalpy between the board with 2.7% and without moisture becomes smaller at increasing temperatures.

The thermal conductivity is influenced mostly at room temperature by the moisture content. After the evaporation of the moisture, the thermal conductivity becomes comparable as can be noticed from Figure 6.16(b).

Figure 6.17 shows the effect of the bulk density of the gypsum plasterboard on the different effective thermal properties, assuming boards with 100% dihydrate content and 0% moisture present in the board. The specific heat is equal for all boards equal, which is

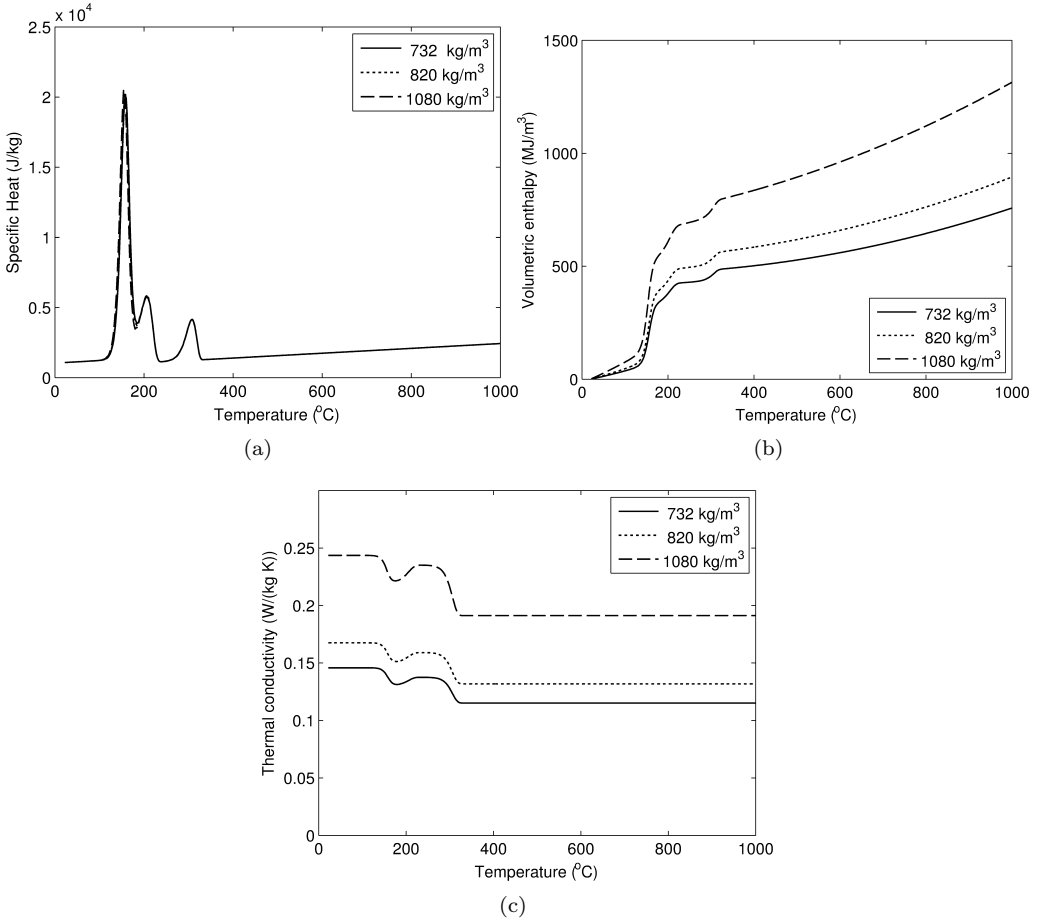


**Figure 6.17:** The effect of the density of the board (100% dihydrate and 0% moisture) on the (a) Specific heat (b) enthalpy and (c) thermal conductivity.

logically since mass-component in the unit of specific heat. Both the volumetric enthalpy and the thermal conductivity increase with increasing bulk density of the board. The increase in thermal conductivity can be explained since, the board will contain more solid material at higher density, which is the main conductor in a porous medium.

## 6.8 Summary/Conclusion

The thermal conductivity of gypsum plasterboard up to a temperature of 105°C can be described best by a three-phase system as first introduced by Somerton et al. (1974). This method requires information about the thermal conductivities which are provided by two-phase systems and the saturation of the voids. The two two-phase systems govern the cases with no saturation and full saturation of the voids.

For the underlying two-phase systems the Zehner and Schlunder equation met shape-factor ( $C$ ) of 5 yields good results. Furthermore, a moisture content of 2.8 % moisture on the mass of the gypsum should be used in order to adjust the thermal conductivity of the board due to the effect of moisture. Using this moisture content of 2.8% and the equation of Zehner and Schlunder with  $C = 5$  and Somerton, measured values for the thermal conductivity of several plasterboards from literature up to 105°C can be predicted excellently. This amount of moisture content is in line with the values reported in literature, and here it appears to depend only on the gypsum content of the solid phase. For more elevated temperatures, the two-phase equations (air/solid) also proves to be useful, when one takes account of the appropriate changes in the type of solid (by dehydration and decarbonation) and related volume (void fraction) changes.

Furthermore it was noticed that the density, the moisture content and the mass composition of the gypsum plasterboard has an influence on its effective thermal properties. Depending on the desired properties the board can be tailored by modifying the moisture and calcium carbonate content. Therefore it is important to also to define the temperature range in which this desired property is requested, since the degradation reactions has an influence on the properties.

## Stabilization/solidification\*

### 7.1 Introduction

In the Netherlands, there is a large demand for primary construction materials. At the same time, many locations in the Netherlands are contaminated and need to be remediated according to the national environmental laws (BBK, 2007; WBB, 1986). Since the amendment to the National Waste Management plan in 2005, immobilisation is considered to be equivalent to remediation of waste (LAP, 2005). Immobilisation of contaminated soil can be a partial solution for both needs. Immobilisation also fits the sustainable building concept, because waste materials are re-used, so less primary construction material is needed. Immobilisation is a technical operation, in which the physical and/or chemical properties of a waste is changed in such manner that the distribution of contaminants by leaching, erosion and dispersion is significantly reduced (CUR, 1997). Three forms of immobilisation can be distinguished namely, chemical, thermal and 'cold' immobilisation. The so-called 'cold' immobilisation is a technical process in which contaminants are covered by inorganic (cement) or organic (bitumen) binders. In case of chemical immobilisation, poorly soluble compounds are formed, which avoid that the contaminants can leach out to the environment. In this chapter, immobilisation is performed with hydraulic binders (slag cement, quicklime and hemihydrate). Two fixation methods are applied using these binders namely, physical fixation due to low diffusion through the dense cement stone and chemical fixation by incorporation in the cement gel and formation of poorly soluble compounds (CUR, 1997).

For this chapter, the Soil Quality Decree (BBK, 2007) is the most relevant Dutch regulation. This decree describes the requirements from environmental perspective. It distinguishes two categories namely soils and dredging sludges, and building materials. Soils and dredging sludges are defined as materials consisting of mineral particles with a maximum particle size of 2 millimeter and a maximum content of organic matter up to the amount which is present in nature. Furthermore the presence of shells and gravel with size of 2 to 63 millimeter is allowed, when these particle are naturally present. The decree regulates the application of soils and dredging sludges and therefore defines requirements to composition. There are three limits distinguished namely, background limit, the limit for the application in living area and the limits for application in industrial areas. In order to compare the measured composition of a soil with these limits, the measured value needs to be corrected for the physical parameters of the soil (e.g. the amount of lutum (small particles) and organic matter). The correction equation (RBK,

---

\*Parts of this chapter were published elsewhere (De Korte and Brouwers, 2009b) and have been updated with changes in legislation (BBK, 2007)

**Table 7.1:** Correction parameters for the composition values of soils and dredging sludges (Eq. (7.1)).

Component	A	B	C
Antimony	1	0	0
Arsenic	15	0.4	0.4
Barium	30	5	0
Beryllium	8	0.9	0
Cadmium	0.4	0.007	0.021
Chromium	50	2	0
Cobalt	2	0.28	0
Copper	15	0.6	0.6
Mercury	0.2	0.0034	0.0017
Lead	50	1	1
Molybdenum	1	0	0
Nickel	10	1	0
Thallium	1	0	0
Tin	4	0.6	0
Vanadium	12	1.2	0
Zinc	50	3	1.5
Organic compounds	0	0	1
Other compounds	1	0	0

2007) reads;

$$G_{cor} = G_{meas} \frac{A + 25B + 10C}{A + B \cdot m_{lutum} + C \cdot m_{om}} \quad (7.1)$$

with  $G_{cor}$  the corrected value,  $G_{meas}$  the measured composition of the soil, A, B and C the correction parameters (Table 7.1),  $m_{lutum}$  the mass percentage of mineral parts with a diameter smaller than 2  $\mu\text{m}$  based on dry material and  $m_{om}$  the mass percentage of the organic matter based the mass of the dry material. In Section 7.2, the equation has been applied for the correction of the composition for the applied soils.

The second category are building materials, which are defined by BBK (2007) as materials with a cumulative mass percentage of silicium, calcium and aluminate higher than 10 % in their applied usage with exception of soils, sledging sludge, metallical aluminates and window glazing. The BBK (2007) divides building materials into three different categories:

1. Shaped building materials.
2. Non-shaped building materials without insulation management control (Dutch: IBC) measures.
3. Non-shaped building materials that need IBC-measures, termed an IBC-building material.

To distuigh if a building material belongs in the shaped group, the following requirements need to be satisfied:

**Table 7.2:** Maximum composition values organic parameters for building materials (RBK, 2007).

Parameter	Maximum value (mg/kg dm)
Aromatic substances	
Benzene	1
ethylbenzene	1.25
toluene	1.25
xylene (sum)	1.25
phenol	1.25
Polycyclic aromatic hydrocarbons (PAKs)	
Naphthalene	5
Phenanthrene	20
Anthracene	10
fluoranthene	35
Chrysene	10
Benzo(a)anthracene	40
Benzo(a)pyrene	10
Benzo(k)fluoranthene	40
Indeno (1.2.3cd) pyrene	40
Benzo(ghi)perylene	40
PAKs (sum)	50
Other parameters	
PCBs (sum)	0.5
mineral oil	500
Asbestos	100

**Table 7.3:** Maximum emission limits for building materials (RBK, 2007).

Parameter	Shaped ( $E_{64d}$ in $\text{mg}/\text{m}^2$ )	Non-shaped ( $\text{mg}/\text{kg}$ d.s.)	IBC ( $\text{mg}/\text{kg}$ dm)
Antimony (Sb)	8.7	0.32	0.7
Arsenic (As)	260	0.9	2
Barium (Ba)	1,500	22	100
Cadmium (Cd)	3.8	0.04	0.06
Chromium (Cr)	120	0.63	7
Cobalt (Co)	60	0.54	2.4
Copper (Cu)	98	0.9	10
Mercury (Hg)	1.4	0.02	0.08
Lead (Pb)	400	2.3	8,3
Molybdenum (Mo)	144	1	15
Nickel (Ni)	81	0.44	2.1
Selenium (Se)	4.8	0.15	3
Tin (Sn)	50	0.4	2.3
Vanadium (V)	320	1.8	20
Zinc (Zn)	800	4.5	14
Bromide (Br)	670	20	34
Chloride (Cl)	110,000	616	8,800
Fluoride (F)	2,500	55	1,500
Sulphate ( $\text{SO}_4$ )	165,000	1,730	20,000

1. The smallest element in the material should have a volume of at least  $50 \text{ cm}^3$ .
2. The material needs to be durable shape retaining. A building material is durable shape retaining when during the 64-days diffusion test according to NEN 7375 less than  $30 \text{ g}/\text{m}^2$  loss of mass is measured.

When a building material does not fulfil these requirements, it is automatically considered as non-shaped. If the materials cannot be applied without isolation measures, they belong to the non-shaped IBC building materials. This depends on the composition and emission limits. The composition limits for the organic parameters are the same for all three categories building materials and are presented in Table 7.2. The emission limits depend on the category of the building material and are given in Table 7.3. As one can notice from Table 7.3 the limits have different unit for shaped and non-shaped materials, since the emission tests differ. For non-shaped materials, the emission is determined with the column test (NEN 7373 or NEN 7383) or the availability test (NEN 7371). For shaped materials, the emission is determined by the 64 days diffusion test (NEN 7375). The successful production of a non-shape retaining building material using contaminated dredging sludge, slag cement and lime was presented by Brouwers et al. (2007). Shape-retaining materials need to have a volume of at least  $50 \text{ cm}^3$  and maximum weight loss of  $30 \text{ g}/\text{m}^2$  during the diffusion test (BBK, 2007). An additional problem with the immobilisation of soil is the possible presence of humus within the soil. Humus can retard the hydration of cement and can have a negative influence on the characteristics of a mix. The immobilisates need to be able to replace products which are made from primary

raw material. Therefore, the immobilisates need to fulfil, besides the leaching limits, the same requirements as products based on primary materials. Furthermore the addition of the soil to the cement bounded product is only allowed by Dutch Regulation (BBK, 2007), when the soil is functional part of the material/concrete. Therefore the soil need to replace primary material. In this chapter, as an example, a material to be used in a mega/lego block is produced, at least a compressive strength of 25 N/mm<sup>2</sup> is required. These mega/lego blocks are used as separation walls in concrete factories for resources and storing locations to separate different kind of resources, soil and rubble.

In addition, the immobilisate needs to represent a financially feasible solution, which means that the profit on producing the immobilisate must be the same or better than that of the primary product. Furthermore, this production of the immobilisates should be possible on a large scale. So, financially feasible solutions and production on a large scale are both important criteria for the design of the mix. The research consists of two parts: the main experiment and an additional experiment.

The main experiment is focused on the immobilisation of two soils. One soil is contaminated with lead and cadmium, while the other soil is contaminated with arsenic, chromium, copper, lead, nickel, zinc and mineral oils. In the additional experiment, the influence of humus on the immobilisation process is studied.

Both soils are extracted from contaminated sites within the Netherlands and are representative for the soil types common in the Netherlands. One of the soils is selected because it has a high organic matter, which is common in certain regions of the Netherlands. It is known that organic matter has an influence on the hydration of binders (Chen and Wang, 2006). The first step is to characterize the soils both physically (particle size distribution, dry matter) and chemically (chemical composition). This characterization is described in Section 7.2.

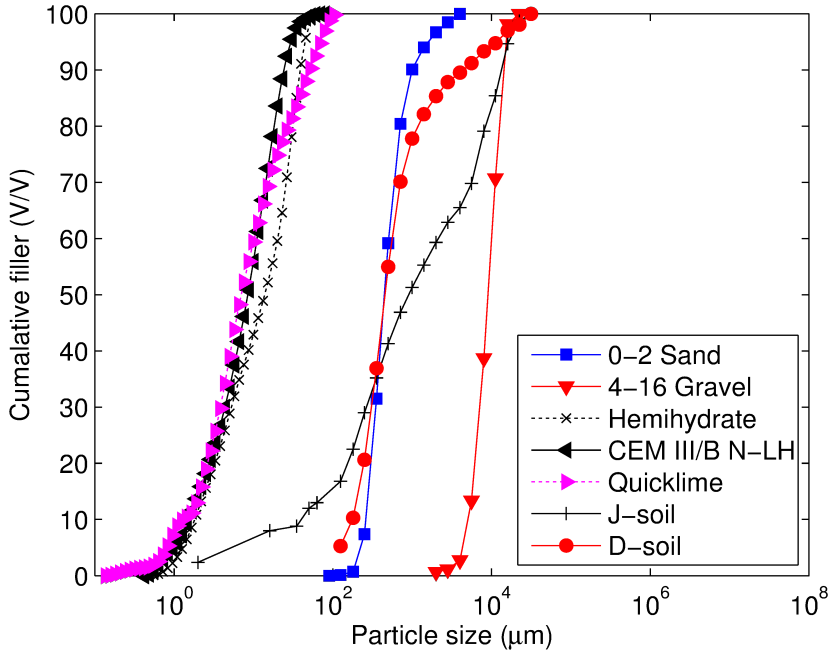
The chemical composition and especially the contaminants of the soils have an influence on the choice of the binders. Therefore Section 7.3 describes, based on a literature research, the choice of two binder combinations and two binder amounts for the immobilisation of the soils. This selection aims to provide the best fit between contaminants and the stabilization/solidification potentials of the binders.

Using the selected binder, a first series of exploratory tests are performed in order to identify the possible problems of the chosen binders (Section 7.4). The next step is the determination of the water demand of the mixes (Section 7.5.1). This is needed because a too high water/binder ratio has a negative influence on the strength of the product, but a too low water/binder ratio will result in problems during mixing. The results of this determination have been used to modify the mix design for the mortar tests (Section 7.5.2). The mortar tests consist of test on compressive strength, tensile splitting strength, leaching of contaminants and financial feasibility. Subsequently, based on the results of the mortar tests, the final binder combination is chosen. This binder combination is used for the production of the final concrete mix. In this mix also a coarse aggregate is added in order to improve the performance. These concrete mixes are tested on compressive strength, tensile splitting strength, leaching and financial feasibility (Section 7.7).

Finally, Section 7.8 gives the financial analysis or economics of all mixes made during the research. The major input variables for this research are the physical and chemical characterisations of the used soils. The main output variables are the compressive and tensile splitting strength, leaching of contaminants, the financial feasibility and possibilities of

**Table 7.4:** Physical and chemical characterization of applied soils.

Parameter	D-soil	J-soil
Dry matter (dm)	94.8 % m/m	63.6 % m/m
Organic matter (H)	2.4 % dm	19.0 % dm
Lutum (L)	7.9 % dm	2.4 % dm
CaSO <sub>4</sub>	1.6 % dm	17.0 % dm

**Figure 7.1:** Particle size distribution of the applied soils, binders and aggregates.

large scale application of the findings in practice.

## 7.2 Materials and methods

### 7.2.1 Materials

Two soils are used within this research. The physical characteristics of both soils, henceforth named D- and J-soil, are presented in Table 7.4 and their particle size distribution is presented in Figure 7.1. The D-soil is poor in humus, clay-containing and sandy soil. The J-soil is a humus rich, clay containing and sandy soil and comes near to a peat soil. Both soils are common soil types in the Netherlands.

Besides the physical characteristics, the environmental characteristics are important. The methods for determining when a material may be used are different for soil and shaped materials. The determination of the leaching, the leaching limits and the contaminant concentration limits differ for these two categories. For soils, the leaching is determined using a column test, which is described in the standard NEN 7373.

In this research a shaped material is produced. For a shaped material, the leaching is measured by the diffusion test, which is described in standard NEN 7375. For the mix design, only the composition is used, because the composition is a measure for the availability of heavy metals for leaching. Since the calculation methods differ for both soils and shaped materials, a direct comparison of the emission of soil and emission of shaped product is not possible. Therefore the emission is very difficult to use for the mix design. As mentioned in Section 7.1, three limits are available for the composition of soils and dredges depending on purposed application namely, the background limit, the limit for application in living areas and the limit for application in industrial areas. Furthermore it was mentioned in Section 7.1 that the measured composition of the soil needs to be corrected depending on the physical parameters of the soil (e.g. the amount of lutum (small particles) and organic matter) in order to be able to compare with legal limits. This correction is done using Eq. (7.1) and correction parameters A, B and C according to Table 7.1. In Tables 7.5(a) and 7.5(b) the composition of soils are described as well as the modified composition limits. The D-soil only contains one pollutant, which renders it Not-Applicable as such: cadmium is above all three limits. The J-soil contains arsenic, cadmium, chromium, copper, lead, zinc and mineral oil levels that are above all three limits. These pollutants render this soil Not-Applicable as well. In this research a third soil is composed, which consists of half J-soil and half sand with particles in the range of 0-2 mm (0-2 sand). This soil has a lower humus level compared to J-soil and is used for the additional experiments in order to measure the effect of humus on the hydration and immobilisation. This soil is termed  $J\frac{1}{2}$ -soil.

Besides the soils, some other materials are used, like binders and aggregates. The used binders were slag cement, quick-lime and hemihydrate. The slag cement used for this research was a CEM III/B 42.5 N LH. Table 7.6 describes the physical properties, chemical composition and strength development of this slag cement (ENCI, 2006). Table 7.7 shows the physical properties of the hemihydrate, while Table 7.8 shows those of quick-lime. Figure 7.1 shows the particle size distribution of the different binders and the two aggregates used within this research.

### 7.2.2 Test methods

The mortar mixtures are mixed using a Hobart mixer, while full concrete mixtures are mixed using a force mixer. The samples are vibrated on medium speed on a vibration table, in order to reduce the air content. All samples are demould after 24 hours and stored under water of  $20 \pm 1$  °C.

For the research six test methods are used to evaluate the developed mixes: (1) slump flow, (2) V-Funnel time, (3) compressive strength, (4) tensile splitting strength, (5) capillary absorption and (6) diffusion/leaching. The slump flow, V-Funnel time, compressive strength and tensile splitting strength tests are described in more detail in Brouwers and Radix (2005). In this section the spread-flow test, capillary absorption and diffusion/leaching tests are described.

The spread flow test is a common way to assess the water demand of pastes and mortars. This yields a relation between the relative slump flow ( $\Gamma$ ) and the water/fines ratio of the paste ( $V_w/V_f$ ). The fines are defined here as all particles smaller than 125  $\mu\text{m}$ . The test is executed analogously to Domone and HsiWen (1997) and ordinary tap water is

**Table 7.5:** Contaminant concentration in (a) D-soil and (b) J-soil and legal limits given by RBK (2007) (\* corrected for small particle and organic matter content, Eq. (7.1)).

(a)

Chemical	Measured* [mg/kg]	Legal limits		
		Background [mg/kg]	Living [mg/kg]	Industrial [mg/kg]
Arsenic	22	20	27	76
Cadmium	34	0.60	1.2	4.3
Chromium	43	55	62	180
Cobalt	32	15	35	190
Copper	49	40	54	190
Mercury	0.27	0.15	0.83	4.8
Lead	206	50	210	530
Molybdenum	3.0	1.5	88.0	190.0
Nickel	43	35	39	100
Zinc	285	140	200	720
Mineral oil	49	190	190	500
Sum PAK	2.1	1.5	6.8	40.0

(b)

Chemical	Measured* [mg/kg]	Legal limits		
		Background [mg/kg]	Living [mg/kg]	Industrial [mg/kg]
Arsenic	581	20	27	76
Cadmium	23	0.6	1.2	4.3
Chromium	680	55	62	180
Copper	3070	40	54	190
Mercury	0.29	0.2	1.2	7.0
Lead	7624	50	210	530
Nickel	198	35	39	100
Zinc	20804	140	200	720
Mineral oil	1700	190	190	500
Sum PAK	4.9	1.5	6.8	40.0

**Table 7.6:** Physical properties, chemical composition and standard strength development of CEM III/B 42.5 N LH (ENCI, 2006).

Properties		
Setting time	230	min.
Specific surface	475	m <sup>2</sup> /kg
Specific density	2950	kg/m <sup>3</sup>
Loose bulk density	1050	kg/m <sup>3</sup>
Hydration heat (isotherm)	< 270	J/g
C-value	1.50	-
Composition		
- Chloride level (Cl <sup>-</sup> )	0.05	% m/m
- Na <sub>2</sub> O equivalent	0.6	% m/m
- Portland cement clinker	26	% m/m
- Blast furnace slag	72	% m/m
- Other ingredients	2	% m/m
Standard strength		
- 2 days	12	N/mm <sup>2</sup>
- 7 days	36	N/mm <sup>2</sup>
- 28 days	59	N/mm <sup>2</sup>

**Table 7.7:** Physical properties of the applied hemihydrate FG-101 (Knauf, 2004).

Properties		
Degree of Purity	> 95	%
Bedding amount <sup>†</sup> (Gypsum in 100 ml water)	> 300	g
Water / gypsum factor	< 0.33	
Crystal water	< 6.20	%
Setting time	4-9	min.
pH-value	7-9	
Bulk density	1250-1450	kg/m <sup>3</sup>
Specific density	2720	kg/m <sup>3</sup>
Degree of whiteness	> 40	%

**Table 7.8:** Properties of quicklime.

Component	Notation	[% m/m]
Loss on ignition		2.5
Silicium dioxide	S	1.2
Aluminium oxide	A	0.22
IJzer (III) oxide	F	0.21
Magnesium oxide	M	1.5
Calcium oxide	C	95.3
Free calcium oxide	C	92.7

used as the mixing water in the present research. The relation between  $V_w/V_p$  and  $\Gamma$  is described by;

$$\frac{V_w}{V_p} = E_p \cdot \Gamma + \beta_p \quad (7.2)$$

with  $E_p$  the deformation coefficient, which is the slope of the function, and  $\beta_p$  the water demand. This method is originally developed for fines only (Okamura and Ouchi, 2003), but the same procedure can be applied on mortar mixes with the use of the same Heagermann cone. Besides the determination of relation between relative slump flow ( $\Gamma$ ) and water/fines ratio ( $V_w/V_f$ ), it is also possible to do this for the water/solid ratio. Solids, in this case, are the binders and sand in the mix, i.e. all solids in case of mortars.

The relative slump ( $\Gamma$ ), used in for spread flow test is determined with:

$$\Gamma = \left( \frac{d_i}{d_0} \right)^2 - 1 \quad \text{with} \quad d_i = \frac{d_1 + d_2}{2} \quad (7.3)$$

where  $d_1$  and  $d_2$  are the maximum diameters, rounded off at 5 mm, and  $d_0$  is the base diameter of the Haegermann cone. The capillary absorption is measured, analogous to Brouwers and Radix (2005), Audenaert et al. (2003) and Zhu and Bartos (2003). Prior to the experiment, the concrete cubes (of age 28 days) are dried in an oven at  $105 \pm 5$  °C for 48 h, and cooled down for 24 h at room temperature. Then, the cubes are placed on bars with a diameter of 10 mm, so that the water level is  $5 \pm 1$  mm above the lower horizontal face of the cube. The mass increase of each cube is measured after 0.25, 0.5, 1, 3, 6, 24, 72 and 168 h. Furthermore, the height of the capillary rise is measured on the 4 vertical side faces (in the centre of the side) of each cube. The mean value of each cube,  $H$ , is used for the analysis. There is a linear relation between the capillary rise and the square root of time (Audenaert et al., 2003; Brouwers and Radix, 2005; Zhu and Bartos, 2003):

$$H = H_0 + SI \cdot T^{0.5} \quad (7.4)$$

In this equation  $H$  is the height of the capillary rise,  $H_0$  the intersection with the y-axis [mm],  $SI$  the sorption index [ $\text{mm}/\text{h}^{0.5}$ ] and  $T$  the time (h). The  $SI$  is a measure for the uptake of water by a concrete surface exposed to rain for instance. In Audenaert et al. (2003) it can be found that  $SI$  should be smaller than  $3 \text{ mm}/\text{h}^{0.5}$ .

Finally the leaching of the hardened product is measured by the diffusion test (NEN 7375). The cubes are places in 1 (in case mortar cubes) and 7 litres (in case of concrete cubes) of water of pH 4 using nitric acid. The acid water is replenished after 0.25, 1, 2.25, 4, 8, 16, 36 and 64 days. This water is analysed on the concentration of heavy metals. From this leached amount the leaching can be calculated according to NEN 7375 and BBK. Further details of the followed calculation procedure can be found in De Korte (2006).

### 7.3 Previous research

In this section, previous research will be presented in five subsections: (7.3.1) the use of (contaminated) soil for the production of concrete blocks, (7.3.2) influence of conta-

minations on the immobilisation; (7.3.3) possible binders, (7.3.4) the amount of binder which is needed and (7.3.5) the composition of the binder. This information will serve as a basis for the new mix designs developed and tested here, presented in the next section.

### 7.3.1 The use of (contaminated) soil for the production concrete blocks

This section will focus on the use of (contaminated) soil for the production concrete blocks from the point of the view of the scientific literature. Contaminated soil is used for the production of concrete blocks in several studies. For instance Hago et al. (2007) point out that organic and inorganic wastes can be stabilized by using fly ash, lime, Portland cement or a combination of these materials. This often results in a pozzolanic reaction that prevents or minimizes the release of contaminants into the environment by producing a solid mixture, decreasing surface area for contaminant transport, improving handling characteristics and reducing mobility of the contaminants into a less toxic form. The use of soils in concrete also introduces some challenges. The main challenge is the presence of organic matter in the soil. Organic soils can retard or prevent the proper hydration of binders such as cement in binder-soil mixtures (Hebib and Farrell, 2003). Clare and Sherwood (1954) and Maclean and Sherwood (1962) suggested that the retardation of the hardening of organic soil-cement mixture is due to the retention by the organic matter of the calcium ions, liberated during the hydrolysis of the cement particles. Therefore, only part of the calcium released during hydration is available for the pozzolanic reaction, and this is believed to be the reason for the difficulty encountered in immobilizing organic soils. Another part of the explanation is that the humic acid reduces the pH of the soil, which has an influence on the hydration rate of the binders. This will result in lower strength development in organic-rich soils compared to organic-poor soils.

Another challenge is the fineness of the soils. A very fine soil will lead to high water need (Venkatarama Reddy and Gupta, 2008) and therefore a lower compressive strength. The fine particles are commonly clay particles. Walker and Stace (1997) point out that 5 to 10% cement is sufficient to stabilize soils with clay mineral contents less than 15% to 30% for non-constructive applications. They point out that the mortar compressive strength after 28 days decreases with the increasing clay content. The compressive strength drops from 9 N/mm<sup>2</sup> for 9% (m/m) clay to 5 N/mm<sup>2</sup> for 30-40% (m/m) clay.

For the practical use of soil immobilisation, the concrete blocks need to show sufficient compressive strength, high durability and low leaching of heavy metals. Shan and Mee-goda (1998) show the possibility to produce concrete blocks with soil with compressive strength of more than 25 N/mm<sup>2</sup>. Guettala et al. (2006) have done research on the durability of stabilized earth concrete under both laboratory and climatic conditions exposure. They noted that all treated walls showed no signs of deterioration after 4 years of exposure in real climatic conditions. They used between 5% and 12% (m/m) of binder based on the soil. They found a compressive strength between 15.4 N/mm<sup>2</sup> for 5% (m/m) cement and 21.5 N/mm<sup>2</sup> for 8% (m/m) cement with 4% (m/m) lime. These compressive strengths are close to the required compressive strength in this research. Yin et al. (2007) for instance shows that a contaminated soil from a scrap metal yard with a high amount of heavy metals could be immobilized successfully. The leaching of the treated materials was low, both for the leaching of the crushed materials and for the whole blocks. Yin et al. (2007) showed that stabilization is effective since the amount that is leaching is

very small compared to the amount available according to the composition of the soil. Besides this, the compressive strength reached  $22 \text{ N/mm}^2$  with 50% (m/m) of binder based on the soil.

Based on these results from literature, it could be concluded that contaminated soil could be used for the production of concrete blocks with a compressive strength of  $15\text{--}20 \text{ N/mm}^2$ , high durability and low leaching of heavy metals. In the present research a concrete with compressive strength of  $25 \text{ N/mm}^2$  is aimed at, since this was the requirement of the producer involved in the project.

### 7.3.2 The influence of contaminants on immobilisation

The contaminants' characteristics influence the degree to which immobilisation is possible. Arsenic, lead, chromium and cadmium are soluble in acid environments. Arsenic and lead are amphoteric, which mean that they are soluble in both acidic and basic environments. Immobilisates which are produced using cement have a high pH. This means that some heavy metals are soluble and available for leaching. The leaching behaviour strongly depends on the oxidation number of the metal. Both arsenic and chromium have more than one oxidation number. Chromium (III) is for instance easier to retain than chromium (VI) (Mattus and Gilliam, 1994).

Heavy metals also influence the hydration of cement. Copper, lead and zinc will retard the hydration of cement (Mattus and Gilliam, 1994). Chromium shortens the gel fibres and increases the matrix porosity (Palomo and Palacios, 2003).

The way heavy metals are incorporated in the hardened product by chemical fixation differs from case to case. Cadmium, zinc and arsenic can replace calcium within CSH (Pomiès et al., 2001). Chromium and lead are absorbed on CSH, but nickel cannot be absorbed within the CSH structure (Bonen and Sarkar, 1995). Chromium (III) can replace aluminium within the CAH-structure (Duchesne and Laforest, 2004). Oxyanions like chromate and molybdate can replace sulphate within ettringite (Chrysochoou and Dermatas, 2006; Zhang and Reardon, 2003). The different binders have a different oxide composition and therefore they have a different binding capacity. This means that the most suitable binder can be selected based on the required binding capacities.

### 7.3.3 Possible binder combinations

In this section the feasible binder combinations are described. The first and most known binder is ordinary Portland cement (OPC). Portland cement is suitable for the immobilisation of most heavy metals. Plain blast furnace slag is more suitable for the immobilisation of heavy metals in humus rich soils. The use of slags results in a lower porosity and permeability compared to the use of Portland cement. A lower porosity normally results in a lower level of leaching (Mattus and Gilliam, 1994). However, a major disadvantage of the use of slag is the slower reaction rate. This reaction rate decreases further due to the presence of heavy metals and humic acid. Hence, an initiator could be needed when slags are employed. The main reason is the absence of a calcium source within slag (Chen, 2007). Possible initiators are quicklime, anhydrite and hemihydrate. The advantage of the use of calcium sulphates is the possible formation of ettringite. Ettringite can fill the pores between the soil particles and so decrease the porosity and permeability. A lower porosity will result in a lower level of leaching. Furthermore ettringite can reduce the

**Table 7.9:** Specific densities of employed materials.

Component	Specific density [kg/m <sup>3</sup> ]
Slag cement	2950
Quicklime	3345
Hemihydrate	2700
Mineral fraction D-soil	2736
Mineral fraction J-soil	2679
Sand	2650
Organic Matter	1480

leaching of some heavy metals by chemical fixation, as described in Section 7.3.2.

Portland cement also acts as activator for slag. The combination of Portland cement and slag, i.e. slag blended cement, results in a higher compressive strength and better immobilisation than when plain Portland cement is used.

Another possible secondary binder is pulverized fly ash (PFA), although it is less suitable than blast furnace slag. For the immobilisation of cadmium and copper, PFA is less suitable (Peysson et al., 2005). For chromium, PFA is completely unsuitable, because it appeared that no strength development took place at all (Palomo and Palacios, 2003). PFA combined with Portland cement is suitable for the immobilisation of copper but unsuitable for lead (Thevenin and Pera, 1999). Besides, as PFA reacts slowly, the strength development is slow too. So fly ash can better not be used for the immobilisation of heavy metals.

The combination of calcium sulfoaluminate cement (CSA) and hemihydrate can be used instead of blast furnace slag. In a ratio of 70/30, CSA/Hemihydrate is suitable for all heavy metals except Cr VI. For Cr VI, a ratio of 80/20 is suitable. The combination of CSA with hemihydrate can result in the formation of ettringite. Ettringite can fill the pores between soil particles and therefore results in lower porosity and permeability, and also a lower level of leaching (Peysson et al., 2005). Furthermore ettringite can reduce the leaching of some heavy metals by chemical fixation (Section 7.3.2). A disadvantage of the combination of CSA with hemihydrate is the introduction of more sulphate into the mix. The leaching of this sulphate is also regulated in the Soil Quality Decree, although the legal limits for sulphate leaching is rather high compared to the leaching of other compounds.

#### 7.3.4 Required binder amount

In this section the determination of the amount of binder per m<sup>3</sup> of concrete is described. An amount of 250 kg binder per m<sup>3</sup> concrete mix is currently used for the production of concrete blocks by Dusseldorp Group. According to Axelsson et al. (2002), between 100-200 kg/m<sup>3</sup> is needed for the immobilisation of mud, 150-250 kg/m<sup>3</sup> for peat and 70-200 kg/m<sup>3</sup> for hydraulic filling. Nijland et al. (2005) used 250 kg/m<sup>3</sup> for the immobilisation of contaminated clay. Yin et al. (2007) used 900 kg/m<sup>3</sup> for the immobilisation of contaminated soil from a metal scrap yard. Shan and Meegoda (1998) used 480 kg/m<sup>3</sup> for the production of construction blocks based on soil from Taiwan. Walker and Stace

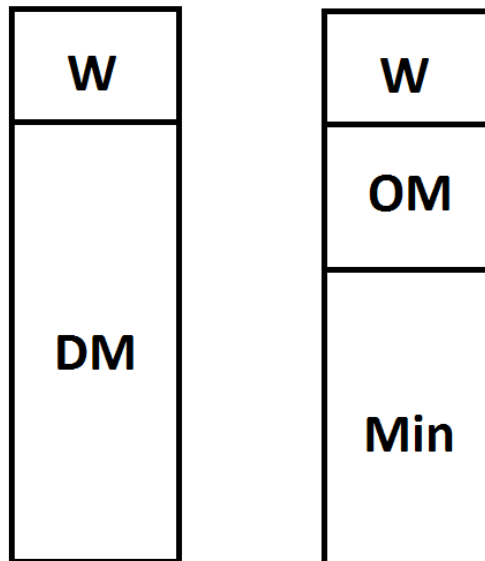


**Figure 7.2:** The composition of the soil, with DM the dry matter, w the water content, OM the organic matter and Min the mineral part.

(1997) used 250 kg/m<sup>3</sup> for soil with less than 15% clay minerals. Guettala et al. (2006) used 150 and 225 kg/m<sup>3</sup> for the production of earth blocks using a sandy-clayed (non-contaminated) soil.

Based on these findings, here also a minimum binder level of 250 kg/m<sup>3</sup> is considered. The binder amount of 350 kg/m<sup>3</sup> is selected as well to overcome the possible negative effects of heavy metals and humus. A binder amount of 500 kg/m<sup>3</sup> is introduced to investigate if the addition of extra binder can neutralize the possible negative effect of large quantities of humus. Hence, in this research, binder amounts of 250, 350 and 500 kg/m<sup>3</sup> are selected.

In order to calculate the mass-based ratio of binder on the dry soil from the required binder per cubic meter soil, the density of the soil and the binder combination need to be known. Both these densities can be calculated using the effective density approach, uniform to Eq. (6.30) for volume-based. The mass-based effective density reads;

$$\rho_e = \frac{1}{\sum \frac{\delta_i}{\rho_i}} \quad (7.5)$$

with  $\delta_i$  the mass-fraction of component  $i$  and  $\rho_i$  the specific density of component  $i$ . This general equation can be also be applied to the soil. In Table 7.9, the mass-fraction of the soils are given. Based on these mass fraction Eq. (7.5) can be rewritten specifically for soils and it reads;

$$\rho_e = \frac{1}{\frac{x_{ds}(1-\delta_{om})}{\rho_{min}} + \frac{x_{ds}\delta_{om}}{\rho_{om}} + \frac{1-x_{dm}}{\rho_w}} \quad (7.6)$$

with  $x_{dm}$  the mass-fraction dry matter in the soil and  $\delta_{om}$  the amount organic matter in the dry matter. These fractions are illustrated in Figure 7.2. Using this equation and the parameters given for the soil in Table 7.9, wet D-soil has an apparent or bulk density of 2422 kg/m<sup>3</sup> and wet J-soil has an apparent density of 1568 kg/m<sup>3</sup>. When volumes binder ( $V_b$ ) and soil ( $V_s$ ) together is unity, the mass-fraction binder on dry soil can be calculated by;

$$\frac{m_b}{m_{s,dm}} = \frac{V_b \rho_b}{x_{ds} V_s \rho_s} \quad (7.7)$$

$$\frac{m_b}{m_{s,dm}} = \frac{m_b}{x_{ds} \left(1 - \frac{m_b}{\rho_b}\right) \rho_s} \quad (7.8)$$

with  $\rho_s$  the apparent or bulk density of the soil (Eq. (7.6)),  $\rho_b$  the specific density of the binder using Eq. (7.5) and Table 7.9. These amounts (250, 350 and 500 kg/m<sup>3</sup>) correspond to 12, 17 and 26 % (m/m) on dry matter of D-soil, while the amount of 350 kg for the J-soil corresponds to 40% and 500 kg to 61% dm.

### 7.3.5 The composition of the binder

This section summarizes possible binder combinations that will be used in this research. The first binder combination is slag cement and quicklime. This ratio is set to 90/10. Brouwers et al. (2007) researched the immobilisation on heavily contaminated (Class 4) dredging sludge. The ratio of 90/10 slag cement/quicklime gave good results. This finding is compatible with Janz and Johansson (2002), who point out that the optimal mix

lies between 60-90% slag cement and 40-10% quicklime.

The choice of a ratio of 60/40 slag cement/hemihydrate is based on the research of Huang (1997). This ratio was confirmed by the research of Peysson et al. (2005). Peysson et al. (2005) indicated that 70% CSA and 30% gypsum is a suitable binder for the immobilisation of most heavy metals. CSA itself also contains calcium oxide and sulphate. Because of that, the levels of calcium and calcium sulphate are higher than at the same ratio of slag cement and hemihydrate. In order to compensate this, here the proportion of hemihydrate is increased to 40%.

## 7.4 Exploratory tests

As a preparation for the main research, some exploratory tests are done to identify possible problems which could arise with the application of soil in concrete mixes.

In these exploratory tests, two mix designs are tested on workability, air-content, compressive strength and leaching. The main difference between the two mix designs was the binder combination. The first combination concerned blast furnace slag cement and quicklime and in the second combination blast furnace slag cement and gypsum are involved. The first tests show that water present within the soil was insufficient for reaching a good workability. Therefore the addition of extra water and superplasticizer is needed and the standard mixtures from literature are modified in order to reach a good workability. Table 7.10 shows the composition of these mixtures made during exploratory tests, as well as the results of the fresh mixes. The tests on hardened concrete show small differences between the two mixtures. Neither of the mixtures fulfill the requirement for the 28 days compressive strength of 25 N/mm<sup>2</sup>. The low compressive strength of both mixtures can be explained by a too high water/binder ratio, but also the particle size distribution of the mixture is not optimal, as one can notice from Figure 7.3. Therefore, the packing of the mix is not optimal, which will result in a lower compressive strength (Reinhardt, 1998). The current particle size distribution (Figure 7.3) is missing particles in the coarser range. Therefore, the mixtures in the pre-research can be characterized as being more a mortar than a concrete. But the required compressive strength is for a concrete. In order to get a concrete a coarser aggregates should be added. The problem of the high water/binder ratio is addressed in the mortar tests (Section 7.5) and water demand analysis (Section 7.6), while the problem of the particle size distribution is tackled in the concrete tests (Section 7.7).

The mixes are also evaluated in regard to their environmental performance. Tables 7.11(a) and 7.11(b) show the calculated emission (based on measurements) according to the Dutch standard NEN 7375. This emission is calculated for the leaching during the diffusion test. The detailed computation procedure can be found in De Korte (2006). The third column of both these tables show the maximum limit of emission according to Dutch legislation (RBK, 2007).

Both tables show that the measured emissions during diffusion-test were lower than the maximum allowed emissions according to the Dutch law (RBK, 2007). The emission of sulphate for D-HH-250v approaches the limits. A high leaching of sulphate is considered negative due to the limitations for the leaching of sulphate according to the Soil Quality Decree. The solubility of gypsum, hemihydrate and anhydrite is relatively high, which results in a high leaching of sulphate. This means that mix with hemihydrate

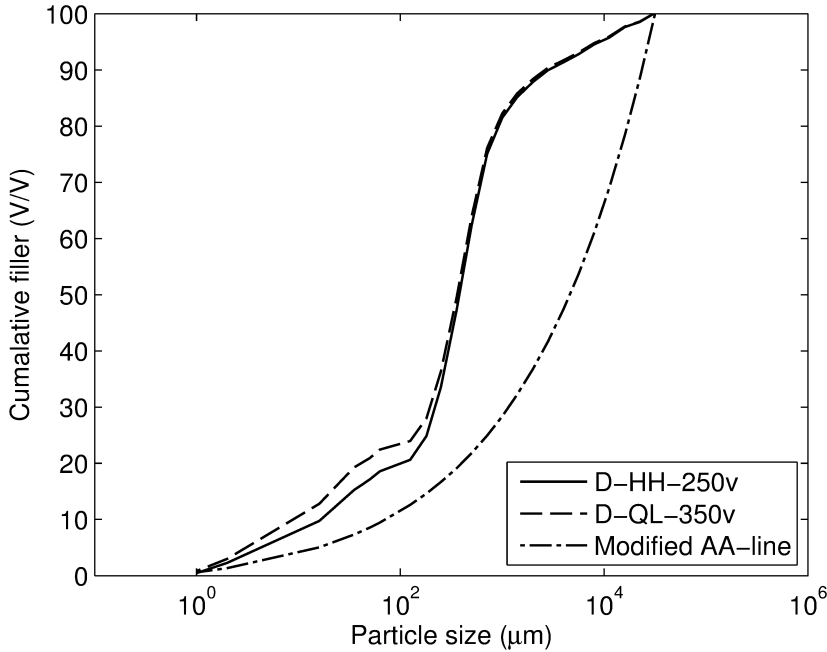


**Figure 7.3:** The cumulative finer function of the mixtures for exploratory tests and the target line, Eq. (7.11) (with  $q = 0.35$ ,  $d_{\min} = 0.5 \mu\text{m}$  and  $d_{\max} = 31.5 \text{ mm}$ ).

**Table 7.10:** Mix designs (in  $\text{kg}/\text{m}^3$ ) and measured properties of concrete cubes ( $150 \times 150 \times 150 \text{ mm}$ ) made for the exploratory research.

	D-HH-250v	D-QL-350v	Unit
Mix design			
- Blast furnace slag cement	193.5	332.8	$\text{kg}/\text{m}^3$
- Quick-lime	-	37.0	$\text{kg}/\text{m}^3$
- Gypsum (Hemihydrate)	129.0	-	$\text{kg}/\text{m}^3$
- Mix water	197.8	282.9	$\text{kg}/\text{m}^3$
- Superplasticizer-solution	0.0	1.5	$\text{kg}/\text{m}^3$
- DD ISM soil dry	1544.6	1324.1	$\text{kg}/\text{m}^3$
- DD ISM soil water	84.7	72.6	$\text{kg}/\text{m}^3$
- Total mass	2149.7	2050.9	$\text{kg}/\text{m}^3$
Hardened properties			
- Density			
- 7 days	2079	-	$\text{kg}/\text{m}^3$
- 28 days	2083	2072	$\text{kg}/\text{m}^3$
- Compressive strength			
- 7 days	12.6	-	$\text{N}/\text{mm}^2$
- 28 days	19.9	20.6	$\text{N}/\text{mm}^2$
- Tensile splitting strength			
- 28 days	2.20	3.14	$\text{N}/\text{mm}^2$

**Table 7.11:** Leaching data (a) D-HH-250v (b) D-QL-350v (in mg/m<sup>2</sup>) and shaped maximum emissions according to RBK (2007).

(a)		
	Measured emission [mg/m <sup>2</sup> ]	Maximum emission [mg/m <sup>2</sup> ]
Sulphate	84 000	165 000
Cadmium	0.5	3.8
Chromium	2.8	120
Copper	2.0	98
Nickel	2.7	8.1
Lead	13	400
Zinc	10	800
Cobalt	1.7	60
Arsenic	8.8	260

(b)		
	Measured emission [mg/m <sup>2</sup> ]	Maximum emission [mg/m <sup>2</sup> ]
Sulphate	7 000	165 000
Cadmium	0.04	3.8
Chromium	0.13	120
Copper	0.04	98
Nickel	0.11	8.1
Lead	0.42	400
Zinc	0.14	800
Cobalt	0.06	60
Arsenic	0.84	260

are less suitable than mix with quicklime. The retention capability of heavy metals is also important for the immobilisates. Quicklime mixes can retain heavy metals better than the hemihydrate mixes. But here it appears that both hemihydrate and quicklime are suitable for retaining heavy metals within the immobilisates (Table 7.11). Both the hemihydrate and quicklime mixes have a sustainable shape retention during diffusion tests.

## 7.5 Mortar experiments

In this section the results of the experiments on mortar are described. The purpose of the mortar test is to solve the problem with the high water/binder ratio found in the exploratory tests by determining the water demand of the mixtures in order to achieve acceptable compressive strength. Therefore, the experiments on mortar are divided into two parts. The first part is the determination of the water demand in order to find the optimal balance between good flowability and low water content in order to achieve a high compressive strength and low leaching properties. The second part concerns the production of mortar cubes (50\*50\*50 mm<sup>3</sup>). The mix used for casting these mortar cubes was based on the results of the water demand part. The compressive strength, capillary absorption and diffusion of these mortar cubes will be determined. The results of the main and additional experiment are incorporated in this section. Section 7.5.3 will address the main findings of the additional experiment. The derived water demands from this sections are used in the mix design of the concrete in Section 7.7.

### 7.5.1 Water demand

The water demand determination is carried out using the slump flow test for the mortar mix. This mortar mix includes binders, soil (fraction that passes the 4 mm sieve) and sand. The soil is sieved in order to make it possible to use a small mortar mixer. The D-soil could be sieved wet, but for the J-soil this is not possible. The J-soil is therefore dried during 24 hours at 105 +/- 5 °C. Before using this soil for the mortar mixes, the amount of water evaporated during drying is re-added, and is mixed with the soil. These soil-water mixes stand for 30 minutes, so the soil can absorb the water. By doing so a wet soil can be simulated, which is closer to the practice since a wet soil is used in the immobilisation process as well.

The mixes are detailed in Tables 7.12 and 7.13. The slump flow is measured for different water/fines ratios (m/m) and with differed amounts of superplasticizer (Glenium 51), based on the mass of fine particles in the mix. The mass of fines is the sum of all particles smaller than 125 µm present in the mix, including the soil. The function of a superplasticizer is to reduce the quantity of water while maintaining the same workability. The relative slump flow is plotted against the water/fines ratio to construct the spread-flow line. The relative slump flow is computed with Eq. (7.3) with  $d_1$  and  $d_2$  as the diameters of the slump flow and  $d_0$  the base diameter of the Haegermann cone. The water demand ( $\beta_p$ ) of a mix is the interception point of the linear regression function based on these results (Okamura and Ouchi, 2003), as shown in Figure 7.4 (see also Section 7.2 and Eq. (7.2)). In Figure 7.5 and Table 7.14, the water demands of mixes for different amounts of superplasticizer are shown.

The different binder types all have their specific water demand. The mixes with slag

**Table 7.12:** Mix designs (in kg/m<sup>3</sup>), fresh and hardened properties (mortar) of the D-mixes.

Mix design	Traditional Mix	D-QL-250m	D-HH-250m	D-QL-350m	D-QL-500m	Unit
- Slag cement		195.3	130.2	303.3	360.5	kg/m <sup>3</sup>
- Portland cement	250					kg/m <sup>3</sup>
- Quicklime		21.7		33.7	40.1	kg/m <sup>3</sup>
- Hemihydrate			86.8			kg/m <sup>3</sup>
- D soil (dry)		1590.2	1598.8	1538.2	1499.5	kg/m <sup>3</sup>
- Sand	1950					kg/m <sup>3</sup>
- Water D soil		87.2	87.7	84.4	82.2	kg/m <sup>3</sup>
- Superplasticizer		4.7	4.9	6.4	7.2	kg/m <sup>3</sup>
- Mix water	125	214.2	206.6	195.3	190.3	kg/m <sup>3</sup>
Fresh Properties						
- Slump flow	-	108-109	107-108	139-140	107-110	mm
- Relative slump flow	-	0.177	0.156	0.946	0.177	
Hardened properties						
- Compressive strength						
- 7 days	-	1.19	3.09	8.31	10.05	N/mm <sup>2</sup>
- 28 days	-	4.77	4.57	8.55	23.62	N/mm <sup>2</sup>
- Density						
- 7 days	-	1647	1603	1773	1941	kg/m <sup>3</sup>
- 28 days	-	-	-	1761	1968	kg/m <sup>3</sup>

**Table 7.13:** Mix designs (in kg/m<sup>3</sup>), fresh and hardened properties (mortar) of the J-mixes.

Mix design	Traditional Mix	J-QL-350m	J-HH-350m	J <sub>2</sub> <sup>1</sup> -QL-350m	J <sub>2</sub> <sup>1</sup> -HH-350m	J-QL-500m	Unit
- Slag cement		298.4	198.2	408.4	259.7	431.7	kg/m <sup>3</sup>
- Portland cement	250	33.2	132.1	45.0	173.1	48.0	kg/m <sup>3</sup>
- Quick lime							kg/m <sup>3</sup>
- Hemihydrate							kg/m <sup>3</sup>
- J soil(dry)		863.2	854.4	590.7	559.7	823.8	kg/m <sup>3</sup>
- Water J soil		494.7	489.7	338.5	320.8	472.2	kg/m <sup>3</sup>
- Sand 0-2				590.8	559.6		kg/m <sup>3</sup>
- Sand + gravel	1950						kg/m <sup>3</sup>
- Superplasticizer		8.4	8.5	9.0	8.9	10.5	kg/m <sup>3</sup>
- Mix water	125	44.6	47.8	36.9	78.5	32.8	kg/m <sup>3</sup>
Fresh properties							
- Slump flow	-	103 - 104	100 - 103	148-149	109-110	152-146	mm
- Relative slump flow	-	0.071	0.030	1.205	0.188	1.220	
Hardened properties							
- Compressive strength							
- 7 days	-	-	0.75	2.27	3.81		N/mm <sup>2</sup>
- 21 days	-	-	-	-	-	5.68	N/mm <sup>2</sup>
- 28 days	-	0.68	1.64	7.33	6.51	6.64	N/mm <sup>2</sup>
- Density							
- 7 days	-	1640	1600	1868	1799	1707	kg/m <sup>3</sup>

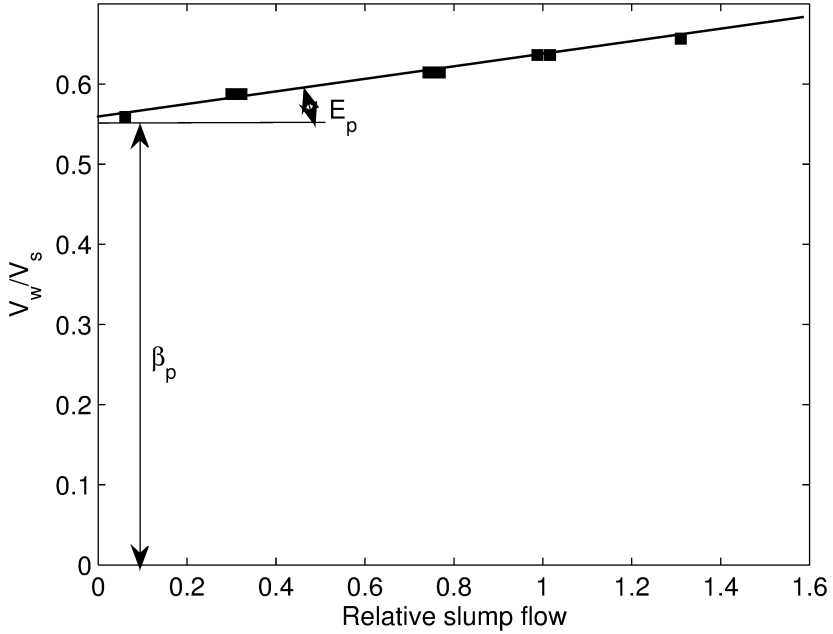


Figure 7.4: Spread-flow line for D-QL-250m for 5.1 gram of superplasticizer per litre fines.

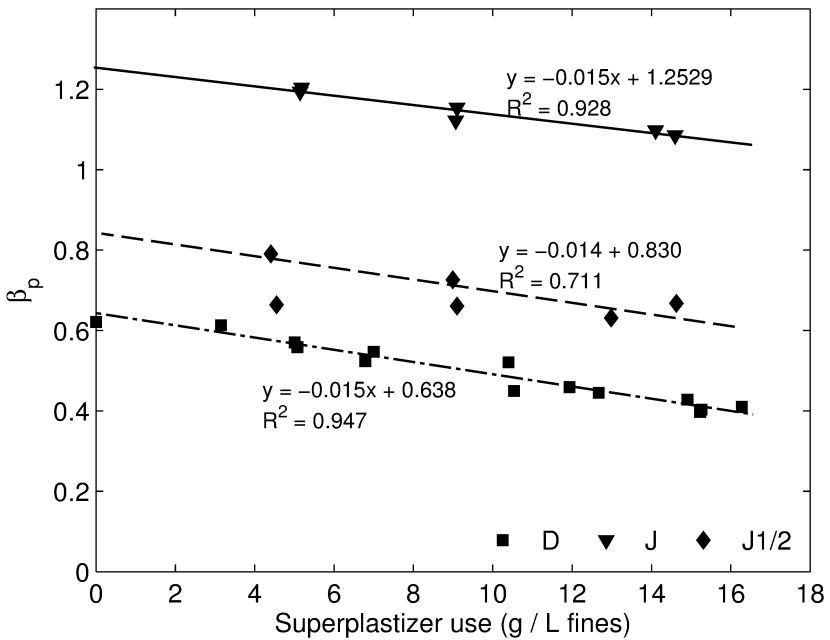


Figure 7.5: The water demand ( $\beta_p$ ) versus superplasticizer dosage for D-soil ( $215 < \text{binder} < 400 \text{ kg/m}^3$ ), J-soil ( $330 < \text{binder} < 480 \text{ kg/m}^3$ ) and  $J_{1/2}$ -soil ( $430 < \text{binder} < 455 \text{ kg/m}^3$ ).

**Table 7.14:** Superplasticizer amount in the mix versus water demand ( $\beta_p$ ) of the mix.

	SP [g / L fines]	$\beta_p$
D-HH-250m	16.3	0.410
	6.8	0.524
	11.9	0.459
D-QL-250m	10.4	0.521
	14.9	0.428
	5.1	0.558
D-QL-350m	15.3	0.403
	7.0	0.547
	3.2	0.613
D-QL-500m	12.7	0.445
	10.5	0.450
	5.0	0.570
J-QL-350m	15.2	0.398
	0.0	0.621
	9.1	1.154
J-HH-350m	5.1	1.194
	14.1	1.098
	9.1	1.122
J $\frac{1}{2}$ -QL-350m	5.2	1.204
	14.6	1.086
	4.6	0.664
J $\frac{1}{2}$ -HH-350m	9.1	0.661
	13.0	0.631
	9.0	0.726
	14.6	0.667
	4.4	0.791

**Table 7.15:** Performance overview of binders on most important aspects (++ very suitable, + suitable, - unsuitable).

Aspect	Quicklime	hemihydrate
Early strength		+
Final strength	+	
Leaching sulphate		-
Retaining heavy metals	+	++
Sustainable shape retaining	+	+
Humus neutralisation		+

**Table 7.16:** Leaching results of mortar cubes (in mg/m<sup>2</sup>).

	Maximum emission	Measured emission		
	[mg/m <sup>2</sup> ]	D-QL-250m	D-QL-350m	J-QL-500m
Sulphate	165,000	30,400	52,100	10,200
Cadmium	3.8	0.04	0.05	0.07
Chromium	120	0.04	0.04	1.4
Copper	98	0.11	0.10	14
Nickel	8.1	0.11	0.11	3.5
Lead	400	0.45	0.45	3.5
Zinc	800	0.37	0.38	1.4
Cobalt	60	0.07	0.07	1.4
Arsenic	260	0.84	0.84	3.5

cement and hemihydrate have a lower water demand ( $\beta_p$  measured as water/fines ratio) than the mixes with slag cement and quicklime. Also, the mixes with 350 kg/m<sup>3</sup> binder have a lower water demand ( $\beta_p$ ) than mixes with 250 kg/m<sup>3</sup> binder. This lower water demand for higher binder amounts is partly caused by the chosen definition of water demand. Water demand is defined as the volume of water in the mix divided by the fines volume (all particles smaller than 125  $\mu\text{m}$ , including those of the soil). Mixes with a higher binder content also have a higher total fines content and hence, at same water content a lower water/fines ratio. But this effect can not explain the difference completely, because the total amount of water in the mixes is lower at higher binder contents. A possible explanation could be that the soil absorbed some of the mix water, so it is not available for enabling flowability. The mixes with higher binder content have a lower soil content. The mixes with J $\frac{1}{2}$  have a lower water demand than the normal J-mixes, which can be expected as J $\frac{1}{2}$  contains less fines. Section 7.6 contains a more detailed analysis of this effect/phenomenon.

### 7.5.2 Mortar cubes

The mixes for mortar cubes are based on the results from the water demand study. A relative slump flow of 0.2 and a superplasticizer use of 15 g/l fines form the two constraints used for the mix designs. The mix compositions are presented in Tables 7.12 and 7.13. The hardened mortar is tested for compressive strength, density, leaching and capillary

absorption. The last two properties can only be measured for the mixes containing slag cement and quicklime, because hemihydrate and gypsum readily dissolve when they come into contact with water.

The results of the experiments are presented in Tables 7.12 and 7.13. A difference in the flowability is visible during the mixing. First, the mix is very dry and after a few minutes the mix becomes flowable. This time gap can be explained by the time the superplasticizer needs to form a thin layer around the particles (Hewlett, 1998), as is shown by i.e. Brouwers and Radix (2005); Hunger and Brouwers (2009); Quercia et al. (2012).

In Table 7.15, a comparison between the quicklime and hemihydrate mixes is presented. The mixes containing quicklime have a lower early strength than comparable mixes with hemihydrate. The mix with quicklime can be crushed manually. These effects become very clear when the humus content of the soil increases. The 500 kg/m<sup>3</sup> variant of the J-soil with 19% humus can be crumbled manually after 1 day, but achieved a good compressive strength after 28 days. After 28 days, almost every mix with quicklime have a higher compressive strength than the comparable mix with hemihydrate. In general, the compressive strength increases when the binder amount increases. This effect is partly caused by a decrease of the water/fines ratio, which has a direct relation on the compressive strength (Hunger and Brouwers, 2006) and partly to the binder as such.

Table 7.16 shows the results of the diffusion test for a selection of the mortar cubes. As one can notice from Table 7.16, the leaching of the tested mixtures with D-soil (D-QL-250m and D-QL-350m) are clearly within the limits of the Soil Quality Regulation (RBK, 2007), although the sulphate leaching level is rather high. The leaching of D-QL-250m and D-QL-350m are almost the same except for the sulphate leaching, which is higher for D-QL-350m. The leaching of copper and nickel from the mixture with J-soil is considerable higher than for tested D-soil mixtures, while the leaching of the other heavy metal is comparable and the sulphate leaching is lower. From Table 7.5, one can notice that the content of most heavy metals in the J-soil was also higher than in the D-soil, which can be a partial explanation for the higher leaching. The tested mortar cubes retain their shape during the diffusion test.

### 7.5.3 Additional experiment

The mixes with hemihydrate appear to be more suitable for immobilisation of humus rich soils. This effect becomes apparent at humus levels of 9.5 and 19%. There is a threshold visible for the mixes with a high humus level. The compressive strength of the 350 kg/m<sup>3</sup> variants is lower than 1.7 N/mm<sup>2</sup>, while the 500 kg/m<sup>3</sup> variant has a compressive strength of 6.7 N/mm<sup>2</sup>. This is also the compressive strength for a mix containing half soil and half 0-2 sand (J<sub>1/2</sub>) and 350 kg/m<sup>3</sup> binder. So an alternative to reducing the humus content by mixing with sand is the use of more binder (Table 7.17). But humus also increases the capillary absorption, and this was not reduced by adding extra binder (Figure 7.6). From these capillary absorption tests it follows that capillary absorption increases when the level of humus is increased. From the financial point of view, adding extra binder is more desirable (Section 7.8). This is because the soil used in the mix does not need to be remediated, which generates revenues as remediation costs of soil can be avoided. By the application of the soil in the mix, there is no need for this remediation, so the saved cost of remediation can be seen a revenue. On the other hand,

**Table 7.17:** Comparison between different alternatives for immobilisation of soil with high humus content (++ very good, + good/better, - bad/less).

	Mix with 0-2 sand	Extra binder
Compressive strength	+	+
Capillary water absorption	+	-
Financial feasibility	-	+

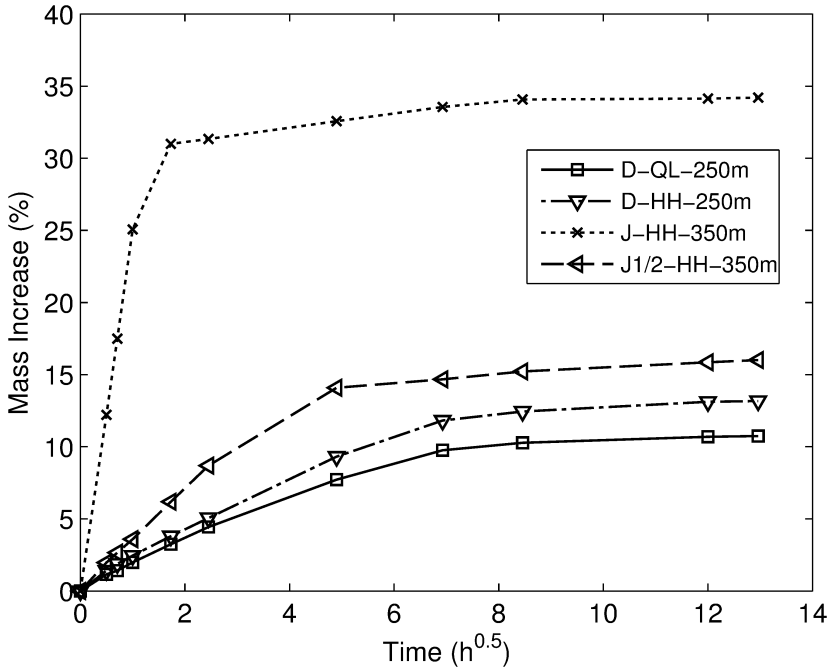


**Figure 7.6:** Capillary water absorption of the mortar cubes during exposure.

the addition of sand will lead to extra costs.

## 7.6 Analysis of the water demand

As detailed in Section 7.5.1, it is observed that the water demand of a mix decreases when the binder content increases. This is contrary to what would be expected, namely that a higher fines content results in a higher water demand. A possible explanation can be that the soil is finer than the binder, but this was not the case (Figure 7.1). In this section the relationship between water demand and the properties of the mixes is examined in more detail.

### 7.6.1 Spread-flow analysis

As discussed in Section 7.2.2, there is a relation between relative slump flow ( $\Gamma$ ) and volume-based water/solid ratio (Figure 7.4). The  $\Gamma$  of the different mixes at different

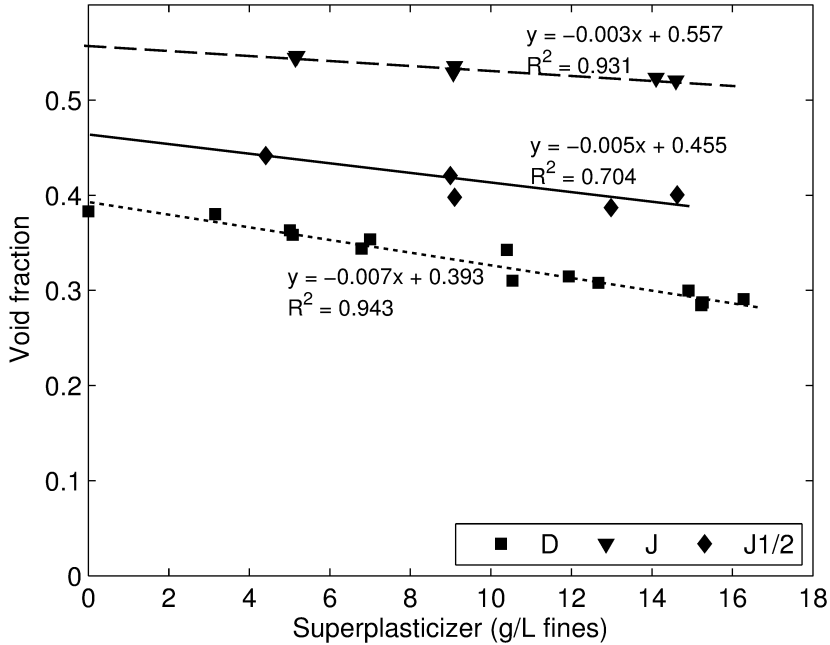


**Figure 7.7:** Void fraction versus superplasticizer dosage for the three employed soils.

amount of superplasticizer (SP) is shown in Figure 7.5. Having a closer look at Figure 7.5, it can be noticed that the  $\Gamma$  of three soils are independent of the used mix design, which differs in amount of binder and binder combination. It furthermore appears that for each soil it depends linearly on the applied superplasticizer dosage only.

### 7.6.2 Void Fraction

For every soil a spread-flow line can be drawn, yielding  $\beta_p$  and  $E_p$  (Figure 7.4). In order to analyse the lines, in the soil volume a distinction is made between the mineral and organic matter volumes, since these two parts have a different specific density. The mineral phase has a density between 2650 and 2750 kg/m<sup>3</sup>, while organic matter has a density of 1480 kg/m<sup>3</sup>. Table 7.9 shows the specific densities used for the calculation. It is also possible to calculate the void fraction based on the  $\beta_p$  of the mixes. According to Brouwers and Radix (2005) this can be done by

$$\varphi_w(\Gamma = 0) = \frac{V_w}{V_t} = \frac{V_w}{V_w + V_s} = \frac{\beta_p}{\beta_p + 1} \quad (7.9)$$

in which  $\beta_p$  is the interception of the spread flow line with the abscissa. From Section 7.6.1 it is known that  $\beta_p$  depends linearly on the applied superplasticizer (SP) dosage. Therefore the void fraction depends on the SP dosage. This is shown in Figure 7.7.

**Table 7.18:** Fitted distribution modulus of the mortar mixtures.

Mix	q	R <sup>2</sup>
D-QL-250m	0.335	0.737
D-HH-250m	0.333	0.737
D-QL-350m	0.291	0.762
D-QL-500m	0.269	0.774
J-QL-350m	0.124	0.932
J-HH-350m	0.121	0.932
J-QL-500m	0.066	0.937
J $\frac{1}{2}$ -QL-350m	0.194	0.837
J $\frac{1}{2}$ -HH-350m	0.190	0.842

### 7.6.3 Particle packing theory

The packing of a granular mix is closely related to the particle size distribution. Continuously graded granular mixtures are often based on the Fuller parabola. The cumulative finer fraction is given as

$$F(d) = \left( \frac{d}{d_{max}} \right)^{0.5} \quad (7.10)$$

where  $d$  is the sieve term and  $d_{max}$  represents the maximum sieve size (i.e. where 100% passing takes place). The introduction of a distribution modulus  $q$  by Andreassen and Andersen (1930) and a minimum particle size by Plum (1950) led to an alternative equation, which reads as follows

$$F(d) = \frac{d^q - d_{min}^q}{d_{max}^q - d_{min}^q} \quad (7.11)$$

It is believed that values of  $q$  that range from 0 to 0.28 lead to optimum packing for self-compacting concrete (Hunger and Brouwers, 2006). Hummel (1959) mentioned an optimum distribution modulus of 0.4 for spherically shaped aggregates and 0.3 for more angularly shaped aggregates. According to Brouwers (2006), several researchers refer to a distribution modulus of 0.37 for spatial grain distribution in order to obtain optimal packing and therefore minimum void fraction.

Using the particle size distribution of the mixes, the distribution modulus is optimized by minimizing the sum of the squares of the residuals (RSS). Table 7.18 shows the calculated distribution moduli for all mixes, for which holds  $d_{max} = 2.8$  mm and  $d_{min} = 1$   $\mu$ m based on Figure 7.1 for all solids. The distribution modulus versus the void fraction is shown in Figure 7.8. The relation between both characteristics can be described according to a quadratic function. The void fraction is minimal at a distribution modulus of about 0.29. This is in line with the range which is mentioned by previous authors (Hummel, 1959, Brouwers, 2006, Hunger and Brouwers, 2006).

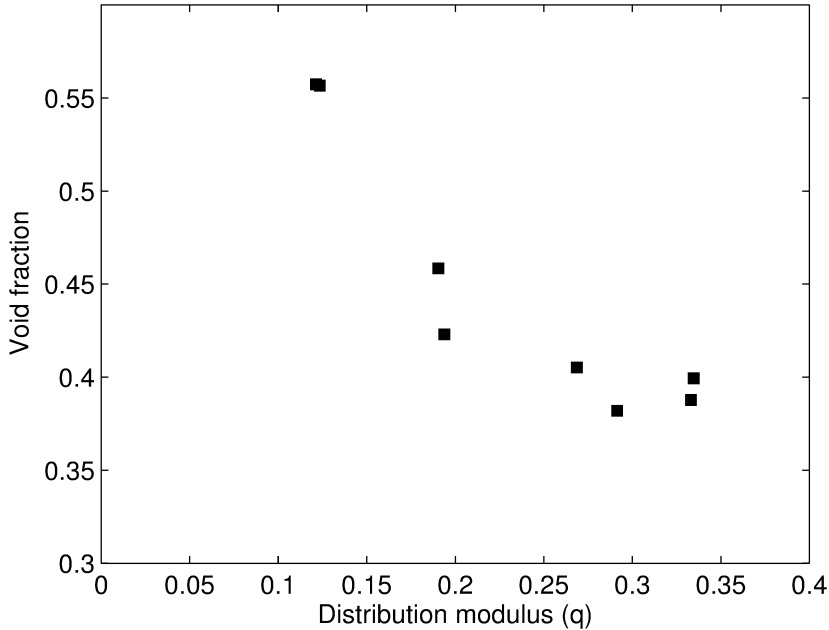


**Figure 7.8:** Derived void fraction ( $\beta_p/(\beta_{p+1})$ ) and distribution modulus ( $q$ ) for  $\Gamma = 0$  and  $SP = 0$ .

## 7.7 Concrete mix results

The results of the mortar research are used for the preparation of the concrete mixes. In this part of the research, only D-Soil is used. A combination of slag cement and quicklime forms the basis of the mixes. This binder combination performed well on all aspects during the mortar tests and does not have major drawbacks. Better results are to be expected from this combination compared to the binder combination slag cement with hemihydrate, for instance in regard to leaching (Sections 7.4, 7.5.2) and financial aspects (Section 7.8).

Concrete is distinct from mortar because of the presence of bigger aggregates. The concrete mix consisted of 70-75% mortar and 25-30% coarse aggregates (Brouwers and Radix, 2005). The concrete mixes are based on the mortar mixes D-QL-350m and D-QL-500m (Table 7.12).

Based on these two mixes, a preliminary mix was designed. This mix was optimized to meet two objectives. The first objective was the optimisation of the particle size distribution. This means a minimization of the sum of absolute deviations from the modified Andreasen and Andersen line with  $q = 0.35$ ,  $d_{\min} = 1 \mu\text{m}$  and  $d_{\max} = 16 \text{ mm}$ . The second target was to design a mix which is more cost effective than the present one (Section 7.8).

Table 7.19(a) shows the composition of the concrete mixes. In Figure 7.9, the particle size distribution of the final mixes is shown. The deviation of the mixes from the modified Andreasen and Andersen line is shown in Table 7.19(a). These mixes were selected (out

**Table 7.19:** (a) Mix designs (in kg/m<sup>3</sup>) and deviations from modified Andreasen and Andersen line of the traditional and final concrete mixes and (b) fresh and hardened properties of the final concrete mixes.

(a)			
	Traditional	D-QL-350e	D-QL-500e
Mix design			
- Slag cement	250kg/m <sup>3</sup>	209.5 kg/m <sup>3</sup>	274.9 kg/m <sup>3</sup>
- Quick lime	-	23.3 kg/m <sup>3</sup>	30.6 kg/m <sup>3</sup>
- Hemihydrate			
- Dry DD ISM soil	-	1104.0 kg/m <sup>3</sup>	1143.7 kg/m <sup>3</sup>
- Water DD ISM soil	-	60.6 kg/m <sup>3</sup>	62.7 kg/m <sup>3</sup>
- Sand 0-2	1076kg/m <sup>3</sup>		
- Gravel 4-16	861 kg/m <sup>3</sup>	740.7 kg/m <sup>3</sup>	621.8 kg/m <sup>3</sup>
- Water Extra	155 kg/m <sup>3</sup>	138.0 kg/m <sup>3</sup>	141.2 kg/m <sup>3</sup>
- SP-solution	-	4.4 kg/m <sup>3</sup>	5.4 kg/m <sup>3</sup>
Distribution modulus			
- $\sum  PSD - AA /n$		4.93%	5.52%
- $\sum (PSD - AA)^2/n$		0.41%	0.74%
(b)			
	D-QL-350e	D-QL-500e	
Fresh properties			
- Slump flow	280-280 mm (Batch 1) 220-220 mm (Batch 2)	200-200 mm (Batch 1) 510- 520 mm (Batch 2)	
- Relative Slump flow	0.96 (Batch 1) 0.21 (Batch 2)	0 (Batch 1) 5.63 (Batch 2)	
- V-Funnel	13 and 14 sec. (Batch 1)	15 and 13 sec. (Batch 2)	
- V-Funnel after 5 min	25 sec. (Batch 1)	16 sec (Batch 2)	
Hardened properties			
- Compressive strength			
- Estimated (Eq. (7.12))	33.2 N/mm <sup>2</sup>	38.5 N/mm <sup>2</sup>	
- Estimated (Eq. (7.13))	31.4 N/mm <sup>2</sup>	41.2 N/mm <sup>2</sup>	
- Measured	18.6 N/mm <sup>2</sup>	30.3 N/mm <sup>2</sup>	
- Tensile splitting strength			
- Estimated (Eq. (7.14))	1.93 N/mm <sup>2</sup>	2.52 N/mm <sup>2</sup>	
- Measured	1.96 N/mm <sup>2</sup>	2.66 N/mm <sup>2</sup>	
- Density			
- Calculated	2280 kg/m <sup>3</sup>	2280 kg/m <sup>3</sup>	
- Measured	2093 kg/m <sup>3</sup>	2206 kg/m <sup>3</sup>	
- Air content			
- Invoked at mix design	1 % V/V	1 % V/V	
- Derived from real density	9.2 % V/V	4.2 % V/V	

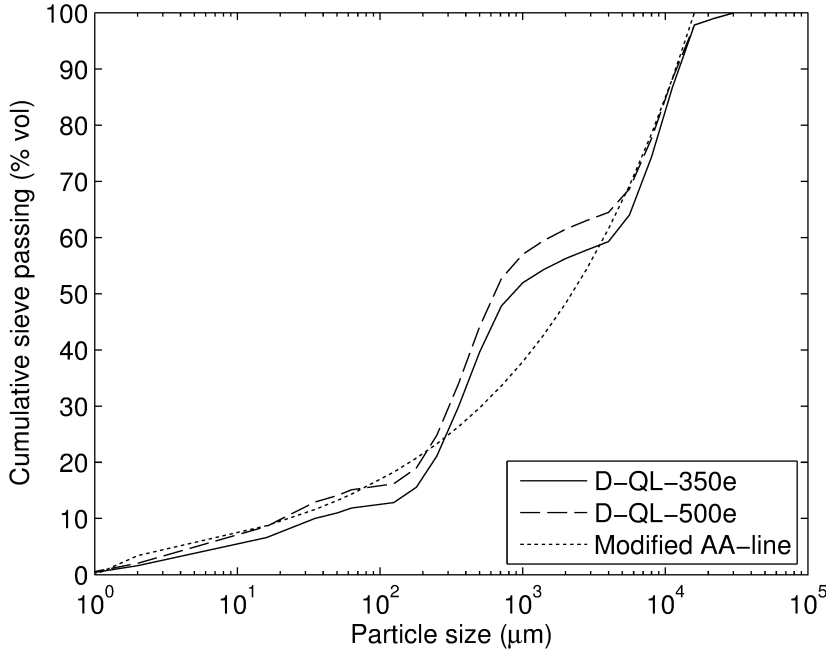


**Figure 7.9:** Cumulative finer function of final mixes and the target line, Eq. (7.11) (with  $q = 0.35$ ,  $d_{\min} = 1 \mu\text{m}$  and  $d_{\max} = 16 \text{mm}$ ).

of a number of possible mixes) because they had an acceptable deviation from the target function (the modified Andreassen and Andersen-line, Eq. (7.11)) and lowest costs.

### 7.7.1 Tests on fresh concrete

The fresh concrete tests can be divided into slump flow and V-funnel tests. Two batches were made of each mix. The results of these tests are presented in Table 7.19(b). The mixes were designed for a relative slump flow of 0.2. The relative slump flow and V-Funnel time differed considerably between the batches. The second batch of D-QL-500e is almost self-compacting, whereas the first batch was completely unflowable. This can be due to fluctuations in the soil composition. For instance the amount of fines (all particles smaller than  $125 \mu\text{m}$ ) in the soil differs, resulting in a change in the water/fines ratio and the superplasticizer content on fines. But differences in the sulphate level can also result in a different flowability and workability (Schmidt, 2014). Fluctuations in the flowability and workability of a mix can cause problems, when the mix is used in a production line. A solution for this problem is homogenizing the soil prior to treatment, in order to reduce fluctuations in the composition of the soil and so fluctuations in the flowability and workability.

### 7.7.2 Results on hardened concrete

This section deals with the results of the hardened concrete tests, which can be divided into compressive strength, flexural strength, density, capillary absorption and leaching.

The 28 days compressive strength of the D-QL-350e mix did not fulfil the requirement of 25 N/mm<sup>2</sup>, but D-QL-500e did fulfil this requirement. The measured compressive strength values were lower than the expected values based on an empirical equation for the relation between compressive strength and the water/binder ratio (wbr). The compressive strength ( $f_c$ ) of a concrete, with an uncertainty up to 5 N/mm<sup>2</sup>, can be assessed by

$$f_c = \alpha N_n + \frac{\beta}{wbr} - \gamma \quad (7.12)$$

The  $\alpha$ ,  $\beta$  and  $\gamma$  in Eq. (7.12) are depending on the cement that is used. For slag cement these values are 0.75, 18 and 30 (ENCI, 2006). The  $N_n$  is the standard strength of the used cement after  $n$  days. In Table 7.6 the standard strength of the used slag cement (CEM III/B 42,5 N LH) is shown.

Another method for estimating the compressive strength is based on the cement content and its equation reads:

$$f_c = \epsilon \cdot m_c \quad (7.13)$$

with  $\epsilon$  the strength/mass ratio, which depends on the cement, and the  $m_c$  the mass-based cement content of the mix. According to Brouwers and Radix (2005),  $\epsilon$  is 0.15 N/mm<sup>2</sup>, meaning that 1 kg of slag cement/m<sup>3</sup> of concrete can contribute 0.15 N/mm<sup>2</sup> compressive strength. Table 7.19(b) shows the estimated compressive strength using both assessment methods, and the actually measured values. One can notice from Table 7.19(b) that the measured compressive strength is lower than the expected strength based on Eqs 7.12 and 7.13. This could be an indication for poor compaction of the concrete mixtures. Nevertheless the emission of D-QL-350e is clearly within the limitations of the Soil Quality Regulation (RBK, 2007).

The flexural strength of the mixes was 1.96 N/mm<sup>2</sup> for D-QL-350e and 2.66 N/mm<sup>2</sup> for D-QL-500e (Table 7.19(b)). These values were in line with the expectations for the flexural strength based on the measured compressive strength and Eq. (7.14). The expected flexural strength was 1.93 N/mm<sup>2</sup> for D-QL-350e and 2.52 N/mm<sup>2</sup> for D-QL-500e.

$$f_t = 1 \text{ N/mm}^2 + 0.05 f_c \quad (7.14)$$

The density of the mixes is lower than the expected value. This can mean a higher air content of the mixes than initially assumed. The air content can be calculated from the measured and calculated densities (Table 7.19(b)). For D-QL-350e follows an air content of 9.2% and for D-QL-500e 4.2%. This could be again an indication for poor compaction, like it was mentioned before for the compressive strength.

The capillary absorption of both mixes is lower than the requirement for self compacting concretes (less than 3 mm/h<sup>0.5</sup>). D-QL-350e had a sorption-index of 0.77 mm/h<sup>0.5</sup> and D-QL-500e had a sorption-index of 1.21 mm/h<sup>0.5</sup> (Figure 7.10(a)). From Figure 7.10(a), one can notice that height of the front for D-QL-500e seems to decrease over time. This is caused by the inaccuracy of the measurement method. Therefore the sorption-index

**Table 7.20:** Measured leaching values of mixture D-QL-350e.

	Measured emission [mg/m <sup>2</sup> ]	Maximum emission [mg/m <sup>2</sup> ]
Sulphate	3,170	165,000
Cadmium	0.04	3.8
Chromium	0.16	120
Copper	0.08	98
Nickel	0.11	8.1
Lead	0.42	400
Zinc	0.35	800
Cobalt	0.06	60
Arsenic	0.84	260

could be lower. Based on the mass increase during the absorption test (Figure 7.10(b)), one can notice the absorption slowing down.

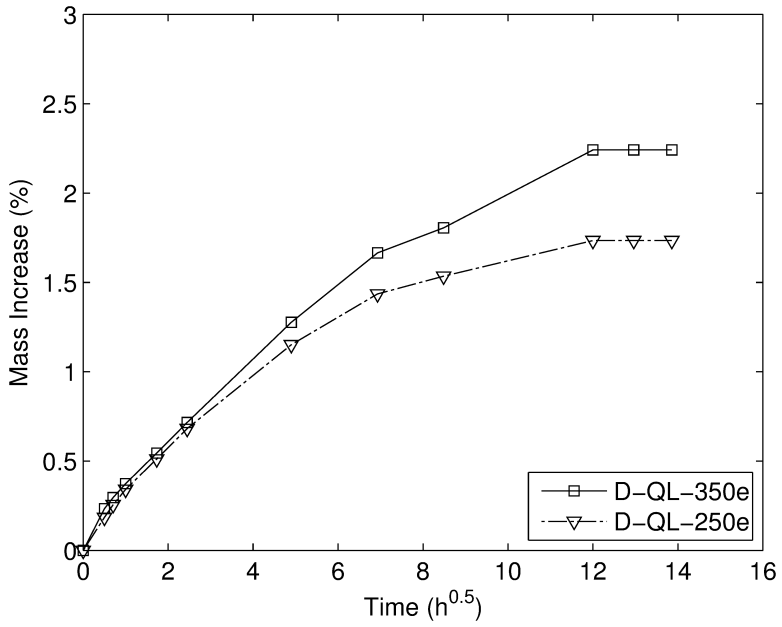
The leaching of final mixes was very low compared to the limits of the RBK (2007). In Table 7.20, the results of the test are displayed for D-QL-350e. The mixes fulfil the requirements of the RBK regarding leaching.

## 7.8 Financial analysis

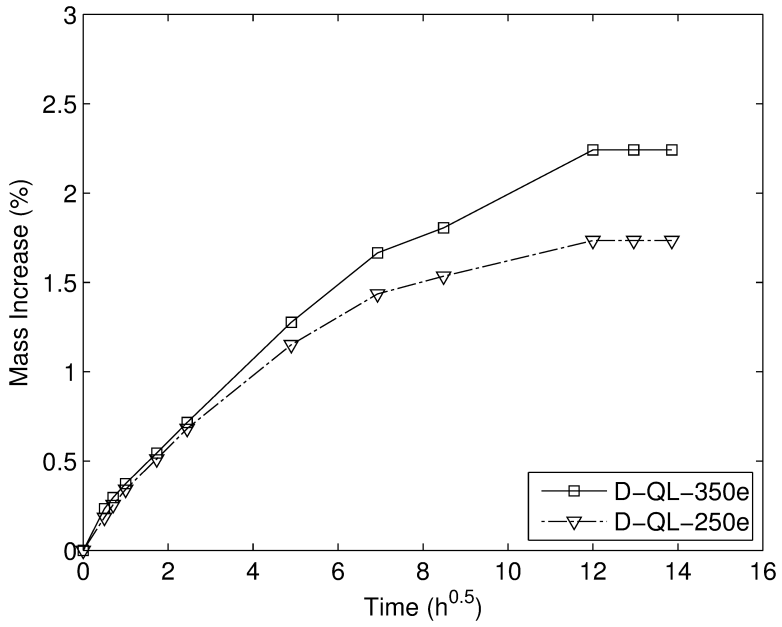
In this section the financial results of the produced concrete mixes are analysed. The new mixes are therefore compared with a traditional mix design (Table 7.19). The new mixtures result in benefits and extra cost compared to the traditional mix. The total benefit can be split into the material benefits/costs and extra benefits. The cost of disposal of the soil can be avoided (25 €/ton), since the soil is immobilised. This results in an extra benefit, which can be used to finance the extra material costs of immobilisation. The material benefit is defined as the original material costs minus the new material costs. So less material costs lead to a positive material benefit and more material costs to a negative material benefit. Table 7.21 shows the assumed material prices. Table 7.22 shows the material costs and material, soil and total financial benefit of the new mixtures compared to the reference mixtures.

For only two mixtures, the material costs are slightly higher than the materials cost of the traditional mix design. For the other mix designs, there is reduction of the material cost. The lower material costs are the result of the substitution of sand and gravel. The use of these resources lead to a higher material cost, while the soil leads to a benefit, due to avoiding disposal costs of the soil.

The last column of Table 7.22 shows the total benefit. This reveals that all new mix designs are more favorable from a financial point of view, than a traditional mix design. The mix design with half J-soil and half 0-2 sand have the poorest financial result. This is caused by a lower soil use and higher material use. These J $\frac{1}{2}$ -mixtures had the purpose to reduce the negative effects of humus. Based on the financial results, the use of binder is more advantageous, but less sustainable due to use of more binder. The J-QL-500m mix design is an example of the use of more binder to reduce the effects of humus. This mix design has a material cost comparable to the present situation, but a lower material cost



(a)



(b)

**Figure 7.10:** (a) Height front and (b) mass increase of capillary water absorption as function of time for final designs.

**Table 7.21:** Assumed material costs (in €/ton).

Material	Costs [€/ton]
Water	1.15
Slag cement (CEM III/B 42,5 N)	80.-
Hemihydrate (FG-101)	25.-
Quicklime	110.-
Waternglas-solution	200.-
0-2 Sand	17.-
4-16 Gravel	18.-
Recycled aggregate	5.-
Superplasticizer solution	300.-
Remediation of soil	-25.-

**Table 7.22:** Material cost and the indicative financial benefits (+) and costs (-) of using the new mix designs with respect to the traditional mix (in €/m<sup>3</sup>).

	Material cost [€/m <sup>3</sup> ]	Material benefits [€/m <sup>3</sup> ]	Soil benefits [€/m <sup>3</sup> ]	Total benefits [€/m <sup>3</sup> ]
Traditional	42.77	-	-	-
D-HH-250v	18.93	23.84	40.73	64.57
D-QL-350v	31.47	11.30	34.92	46.22
D-QL-250m	19.67	23.10	41.94	65.04
D-HH-250m	14.29	28.48	42.16	70.64
D-QL-350m	30.12	12.65	40.58	53.23
D-QL-500m	35.63	7.14	39.54	46.68
J-QL-350m	30.10	12.67	33.95	46.62
J-HH-350m	21.76	21.01	33.60	54.61
J $\frac{1}{2}$ -QL-350m	50.41	-7.64	23.23	15.59
J $\frac{1}{2}$ -HH-350m	37.38	5.39	22.01	27.41
J-QL-500m	43.00	-0.23	32.40	32.17
D-QL-350e	34.13	8.64	29.12	37.75
D-QL-500e	38.33	4.44	30.16	34.60

compared to J $\frac{1}{2}$ -QL-350m. Besides, J-QL-500m also incorporates more soil compared to the J $\frac{1}{2}$  mix designs, which leads to a higher benefit.

Table 7.22 also shows a difference between the quicklime (QL) and hemihydrate (HH) mix designs. The hemihydrate mixtures are more cost effective than the comparable quick-lime mix designs. This is mainly caused by the lower cost price of hemihydrate and the composition of the binder combination. The binder combination used are 60% blast furnace slag cement with 40% gypsum and 90% blast furnace cement with 10% quicklime. Since hemihydrate is the cheapest binder and quick-lime the most expensive of the three binders (Table 7.21), the binder combination with hemihydrate is favorable compared to the other combination.

## 7.9 Conclusions

The present chapter consists of a main experiment (Sections 7.4, 7.5.2 and 7.7) and an additional experiment (Section 7.5.3). First, the conclusions of the main experiment are given and next the conclusions of the additional experiment are described.

### 7.9.1 Main experiment

The results of the experiments have been examined for their financial feasibility, feasibility for production on large scale, shape retaining and strength. All mixes within the experiment were more cost effective than traditional mixes with primary material. This means that the mixes are financially feasible for production of immobilisates, because the costs of materials are lower than for normal concrete blocks, since fewer primary materials are needed and the cost of remediation of the contaminated soil can be prevented. The mixes are suitable for production of immobilisates on a large scale. The design of these mixes is adapted to the use of wet soil, instead of the dried material within the 'normal' laboratory concrete production. The J-soil used is dried prior to the production of mortar cubes, in order to make sieving of the soil possible. After sieving, water is added to the soil and the soil is given the opportunity to absorb this water for 30 minutes before the mix is made. This process is developed in order to have a close fit between the results in laboratory and practice.

The leaching of the mixes containing D-soil was tested according to the requirements of the Soil Quality Decree i.e. the diffusion test. The leaching of sulphate is near the limit for the mixes with hemihydrate during exploratory research, due to the solubility of gypsum when in contact with water. This means that considering this aspect the mixes with hemihydrate are less suitable than the mixes with quicklime.

The J and D mixes were durable shape retaining. This means that the products can be categorised as a shaped material, which also implies that the diffusion (leaching) tests are indeed applicable.

The compressive strength of the mixes containing hemihydrate was higher in the first days of hydration, but after 28 days the mixes containing quicklime have a higher compressive strength. The strength of the final mix D-QL-500e (306 kg binder/m<sup>3</sup> concrete) is higher than the required compressive strength of 25 N/mm<sup>2</sup>. The other mixes have a compressive strength of less than 25 N/mm<sup>2</sup>. When a slightly lower compressive strength is acceptable, e.g. 20 N/mm<sup>2</sup>, then already D-QL-350e (233 kg binder/m<sup>3</sup> concrete) is sufficient. When a compressive strength of 17.5 N/mm<sup>2</sup> is acceptable, then the mixtures

from the exploratory research are satisfactory.

Given these results, the final mixes of D soil, quicklime and slag cement (306 kg binder / m<sup>3</sup> concrete) fulfil all the objectives. So the results of the main experiment fulfilled both the technical and financial requirements.

### 7.9.2 Additional experiment

The mixes with hemihydrate were more suitable for the immobilisation of humus rich soils. This is owing to the better strength development of these mixes compared to mixes containing quicklime. The cubes based on quicklime can easily be deformed during the first days of hydration.

Two possible ways to reduce the effects of humus are considered during this research. The first method is the mixing of J-soil with 0-2 sand to achieve a soil with a reduced humus level. The J<sub>2</sub><sup>1</sup>-soil mixes have a compressive strength slightly lower than the comparable D-soil mixes. The second method is the use of more binder. Increasing the binder content from 331 to 480 kg/m<sup>3</sup> (J-QL-350m and J-QL-500m respectively) give a comparable strength development to the first method. The 28 day strength is slightly lower than the compressive strength of the J<sub>2</sub><sup>1</sup>-soil mixture. Extra binder reduces the negative effect on the compressive strength, but does not reduce the higher capillary absorption of humus rich mixes. This capillary absorption is equal to the one of the J-soil mixes. A higher capillary absorption may indicate a higher level of leaching as well.

The financial feasibility of the mixes with more binder was higher than the one of the J<sub>2</sub><sup>1</sup>-soil mixes. This is caused by the addition of more sand than binder. But also the reduction of soil in the extra binder mixes is lower than in the half soil mixes. For the addition of soil in the mixes, a benefit is generated, as the cost for the remediation of the soil can be avoided.

Given the results, it seems that it is not possible to immobilize soil with a humus content of 19% with 331 kg/m<sup>3</sup> binder only. Based on the present research, two possible solutions are available to immobilize such soils. The first method is the reduction of humus content by replacing half of the soil with 0-2 sand, but from a financial point of view, it is more attractive to increase the proportion of binder. The increase to 480 kg/m<sup>3</sup> of binder (J-QL-350m) is a way to achieve the required compressive strength, however without reducing the high capillary absorption, which is a result of the presence of humus.



## Conclusions, recommendations and social relevance

This thesis focuses on the micro-structural development of cement/gypsum based materials during hydration, application and fire. Since micro-structural development during these phases is too broad to be addressed fully in this thesis, six subjects from different fields of sciences are selected. These subjects are divided over the hydration, application and fire phases of the life-cycle. For the research, cellular automata systems, mathematical models and experiments were used as methods to obtain the results. Furthermore this thesis focuses on the physical and chemical improvement of cement hydration model for binders consisting of Portland clinker phases and calcium sulphates.

### 8.1 Conclusions

The research performed in this thesis, has lead to the following conclusions;

#### Packing (Chapter 2)

- Cellular automata systems can be applied for regular and random packing of digitized spheres.
- A 'new' routine based on Lubachevsky and Stillinger algorithm can successfully be applied for the random packing of digitized spheres.
- The packing fractions are related to the size ratio (box versus particle size).
- Digitized roundness and Wadell's sphericity are successfully applied to describe the shape of digitized spheres.
- The product of Wadell's sphericity or digitized roundness, respectively, and packing fraction lead to comparable results as the packing fraction results for spheres found in literature.
- New particle shapes for the diameters 7, 11 and 21 are successfully introduced in order to overcome the effect of digitizing the particles noticed during the simulations.

#### Chemical reaction kinetics (Chapter 3)

- Cellular automata approach is suitable to simulate the chemical reaction controlled and diffusion controlled reactions
- A modification of dissolution routine of CEMHYD3D has been introduced in order to retain spherical shape of particle during dissolution.

- A general and original linear relation between time and cycles, based on chemical model and cellular automata parameters, is derived to describe the dissolution of isolated particles in a dilute systems.
- A hybrid model, combining chemical reaction controlled and diffusion controlled reaction models, has been successfully introduced and tested. Special attention has been paid to the so-called transition point in the hybrid model, at which the system goes from surface (chemical reaction) to diffusion controlled.

#### **Multi-cycle and multi-scale hydration modelling (Chapter 4)**

- In order to study smaller time-steps and at higher resolution, multi-cycle and multi-scale modifications were introduced, respectively. This included modification of dissolution probability, the dissolution routine and the number of diffusion steps. These modifications are successfully applied to CEMHYD3D.
- For the multi-scale modification, two methods have been introduced to obtain the microstructure at higher resolution, namely splitting of voxels and scaling of particles. Both methods have been applied and give comparable results.
- The modified version of CEMHYD3D is suitable for multi-cycle and multi-scale modelling of ordinary Portland cement (OPC) with a particle size distribution.

#### **Ultrasonic sound speed analysis of hydrating hemihydrate (Chapter 5)**

- Three situations can be distinguish for the description of the sound velocity during the hydration process, namely slurry (starting situation), hardened product (end situation) and material during hydration (situation in between slurry and hardened product).
- The model of Robeyst et al. (2008) can be applied to describe the sound velocity through a slurry, since good agreement between experimental values and model predictions is found, when taking into account an air content of 2.7 % (V/V) on the applied hemihydrate.
- The series arrangement model of Ye (2003) is suitable to model the sound velocity through porous hardened material assuming a sound velocity through dihydrate of 6800 m/s.
- The hydration model of Schiller (1974) and relation between hydration degree and sound velocity given by Smith (2002) can be combined to derive the hydration curve from the ultrasonic sound velocity successfully.
- The ultrasonic sound velocity experiments could be applied to fit the parameters of the Schiller model. The results from this fitting showed that the parameters  $K_0$  (induction time) and  $K_1$  (gypsum growth) are positively linearly related to the water/binder ratio, while parameter  $K_2$  (dissolution of hemihydrate) is unrelated to the water/binder ratio.

### **Thermal conductivity of gypsum products (Chapter 6)**

- The thermal conductivity of gypsum plasterboards up to a temperature of 105 °C can be best described using a three-phase system consisting of solid phases and mixed liquid/gas phases (water/air) in the voids. For the calculation two two-phase systems are mixed. These two-phase systems consist of a solid phase and voids which are saturated with either dry air or water.
- The Zehner and Schlunder equation with shape factor C of 5 is the most suitable equation to describe the thermal conductivity of two-phase systems, among the equations tested in this research.
- A moisture content of 2.8 % on the gypsum mass proved to explain the thermal conductivity of the boards successfully. This moisture content is in line with values found in literature.
- The two-phase system can also be successfully applied at elevated temperatures (> 105 °C) to describe the thermal conductivity when taking into account the occurrence of the decomposition reactions and their linked changes to volume and chemical composition of gypsum products.

### **Stabilisation/solidification of contaminated soil (Chapter 7)**

- The final mix designs were assessed for their financial feasibility, feasibility for large scale production, shape retaining and strength. All these requirements were met during the research and are described below.
- All mixes are more cost effective than the current mix design with primary materials, because the cost of materials used were lower than for normal concrete blocks, since fewer primary materials were needed and the cost of remediation of contaminated soil can be prevented.
- The mix designs are suitable for large scale production.
- The leaching of the mixes containing D-soil were tested according to the requirements of the Dutch Soil Quality Decree and only the leaching of sulphate was near the limit for the mixtures with hemihydrate in the binder.
- All mixtures were durable shape retaining and therefore can be categorized as shaped material according to the Dutch Soil Quality Decree.
- The compressive strength of the mixtures containing hemihydrate was higher compared to mixtures containing quicklime during the first days of hydration, but after 28 days the quicklime mixtures have a higher compressive strength.
- Depending on the required compressive strength, several mix designs can be suitable and the correct binder amount can be selected.
- Humus proved to have a strong influence on the hydration of cement. The mixtures containing hemihydrate were more suitable than the mixtures with quicklime

binder. Two possible ways to reduce the effects of humus were considered during the research. The first method is reduction of humus content by mixing in fresh primary 0-2 sand and the second method is the addition of additional binder. Both methods were applied successfully.

## 8.2 Recommendations

This section describes the recommendations for future research based on the findings of this research.

1. In this thesis, it is demonstrated that packing of mono-sized digitized particles/spheres was possible. In order to be useful in practice, the packing of mono-sized particles should be extended to granular mixtures. The packing of granular mixtures is interesting, for the optimization of mix designs for cement/gypsum based 'concrete'.
2. During the multi-scale modelling, the same particle size distribution have been used at different resolutions. The ability to use particles smaller than 1  $\mu\text{m}$  and the use of a refined particle size distribution has not been tested yet. In the future, these possibilities should be tested and model should be calibrated for this.
3. For the design of the ultrasonic based hemihydrate hydration model, only four mixtures were used. In future research the model should be calibrated using more different water/binder ratios and hemihydrates with different fineness/particle size distribution and composition (level of dihydrate, calcium carbonate).
4. During the analysis of the ultrasonic sound velocity hydration curve, indications for the explanation of the induction time were found, but the number of data-points was too limited for the development of a sound scientific model. Therefore additional data needs to be obtained and further analysis is needed.
5. In this thesis, the hydration of Portland cement (OPC) with calcium sulphate has been successfully numerical modelled using CEMHYD3D. Currently the hydration of plain hemihydrate is not incorporated in CEMHYD3D since the differences in reaction kinetics between OPC and hemihydrate. Although the hydration of calcium sulphate has been experimentally determined and has been analytically modelled in Chapter 5, the translation to the numerical CEMHYD3D model is a possibility for further research.
6. The current research has shown that the thermal conductivity of gypsum plasterboards can be predicted using a three-phase model making use of the Zehner and Schlunder equation. Research by Kontogeorgos and Founti (2013) making use of the model presented in Chapter 6 and extended the model with radiation within the pores. Further research containing more gypsum plasterboards with known composition and pore size distribution should be used to test this. A research by Yu (2012) and Yu and Brouwers (2012, 2013) has already done this on small scale, but this research only resulted in a limited number additional data points.
7. With regards to the stabilisation/solidification research, one should notice that up to now only laboratory tests with the mix designs developed in this research

were performed. Further tests in practice are needed to assess the feasibility in practice before successfully introducing them to the market, especially research to the production process is needed.

### 8.3 Social relevance

Whereas the rest of this thesis focuses on the scientific results and relevance, the current subsection will present the social relevance of the performed research in this thesis. Social relevance in the case of this thesis is defined as the possible applications of the scientific results in industrial and other social domains.

Chapter 2 of this thesis focuses on the regular and random packing of mono-sized digitized particles. When reading an introduction on packing often the example of a packing problem given, is the grocer which have to staple oranges efficiently in his shop. This example certainly give the social relevance of packing, but of course this is limited to justify packing research to society. The most efficient way to staple oranges is the hexagonal close packing and this is already known for centuries, the so-called Kepler conjecture, which was first proven by Gauss (1831). The material section of the unit Building Physics and Systems focuses on the development and improvement of building materials composed of cement, gypsum, lime and cementitious by-products. For the (further) development of these materials, the particle packing is an important parameter. The particle packing, besides other parameters, influences the density, mechanical performance and permeability (Cho et al., 2006). The presented research focuses on mono-sized particles, but this is a starting point, which can be extended to bimodal and poly-disperse random packings. The geometric packing is an important poly-disperse packing as it used in concretes (Brouwers, 2006).

The kinetic study connecting cellular automata with general chemical kinetic models, which is performed in Chapter 3, is relevant for example to the research on dissolution of drugs/medicine in the human body. Also this knowledge on chemical engineering can also be applied for design and optimization of industrial installations.

In Chapter 4, the multi-cycle and multi-scale extension to CEMHYD3D is described. These extensions introduces the possibilities to zoom in and out with respect to time and scale/resolution at the simulation of hydration of cementitious materials. These extensions are social and scientific relevant, since it enables the study and better prediction of the long and short term behaviour as well as the possibility to include smaller particles then before. The minimal size after the extension,  $0.2 \mu\text{m}$ , is in the same range as the smallest particle size present in commercial available cements and calcium sulphates. Better prediction enables the possibility to improve concrete mixtures resulting in improved structural safety as well as providing the possibility to reduce the amount of binder in concrete mixtures. The latter is of interest from financial and environmental perspective.

Currently the hydration and determination of the induction time of cementitious materials is often determined by calorimetry. In Chapter 5, ultrasonic sound velocity monitoring is used for this purpose. The development of this method is social relevant, because it can provide a low cost monitoring method for hydration progression in-situ, which is currently not available. Furthermore, more knowledge on the hydration of calcium sulphates can help with the improvement of the gypsum plasterboards production process. Also

the ultrasonic sound velocity method can be used to accurately determine the induction time of calcium sulphate based materials, which usually is done with the less-accurate knife-cut method.

Energy performance in the building sector is always of interest. One of the elements relevant for the energy performance is the insulation of a building. Since the insulation value is the reciprocal of the thermal conductivity, the research to thermal conductivity at room temperature, as studied in Chapter 6, is relevant for the energy performance. Another social relevance of the thermal conductivity research is its contribution to the fire behaviour study of other research (Kontogeorgos and Founti, 2010, 2013; Yu, 2012). The thermal conductivity together with the specific heat and decomposition energy absorption determines the fire behaviour of a material and fire safety. A low thermal conductivity is positive. Gypsum based materials are used to protect the steel structure during fire and is so important to building fire safety.

The last content chapter of this thesis handles the stabilisation and solidification of contaminated soil in low quality concrete. The social relevance of this chapter can be divided into three elements. The first element is the reduction of the amount of waste materials which otherwise are landfilled. The second element is the reduction of the amount of fine primary materials which are needed for the production of these low quality concretes. The third element of social relevance of this research is that by performing this study, environmental safety, i.e. prohibiting the leaching of contaminations to the environment, of the designed mixes can be assured. These elements are closely related to sustainable building concepts.

## Bibliography

- Adams, D. J. and Matheson, A. J. (1972). Computation of dense random packings of hard spheres, *The Journal of Chemical Physics* **56**(5): 1989.
- Alarcon-Ruiz, L., Platret, G., Massieu, E. and Ehrlacher, A. (2005). The use of thermal analysis in assessing the effect of temperature on a cement paste, *Cement and Concrete Research* **35**(3): 609–613.
- Amathieu, L. and Boistelle, R. (1988). Crystallization kinetics of gypsum from dense suspension of hemihydrate in water, *Journal of Crystal Growth* **88**(2): 183.
- Andersson, R. and Gram, H. E. (1987). Properties of alkali activated slag concrete, *Nordic Concrete Research* **6**(1): 7–18.
- Andreassen, A. H. M. and Andersen, A. (1930). Über die beziehung zwischen kornabstufung and zwischenraum in produkten aus losen körnern (mit einigen experimenten), *Kolloid-Zeitschrift* **50**: 217–228.
- Ang, C. N. and Wang, Y. C. (2004). The effect of water movement on specific heat of gypsum plasterboard in heat transfer analysis under natural fire exposure, *Construction and Building Materials* **18**(7): 505–515.
- Ang, C. and Wang, Y. (2009). Effect of moisture transfer on specific heat of gypsum plasterboard at high temperatures, *Construction and Building Materials* **23**(2): 675–686.
- Arnold, M., Boccaccini, A. R. and Ondracek, G. (1996). Prediction of the poisson's ratio of porous materials, *Journal of Materials Science* **31**(6): 1643–1646.
- Aste, T. (2005). Variations around disordered close packing, *Journal of Physics: Condensed Matter* **17**(24): S2361–S2390.
- Audenaert, K., Boel, V. and De Schutter, G. (2003). Water permeability of self compacting concrete, in G. Grieve and G. Owens (eds), *Proceedings of the 11th International Congress on the Chemistry of Cement*, Vol. 301.
- Austin, J. C., Holmes, A. K., Tebbutt, J. S. and Challis, R. E. (1996). Ultrasonic wave propagation in colloid suspensions and emulsions: recent experimental results, *Ultrasonics* **34**(2-5): 369–374.
- Axelsson, K., Johansson, S. and Andersson, R. (2002). Stabilization of organic soils by cement and pozzolanic reactions - feasibility study, *Report 3*, Swedish Deep Stabilization Research Center, Linköping.

- Axenenko, O. and Thorpe, G. (1996). The modelling of dehydration and stress analysis of gypsum plasterboards exposed to fire, *Computational Materials Science* **6**(3): 281–294.
- Barrett, P. J. (1980). The shape of rock particles, a critical review, *Sedimentology* **27**(3): 291–303.
- BBK (2007). Besluit bodem kwaliteit.
- Belmiloudi, A. and Le Meur, G. (2005). Mathematical and numerical analysis of dehydration of gypsum plasterboards exposed to fire, *Applied Mathematics and Computation* **163**(3): 1023.
- Bénard, J., Bouissières, G., Brusset, H., Dupuis, T., Maillard, A., Pascal, P., Rinck, E. and Silber, P. (1956). *Nouveau Traité de Chime Minérale, Tome IV, Groupe II: Glucinium - Magnésium - Calcium - Strontium - Baryum - Radium*, Masson et Cie, Éditeurs, Paris.
- Bennett, C. H. (1972). Serially deposited amorphous aggregates of hard spheres, *Journal of Applied Physics* **43**(6): 2727.
- Bentz, D. P. (1995). A three-dimensional cement hydration and microstructure program. i. hydration rate, heat of hydration, and chemical shrinkage, *Report NISTIR 5756*, National Institute of Standards and Technology, Gaithersburg, MD, United States.
- Bentz, D. P. (1997). Guide to using CEMHYD3D: a three-dimensional cement hydration and microstructure development modelling package, *Report NISTIR 5977*, NIST.
- Bentz, D. P. (2000). CEMHYD3D: a three-dimensional cement hydration and microstructure development modelling package, version 2.0, *Report NISTIR 6485*, NIST.
- Bentz, D. P. (2005). CEMHYD3D: a three-dimensional cement hydration and microstructure development modeling package. version 3.0, *Report NISTIR 7232*, NIST.
- Bentz, D. P. (2006). Quantitative comparison of real and CEMHYD3D model microstructures using correlation functions, *Cement and Concrete Research* **36**(2): 259–263.
- Bentz, D. P. and Garboczi, E. J. (1991). A digitized simulation model for microstructural development, in S. Mindess (ed.), *Advances in Cementitious Materials (Ceramic Transactions, Vol 16)*, Amer Ceramic Society.
- Bentz, D. P. and Garboczi, E. J. (1992). Guide to using HYDRA3D: a three-Dimensional Digital-Image-Based cement microstructural model, *Report NISTIR 4746*, National Institute of Standards and Technology, Gauthersburg, MD.
- Bentz, D. P., Mizell, S., Satterfield, S., Devaney, J., George, W., Ketcham, P., Graham, J., Porterfield, J., Quenard, D. and Vallee, F. (2002). The visible cement data set, *Journal of Research of the National Institute of Standards and Technology* **107**(2): 137–148.
- Bentz, D. P. and Prasad, K. R. (2007). Thermal performance of fire resistive materials i. characterization with respect to thermal performance models, *Report NISTIR 7401*, Building and Fire Research Laboratory, National Institute of Standards and Technology.

- Bentz, D. P., Schlangen, E., Garboczi, E. J., Skalny, J. and Mindess, S. (1995). Computer simulation of interfacial zone microstructure and its effect on the properties of Cement-Based composites, *Materials Science of Concrete*, Vol. 6, American Ceramic Society, Westerville, OH, pp. 155–195.
- Beretka, J. and Van der Touw, J. W. (1989). Hydration kinetics of calcium sulphate hemihydrate: a comparison of models, *Journal of Chemical Technology and Biotechnology* **44**(1): 19–30.
- Berryman, S. H. and Franceschetti, D. R. (1989). Simulation of diffusion controlled reaction kinetics using cellular automata, *Physics Letters A* **136**(7–8): 348–352.
- Birdi, K. S. (1997). *Handbook of surface and colloid chemistry*, CRC Press, Boca Raton, Fla.
- Bishnoi, S. and Scrivener, K. L. (2009).  $\mu$ ic: A new platform for modelling the hydration of cements, *Cement and Concrete Research* **39**(4): 266–274.
- Blaazer, A., van Gessel, F. T., Glas, G., Hijlkema, D. and Ledderhof, J. (2006). *Bouwproducten: vervaardiging, toepassing, onderhoud, hergebruik*, ThiemeMeulenhoff, Utrecht, The Netherlands.
- Bonen, D. and Sarkar, S. L. (1995). The effects of simulated environmental attack on immobilization of heavy metals doped in cement-based materials, *Journal of Hazardous Materials* **40**(3): 321–335.
- Bouguerra, A. (1999). Temperature and moisture dependence on the thermal conductivity of wood-cement-based composite: experimental and theoretical analysis, *Journal of Physics D: Applied Physics* **32**: 2797–2803.
- Brandt, F. and Bosbach, D. (2001). Bassanite ( $\text{CaSO}_4 \cdot 0.5\text{H}_2\text{O}$ ) dissolution and gypsum ( $\text{CaSO}_4 \cdot 2\text{H}_2\text{O}$ ) precipitation in the presence of cellulose ethers, *Journal of Crystal Growth* **233**(4): 837–845.
- Braun, A., Bärtsch, M., Schnyder, B. and Kötz, R. (2000). A model for the film growth in samples with two moving reaction frontiers — an application and extension of the unreacted-core model, *Chemical Engineering Science* **55**(22): 5273–5282.
- Brouwers, H. J. H. (2004a). The work of powers and brownyard revisited: Composition of portland cement paste, *Report 2004W-006/ CME-001*, University of Twente.
- Brouwers, H. J. H. (2004b). The work of powers and brownyard revisited: Part 1, *Cement and Concrete Research* **34**: 1697–1716.
- Brouwers, H. J. H. (2005). The work of powers and brownyard revisited: Part 2, *Cement and Concrete Research* **35**(10): 1922–1936.
- Brouwers, H. J. H. (2006). Particle-size distribution and packing fraction of geometric random packings, *Physical Review E* **74**(3): 031309.
- Brouwers, H. J. H. (2011). *A hydration model of Portland cement using the work of Powers and Brownyard*, Portland Cement Association, Skokie, Illinois, U.S.

- Brouwers, H. J. H. (2012). Paste models for hydrating calcium sulfates, using the approach by Powers and Brownward, *Construction and Building Materials* **36**: 1044–1047.
- Brouwers, H. J. H., Augustijn, D. C., Krikke, B. and Honders, A. (2007). Use of cement and lime to accelerate ripening and immobilize contaminated dredging sludge, *Journal of Hazardous Materials* **145**(1): 8–16.
- Brouwers, H. J. H. and de Korte, A. C. J. (2014). Multi-cycle and multi-scale cellular automata for hydration simulation (of portland-cement). In progress.
- Brouwers, H. J. H. and Radix, H. J. (2005). Self-compacting concrete: Theoretical and experimental study, *Cement and Concrete Research* **35**(11): 2116–2136.
- Brown, P. W. (1989). Effects of particle size distribution on the kinetics of hydration of tricalcium silicate, *Journal of the American Ceramic Society* **72**(10): 1829–1832.
- Budnikoff, P. P. (1927). Zur theorie der erhärtung des stuckgipses und zur frage der existenz von löslichem anhydrit, *Colloid & Polymer Science* **42**(2): 149–154.
- Bullard, J. W. and Garboczi, E. J. (2006). A model investigation of the influence of particle shape on portland cement hydration, *Cement and Concrete Research* **36**(6): 1007–1015.
- Bullard, J. W., Jennings, H. M., Livingston, R. A., Nonat, A., Scherer, G. W., Schweitzer, J. S., Scrivener, K. L. and Thomas, J. J. (2011). Mechanisms of cement hydration, *Cement and Concrete Research* **41**(12): 1208–1223.
- Bundesverband der Gipsindustrie e.V. (2003). *Gips-Datenbuch*, Bundesverband der Gipsindustrie e.V., Darmstadt, Germany.
- Callister, W. D. (1996). *Materials Science and Engineering: An Introduction*, 4th edn, John Wiley & Sons Inc.
- Carter, R. E. (1961). Kinetic model for Solid-State reactions, *The Journal of Chemical Physics* **34**(6): 2010–2015.
- Caulkin, R., Fairweather, M., Jia, X., Gopinathan, N. and Williams, R. (2006). An investigation of packed columns using a digital packing algorithm, *Computers & Chemical Engineering* **30**(6–7): 1178–1188.
- Çengel, Y. A. (2007). *Heat and mass transfer: a practical approach*, McGraw-Hill, New York.
- Cement en Betoncentrum (2013). Cement en betoncentrum, <http://www.cementenbeton.nl/>.
- Charola, A. E., Pühringer, J. and Steiger, M. (2007). Gypsum: a review of its role in the deterioration of building materials, *Environmental Geology* **52**(2): 207–220.
- Chen, H. and Wang, Q. (2006). The behaviour of organic matter in the process of soft soil stabilization using cement, *Bulletin of Engineering Geology and the Environment* **65**(4): 445–448.

- Chen, W. (2007). *Hydration of slag cement: theory, modeling and application*, PhD thesis, University of Twente, Enschede, the Netherlands.
- Chen, W. and Brouwers, H. J. H. (2008). Mitigating the effects of system resolution on computer simulation of portland cement hydration, *Cement and Concrete Composites* **30**(9): 779–787.
- Chen, W., Brouwers, H. J. H. and Shui, Z. H. (2007). Three-dimensional computer modeling of slag cement hydration, *Journal of Materials Science* **42**(23): 9595–9610.
- Cheng, C. and Kier, L. B. (1995). A cellular automata model of Oil-Water partitioning, *Journal of Chemical Information and Computer Sciences* **35**(6): 1054–1059.
- Cho, G., Dodds, J. and Santamarina, J. C. (2006). Particle shape effects on packing density, stiffness, and strength: Natural and crushed sands, *Journal of Geotechnical and Geoenvironmental Engineering* **132**(5): 591.
- Chong, T. and Sheikholeslami, R. (2001). Thermodynamics and kinetics for mixed calcium carbonate and calcium sulfate precipitation, *Chemical Engineering Science* **56**(18): 5391–5400.
- Chopard, B. and Droz, M. (2005). *Cellular automata modeling of physical systems*, Cambridge University Press, Cambridge; New York.
- Christoffersen, J. and Christoffersen, M. R. (1976). The kinetics of dissolution of calcium sulphate dihydrate in water, *Journal of Crystal Growth* **35**(1): 79–88.
- Chrysochoou, M. and Dermatas, D. (2006). Evaluation of ettringite and hydrocalumite formation for heavy metal immobilization: Literature review and experimental study, *Journal of Hazardous Materials* **136**(1): 20–33.
- Clare, K. E. and Sherwood, P. T. (1954). The effect of organic matter on the setting of soil-cement mixtures, *Journal of Applied Chemistry* **4**: 625–630.
- Clauser, C. and Huenges, E. (1995). Thermal conductivity of rocks and minerals, *Rock Physics and Phase Relations: A Handbook of Physical Constants* p. 105–126.
- Côté, J. and Konrad, J. M. (2005). A generalized thermal conductivity model for soils and construction materials, *Canadian Geotechnical Journal* **42**(2): 443–458.
- Côté, J. and Konrad, J. M. (2009). Assessment of structure effects on the thermal conductivity of two-phase porous geomaterials, *International Journal Of Heat And Mass Transfer* **52**(1-2): 796–804.
- Craft, S. T., Isgor, B., Hadjisophocleous, G. and Mehaffey, J. R. (2008). Predicting the thermal response of gypsum board subjected to a constant heat flux, *Fire and Materials* **32**(6): 333–355.
- Crangle, R. D. (2012). USGS minerals information: Gypsum, <http://minerals.usgs.gov/minerals/pubs/commodity/gypsum/>.

- Crangle, R. D., Neely, P. R. and Roberts, L. (2010). 2008 minerals yearbook; gypsum [Advance release], *Report*, U.S. Geological Survey.
- CUR (1997). Immobilisatie: een haalbaar alternatief, *Report CUR rapport 97-7*, Stichting CUR, Gouda, Netherlands.
- Dab, D., Lawniczak, A., Boon, J. and Kapral, R. (1990). Cellular-automaton model for reactive systems, *Physical Review Letters* **64**(20): 2462–2465.
- Dalui, S. K., Roychowdhury, M. and Phani, K. K. (1996). Ultrasonic evaluation of gypsum plaster, *Journal of Materials Science* **31**(5): 1261–1263.
- Dantas, H. F., Mendes, R. A. S., Pinho, R. D., Soledade, L. E. B., Paskocimas, C. A., Lira, B. B., Schwartz, M. O. E., Souza, A. G. and Santos, I. M. G. (2007). Characterization of gypsum using TMDSC, *Journal of Thermal Analysis and Calorimetry* **87**(3): 691–695.
- De Belie, N. D., Grosse, C. U., Kurz, J. and Reinhardt, H. W. (2005). Ultrasound monitoring of the influence of different accelerating admixtures and cement types for shotcrete on setting and hardening behaviour, *Cement and Concrete Research* **35**(11): 2087–2094.
- De Korte, A. C. J. (2006). *Koude immobilisatie van verontreinigde grond; Koude anorganische immobilisatie van verontreinigde grond met behulp van cement, kalk en gips*, Master thesis, University of Twente.
- De Korte, A. C. J. (2008). Hydration modelling of calcium sulphates, in R. Eligehausen and C. Gehlen (eds), *7th fib international PhD symposium in Civil Engineering*, Vol. 8, Universitat Stuttgart, Stuttgart, Germany, pp. 3–13.
- De Korte, A. C. J. and Brouwers, H. J. H. (2009a). Multi-scale hydration modeling of calcium sulphates, in H. B. Fischer and K. A. Bode (eds), *17th Internationale Baustofftagung*, Vol. 1, F.A. Finger-Institut für Baustoffkunde, Weimar, Germany, pp. 413–418.
- De Korte, A. C. J. and Brouwers, H. J. H. (2009b). Production of non-constructive concrete blocks using contaminated soil, *Construction and Building Materials* **23**(12): 3564–3578.
- De Korte, A. C. J. and Brouwers, H. J. H. (2010). Calculation of thermal conductivity of gypsum plasterboards at ambient and elevated temperature, *Fire and Materials* **34**(2): 55–75.
- De Korte, A. C. J. and Brouwers, H. J. H. (2011). Ultrasonic sound speed of hydrating calcium sulphate hemihydrate; the correlation of sound velocity to hydration degree, in H. B. Fischer, C. Mattes and C. Beuthan (eds), *1. Weimarer Gipstagung*, Vol. 1, F.A. Finger-Institut für Baustoffkunde, Weimar, Germany, pp. 65–71.
- De Korte, A. C. J. and Brouwers, H. J. H. (2013a). A cellular automata approach to chemical reactions; 1 reaction controlled systems, *Chemical Engineering Journal* **228C**: 172–178.

- De Korte, A. C. J. and Brouwers, H. J. H. (2013b). Random packing of digitized particles, *Powder Technology* **233C**: 319–324.
- De Korte, A. C. J. and Brouwers, H. J. H. (2015). Relation between a hybrid surface and diffusion controlled reactions and cellular automata parameters. In progress.
- Desmond, K. W. and Weeks, E. R. (2009). Random close packing of disks and spheres in confined geometries, *Physical Review E* **80**(5): 051305.
- Domone, P. and HsiWen, C. (1997). Testing of binders for high performance concrete, *Cement and Concrete Research* **27**(8): 1141–1147.
- Duchesne, J. and Laforest, G. (2004). Evaluation of the degree of cr ions immobilization by different binders, *Cement and Concrete Research* **34**(7): 1173–1177.
- Elbeyli, I. Y., Derun, E. M., Gülen, J. and Pişkin, S. (2003). Thermal analysis of borogypsum and its effects on the physical properties of portland cement, *Cement and Concrete Research* **33**(11): 1729–1735.
- ENCI (2006). Product information of slag cement 42.5N, *Report*, ENCI, 's Hertogenbosch.
- Erich, S. J. F., Overbeek, A. B. M., vd Heijden, G. H. A., Pel, L., Huinink, H. P., Peelen, W. H. A. and Vervuurt, A. (2008). Validation of FEM models describing moisture transport in heated concrete by magnetic resonance imaging, *HERON* **53**(4): 225.
- Errington, J. R., Debenedetti, P. G. and Torquato, S. (2003). Quantification of order in the Lennard-Jones system, *The Journal of Chemical Physics* **118**(5): 2256–2263.
- Eurogypsum (2011). Living with gypsum: From raw material to finished products.
- Founie, A. (2006). <http://minerals.usgs.gov/minerals/pubs/commodity/gypsum/gypsumcs06.pdf>, U.S. Geological Survey.
- Fraser, S. J. (1987). Discrete models of growth and dynamical percolation in chemistry, *Journal of Computational Chemistry* **8**(4): 428–435.
- Fujii, K. and Kondo, W. (1986). Kinetics of hydration of calcium sulphate hemihydrate, *Journal of the Chemical Society, Dalton Transactions* (4): 729–731.
- Gao, Y. and Kilfoil, M. (2004). Experimental determination of order in non-equilibrium solids using colloidal gels, *Journal of Physics: Condensed Matter* **16**(44): S5191–S5202.
- Garboczi, E. J. and Bentz, D. P. (2001). The effect of statistical fluctuation, finite size error, and digital resolution on the phase percolation and transport properties of the NIST cement hydration model, *Cement and Concrete Research* **31**(10): 1501–1514.
- Gardner, M. (1992). *Mathematical circus: more puzzles, games, paradoxes, and other mathematical entertainments from Scientific American with a preface by Donald Knuth, a postscript from the author, and a new bibliography by Mr. Gardner: thoughts from readers, and 105 drawings and diagrams*, Spectrum series, Mathematical Association of America, Washington, DC.

- Gartner, E. M., Gaidis, J. M. and Skalny, J. (1989). Hydration Mechanisms, I, *Materials Science of Concrete, I*, American Ceramic Society, Westerville, OH, pp. 95–124.
- Gauss, C. F. (1831). Besprechung des buchs van L.A. seeber: Untersuchungen über die eigenschaften der positiven ternären quadratischen formen, *Göttingische Gelehrte Anzeigen* p. 1065.
- Gawin, D., Pesavento, F. and Schrefler, B. (2003). Modelling of hygro-thermal behaviour of concrete at high temperature with thermo-chemical and mechanical material degradation, *Computer Methods in Applied Mechanics and Engineering* **192**(13): 1731–1771.
- Gerlich, J. T., Collier, P. C. R. and Buchanan, A. H. (1996). Design of light steel-framed walls for fire resistance, *Fire and Materials* **20**(2): 79–96.
- Ghazi Wakili, K. and Hugi, E. (2009). Four types of gypsum plaster boards and their thermophysical properties under fire condition, *Journal of Fire Sciences* **27**(1): 27–43.
- Ghazi Wakili, K., Hugi, E., Wullschlegel, L. and Frank, T. (2007). Gypsum board in fire – modeling and experimental validation, *Journal of Fire Sciences* **25**(3): 267–282.
- Ginstling, A. M. and Brounshtein, B. I. (1950). On diffusion kinetics in chemical reactions taking place in spherical powder grains, *Zhur. Priklad. Khim.* **23**: 1249–1259.
- Goetz, R. and Seetharaman, V. (1998). Static recrystallization kinetics with homogeneous and heterogeneous nucleation using a cellular automata model, *Metallurgical and Materials Transactions A* **29**(9): 2307–2321.
- Gómez Álvarez-Arenas, T. E., Elvira Segura, L. and Riera Franco de Sarabia, E. (2002). Characterization of suspensions of particles in water by an ultrasonic resonant cell, *Ultrasonics* **39**(10): 715–727.
- Grosse, C. U. and Lehmann, F. (2008). Ultrasound measurements of the hydration rate of hemihydrates, *Report*, Materialprüfungsanstalt, Universität Stuttgart, Stuttgart, Germany.
- Guettala, A., Abibsi, A. and Houari, H. (2006). Durability study of stabilized earth concrete under both laboratory and climatic conditions exposure, *Construction and Building Materials* **20**(3): 119–127.
- Hadley, G. R. (1986). Thermal conductivity of packed metal powders, *International Journal Of Heat And Mass Transfer* **29**(6): 909–920.
- Haecker, C., Garboczi, E., Bullard, J., Bohn, R., Sun, Z., Shah, S. and Voigt, T. (2005). Modeling the linear elastic properties of portland cement paste, *Cement and Concrete Research* **35**(10): 1948–1960.
- Hago, A., Hassan, H., Al Rawas, A., Taha, R. and Al-Hadidi, S. (2007). Characterization of concrete blocks containing petroleum-contaminated soils, *Construction and Building Materials* **21**(5): 952–957.
- Hamilton, R. L. and Crosser, O. K. (1962). Thermal conductivity of heterogeneous Two-Component systems, *Industrial & Engineering Chemistry Fundamentals* **1**(3): 187–191.

- Hamm, H., Kersten, H. J. and Hueller, R. (2004). 25 years experience gained in the european gypsum industry with the use of FGD gypsum, *Cement International* (4): 92–102.
- Hand, R. (1994). The kinetics of hydration of calcium sulphate hemihydrate: A critical comparison of the models in the literature, *Cement and Concrete Research* **24**(5): 885–895.
- Harker, A. H. and Temple, J. A. G. (1988). Velocity and attenuation of ultrasound in suspensions of particles in fluids, *J. Phys. D: Appl. Phys.* **21**(11): 1576–1588.
- Harmathy, T. Z. (1970). Thermal properties of concrete at elevated temperatures, *Journal Of Materials* **5**(1): 47–&. 0022-2453.
- He, S., Oddo, J. E. and Tomson, M. B. (1994). The nucleation kinetics of calcium sulfate dihydrate in NaCl solutions up to 6 m and 90°C, *Journal of Colloid and Interface Science* **162**(2): 297–303.
- Hebib, S. and Farrell, E. R. (2003). Some experiences on the stabilization of irish peats, *Canadian Geotechnical Journal* **40**(1): 107–120.
- Hewlett, P. C. (1998). *Lea's chemistry of cement and concrete*, Arnold, London, U.K.
- Hilbert, D. and Cohn-Vossen, S. (1999). *Geometry and the imagination*, American Mathematical Soc.
- Hollingsworth, C. A., Seybold, P. G., Kier, L. B. and Cheng, C. (2004). First-order stochastic cellular automata simulations of the lindemann mechanism, *International Journal of Chemical Kinetics* **36**(4): 230–237.
- Horai, K.-i. and Simmons, G. (1969). Thermal conductivity of rock-forming minerals, *Earth and Planetary Science Letters* **6**(5): 359–368.
- Hoyos, M., Bacri, J. C., Martin, J. and Salin, D. (1994). A study of the sedimentation of noncolloidal bidisperse, concentrated suspensions by an acoustic technique, *Physics of Fluids* **6**(12): 3809–3817.
- Huang, X. (1997). On suitability of stabilizer based on chemical analysis of the liquid from stabilized soil, *Proceedings Fourteenth International conference on soil mechanics and foundation engineering*, A.A.Balkema, Rotterdam/Brookshield, Hamburg, pp. 1613–1616.
- Hummel, A. (1959). *Das Beton-ABC - Ein Lehrbuch der Technologie des Schwerbetons und des Leichtbetons*, 12 edn, Wilhelm Ernst & Sohn, Berlin.
- Hunger, M. (2010). *An integral design concept for ecological Self-Compacting Concrete*, PhD thesis, Eindhoven University of Technology, Eindhoven, The Netherlands, Eindhoven, The Netherlands.
- Hunger, M. and Brouwers, H. J. H. (2006). Development of Self-Compacting Eco-Concrete, in H. B. Fischer (ed.), *16th Internationale Baustofftagung*, Vol. 2, F.A. Finger-Institut für Baustoffkunde, Weimar, Germany, pp. 189–198.

- Hunger, M. and Brouwers, H. J. H. (2009). Flow analysis of water-powder mixtures: Application to specific surface area and shape factor, *Cement and Concrete Composites* **31**(1): 39–59.
- Illston, J. M. and Domone, P. L. J. (2001). *Construction materials: their nature and behaviour*, 3rd ed edn, Taylor & Francis, London ; New York.
- Ishida, M. and Wen, C. (1971). Comparison of zone-reaction model and unreacted-core shrinking model in solid–gas reactions—I isothermal analysis, *Chemical Engineering Science* **26**(7): 1031–1041.
- Ishida, M., Wen, C. and Shirai, T. (1971). Comparison of zone-reaction model and unreacted-core shrinking model in solid–gas reactions—II non-isothermal analysis, *Chemical Engineering Science* **26**(7): 1043–1048.
- Jander, W. (1927). Reaktionen im festen zustande bei höheren temperaturen. reaktionsgeschwindigkeiten endotherm verlaufender umsetzungen, *Zeitschrift für anorganische und allgemeine Chemie* **163**(1): 1–30.
- Janz, M. and Johansson, S. E. (2002). The function of different binding agents in deep stabilization, *Report SGI, 9*, Swedish Deep Stabilization Research Center, Linköping.
- Jennings, H. M. (2000). A model for the microstructure of calcium silicate hydrate in cement paste, *Cement and Concrete Research* **30**(1): 101. in file.
- Jia, X., Gan, M., Williams, R. and Rhodes, D. (2007). Validation of a digital packing algorithm in predicting powder packing densities, *Powder Technology* **174**(1-2): 10–13.
- Jia, X., Gopinathan, N. and Williams, R. A. (2002). Modeling complex packing structures and their thermal properties, *Advanced Powder technology* **13**(1): 55–71.
- Jia, X. and Williams, R. (2001). A packing algorithm for particles of arbitrary shapes, *Powder Technology* **120**(3): 175–186.
- Jodrey, W. S. and Tory, E. M. (1985). Computer simulation of close random packing of equal spheres, *Physical Review A* **32**(4): 2347–2351.
- Johansen, O. (1975). *Varmeledningsevne av jordarter*, Ph.D. thesis, Norge tekniske hogskole, Trondheim, Norway.
- Kansal, A. R., Torquato, S. and Stillinger, F. H. (2002). Diversity of order and densities in jammed hard-particle packings, *Physical Review E* **66**(4): 041109.
- Kaviany, M. (1995). *Principles of Heat Transfer in Porous Media*, Mechanical engineering series, second edn, Springer, Berlin, Germany.
- Kier, L. B. (2000). A cellular automata model of bond interactions among molecules, *Journal of Chemical Information and Computer Sciences* **40**(5): 1285–1288.
- Kier, L. B. (2007). Water as a complex system: Its role in ligand diffusion, general anesthesia, and sleep, *Chemistry & Biodiversity* **4**(10): 2473–2479.

- Kier, L. B. and Cheng, C. (1994a). A cellular automata model of an aqueous solution, *Journal of Chemical Information and Computer Sciences* **34**(6): 1334–1337.
- Kier, L. B. and Cheng, C. (1994b). A cellular automata model of water, *Journal of Chemical Information and Computer Sciences* **34**(3): 647–652.
- Kier, L. B. and Cheng, C. (1995). A cellular automata model of dissolution, *Pharmaceutical Research* **12**(10): 1521–1525.
- Kier, L. B., Cheng, C. K. and Seybold, P. G. (2000). Cellular automata models of chemical systems, *SAR and QSAR in Environmental Research* **11**(2): 79–102.
- Kier, L. B., Cheng, C. and Testa, B. (1999). A cellular automata model of the percolation process, *Journal of Chemical Information and Computer Sciences* **39**(2): 326–332.
- Kier, L. B., Cheng, C., Tute, M. and Seybold, P. G. (1998). A cellular automata model of acid dissociation, *Journal of Chemical Information and Computer Sciences* **38**(2): 271–275.
- Kier, L. B. and Seybold, P. G. (2009). Cellular automata modeling of complex biochemical systems, in R. A. Meyers (ed.), *Encyclopedia of Complexity and Systems Science*, Springer New York, pp. 848–865.
- Kier, L. B., Seybold, P. G. and Cheng, C. (2005). *Cellular automata modeling of chemical systems : a textbook and laboratory manual*, Springer, Dordrecht.
- Klepetsanis, P. G., Dalas, E. and Koutsoukos, P. G. (1999). Role of temperature in the spontaneous precipitation of calcium sulfate dihydrate, *Langmuir* **15**(4): 1534–1540.
- Knauf (2004). Productdatenblatt alpha gips FG 101.
- Knudsen, T. (1984). The dispersion model for hydration of portland cement i. general concepts, *Cement and Concrete Research* **14**(5): 622–630.
- Kontogeorgos, D. and Founti, M. (2010). Numerical investigation of simultaneous heat and mass transfer mechanisms occurring in a gypsum board exposed to fire conditions, *Applied Thermal Engineering* **30**(11–12): 1461–1469.
- Kontogeorgos, D. and Founti, M. (2013). A generalized methodology for the definition of reactive porous materials physical properties: Prediction of gypsum board properties, *Construction and Building Materials* **48**: 804–813.
- Koster, M. (2007). *Mikrostruktur-basierte Simulation des Feuchtetransports in Zement- und Sandstein*, PhD-Thesis, RWTH Aachen.
- Lagaly, G., Tufar, W., Minihan, A. and Lovell, A. (2002). Silicates, *Ullmann's Encyclopedia of Industrial Chemistry*.
- Lancia, A., Musmarra, D. and Prisciandaro, M. (1999). Measuring induction period for calcium sulfate dihydrate precipitation, *Aiche Journal* **45**(2): 390–397.

- Landau, L. (1986). *Theory of elasticity*, 3rd english ed., rev. and enl. by E.M. Lifshitz, A.M. Kosevich, and L.P. Pitaevskii. edn, Pergamon Press, Oxford [Oxfordshire] New York.
- LAP (2005). Landelijk afvalbeheer plan 2002-2012, <http://www.wetten.overheid.nl>.
- le Chatelier, H. (1919). Crystalloids against colloids in the theory of cements, *Transactions of the Faraday Society* **14**: 8–11.
- Lees, G. (1964). A new method for determining the angularity of particles, *Sedimentology* **3**(1): 2–21.
- Levenspiel, O. (1984). *The chemical reactor omnibook +*, Distributed by OSU Book Stores, Corvallis, Oregon.
- Levenspiel, O. (1999). *Chemical reaction engineering*, 3rd edn, Wiley, New York, U.S. Octave Levenspiel. ill. ; 26 cm.
- Lewry, A. J. and Williamson, J. (1994). The setting of gypsum plaster .2. the development of microstructure and strength, *Journal of Materials Science* **29**(21): 5524–5528.
- Lide, D. R. (2003). *CRC Handbook of Chemistry and Physics*, 84 edn, CRC press.
- Lienhard, J. H. (1987). *A heat transfer textbook*, 2nd ed edn, Prentice-Hall, Englewood Cliffs, N.J.
- Lipkowitz, K. B., Boyd, D. B., Kier, L. B., Cheng, C. and Seybold, P. G. (2001). Cellular automata models of aqueous solution systems, *Reviews in computational chemistry*, Vol. 17, VCH, New York, N.Y., pp. 205–254.
- Liu, S. T. and Nancollas, G. H. (1971). Kinetics of dissolution of calcium sulfate dihydrate, *Journal of Inorganic and Nuclear Chemistry* **33**(8): 2311–2316.
- Liu, Y., Baudin, T. and Penelle, R. (1996). Simulation of normal grain growth by cellular automata, *Scripta Materialia* **34**(11): 1679–1683.
- Losso, M. and Viveiros, E. (2005). Sound insulation of gypsum board in practice, *Environmental Noise Control*, Rio de Janeiro, Brazil.
- Lubachevsky, B. D. and Stillinger, F. H. (1990). Geometric properties of random disk packings, *Journal of Statistical Physics* **60**(5): 561–583.
- Maclean, D. J. and Sherwood, P. T. (1962). Study of the occurrence and effects of organic matter in relation to the stabilisation of soils with cement, *Proceedings of the 5th International Conference on Soil Mechanics and Foundation Engineering (ICSMFE)*, Dunod, Paris, pp. 269–275.
- Maeda, T. (1927). Some remarks on the colloidal theory of cements, *The Journal of Physical Chemistry* **31**(6): 933–936.
- Maksoud, M. A. and Ashour, A. (1981). Heat of hydration as a method for determining the composition of calcined gypsum, *Thermochimica Acta* **46**(3): 303–308.

- Mansfield, M. L., Rakesh, L. and Tomalia, D. A. (1996). The random parking of spheres on spheres, *The Journal of Chemical Physics* **105**(8): 3245.
- Manzello, S. L., Gann, R. G., Kukuck, S. R. and Lenhert, D. B. (2007). Influence of gypsum board type (X or c) on real fire performance of partition assemblies, *Fire and Materials* **31**(7): 425.
- Mason, G. (1968). Radial distribution functions from small packings of spheres, *Nature* **217**(5130): 733–735.
- Matschei, T., Lothenbach, B. and Glasser, F. P. (2007). Thermodynamic properties of portland cement hydrates in the system CaO-Al<sub>2</sub>O<sub>3</sub>-SiO<sub>2</sub>-CaSO<sub>4</sub>-CaCO<sub>3</sub>-H<sub>2</sub>O, *Cement and Concrete Research* **37**(10): 1379.
- Mattus, C. H. and Gilliam, T. M. (1994). A literature review of mixed waste components: Sensitivities and effects upon solidification/stabilization in cement-based matrices, *Report*, Oak Ridge National Laboratory, Oak Ridge, Tennessee, US.
- Maxwell, J. C. (1873). *A treatise on electricity and magnetism*, Vol. 1, Clarendon Press, Oxford.
- McGeary, R. K. (1961). Mechanical packing of spherical particles, *Journal of the American Ceramic Society* **44**(10): 513–522.
- Mehaffey, J. R., Cuerrier, P. and Carisse, G. (1994). A model for predicting heat transfer through gypsum-board/wood-stud walls exposed to fire, *Fire and Materials* **18**(5): 297–305.
- Meille, S. and Garboczi, E. J. (2001). Linear elastic properties of 2D and 3D models of porous materials made from elongated objects, *Modelling and Simulation in Materials Science and Engineering* **9**(5): 371–390.
- Milke, J., Kodur, V. and Marrion, C. (2001). Overview of fire protection in buildings, *Technical report*, Federal Emergency Management Agency.
- Miller, M. N. (1969). Bounds for effective electrical, thermal, and magnetic properties of heterogeneous materials, *Journal of Mathematical Physics* **10**(11): 1988–2004.
- Mullin, J. W. (1972). *Crystallisation*, second edn, Butterworth and Co (Publishers) Ltd, London.
- Navi, P. and Pignat, C. (1996). Simulation of cement hydration and the connectivity of the capillary pore space, *Advanced Cement Based Materials* **4**(2): 58–67.
- Neuforth, A., Seybold, P. G., Kier, L. B. and Cheng, C. (2000). Cellular automata models of kinetically and thermodynamically controlled reactions, *International Journal of Chemical Kinetics* **32**(9): 529–534.
- Niemann, L. (2005). *Die Reaktionskinetik des Gipsabbindens: Makroskopische Reaktionsraten und Mechanismen in molekularem Massstab*, Dissertation, Universität Karlsruhe.

- Nijland, T. H., van der Zon, W. H., Pachen, H. M. A. and van Hille, T. (2005). Grondstabilisatie met hoogovencement: Verharding en duurzaamheid; stabilisatie voor de boortunnel van randstandrail, *Geotechniek* (Oktober): 44–52.
- NIST (2002). Visible cement dataset [online], <http://visiblecement.nist.gov/>.
- Noyes, A. A. and Whitney, W. R. (1897). The rate of solution of solid substances in their own solutions., *Journal of the American Chemical Society* **19**(12): 930–934.
- Oates, T. (2005). *Lime and Limestone*, Wiley-VCH Verlag GmbH & Co. KGaA.
- Okamura, H. and Ouchi, M. (2003). Self-Compacting concrete, *Journal of Advanced Concrete Technology* **1**(1): 5–15.
- Packter, A. (1974). The precipitation of calcium sulphate dihydrate from aqueous solution : Induction periods, crystal numbers and final size, *Journal of Crystal Growth* **21**(2): 191–194.
- Palomo, A. and Palacios, M. (2003). Alkali-activated cementitious materials: Alternative matrices for the immobilisation of hazardous wastes: Part II. stabilisation of chromium and lead, *Cement and Concrete Research* **33**(2): 289–295.
- Peysson, S., Péra, J. and Chabannet, M. (2005). Immobilization of heavy metals by calcium sulfoaluminate cement, *Cement and Concrete Research* **35**(12): 2261–2270.
- Phani, K. K., Niyogi, S. K., Maitra, A. K. and Roychaudhury, M. (1986). Strength and elastic modulus of a porous brittle solid: An acousto-ultrasonic study, *Journal of Materials Science* **21**(12): 4335–4341.
- Philipse, A. P. (2003). Caging effects in amorphous hard-sphere solids, *Colloids and Surfaces A: Physicochemical and Engineering Aspects* **213**: 167–173.
- Pignatta e Silva, V. (2005). Determination of the steel fire protection material thickness by an analytical process—a simple derivation, *Engineering Structures* **27**(14): 2036–2043.
- Plum, N. M. (1950). The predetermination of water requirement and optimum grading of concrete: Under various conditions, *Report*, The Danish National Institute of Building Research - Statens Byggeforskningsinstitut.
- Pomiès, M., Lequeux, N. and Boch, P. (2001). Speciation of cadmium in cement: Part i. cd<sup>2+</sup> uptake by C-S-H, *Cement and Concrete Research* **31**(4): 563–569.
- Pommersheim, J., Chang, J. and Laird, C. (1985). Kinetics of hydration of calcium sulfate hemihydrate, in P. Barret and L. Dufour (eds), *Reactivity of solids*, Vol. 28A of *Material Science Monographs*, Elsevier, Amsterdam-London-New York-Tokyo, pp. 511–516.
- Posnjak, E. (1938). The system CaSO<sub>4</sub>-H<sub>2</sub>O, *American Journal of Science* **235**: 247–272.
- Quercia, G., Hüskén, G. and Brouwers, H. (2012). Water demand of amorphous nano silica and its impact on the workability of cement paste, *Cement and Concrete Research* **42**(2): 344–357.

- Raghavan, S. and Sahay, S. S. (2007). Modeling the grain growth kinetics by cellular automaton, *Materials Science and Engineering: A* **445-446**: 203–209.
- Raghavan, S. and Sahay, S. S. (2009). Modeling the topological features during grain growth by cellular automaton, *Computational Materials Science* **46**(1): 92–99.
- Raju, K. U. G. and Atkinson, G. (1990). The thermodynamics of "scale" mineral solubilities. 3. calcium sulfate in aqueous sodium chloride, *Journal of Chemical and Engineering Data* **35**(3): 361–367.
- Ramkrishna, D. and Amundson, N. R. (2004). Mathematics in chemical engineering: A 50 year introspection, *AIChE Journal* **50**(1): 7–23.
- RBK (2007). Regeling bodem kwaliteit.
- Reinhardt, H. W. (1998). *Beton, als constructiemateriaal, eigenschappen en duurzaamheid*, Delft University Press, Delft, The Netherlands.
- Reinhardt, H. W. and Grosse, C. U. (2004). Continuous monitoring of setting and hardening of mortar and concrete, *Construction and Building Materials* **18**(3): 145–154.
- Reinhardt, H. W., Grosse, C. U., Herb, A., Weiler, B. and Schmidt, G. (1999). Verfahren zur untersuchung eines erstarrenden und/oder erhärtenden werkstoffs mittels ultraschall. Patent No. 198 56 259.4. German Patent Office, Munich, Germany.
- Ridge, M. J. (1964). Hydration of calcium sulphate hemihydrate, *Nature* **204**(4953): 70–71.
- Ridge, M. J., King, G. A. and Molony, B. (1972). Reconsideration of a theory of the setting of gypsum plaster, *Journal of Applied Chemistry and Biotechnology* **22**(10): 1065–1075.
- Ridge, M. J. and Surkevicius, H. (1961). Variations in the kinetics of setting of calcined gypsum. i. effects of retarders and accelerators, *Journal of Applied Chemistry* **11**(11): 420–427.
- Ridge, M. J. and Surkevicius, H. (1966). The reactivity of calcium sulphate hemihydrate, *Journal of Applied Chemistry* **16**(3): 78–80.
- Ridge, M. J., Surkevicius, H. and Lardner, K. I. (1962). Hydration of calcium sulphate hemihydrate. II. acceleration by neutral salts, *Journal of Applied Chemistry* **12**(6): 252–256.
- Rintoul, M. D. and Torquato, S. (1996). Metastability and crystallization in Hard-Sphere systems, *Physical Review Letters* **77**(20): 4198.
- Robeyst, N., Grosse, C. U. and De Belie, N. (2009). Measuring the change in ultrasonic p-wave energy transmitted in fresh mortar with additives to monitor the setting, *Cement and Concrete Research* **39**(10): 868–875.

- Robeyst, N., Gruyaert, E., Grosse, C. U. and De Belie, N. D. (2008). Monitoring the setting of concrete containing blast-furnace slag by measuring the ultrasonic p-wave velocity, *Cement and Concrete Research* **38**(10): 1169–1176.
- Rosenhain, W. (1916). *An introduction to the study of physical metallurgy*, 2nd edn, Constable & Company LTD., London.
- Roskill Information Services Ltd. (2009). Gypsum and anhydrite - global industry markets and outlook (10th), *Report*, Roskill Information Services Ltd., London, U.K.
- Roth, D., Stang, D., Swickard, S. and DeGuire, M. (1990). Review and statistical analysis of the ultrasonic velocity method for estimating the porosity fraction in polycrystalline materials, *Report 102501*, NASA, Cleveland, Ohio.
- Sakalli, Y. (2011). Personal communication.
- Sarig, S. and Mullin, J. W. (1982). Effect of trace impurities on calcium sulphate precipitation, *Journal of Chemical Technology and Biotechnology* **32**(4): 525–531.
- Sayers, C. and Dahlin, A. (1993). Propagation of ultrasound through hydrating cement pastes at early times, *Advanced Cement Based Materials* **1**(1): 12–21.
- Schierholtz, O. J. (1958). The crystallization of calcium sulphate dihydrate, *Canadian Journal of Chemistry* **36**: 1057–1063.
- Schiller, K. (1962). Mechanism of re-crystallisation in calcium sulphate hemihydrate plasters, *Journal of Applied Chemistry* **12**(3): 135–144.
- Schiller, K. (1963). The setting of a slurry, *Journal of Applied Chemistry* **13**(12): 572–575.
- Schiller, K. (1965). Hydration of calcium sulphate hemihydrate, *Nature* **205**: 1208–1209.
- Schiller, K. (1974). The course of hydration: Its practical importance and theoretical interpretation, *Journal of Applied Chemistry and Biotechnology* **24**(7): 379–385.
- Schiller, K. K. (1958). Porosity and strength of brittle solids (with particular reference to gypsum), *Mechanical properties of non-brittle materials*, Butterworths Scientific Publications, London, UK, pp. 35–49.
- Schmidt, W. (2014). *Design Concepts for the Robustness Improvement of Self-Compacting Concrete, Effects of admixtures and mixture components on the rheology and early hydration at varying temperatures*, PhD thesis, Eindhoven University of Technology, Eindhoven, The Netherlands.
- Schofield, P. F., Stretton, I. C., Knight, K. S. and Hull, S. (1997). Powder neutron diffraction studies of the thermal expansion, compressibility and dehydration of deuterated gypsum, *Physica B: Condensed Matter* **234-236**: 942–944.
- Scott, G. D. (1960). Packing of spheres: Packing of equal spheres, *Nature* **188**(4754): 908–909.

- Scott, G. D. and Kilgour, D. M. (1969). The density of random close packing of spheres, *Journal of Physics D: Applied Physics* **2**(6): 863–866.
- Sebbahi, S., Chameikh, M. L. O., Sahban, F., Aride, J., Benarafa, L. and Belkbir, L. (1997). Thermal behaviour of moroccan phosphogypsum, *Thermochimica Acta* **302**(1–2): 69–75.
- Seybold, P. G., Kier, L. B. and Cheng, C. (1997). Simulation of First-Order chemical kinetics using cellular automata, *Journal of Chemical Information and Computer Sciences* **37**(2): 386–391.
- Shan, H. and Meegoda, J. N. (1998). Construction use of abandoned soils, *Journal of Hazardous Materials* **58**(1–3): 133–145.
- Sherwood, J. D. (1997). Packing of spheroids in three-dimensional space by random sequential addition, *Journal of Physics A: Mathematical and General* **30**: L839–L843.
- Singh, N. and Middendorf, B. (2007). Calcium sulphate hemihydrate hydration leading to gypsum crystallization, *Progress in Crystal Growth and Characterization of Materials* **53**(1): 57–77.
- Smilauer, V. (2005). *Elastic properties of hydrating cement paste determined from hydration models*, PhD thesis, Czech Technical University, Prague, Czech Republic.
- Smilauer, V. and Bittnar, Z. (2006). Microstructure-based micromechanical prediction of elastic properties in hydrating cement paste, *Cement and Concrete Research* **36**(9): 1708–1718.
- Smith, A. (2002). Correlation between hydration mechanism and ultrasonic measurements in an aluminous cement: effect of setting time and temperature on the early hydration, *Journal of the European Ceramic Society* **22**: 1947–1958.
- Söhnel, O. and Garside, J. (1992). *Precipitation, Basic principles and industrial applications*, first edn, Butterworth-Heinemann Ltd., Oxford.
- Solberg, C. and Hansen, S. (2001). Dissolution of  $\text{CaSO}_4 \cdot 1/2\text{H}_2\text{O}$  and precipitation of  $\text{CaSO}_4 \cdot 2\text{H}_2\text{O}$ -A kinetic study by synchrotron x-ray powder diffraction, *Cement and Concrete Research* **31**(4): 641–646.
- Somerton, W., Keese, J. and Chu, S. (1974). Thermal behavior of unconsolidated oil sands, *Soc Pet Eng AIME J* **14**(5): 513–521.
- Song, C., Wang, P. and Makse, H. A. (2008). A phase diagram for jammed matter, *Nature* **453**(7195): 629–632.
- Steinhardt, P. J., Nelson, D. R. and Ronchetti, M. (1981). Icosahedral bond orientational order in supercooled liquids, *Physical Review Letters* **47**(18): 1297.
- Steinhardt, P. J., Nelson, D. R. and Ronchetti, M. (1983). Bond-orientational order in liquids and glasses, *Physical Review B* **28**(2): 784.

- Sudmalis, M. and Sheikholeslami, R. (2000). Coprecipitation of  $\text{CaCO}_3$  and  $\text{CaSO}_4$ , *The Canadian Journal of Chemical Engineering* **78**(1): 21–31.
- Sultan, M. A. (1996). A model for predicting heat transfer through noninsulated unloaded steel-stud gypsum board wall assemblies exposed to fire, *Fire Technology* **32**(3): 239–259.
- Suzuki, M., Shinmura, T., Imura, K. and Hirota, M. (2008). Study of the wall effect on particle packing structure using x-ray micro computed tomography, *Advanced Powder Technology* **19**(2): 183–195.
- Szekely, J., Evans, J. W. and Sohn, H. Y. (1976). *Gas-solid reactions*, Academic Press, New York.
- Takeda, H. (2003). A model to predict fire resistance of non-load bearing wood-stud walls, *Fire and Materials* **27**(1): 19–39.
- Taylor, H. F. W. (1997). *Cement chemistry*, 2nd edn, Thomas Telford Publishing.
- Testa, B., Kier, L. B. and Cheng, C. (2002). A cellular automata model of water structuring by a chiral solute, *Journal of Chemical Information and Computer Sciences* **42**(3): 712–716.
- Thevenin, G. and Pera, J. (1999). Interactions between lead and different binders, *Cement and Concrete Research* **29**(10): 1605–1610.
- Thomas, G. (2002). Thermal properties of gypsum plasterboard at high temperatures, *Fire and Materials* **26**(1): 37–45.
- Tobochnik, J. and Chapin, P. M. (1988). Monte carlo simulation of hard spheres near random closest packing using spherical boundary conditions, *The Journal of Chemical Physics* **88**: 5824.
- Torquato, S. (2002). *Random heterogeneous materials : microstructure and macroscopic properties*, Springer, New York.
- Torquato, S. and Jiao, Y. (2009). Dense packings of polyhedra: Platonic and archimedean solids, *Physical Review E* **80**(4): 041104.
- Torquato, S. and Jiao, Y. (2010). Robust algorithm to generate a diverse class of dense disordered and ordered sphere packings via linear programming, *Physical Review E* **82**(6): 061302.
- Torquato, S. and Stillinger, F. H. (2010). Jammed hard-particle packings: From kepler to bernal and beyond, *Reviews of Modern Physics* **82**(3): 2633–2672.
- Torquato, S., Truskett, T. M. and Debenedetti, P. G. (2000). Is random close packing of spheres well defined?, *Physical Review Letters* **84**(10): 2064.
- Triollier, M. and Guillot, B. (1976). The hydration of calcium sulphate hemihydrate, *Cement and Concrete Research* **6**(4): 507–514.

- Ulam, S. M. (1952). Random processes and transformations, *Proc. Int. Congr. Math.*, Vol. 2, p. 264.
- Ulam, S. M. (1976). *Adventures of a mathematician*, Charles Schribner's Sons, New York.
- Van Breugel, K. (1995a). Numerical simulation of hydration and microstructural development in hardening cement-based materials (I) theory, *Cement and Concrete Research* **25**(2): 319–331.
- Van Breugel, K. (1995b). Numerical simulation of hydration and microstructural development in hardening cement-based materials: (II) applications, *Cement and Concrete Research* **25**(3): 522–530.
- Van Breugel, K. (1997). *Simulation of hydration and formation of structure in hardening cement-based materials*, 2nd edn, Delft University Press, Delft, The Netherlands.
- Van Breugel, K. (2004). Modelling of cement-based systems—the alchemy of cement chemistry, *Cement and Concrete Research* **34**(9): 1661–1668.
- Van der Weeën, P., Baetens, J. M. and Baets, B. D. (2011). Design and parameterization of a stochastic cellular automaton describing a chemical reaction, *Journal of Computational Chemistry* **32**(9): 1952–1961.
- Van Eijk, R. J. (2001). *Hydration of cement mixtures containing contaminants : design and application of the solidified product*, PhD thesis, University of Twente, Enschede, the Netherlands.
- Van Oss, H. G. (2012). USGS - minerals information: Cement, <http://minerals.usgs.gov/minerals/pubs/commodity/cement/>.
- Venkatarama Reddy, B. and Gupta, A. (2008). Influence of sand grading on the characteristics of mortars and soil-cement block masonry, *Construction and Building Materials* **22**(8): 1614–1623.
- Verma, L. S., Shrotriya, A. K., Singh, R. and Chaudhary, D. R. (1991). Thermal conduction in two-phase materials with spherical and non-spherical inclusions, *Journal of Physics D: Applied Physics* **24**(10): 1729–1737.
- Visscher, W. M. and Bolsterli, M. (1972). Random packing of equal and unequal spheres in two and three dimensions, *Nature* **239**: 504–507.
- Volmer, M. (1922). Über gerichtetes kristallwachstum, *Zeitschrift für Physik* **9**(1): 193–196.
- Von Neumann, J. (1966). *Theory of self-replicating automata*, University of Illinois Press, Urbana.
- Šesták, J. and Berggren, G. (1971). Study of the kinetics of the mechanism of solid-state reactions at increasing temperatures, *Thermochimica Acta* **3**(1): 1–12.
- Wadell, H. (1932). Volume and shape of rock particles, *Journal of Geology* **40**: 443–451.

- Wadell, H. (1933). Sphericity and roundness of rock particles, *Journal of Geology* **41**: 310–331.
- Walker, P. and Stace, T. (1997). Properties of some cement stabilised compressed earth blocks and mortars, *Materials and Structures* **30**(9): 545–551.
- Waples, D. and Waples, J. (2004). A review and evaluation of specific heat capacities of rocks, minerals, and subsurface fluids. part 1: Minerals and nonporous rocks, *Natural Resources Research* **13**(2): 97–122.
- WBB (1986). Wet bodembescherming, <http://www.wetten.overheid.nl>.
- Wentworth, C. K. (1922). A scale of grade and class terms for clastic sediments, *The Journal of Geology* **30**(5): 377–392.
- Widom, B. (1966). Random sequential addition of hard spheres to a volume, *The Journal of Chemical Physics* **44**(10): 3888.
- Williams, S. R. and Philipse, A. P. (2003). Random packings of spheres and spherocylinders simulated by mechanical contraction, *Physical Review E* **67**(5): 051301.
- Wirsching, F. (2005). Calcium sulfate, - *Ullmann's Encyclopedia of Industrial Chemistry*, Wiley-VCH Verlag GmbH & Co. KGaA, Weinheim, Germany.
- Wolfram, S. (1983a). Cellular automata, *Los Alamos Science* (Fall): 2–21.
- Wolfram, S. (1983b). Statistical mechanics of cellular automata, *Reviews of Modern Physics* **55**(3): 601–644.
- Wolfram, S. (1984). Preface, *Physica D: Nonlinear Phenomena* **10**(1–2): vii–xii.
- Wouterse, A. (2008). *Random packing of colloids and granular matter*, PhD thesis, Utrecht University, Utrecht, The Netherlands.
- Wullschleger, L. and Ghazi Wakili, K. (2008). Numerical parameter study of the thermal behaviour of a gypsum plaster board at fire temperatures, *Fire and Materials* **32**(2): 103–119.
- Yagi, S. and Kunii, D. (1961a). Fluidized-solids reactors with continuous solids feed—I: residence time of particles in fluidized beds, *Chemical Engineering Science* **16**(3–4): 364–371.
- Yagi, S. and Kunii, D. (1961b). Fluidized-solids reactors with continuous solids feed—II: conversion for overflow and carryover particles, *Chemical Engineering Science* **16**(3–4): 372–379.
- Yagi, S. and Kunii, D. (1961c). Fluidized-solids reactors with continuous solids feed—III: conversion in experimental fluidized-solids reactors, *Chemical Engineering Science* **16**(3–4): 380–391.
- Ye, G. (2003). *Experimental study and numerical simulation of the development of the microstructure and permeability of cementitious materials*, PhD-Thesis, Delft University of Technology, The Netherlands, Delft, The Netherlands.

- Ye, G., Van Breugel, K. and Fraaij, A. L. A. (2003). Numerically simulated pore structure and transport properties of cementitious materials, *Proceedings of 11th International Congress on the Chemistry of Cement*, Durban, South Africa, pp. 1793–1802.
- Yin, C., Ghazaly Shaaban, M. and Bin Mahmud, H. (2007). Chemical stabilization of scrap metal yard contaminated soil using ordinary portland cement: Strength and leachability aspects, *Building and Environment* **42**(2): 794–802.
- Ylmén, R., Jäglid, U., Steenari, B. and Panas, I. (2009). Early hydration and setting of portland cement monitored by IR, SEM and vicat techniques, *Cement and Concrete Research* **39**(5): 433–439.
- Yu, Q. and Brouwers, H. (2013). Design of a novel calcium Sulfate-Based lightweight composite: Towards excellent thermal properties, *Advanced Materials Research* **651**: 745–750.
- Yu, Q. L. (2012). *Design of environmentally friendly calcium sulfate-based building materials Towards an improved indoor air quality*, PhD thesis, Eindhoven University of Technology, Eindhoven, The Netherlands.
- Yu, Q. L. and Brouwers, H. J. H. (2011). Microstructure and mechanical properties of  $\beta$ -hemihydrate produced gypsum: an insight from its hydration process, *Construction and Building Materials* **25**(7): 3149–3157.
- Yu, Q. L. and Brouwers, H. J. H. (2012). Thermal properties and microstructure of gypsum board and its dehydration products: A theoretical and experimental investigation, *Fire and Materials* **36**(7): 575–589.
- Zahedi Sohi, H. and Khoshandam, B. (2012). Cellular automata modeling of non-catalytic gas–solid reactions, *Chemical Engineering Journal* **200–202**: 710–719.
- Zehner, P. and Schlunder, E. U. (1970). Thermal conductivity of granular materials at moderate temperatures, *Chemie Ingenieur Technik* **42**(14): 933–941.
- Zehner, P. and Schlünder, E. U. (1972). Einfluß der wärmestrahlung und des druckes auf den wärmetransport in nicht durchströmten schüttungen chem, *Ing.-Tech* **44**(23): 1303–1308.
- Zhang, M. and Reardon, E. J. (2003). Removal of b, cr, mo, and se from wastewater by incorporation into hydrocalumite and ettringite, *Environmental Science & Technology* **37**(13): 2947–2952.
- Zhu, W. and Bartos, P. J. M. (2003). Permeation properties of self-compacting concrete, *Cement and Concrete Research* **33**(6): 921–926.
- Zinchenko, A. Z. (1994). Algorithm for random close packing of spheres with periodic boundary conditions, *Journal of Computational Physics* **114**(2): 298–307.
- Zygourakis, K. and Sandmann, C. W. (1988). Discrete structural models and their application to gas-solid reacting systems, *AIChE Journal* **34**(12): 2030–2040.



## **Physical properties**

Compound	M (g/mole)	C <sub>p</sub> (J/Kg K)	H <sub>f</sub> (KJ/mol)	ω (cm <sup>3</sup> /mol)	Source
C <sub>1.7</sub> S	155.4	747.7	-2177		(Bentz and Prasad, 2007)
C <sub>1.7</sub> SH <sub>2.62</sub>	202.6	1650.0	-2890		(Matschei et al., 2007; Taylor, 1997)
C <sub>0.83</sub> SH <sub>1.3</sub>			-1916	59	(Matschei et al., 2007)
C <sub>1.7</sub> SH <sub>4</sub>	227.47			109.02	(Brouwers, 2004a)
C <sub>1.7</sub> SH <sub>3.2</sub>	213.09			94.60	(Taylor, 1997)
C <sub>1.67-1.7</sub> SH <sub>2.1</sub>	193.27		-2723	88.66	(Matschei et al., 2007)
C <sub>1.7</sub> SH <sub>1.5</sub>	182.45			72.7	(Jennings, 2000)
C <sub>1.7</sub> SH <sub>1.2</sub>	177.05			62.00	(Brouwers, 2004a; Taylor, 1997)
C <sub>2</sub> S	172.05		-2311.6	51.79	(Alarcon-Ruiz et al., 2005)
C <sub>3</sub> AH <sub>1.5</sub>					
C <sub>3</sub> AH <sub>6</sub>			-5548.8	149.71	
C <sub>4</sub> AH <sub>7</sub>				198.43	
C <sub>4</sub> AH <sub>11</sub>					
C <sub>4</sub> AH <sub>13</sub>			-8318.0	273.97	
C <sub>4</sub> AH <sub>19</sub>				370.86	
C <sub>4</sub> AH <sub>22</sub>				419.51	
C <sub>4</sub> A <sub>3</sub> H <sub>3</sub>			-9255 est.		
C <sub>12</sub> A <sub>7</sub>			-19200 est.	517.62	
C <sub>12</sub> A <sub>7</sub> H			-19670 est.	517.38	
CA <sub>2</sub>	-5810 est.				
Talc	381.32 calc	750		135.26	(Horai and Simmons, 1969; Waples and Waples, 2004)
Vermiculite	440 calc	840		191.3	(Lagaly et al., 2002)

## **Thermal properties**

Phase	Density Kg/m <sup>3</sup>	Mol.vol. Cm <sup>3</sup> /mol	Mol. Mass g/mol	Formation heat kJ/mol	Solubility p-value	C <sub>p</sub> kJ/(K kg)	λ W/(mK)
AH III	2580	53.22	136.14	-1424.6	4.41	0.732	4.8
AH II	2950		136.14	-1433.6			
HH	2733	53.22	145.15	-1574.6	3.4934	0.8233	3.0
DH	2310	74.54	172.17	-2022.6	4.58	1.0815	1.2
CaO	3345	16.76	56.08	-636	Reaction	0.763	
CaCO <sub>3</sub>	2700	37.07	100.09	-1207	8.06	0.818	
Ca(OH) <sub>2</sub>	2242	33.05	74.08	-986.1	5.19	0.97...	
C <sub>3</sub> S	3120	73.18	228.32	-2927.82			
C <sub>2</sub> S	3326	51.79	172.25	-2311.6			
C <sub>3</sub> A	3060	88.30	270.2	-3587.8			
ETTR	1775	707.04	1255.26	-17539.0			
C <sub>4</sub> AH <sub>13</sub>				-8318			
HYTAL				-4539.45			
Monosulfate				-8784.3			
H <sub>2</sub> O(g)			18	-242		1.87	0.016
H <sub>2</sub> O(l)	1000	18	18	-286		4.18	0.60
CO <sub>2</sub> (g)	1.986	22160	44.01	-393.5	-1.19 (333 K)	0.82	0.014
Air	1.293		28.56			1 0.024	

## **Properties of Calciumsulfate**

**Table C.1:** The main phases within the  $\text{CaSO}_4$ -system.

Characteristic	dihydrate	hemihydrate	anhydrite III
Formula	$\text{CaSO}_4 \cdot 2\text{H}_2\text{O}$	$\text{CaSO}_4 \cdot 0.5\text{H}_2\text{O}$	$\text{CaSO}_4$
Molecular Mass	172.17	145.15	136.14
Thermodynamic stability	< 40	metastable	metastable
Forms / Stages		two forms: $\alpha, \beta$	three stages:
Other names			
Synthesis conditions			
Production temperature			

**Table C.2:** Physical properties according to Wirsching (2005).

property	dihydrate	$\alpha$ -HH	$\beta$ -HH	AH-III
water of crystallization	20.92	6.21	6.21	0.00
Density	2.31	2.757	2.619-2.637	2.580
Hardness	1.5			
Solubility	0.21	0.67	0.88	

**Table C.3:** Chemical composition of some calcium sulfates (Wirsching, 2005).

Chemical compound	Zechstein gypsum	Keuper gypsum	Zechstein anhydrit	Keuper anhydrit
Combined water	19.1	20.1	1.3	0.8
S ( $\text{SO}_3$ )	46.4	45.4	55.1	51.0
C ( $\text{CaO}$ )	33.6	32.5	40.3	38.7
M ( $\text{MgO}$ )	0.05	0.28	0.95	1.71
$\text{SrO}_3$	0.07	0.16	0.07	0.14
F + A ( $\text{Fe}_2\text{O}_3 + \text{Al}_2\text{O}_3$ )	0.01	0.08	0.01	0.39
HCl-insoluble residue	0.10	0.47	0.10	2.49
N ( $\text{Na}_2\text{O}$ )	0.02	0.01	0.04	0.11
Total ( $\text{P}_2\text{O}_5$ )	0.0	0.0	0.0	0.0
Organics	0.0	0.0	0.0	0.0
Ignition loss	0.54	0.71	2.08	4.45

**Table C.4:** Characteristic properties of calcined gypsum (Wirsching, 2005).

Type of plaster	$\beta$ -Hemihydrate
mode of production	rotary kiln
g plaster per 100 g water	137
water to plaster ratio	0.73
initial setting time (min)	13
final setting time (min)	28
Flexural strength (N/mm <sup>2</sup> )	4.8
Compressive Strength (N/mm <sup>2</sup> )	11.2
hardness (N/mm <sup>2</sup> )	19.1
Density of hardened specimen (Kg/m <sup>3</sup> )	1069

**Table C.5:** Phase composition of plaster of Paris (Wirsching, 2005).

	Plaster of Paris
Dihydrate	$\text{CaSO}_4 \cdot 2\text{H}_2\text{O}$
$\beta$ -Hemihydrate	$\beta\text{-CaSO}_4 \cdot 0.5\text{H}_2\text{O}$
$\beta$ -Anhydrate III	$\beta\text{-CaSO}_4\text{III}$
Anhydrate II	$\text{CaSO}_4\text{II}$
	0
	75
	20
	5

## Analysis derivation multi-cycle

During the derivation of the multi-cycle modification in Chapter 4, the following equations are proposed;

$$P_{D,K} = 1 - (1 - P_{D,1})^{\frac{1}{k}} \quad (\text{D.1})$$

$$P_{D,k} = k \left( 1 - \sqrt[k]{1 - \frac{1}{k} P_{D,1}} \right) \quad (\text{D.2})$$

$$P_{D,k} = \frac{1}{k} P_{D,1} \quad (\text{D.3})$$

Figure D.1 shows the results of applying the three different versions of the equation in CEMHYD3D for a cement system with water-binder ratio of 1.2 and containing 100% C<sub>3</sub>S mono sized particles with size of 15. For the testing of the right expression for P<sub>D,k</sub> a P<sub>D,1</sub> of 0.2 has been applied to magnify the differences between the three expressions. Normally the probability for C<sub>3</sub>S is 0.027. In the figures, the cycles have been corrected according to Eq. (4.6). As one can notice from these three figures, Eq. (D.3) is correct. Therefore this version is used for the simulations performed in this Thesis.

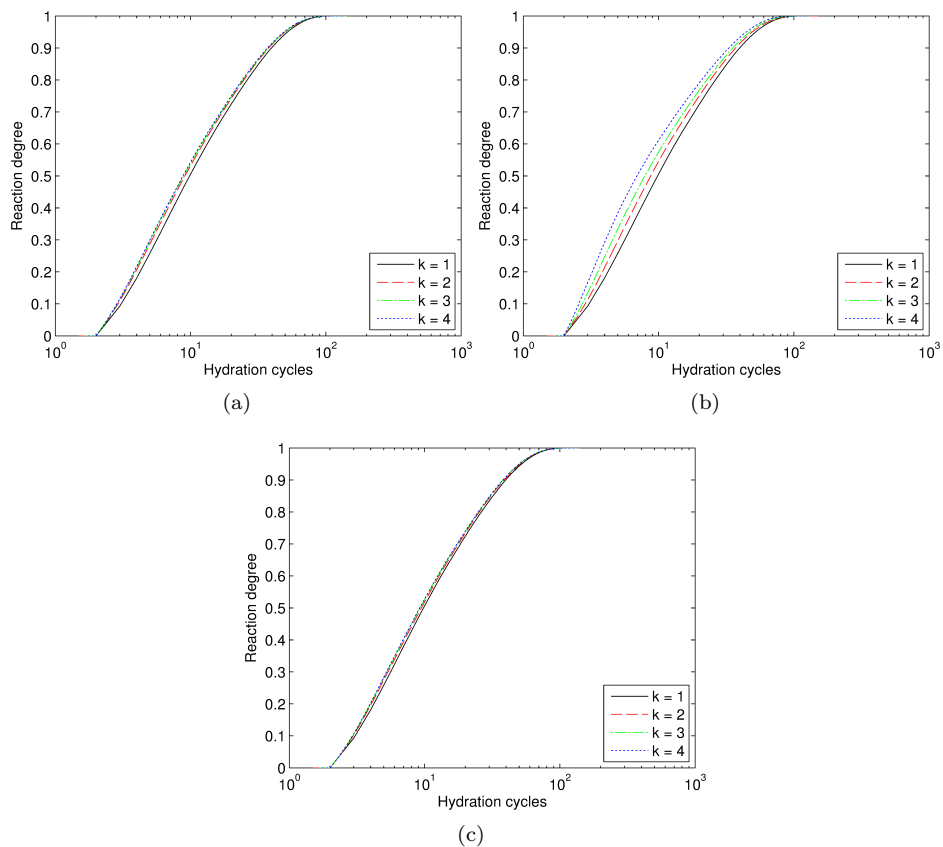


**Figure D.1:** Multi-cycle hydration curves using (a) Eq. (D.1), (b) Eq. (D.2) and (c) Eq. (D.3).

## List of symbols and abbreviations

### Latin

C	Concentration	(g/l)
C	Cycle	-
C <sub>1</sub>	Cycle in system with k = 1 and s = 1	-
C <sub>e</sub>	Concentration at external surface of a particle	(g/l)
C <sub>k</sub>	Cycle in system with multi-cycle factor k	-
c	Sound velocity	(m/s)
c <sub>air</sub>	Volume fraction air in the voids	-
c <sub>e</sub>	Effective sound velocity	(m/s)
c <sub>f</sub>	Sound velocity of fluid	(m/s)
c <sub>s</sub>	Sound velocity of solid	(m/s)
< C >	Average number of contacts in the packed system	-
< c >	Contact number	-
D <sub>1</sub>	Number of diffusion steps	-
D <sub>e</sub>	Effective diffusion coefficient	(m <sup>2</sup> /s)
D <sub>k</sub>	Number of diffusion steps for multi-cycle factor k	-
d	Diameter (of particle)	(m)
< d >	Average distance during random walk	(m)
F	Shape factor of a particle	-
f	Packing fraction	-
f <sub>e</sub>	Packing fraction corrected for digitized roundness of particle	-
f <sub>ψ</sub>	Packing fraction corrected for sphericity of particle	-
G	Shear modulus	(Pa)
G <sub>e</sub>	Effective shear modulus	(N/m <sup>2</sup> )
g <sub>2</sub>	Radial distribution function (RDF)	-
H <sub>box</sub>	Height of the box used in a cellular automata system	(μm)
K	Bulk modulus	(N/m <sup>2</sup> )
K <sub>0</sub>	Parameter Schiller model (induction time)	(s)
K <sub>1</sub>	Parameter Schiller model	(s)
K <sub>2</sub>	Parameter Schiller model	(s)
K <sub>air</sub>	bulk modulus of air	(N/m <sup>2</sup> )
K <sub>e</sub>	Effective bulk modulus	(N/m <sup>2</sup> )
K <sub>f</sub>	Bulk modulus of the fluid	(N/m <sup>2</sup> )
K <sub>s</sub>	Bulk modulus of the solid	(N/m <sup>2</sup> )
K <sub>water</sub>	Bulk modulus of water	(N/m <sup>2</sup> )
k	Multi-cycle factor	-
k <sub>1</sub>	Rate constant chemical reaction controlled model	(m/s)

$k_2$	Rate constant ash diffusion model	(m <sup>2</sup> /s)
$k_b$	Boltzmann constant (1.38066·10 <sup>-23</sup> J/K)	
$L_{\text{box}}$	Size of the box used in a cellular automata system	(μm)
$l$	length (of particle)	(m)
$l_0$	Average step size during random walk	(m)
$M$	Molar mass	(g/mole)
$N$	Number of particles	-
$N_{\text{con}}$	Number of contacts in a packed system	-
$n_m$	The number of moves of disks/spheres in each placing round	-
$n_t$	The maximum number of attempts to move a disk/sphere	-
$P_1$	Reaction probability in chemical reaction controlled model	-
$P_2$	Reaction probability in ash diffusion controlled model	-
$P_{D,0}$	Basic dissolution probability	-
$P_{D,1}$	Dissolution probability of diffusion controlled system for $k = 1$ and $s = 1$	-
$P_{D,k}$	Dissolution probability for system with multi-cycle factor $k$	-
$P_{D,k,s}$	Dissolution probability for system with multi-cycle factor $k$ and multi-scale factor $s$	-
$P_{D,s}$	Dissolution probability for system with multi-scale factor $s$	-
$P_{N,1}$	Nucleation probability for $k = 1$ and $s = 1$	-
$P_{N,k}$	Nucleation probability for multi-cycle factor $k$	-
$Q$	Bond orientation order	-
$Q_4$	Cubic symmetry of a system	-
$Q_6$	Icosahedrally orientation of a system	-
$R$	Growth rate	(mol/(m <sup>2</sup> s))
$r$	Radius (of a particle)	(m)
$r_0$	Radius of initial particle	(m)
$r_c$	Radius of shrinking core	(m)
$r_c$	Critical size	(m)
$r_{c,\text{tr}}$	Radius of shrinking core at transition point	(m)
$r_e$	External radius of particle including ash layer	(m)
$r_{e,\text{tr}}$	External radius of particle including ash layer at transition point	(m)
$r_p$	Radius of a particle	(m)
$S$	Size and shape parameter for particles during ultrasonic analysis	-
$S$	Surface area	(m <sup>2</sup> )
$S_0$	Surface area of initial particle	(m <sup>2</sup> )
$S_c$	Surface area of unreacted core	(m <sup>2</sup> )
$S_e$	External surface area of a particle	(m <sup>2</sup> )
$S_p$	Surface area of the digitized particle	(m <sup>2</sup> )
$S_t$	Surface area of one of the top surfaces of a digitized particle	(m <sup>2</sup> )
$s$	Multi-scale factor	-
$s_1$	Saturation rate pore volume water	-
$T$	Translational order metric	-
$t$	Time	(s)

$t_{tr}$	Time of the transition point	(s)
$V$	Volume	(m <sup>3</sup> )
$V_0$	Volume of the initial particle	(m <sup>3</sup> )
$V_c$	Volume of the shrinking core of particle	(m <sup>3</sup> )
$V_{cs}$	Volume of circumscribing sphere	(m <sup>3</sup> )
$V_e$	Volume of a particle including ash layer	(m <sup>3</sup> )
$V_f$	Volume of fines (particles < 125 $\mu\text{m}$ ) in a mixture	-
$V_p$	Volume of a digitized particle	(m <sup>3</sup> )
$V_s$	Volume of the solids	(m <sup>3</sup> )
$V_T$	Volume of the container	(m <sup>3</sup> )
$V_T$	Total volume	(m <sup>3</sup> )
$v$	Volume increase ratio during reaction	-
wbr	Water/binder ratio (m/m)	-
< z >	Parking number	-

### Greek

$\alpha$	Reaction degree	-
$\alpha$	Activity	-
$\alpha_{tr}$	Reaction degree at transition point	-
$\beta$	Supersaturation	-
$\beta_a$	Fitting parameter for the ash diffusion controlled model	-
$\beta_c$	Fitting parameter for the chemical reaction controlled model	-
$\gamma_c$	Caging number	-
$\delta$	Distance between (Chap. 2)	(m)
$\delta$	Layer thickness	(m)
$\delta_i$	Volume fraction of phase i	-
$\delta_{tr}$	Layer thickness at transition point	(m)
$\epsilon$	Digitized roundness	-
$\kappa$	$\lambda_s/\lambda_f$	-
$\lambda$	Thermal conductivity	W/(m K)
$\lambda_e$	Effective thermal conductivity of the mix	W/(m K)
$\lambda_s$	Thermal conductivity of the solid	W/(m K)
$\lambda_g$	Effective thermal conductivity of a saturated system with dry air	W/(m K)
$\lambda_i$	Thermal conductivity of the phase i	W/(m K)
$\lambda_l$	Effective thermal conductivity of a saturated system with water	W/(m K)
$\lambda_f$	Thermal conductivity of the fluid in the voids	W/(m K)
$\lambda_{meas}$	Measured thermal conductivity	W/(m K)
$\varphi$	Void fraction	-
$\varphi_c$	Volume fraction (unhydrated) binder	-
$\varphi_{hp}$	Volume fraction hardened product	-
$\varphi_s$	Volume fraction solids	-
$\varphi_t$	Volume fraction fluids	-
$\varphi_w$	Volume fraction water	-

$\psi$	Sphericity of a particle	-
$\omega$	Molar volume	(cm <sup>3</sup> /mole)
$\rho$	Specific Density	(kg/m <sup>3</sup> )
$\rho_a$	Apparent density	(kg/m <sup>3</sup> )
$\rho_f$	Specific density of the fluid	(kg/m <sup>3</sup> )
$\rho_s$	Specific density of the solid	(kg/m <sup>3</sup> )
$\tau_1$	Full reaction time according to chemical reaction controlled model	(s)
$\tau_2$	Full reaction time according to ash diffusion controlled model	(s)
$\tau_3$	Full reaction time according to hybrid reaction model	(s)
$\nu$	Poisson ratio	-

### Abbreviations

bcc	Body centred cubic
CA	Cellular Automata
CSA	Calcium silicate aluminate
CSH	Calcium silicate hydrate
CH	Portlandite
DH	Di-hydrate (gypsum)
fcc	face centred cubic
HCP	Hexagonal close packed
HH	Hemihydrate
hp	Hardend product
LPS	Larger particle system
RCP	Random Close Packed
RDF	Radial distribution function
RLP	Random Loose Packed
RSA	Random sequential addition
sc	Simple cubic

## Summary

### *Hydration and thermal decomposition of cement/calcium-sulphate based materials*

This thesis aims to extend existing insights on micro-structural development of cement / gypsum-based materials during hydration, application and fire. Therefore three different methods are applied, namely cellular automata, experiments and mathematical models. Since micro-structural development is quite broad, four subjects from different fields of science were chosen and were described in four separated chapters.

*Chapter 2* describes the random packing of regularly shaped particles from the perspective of digitized particles. The packing of regularly and irregularly shaped particles have been studied extensively in literature using experiments and numerical simulations. The use of cellular automata computer simulations is scarcely described in literature. Cellular automata systems are employed for the simple mathematical idealizations of complex systems in physics, chemistry and engineering (Wolfram, 1983). In order to be able to use a cellular automata system to study the packing of particles, the particle needs to be digitized. Two packing routines have been applied for the creation of random packing, namely the packing routines available in the cellular automata cement hydration model by Bentz (1995) and a modified version based on the Lubachevsky and Stillinger algorithm (Lubachevsky and Stillinger, 1990). The results have shown that the packing routine of Bentz is not suitable for the random packing of mono-sized digitized particles, while the special modified Lubachevsky and Stillinger algorithm showed that the packing fraction obtained was related to the size ratio (box size divided by particle size). When correcting the packing fractions obtained for digitized particles with parameters describing the shape of the digitized particles (Wadell sphericity and digitized roundness), the results of these particles are in line with results for mono-sized spheres from literature.

In *Chapter 3*, direct links between cellular automata and different chemical reaction models, to study the reaction of particles, are derived. Previous research on first and second order reactions is based on the concentration of the reactant. The present chapter describes the reaction kinetics based on particles and takes into account the shape and specific surface of these particles.

As a vehicle for this study of cellular automata, a simplified version of the CEMHYD3D model is used. During the research it was found that during the dissolution of particles, additional reactive surface was created due to the dissolution of voxels in the middle of the top-surfaces. Therefore a modification of the dissolution routine within CEMHYD3D was introduced. This modification introduced the preference of the system to dissolve voxels on the outside of the particles rather than the middle of the top-surfaces of the

particles. In this way the increase of reactive surface is prohibited and a spherical shape maintained.

Using this modification, it is shown that the dissolution of digitized particle can be described based on the chemical reaction controlled system. Based on 165 simulations a general linear relation between cycles and time was derived. The derived model can describe the reaction sufficient up to 99.9%. Therefore it can be concluded that the single 'cellular automata' particle is unambiguously related to the chemical controlled reactions. Furthermore it was shown that cellular automata can be applied to describe the dissolution of particles with constant and growing particle size during dissolution. This can be done by combining the models for surface and diffusion controlled reactions. The chapter describes therefore a hybrid model containing a surface and diffusion controlled phase and it is shown that the application of this model is successful.

The modifications of dissolution routine introduced in Chapter 3 were used in *Chapter 4* to enable the multi-cycle and multi-scale simulations. Multi-cycle and multi-scale simulations are required in order to study binders with shorter reaction time (i.e. calcium sulphates) and with smaller particle sizes. CEMHYD3D was originally developed with minimal particle size of 1  $\mu\text{m}$ , using the introduced multi-scale modification within CEMHYD3D it is possible to reduce the minimum size to 0.2  $\mu\text{m}$ . Within the chapter it is proven that both multi-cycle and multi-scale modifications can be successfully applied within CEMHYD3D. For this successful application, it was necessary to modify the dissolution probability which is used within CEMHYD3D.

The hydration of hemihydrate to dihydrate and cement is studied by IR, SEM and Vicat techniques. Because the speed of hydration it is more difficult to measure the hydration curve and the different processes which take place. For the measurement of the hydration of cement and concrete, in the last decade, ultrasonic sound velocity measurements have been applied successfully (De Belie et al., 2005; Reinhardt and Grosse, 2004; Robeyst et al., 2008). This method has the advantage over the more traditional methods, such as the aforementioned Vicat-needle, SEM and IR, that ultrasonic measurements are continuous (Ylmén et al., 2009). Especially for hemihydrate hydration, due to the short hydration time, it is difficult to stop the hydration for discontinuous measurements. *Chapter 5* presents the performed research on the relation between hydration, and associated microstructure development, of  $\beta$ -hemihydrate to dihydrate (gypsum) and ultrasonic sound velocity through gypsum-based materials. Therefore an overview of available kinetic and volumetric hydration models for gypsum is given. The presented models predict the sound velocity through slurries and hardened products. These states correspond to the starting and ending times of the hydration process. In this way, the sound velocity is used to quantify the composition of the fresh slurry as well as the hardening and hardened porous material. During the research a linear relation between the amount of hydration product (gypsum) formed and sound velocity (Smith, 2002) is obtained. Using the equations of Schiller (1974) for the hydration process and of Brouwers (2011) for the volume fractions of binder, water and hydration products during the hydration process, it is shown that not only the initial and final state of hydration can be described, but also the hydration process itself.

*Chapter 6* is describing the thermal conductivity of gypsum plasterboards at ambient and elevated temperatures using derived data from the microstructure (density, void fraction, chemical composition), whereas the previous two chapters resulted in a microstructure. The thermal conductivity is an interesting property since it partly determines the heat transfer during fire together with the volumetric enthalpy of a material. The ratio between both mechanisms is called the thermal diffusion and depends on the density, specific heat and thermal conductivity of a material. Plasterboard often protects steel structures of buildings because it conducts heat slowly and absorbs the heat of the fire by its volumetric enthalpy. Within this chapter the thermal conductivity of gypsum plasterboard is described using a mathematical model. The model assumes that the thermal conductivity of gypsum plasterboard (i.e. a porous medium) is a three-phase system, which contains a solid phase and a water/air mix in the voids (the liquid and gas phase, respectively). Different theoretical equations for both dry and moistured plasterboards were presented and tested. The equation proposed by Zehner and Schlünder (1972) with shape-factor  $C$  of 5 gave good agreement with experimental data of the different boards. The composition and moisture content of the boards influence the thermal conductivity. The performed research has shown that moisture plays an important role in the thermal conductivity at ambient temperature and that the composition and moisture content are related. Regression analysis has pointed out that the moisture content depends only on the gypsum content based on the used model. A value of 2.8% absorbed water on the mass of gypsum was found. The final step made in this chapter is the computation of the thermal conductivity of board at elevated temperature. A close fit between computed and experimental values derived from literature at elevated temperatures was found.

In *Chapter 7* hemihydrate is used to immobilize a heavily contaminated humus-rich peat soil and a lightly contaminated humus-poor sand soil, extracted from a field location in the Netherlands as an example for the application of hemihydrate in practice for another use than the production of plasterboard. The two types of soil used in this chapter are very common in the Netherlands. The purpose is to develop financial feasible, good quality immobilisates, which can be produced on large scale. To this end, two binder combinations were examined, namely slag cement with quicklime and slag cement with hemi-hydrate. The mixes with hemi-hydrate proved to be better for the immobilization of humus rich soils, having a good early strength development. The heavily contaminated soil with 19% humus (of dm) could not be immobilized using 398 kg slag cement and 33 kg quicklime per  $\text{m}^3$  concrete mix (binder = 38.4 % dm soil). It is possible to immobilize this soil using 480 kg binder (432 kg slag cement, 48 kg quicklime) per  $\text{m}^3$  of mix (58.2 % dm). An alternative to the addition of extra binder (slag cement with quicklime) is mixing the soil with 0-2 sand. This not only improved the compressive strength of the immobilisates, but also reduced the capillary absorption. All the mixes with the lightly contaminated soil were cost-effective and suitable for production of immobilisates on a large scale. These mixes had good workability, a good compressive strength and a low capillary absorption. The leaching of all mixes was found to be much lower than required by the regulations. Given these results, the final mixes in the main experiment fulfilled all the financial and technical objectives.



# Samenvatting

## *Hydratatie and thermische ontbinding van cement/calcium-sulfaat gebaseerde materialen*

Dit proefschrift beoogt de bestaande inzichten over microstructuur ontwikkeling van cement / gips gebaseerde materialen tijdens hydratatie, gebruik en brand uit te breiden. Drie verschillende methoden zijn hierbij toegepast, namelijk cellulaire automaten, experimenten en wiskundige modellen. Omdat microstructuurontwikkeling een vrij breed veld is, zijn zes onderwerpen uit verschillende wetenschapsgebieden gekozen en beschreven in zes verschillende hoofdstukken.

*Hoofdstuk 2* beschrijft de random pakking van regelmatig gevormde deeltjes vanuit het perspectief van gedigitaliseerde deeltjes. De pakking van regelmatig en onregelmatig gevormde deeltjes is uitgebreid bestudeerd in de literatuur door middel van experimenten en numerieke simulaties. Het gebruik van cellulaire automaten computersimulaties voor pakkingen is beperkt beschreven in de literatuur. Cellulaire automaten systemen worden gebruikt voor de eenvoudige wiskundige idealiseringen van complexe systemen in de natuurkunde, scheikunde en techniek (Wolfram, 1983b). Om cellulaire automaten te kunnen gebruiken voor het bestuderen van de pakking van deeltjes te bestuderen, moeten de deeltjes worden gedigitaliseerd. Twee pakkingsroutines zijn toegepast voor het creëren van random pakking, namelijk de pakkingsroutine die gebruikt is in het cellulaire automata cement hydratatie model van Bentz (1995) en een gewijzigde versie op basis van de Lubachevsky en Stillinger algoritme (Lubachevsky and Stillinger, 1990). De resultaten laten zien dat de pakking routine van Bentz niet geschikt is voor de random pakking van gedigitaliseerde deeltjes met gelijkmatige afmetingen, terwijl de verkregen pakkingfracties met de aangepaste Lubachevsky en Stillinger algoritme zijn gerelateerd aan de grootte ratio (afmeting van container gedeeld door deeltjes grootte). Na het corrigeren van de verkregen pakkingfracties met parameters die de vorm van de gedigitaliseerde deeltjes beschrijven (Wadell bolvormigheid en gedigitaliseerde rondheid), zijn de resultaten van deze deeltjes in overeenstemming met de resultaten uit de literatuur voor bollen van gelijke afmeting.

In *Hoofdstuk 3*, zijn directe verbanden afgeleid tussen cellulaire automaten en verschillende chemische reactie modellen voor de beschrijving van de reacties van de deeltjes. Eerder onderzoeken naar eerste en tweede orde reacties zijn gebaseerd op de concentratie van de reactant. Dit hoofdstuk beschrijft de reactiekinetiek op basis van deeltjes en houdt rekening met de vorm en het specifiek oppervlak van deze deeltjes. Als hulpmiddel voor het onderzoek van cellulaire automaten wordt een vereenvoudigde versie van het CEMHYD3D model gebruikt. Tijdens het onderzoek is gebleken dat tij-

dens het oplossen van deeltjes, aanvullende reactieve oppervlak wordt gecreëert door het oplossen van voxels in het midden van de zogenaamde topvlakken. Daarom is een wijziging van de oplosroutine binnen CEMHYD3D geïntroduceerd. Deze wijziging leidt er toe dat het systeem een voorkeur heeft om voxels op te lossen aan de buitenkant van de deeltjes in plaats van in het midden van de topvlakken van de deeltjes. Op deze manier wordt de toename van reactieve oppervlak voorkomen en wordt een bolvorm gehandhaafd.

Met deze wijziging is aangetoond dat het oplossen van gedigitaliseerde deeltje kan worden beschreven op basis van het chemische reactie gecontroleerd mechanisme. Gebaseerd op 165 simulaties is een algemeen lineair verband afgeleid tussen de cycli en de tijd. Het afgeleide model beschrijft de reactie in voldoende mate tot een reactiegraad van 99,9 %. Daardoor kan worden geconcludeerd dat chemische gecontroleerde reacties eenduidig kunnen worden beschreven door de bestudering van het oplossen van een enkel 'cellulaire automaten' deeltje.

Verder werd aangetoond dat cellulaire automaten kunnen worden toegepast om het oplossen van deeltjes met constante en groeiende deeltjesgrootte te beschrijven. Dit kan gedaan worden door het combineren van de modellen voor oppervlak en diffusie gecontroleerde reacties. Het hoofdstuk leidt tot een gecombineerd hybride model en er wordt aangetoond dat de toepassing van dit model succesvol is.

De wijzigingen van de oplosroutine geïntroduceerd in Hoofdstuk 3 worden gebruikt in *Hoofdstuk 4* om de multi-cycli en multi-schaal simulaties mogelijk te maken. Multi-cycli en multi-schaal simulaties zijn nodig om bindmiddelen te bestuderen met kortere reactietijd (bijv. calcium sulfaat) en met kleinere deeltjesgrootte. CEMHYD3D werd oorspronkelijk ontwikkeld met minimale deeltjesgrootte van 1  $\mu\text{m}$ . Met de geïntroduceerde multi-schaal modificatie in CEMHYD3D is het mogelijk om de minimale korrelgrootte te verkleinen tot 0,2  $\mu\text{m}$ . Binnen het hoofdstuk wordt aangetoond dat zowel multi-cycli en multi-schaal wijzigingen met succes kunnen worden toegepast binnen CEMHYD3D. Voor deze succesvolle toepassing moest de oploskans, die wordt gebruikt in CEMHYD3D, worden gewijzigd.

Hydratie van hemihydraat en cement wordt in het algemeen onderzocht door middel van IR, SEM en Vicat technieken. Door de snelheid van hydratatie is het moeilijk om de hydratatie-curve te meten en de verschillende processen die plaatsvinden te onderscheiden. Voor het meten van de hydratatie van cement en beton, zijn in de afgelopen tien jaar ultrasoon geluid snelheidsmetingen met succes toegepast (De Belie et al., 2005; Reinhardt and Grosse, 2004; Robeyst et al., 2008). Deze werkwijze heeft als voordeel boven de meer traditionele methoden, zoals de bovengenoemde Vicat naald, SEM en IR, dat ultrasone metingen continu zijn (Ylmén et al., 2009). Vooral bij de hydratatie van hemihydraat is het moeilijk de hydratatie te stoppen voor discontinue metingen vanwege de korte duur van de hydratatie en de daardoor gintroduceerde fouten. *Hoofdstuk 5* presenteert het onderzoek gedaan naar de relatie tussen hydratatie en bijbehorende microstructuurontwikkeling van de reactie van  $\beta$ -hemihydraat naar dihydraat (gips) en ultrasoon geluid snelheid door gips gebaseerde materialen. Daarvoor wordt een overzicht van de beschikbare kinetische en volumetrische hydratatie modellen voor gips gegeven. De gepresenteerde modellen voorspellen de geluidssnelheid door verse mengsels en uit-

geharde producten. Deze toestanden corresponderen met de begin- en eindtijden van het hydratatie-proces. Op deze wijze wordt de geluidssnelheid gebruikt om de samenstelling van het verse mengsel, de verharding en het uitgeharde poreuze materiaal kwantificeren. Tijdens het onderzoek is een lineair verband tussen de hoeveelheid gevormd hydratatieproduct (gips) en geluidssnelheid (Smith, 2002) verkregen. Gebruikmakend van de vergelijkingen van Schiller (1974) voor het hydratatie-proces en de vergelijkingen van Brouwers (2011) voor de volumefracties van bindmiddel, water en hydratatie-producten tijdens het hydratatieproces, wordt er aangetoond dat niet alleen de initiële en uiteindelijke hydratatie toestand kunnen worden beschreven maar ook de hydratatieproces zelf kan worden beschreven.

*Hoofdstuk 6* beschrijft de thermische geleiding van gipsplaten bij kamertemperatuur en bij verhoogde temperaturen met behulp van afgeleide gegevens op basis van de microstructuur (dichtheid, lege holten, chemische samenstelling). De thermische geleiding is een interessant eigenschap, aangezien het mede de warmteoverdracht tijdens brand bepaald in samenspraak met de volumetrische enthalpie van een materiaal. De verhouding tussen beide mechanisme heet thermische diffusie en is afhankelijk van de dichtheid, soortelijke warmte en thermische geleiding van een materiaal. Gipsplaten beschermen vaak staalconstructies van gebouwen omdat deze platen warmte langzaam geleiden en de warmte van het vuur door middel van de volumetrische enthalpie absorberen. In dit hoofdstuk wordt de thermische geleiding van gipsplaten beschreven gebruikmakend van een wiskundig model. Het model neemt aan dat de thermische geleiding van gipskarton (een poreus medium) een driefasig systeem is, waarbij het een vaste fase en een water / luchtmengsel in de holten (de vloeistof- en gasfase respectievelijk) bevat. Verschillende theoretische vergelijkingen voor zowel droge als 'vochtige' gipsplaten worden gepresenteerd en getest. De vergelijking van Zehner and Schlünder (1972) met een vorm-factor  $C$  van 5 geeft een goede overeenkomst met de experimentele gegevens van de verschillende boards. De samenstelling en het vochtgehalte van de platen beïnvloedt de thermische geleiding. Het uitgevoerde onderzoek heeft aangetoond dat vocht een belangrijke rol speelt in de thermische geleiding bij omgevingstemperatuur en dat er een verband is tussen de samenstelling en het vochtgehalte. Op basis van een regressieanalyse en het gebruikte model kan worden geconcludeerd dat het vochtgehalte alleen afhankelijk is van de massafractie gips in de plaat. Een waarde van 2,8% geabsorbeerd water op de massa gips werd gevonden tijdens deze analyse. De laatste stap in dit hoofdstuk was de berekening van de thermische geleiding van het gipsplaat bij verhoogde temperaturen. Een goede overeenkomst tussen berekende en experimentele waarden bij verhoogde temperaturen is gevonden.

In *Hoofdstuk 7* wordt hemihydraat gebruikt om een sterk vervuilde humusrijke veengrond en een licht verontreinigde humus-arme zandgrond, afkomstig uit een veldlocaties in Nederland te immobiliseren als een voorbeeld van de toepassing van hemihydraat in de praktijk anders dan voor de productie van gipsplaat. De twee bodemtypes gebruikt in dit hoofdstuk komen veel voor in Nederland. Het doel is het ontwikkelen van een financiële haalbaar, goede kwaliteit immobilisaat, die geproduceerd kan worden op grote schaal. Hiervoor zijn twee binder combinaties onderzocht, namelijk hoogovencement met kalk en hoogovencement met hemihydraat. De recepturen met hemihydraat bleken beter voor de

immobilisatie van humusrijke bodems. Deze recepturen hebben een goede vroege sterkte ontwikkeling. De zwaar verontreinigde grond met 19% humus (droge stof) kon niet worden geïmmobiliseerd met behulp van 398 kg hoogovencement en 33 kg ongebluste kalk per m<sup>3</sup> betonspecie (bindmiddel = 38,4% droge stof grond). Het is mogelijk gebleken om deze grondsoort te immobiliseren met 480 kg bindmiddel (432 kg hoogovencement, kalk 48 kg) per m<sup>3</sup> mix (58,2% droge stof). Een alternatief voor de toevoeging van extra bindmiddel (hoogovencement met ongebluste kalk) is om de grond te mengen met 0-2 zand. Dit is niet alleen een verbetering van de druksterkte van de immobilisaten, maar vermindert ook de capillaire absorptie. Alle recepturen met de licht verontreinigde grond zijn kosteneffectief en zijn geschikt voor grootschalige productie. Deze recepturen hadden een goede verwerkbaarheid, een goede druksterkte en een lage capillaire absorptie. De uitloging van alle recepturen bleek veel lager dan de wettelijke grenzen. Gezien deze resultaten, voldeden de uiteindelijke recepturen aan alle financiële en technische doelstellingen.

## Relevant publications

Publications produced in this PhD project are listed below:

### Peer-reviewed journals

1. Korte, A.C.J. de and H.J.H. Brouwers (2015). Relation between a hybrid surface and diffusion controlled reactions and cellular automata parameters (Submitted).
2. Brouwers, H.J.H. and A.C.J. de Korte (2014). Multi-cycle and multi-scale cellular automata for hydration simulation (of Portland cement) (Submitted).
3. Korte, A.C.J. de and H.J.H. Brouwers (2013). A cellular automata approach to chemical reactions; 1 Reaction controlled systems. *Chemical Engineering Journal*, Vol. 228C, pp 172-178.
4. Korte, A.C.J. de and H.J.H. Brouwers (2013). Packing of digitized particles. *Powder Technology*, Vol. 233, pp 319-324.
5. Korte, A.C.J. de and H.J.H. Brouwers (2011). Ultrasonic sound speed of hydrating calcium sulphate hemihydrate. *Journal of Materials Science*, Vol. 46 (22), pp 7228-7239.
6. Korte, A.C.J. de and H.J.H. Brouwers (2010). Calculation of thermal conductivity of gypsum plasterboards at ambient temperature and exposed to fire. *Fire and Materials*, Vol. 34 (2), pp. 55-75.
7. Korte, A.C.J. de and H.J.H. Brouwers (2009). Production of non-constructive concrete blocks using contaminated soil. *Construction and Building Materials*, Vol. 23 (12), pp. 3564-3578.

### Conference proceedings

1. Korte, A.C.J. de, and Brouwers, H. J. H. (2011). Ultrasonic sound speed of hydrating calcium sulphate hemihydrate; Part 2, The correlation of sound velocity to hydration degree. In H. B. Fischer, Chr. Mattes and C. Beuthan (Eds.), 1. Weimarer Gipstagung (Vol. 1, pp 65-71). Weimar, Germany: F.A. Finger-Institut für Baustoffkunde, Weimar.
2. Korte, A.C.J. de, and Brouwers, H. J. H. (2011). Ultrasonic sound speed of hydrating calcium sulphate hemihydrate; Part 1, The calculation of sound speed of slurries and hardened porous material. In H. B. Fischer, Chr. Mattes and C. Beuthan (Eds.), 1. Weimarer Gipstagung (Vol. 1, pp 55-64). Weimar, Germany: F.A. Finger-Institut für Baustoffkunde, Weimar.
3. Korte, A.C.J. de, and Brouwers, H. J. H. (2010). Ultrasonic sound speed measurement as method for the determining the hydration degree of hydration degree. In G. Fisher, M. R. Geiker, O. Hededal, L. Ottosen, and H. Stang (Eds.), *Proceedings 8th fib international PhD symposium in Civil Engineering* (Vol. 1, pp. 593-597). Kgs. Lyngby, Denmark: DTU Byg.

4. Korte, A.C.J. de, and H.J.H. Brouwers (2009). Multi-scale hydration modeling of calcium sulphates. In H. B. Fischer and K. A. Bode (Eds.), 17th Internationale Baustofftagung (Vol. 1, pp. 413-418). Weimar, Germany: F.A. Finger-Institut für Baustoffkunde, Weimar.
5. Yu, Q.L., H.J.H. Brouwers and A.C.J. de Korte (2009). Gypsum hydration: a theoretical and experimental study. In H. B. Fischer and K. A. Bode (Eds.), 17th Internationale Baustofftagung (Vol. 1, pp. 783-788). Weimar, Germany: F.A. Finger-Institut für Baustoffkunde, Weimar.
6. Korte, A.C.J. de, and H.J.H. Brouwers (2009). Thermal conductivity of gypsum plasterboards; at ambient temperature and exposed to fire. In F. Wald, P. Kallerova, and J. Chloubka (Eds.), Proceedings of International Conference Applications of Structural Fire Engineering (Vol. 1, pp. 158-163). Prague, Czech Republic: Czech Technical University, Prague, Czech Republic.
7. Korte, A.C.J. de, (2008). Hydration modelling of calcium sulphates. In R. Eligehausen and C. Gehlen (Eds.), 7th fib international PhD symposium in Civil Engineering. Stuttgart, Germany (vol. 8, pp. 3-13). Stuttgart, Germany: Universität Stuttgart. Available from: 2008 Universität Stuttgart, Germany
8. Korte, A.C.J. de, and H.J.H. Brouwers (2008). Contaminated soil concrete blocks. In M.C. Limbachiya & H.Y. Kew (Eds.), Excellence in concrete Construction through innovation, 9-10 September 2008, Kingston upon Thames, United Kingdom (pp. 107-118) London, UK: CRC Press Taylor & Francis group (ISBN 978-0-415-47592-1)
9. Korte, A.C.J. de, and H.J.H. Brouwers (2008). Hydration Modeling of Calcium Sulphates. In H. Al-Mattarneh, K.N. Mustapha and M.P. Nuruddin (Eds.), International Conference on Construction and Building Technology, ICCBT 2008, 16-20 June 2008, Kuala Lumpur, Malaysia (pp 433-444) (ISBN 978-967-305-152-6)

---

## Curriculum Vitea

Ariën de Korte was born in Wageningen, The Netherlands on January 22, 1983. He finished his primary and secondary school education in Zetten, the Netherlands. He started in 2001 a study Industrial Engineering and Management with as technical specialisation Construction Engineering and Management at the University of Twente in Enschede, The Netherlands. He received his degree (Ingenieur) in 2006 in the field of stabilization of contaminated soil by use of cement/calcium sulphate binders. Besides following courses at the University of Twente, he also followed some courses and did some research on sport physics at the VU University Amsterdam, The Netherlands.

After his study, he became PhD student in January 2007 under supervision of prof.dr.ir. H.J.H. Brouwers. His research involves the application of cellular automata models for packing, hydration and fire studies. His research on hydration and fire behaviour of gypsum plasterboards was funded by the EU-funded project 'the Integrated Safe and Smart Build concept' (acronym I-SSB). Besides this PhD thesis, the current research has lead to this seven original journal articles and several conference papers.

In his leisure time he likes practicing sports such as cycling and swimming. Furthermore he is part of the team of electronic timing of the Stichting Elektronische Tijdwaarneming Wedstrijdzwemmen Gelderland and freelance operator for Ares21-timing devices at VdH Leerdam.



**Bouwstenen** is een publikatiereeks van de Faculteit Bouwkunde, Technische Universiteit Eindhoven. Zij presenteert resultaten van onderzoek en andere activiteiten op het vakgebied der Bouwkunde, uitgevoerd in het kader van deze Faculteit.

**Bouwstenen** zijn telefonisch te bestellen op nummer  
040 - 2472383

Kernredactie  
MTOZ

Reeds verschenen in de serie

## **Bouwstenen**

nr 1

### **Elan: A Computer Model for Building Energy Design: Theory and Validation**

Martin H. de Wit

H.H. Driessen

R.M.M. van der Velden

nr 2

### **Kwaliteit, Keuzevrijheid en Kosten: Evaluatie van Experiment Klarendal, Arnhem**

J. Smeets

C. le Nobel

M. Broos

J. Frenken

A. v.d. Sanden

nr 3

### **Crooswijk: Van 'Bijzonder' naar 'Gewoon'**

Vincent Smit

Kees Noort

nr 4

### **Staal in de Woningbouw**

Edwin J.F. Delsing

nr 5

### **Mathematical Theory of Stressed Skin Action in Profiled Sheeting with Various Edge Conditions**

Andre W.A.M.J. van den Bogaard

nr 6

### **Hoe Berekenbaar en Betrouwbaar is de Coëfficiënt $k$ in $x$ -ksigma en $x$ -ks?**

K.B. Lub

A.J. Bosch

nr 7

### **Het Typologisch Gereedschap: Een Verkennende Studie Omtrent Typologie en Omtrent de Aanpak van Typologisch Onderzoek**

J.H. Luiten

nr 8

### **Informatievoorziening en Beheerprocessen**

A. Nauta

Jos Smeets (red.)

Helga Fassbinder (projectleider)

Adrie Proveniers

J. v.d. Moosdijk

nr 9

### **Strukturering en Verwerking van Tijdgegevens voor de Uitvoering van Bouwwerken**

ir. W.F. Schaefer

P.A. Erkelens

nr 10

### **Stedebouw en de Vorming van een Speciale Wetenschap**

K. Doevendans

nr 11

### **Informatica en Ondersteuning van Ruimtelijke Besluitvorming**

G.G. van der Meulen

nr 12

### **Staal in de Woningbouw, Korrosie-Bescherming van de Begane Grondvloer**

Edwin J.F. Delsing

nr 13

### **Een Thermisch Model voor de Berekening van Staalplaatbetonvloeren onder Brandomstandigheden**

A.F. Hamerlinck

nr 14

### **De Wijkgedachte in Nederland: Gemeenschapsstreven in een Stedebouwkundige Context**

K. Doevendans

R. Stolzenburg

nr 15

### **Diaphragm Effect of Trapezoidally Profiled Steel Sheets: Experimental Research into the Influence of Force Application**

Andre W.A.M.J. van den Bogaard

nr 16

### **Versterken met Spuit-Ferrocement: Het Mechanische Gedrag van met Spuit-Ferrocement Versterkte Gewapend Betonbalken**

K.B. Lubir

M.C.G. van Wanroy

nr 17

**De Tractaten van  
Jean Nicolas Louis Durand**  
G. van Zeyl

nr 18

**Wonen onder een Plat Dak:  
Drie Opstellen over Enkele  
Vooronderstellingen van de  
Stedebouw**  
K. Doevendans

nr 19

**Supporting Decision Making Processes:  
A Graphical and Interactive Analysis of  
Multivariate Data**  
W. Adams

nr 20

**Self-Help Building Productivity:  
A Method for Improving House Building  
by Low-Income Groups Applied to Kenya  
1990-2000**  
P. A. Erkelens

nr 21

**De Verdeling van Woningen:  
Een Kwestie van Onderhandelen**  
Vincent Smit

nr 22

**Flexibiliteit en Kosten in het Ontwerpproces:  
Een Besluitvormingondersteunend Model**  
M. Prins

nr 23

**Spontane Nederzettingen Begeleid:  
Voorwaarden en Criteria in Sri Lanka**  
Po Hin Thung

nr 24

**Fundamentals of the Design of  
Bamboo Structures**  
Oscar Arce-Villalobos

nr 25

**Concepten van de Bouwkunde**  
M.F.Th. Bax (red.)  
H.M.G.J. Trum (red.)

nr 26

**Meaning of the Site**  
Xiaodong Li

nr 27

**Het Woonmilieu op Begrip Gebracht:  
Een Speurtocht naar de Betekenis van het  
Begrip 'Woonmilieu'**  
Jaap Ketelaar

nr 28

**Urban Environment in Developing Countries**  
editors: Peter A. Erkelens  
George G. van der Meulen (red.)

nr 29

**Stategische Plannen voor de Stad:  
Onderzoek en Planning in Drie Steden**  
prof.dr. H. Fassbinder (red.)  
H. Rikhof (red.)

nr 30

**Stedebouwkunde en Stadsbestuur**  
Piet Beekman

nr 31

**De Architectuur van Djenné:  
Een Onderzoek naar de Historische Stad**  
P.C.M. Maas

nr 32

**Conjoint Experiments and Retail Planning**  
Harmen Oppewal

nr 33

**Strukturformen Indonesischer Bautechnik:  
Entwicklung Methodischer Grundlagen  
für eine 'Konstruktive Pattern Language'  
in Indonesien**  
Heinz Frick arch. SIA

nr 34

**Styles of Architectural Designing:  
Empirical Research on Working Styles  
and Personality Dispositions**  
Anton P.M. van Bakel

nr 35

**Conjoint Choice Models for Urban  
Tourism Planning and Marketing**  
Benedict Dellaert

nr 36

**Stedelijke Planvorming als Co-Productie**  
Helga Fassbinder (red.)

nr 37

**Design Research in the Netherlands**

editors: R.M. Oxman  
M.F.Th. Bax  
H.H. Achten

nr 38

**Communication in the Building Industry**

Bauke de Vries

nr 39

**Optimaal Dimensioneren van  
Gelaste Plaatliggers**

J.B.W. Stark  
F. van Pelt  
L.F.M. van Gorp  
B.W.E.M. van Hove

nr 40

**Huisvesting en Overwinning van Armoede**

P.H. Thung  
P. Beekman (red.)

nr 41

**Urban Habitat:  
The Environment of Tomorrow**

George G. van der Meulen  
Peter A. Erkelens

nr 42

**A Typology of Joints**

John C.M. Olie

nr 43

**Modeling Constraints-Based Choices  
for Leisure Mobility Planning**

Marcus P. Stemerding

nr 44

**Activity-Based Travel Demand Modeling**

Dick Ettema

nr 45

**Wind-Induced Pressure Fluctuations  
on Building Facades**

Chris Geurts

nr 46

**Generic Representations**

Henri Achten

nr 47

**Johann Santini Aichel:  
Architectuur en Ambiguiteit**

Dirk De Meyer

nr 48

**Concrete Behaviour in Multiaxial  
Compression**

Erik van Geel

nr 49

**Modelling Site Selection**

Frank Witlox

nr 50

**Ecolemma Model**

Ferdinand Beetstra

nr 51

**Conjoint Approaches to Developing  
Activity-Based Models**

Donggen Wang

nr 52

**On the Effectiveness of Ventilation**

Ad Roos

nr 53

**Conjoint Modeling Approaches for  
Residential Group preferences**

Eric Molin

nr 54

**Modelling Architectural Design  
Information by Features**

Jos van Leeuwen

nr 55

**A Spatial Decision Support System for  
the Planning of Retail and Service Facilities**

Theo Arentze

nr 56

**Integrated Lighting System Assistant**

Ellie de Groot

nr 57

**Ontwepend Leren, Leren Ontwerpen**

J.T. Boekholt

nr 58

**Temporal Aspects of Theme Park Choice  
Behavior**

Astrid Kemperman

nr 59

**Ontwerp van een Geïndustrialiseerde  
Funderingswijze**

Faas Moonen

nr 60

**Merlin: A Decision Support System for Outdoor Leisure Planning**

Manon van Middelkoop

nr 61

**The Aura of Modernity**

Jos Bosman

nr 62

**Urban Form and Activity-Travel Patterns**

Daniëlle Snellen

nr 63

**Design Research in the Netherlands 2000**

Henri Achten

nr 64

**Computer Aided Dimensional Control in Building Construction**

Rui Wu

nr 65

**Beyond Sustainable Building**

editors: Peter A. Erkelens  
Sander de Jonge  
August A.M. van Vliet

co-editor: Ruth J.G. Verhagen

nr 66

**Das Globalrecyclingfähige Haus**

Hans Löfflad

nr 67

**Cool Schools for Hot Suburbs**

René J. Dierkx

nr 68

**A Bamboo Building Design Decision Support Tool**

Fitri Mardjono

nr 69

**Driving Rain on Building Envelopes**

Fabien van Mook

nr 70

**Heating Monumental Churches**

Henk Schellen

nr 71

**Van Woningverhuurder naar Aanbieder van Woongenot**

Patrick Dogge

nr 72

**Moisture Transfer Properties of Coated Gypsum**

Emile Goossens

nr 73

**Plybamboo Wall-Panels for Housing**

Guillermo E. González-Beltrán

nr 74

**The Future Site-Proceedings**

Ger Maas

Frans van Gassel

nr 75

**Radon transport in Autoclaved Aerated Concrete**

Michel van der Pal

nr 76

**The Reliability and Validity of Interactive Virtual Reality Computer Experiments**

Amy Tan

nr 77

**Measuring Housing Preferences Using Virtual Reality and Belief Networks**

Maciej A. Orzechowski

nr 78

**Computational Representations of Words and Associations in Architectural Design**

Nicole Segers

nr 79

**Measuring and Predicting Adaptation in Multidimensional Activity-Travel Patterns**

Chang-Hyeon Joh

nr 80

**Strategic Briefing**

Fayez Al Hassan

nr 81

**Well Being in Hospitals**

Simona Di Cicco

nr 82

**Solares Bauen: Implementierungs- und Umsetzungs-Aspekte in der Hochschulausbildung in Österreich**

Gerhard Schuster

nr 83

**Supporting Strategic Design of  
Workplace Environments with  
Case-Based Reasoning**

Shauna Mallory-Hill

nr 84

**ACCEL: A Tool for Supporting Concept  
Generation in the Early Design Phase**

Maxim Ivashkov

nr 85

**Brick-Mortar Interaction in Masonry  
under Compression**

Ad Vermeltfoort

nr 86

**Zelfredzaam Wonen**

Guus van Vliet

nr 87

**Een Ensemble met Grootstedelijke Allure**

Jos Bosman

Hans Schippers

nr 88

**On the Computation of Well-Structured  
Graphic Representations in Architectural  
Design**

Henri Achten

nr 89

**De Evolutie van een West-Afrikaanse  
Vernaculaire Architectuur**

Wolf Schijns

nr 90

**ROMBO Tactiek**

Christoph Maria Ravesloot

nr 91

**External Coupling between Building  
Energy Simulation and Computational  
Fluid Dynamics**

Ery Djunaedy

nr 92

**Design Research in the Netherlands 2005**

editors: Henri Achten

Kees Dorst

Pieter Jan Stappers

Bauke de Vries

nr 93

**Ein Modell zur Baulichen Transformation**

Jalil H. Saber Zaimian

nr 94

**Human Lighting Demands:  
Healthy Lighting in an Office Environment**

Myriam Aries

nr 95

**A Spatial Decision Support System for  
the Provision and Monitoring of Urban  
Greenspace**

Claudia Pelizaro

nr 96

**Leren Creëren**

Adri Proveniërs

nr 97

**Simlandscape**

Rob de Waard

nr 98

**Design Team Communication**

Ad den Otter

nr 99

**Humaan-Ecologisch  
Georiënteerde Woningbouw**

Juri Czabanowski

nr 100

**Hambase**

Martin de Wit

nr 101

**Sound Transmission through Pipe  
Systems and into Building Structures**

Susanne Bron-van der Jagt

nr 102

**Het Bouwkundig Contrapunt**

Jan Francis Boelen

nr 103

**A Framework for a Multi-Agent  
Planning Support System**

Dick Saarloos

nr 104

**Bracing Steel Frames with Calcium  
Silicate Element Walls**

Bright Mweene Ng'andu

nr 105

**Naar een Nieuwe Houtskeletbouw**

F.N.G. De Medts

nr 108

**Geborgenheid**

T.E.L. van Pinxteren

nr 109

**Modelling Strategic Behaviour in Anticipation of Congestion**

Qi Han

nr 110

**Reflecties op het Woondomein**

Fred Sanders

nr 111

**On Assessment of Wind Comfort by Sand Erosion**

Gábor Dezsö

nr 112

**Bench Heating in Monumental Churches**

Dionne Limpens-Neilen

nr 113

**RE. Architecture**

Ana Pereira Roders

nr 114

**Toward Applicable Green Architecture**

Usama El Fiky

nr 115

**Knowledge Representation under Inherent Uncertainty in a Multi-Agent System for Land Use Planning**

Liyang Ma

nr 116

**Integrated Heat Air and Moisture Modeling and Simulation**

Jos van Schijndel

nr 117

**Concrete Behaviour in Multiaxial Compression**

J.P.W. Bongers

nr 118

**The Image of the Urban Landscape**

Ana Moya Pellitero

nr 119

**The Self-Organizing City in Vietnam**

Stephanie Geertman

nr 120

**A Multi-Agent Planning Support System for Assessing Externalities of Urban Form Scenarios**

Rachel Katoshevski-Cavari

nr 121

**Den Schulbau Neu Denken, Fühlen und Wollen**

Urs Christian Maurer-Dietrich

nr 122

**Peter Eisenman Theories and Practices**

Bernhard Kormoss

nr 123

**User Simulation of Space Utilisation**

Vincent Tabak

nr 125

**In Search of a Complex System Model**

Oswald Devisch

nr 126

**Lighting at Work: Environmental Study of Direct Effects of Lighting Level and Spectrum on Psycho-Physiological Variables**

Grazyna Górnicka

nr 127

**Flanking Sound Transmission through Lightweight Framed Double Leaf Walls**

Stefan Schoenwald

nr 128

**Bounded Rationality and Spatio-Temporal Pedestrian Shopping Behavior**

Wei Zhu

nr 129

**Travel Information: Impact on Activity Travel Pattern**

Zhongwei Sun

nr 130

**Co-Simulation for Performance Prediction of Innovative Integrated Mechanical Energy Systems in Buildings**

Marija Trčka

nr 131

**Allemaal Winnen**

M.J. Bakker

nr 132

**Architectural Cue Model in Evacuation Simulation for Underground Space Design**  
Chengyu Sun

nr 133

**Uncertainty and Sensitivity Analysis in Building Performance Simulation for Decision Support and Design Optimization**  
Christina Hopfe

nr 134

**Facilitating Distributed Collaboration in the AEC/FM Sector Using Semantic Web Technologies**  
Jacob Beetz

nr 135

**Circumferentially Adhesive Bonded Glass Panes for Bracing Steel Frame in Façades**  
Edwin Huvener

nr 136

**Influence of Temperature on Concrete Beams Strengthened in Flexure with CFRP**  
Ernst-Lucas Klamer

nr 137

**Sturen op Klantwaarde**  
Jos Smeets

nr 139

**Lateral Behavior of Steel Frames with Discretely Connected Precast Concrete Infill Panels**  
Paul Teewen

nr 140

**Integral Design Method in the Context of Sustainable Building Design**  
Perica Savanović

nr 141

**Household Activity-Travel Behavior: Implementation of Within-Household Interactions**  
Renni Anggraini

nr 142

**Design Research in the Netherlands 2010**  
Henri Achten

nr 143

**Modelling Life Trajectories and Transport Mode Choice Using Bayesian Belief Networks**  
Marloes Verhoeven

nr 144

**Assessing Construction Project Performance in Ghana**  
William Gyadu-Asiedu

nr 145

**Empowering Seniors through Domotic Homes**  
Masi Mohammadi

nr 146

**An Integral Design Concept for Ecological Self-Compacting Concrete**  
Martin Hunger

nr 147

**Governing Multi-Actor Decision Processes in Dutch Industrial Area Redevelopment**  
Erik Blokhuis

nr 148

**A Multifunctional Design Approach for Sustainable Concrete**  
Götz Hüsken

nr 149

**Quality Monitoring in Infrastructural Design-Build Projects**  
Ruben Favié

nr 150

**Assessment Matrix for Conservation of Valuable Timber Structures**  
Michael Abels

nr 151

**Co-simulation of Building Energy Simulation and Computational Fluid Dynamics for Whole-Building Heat, Air and Moisture Engineering**  
Mohammad Mirsadeghi

nr 152

**External Coupling of Building Energy Simulation and Building Element Heat, Air and Moisture Simulation**  
Daniel Cóstola

nr 153

**Adaptive Decision Making In  
Multi-Stakeholder Retail Planning**

Ingrid Janssen

nr 154

**Landscape Generator**

Kymo Slager

nr 155

**Constraint Specification in Architecture**

Remco Niemeijer

nr 156

**A Need-Based Approach to  
Dynamic Activity Generation**

Linda Nijland

nr 157

**Modeling Office Firm Dynamics in an  
Agent-Based Micro Simulation Framework**

Gustavo Garcia Manzato

nr 158

**Lightweight Floor System for  
Vibration Comfort**

Sander Zegers

nr 159

**Aanpasbaarheid van de Draagstructuur**

Roel Gijsbers

nr 160

**'Village in the City' in Guangzhou, China**

Yanliu Lin

nr 161

**Climate Risk Assessment in Museums**

Marco Martens

nr 162

**Social Activity-Travel Patterns**

Pauline van den Berg

nr 163

**Sound Concentration Caused by  
Curved Surfaces**

Martijn Vercaamen

nr 164

**Design of Environmentally Friendly  
Calcium Sulfate-Based Building Materials:  
Towards an Improved Indoor Air Quality**

Qingliang Yu

nr 165

**Beyond Uniform Thermal Comfort  
on the Effects of Non-Uniformity and  
Individual Physiology**

Lisje Schellen

nr 166

**Sustainable Residential Districts**

Gaby Abdalla

nr 167

**Towards a Performance Assessment  
Methodology using Computational  
Simulation for Air Distribution System  
Designs in Operating Rooms**

Mônica do Amaral Melhado

nr 168

**Strategic Decision Modeling in  
Brownfield Redevelopment**

Brano Glumac

nr 169

**Pamela: A Parking Analysis Model  
for Predicting Effects in Local Areas**

Peter van der Waerden

nr 170

**A Vision Driven Wayfinding Simulation-System  
Based on the Architectural Features Perceived  
in the Office Environment**

Qunli Chen

nr 171

**Measuring Mental Representations  
Underlying Activity-Travel Choices**

Oliver Horeni

nr 172

**Modelling the Effects of Social Networks  
on Activity and Travel Behaviour**

Nicole Ronald

nr 173

**Uncertainty Propagation and Sensitivity  
Analysis Techniques in Building Performance  
Simulation to Support Conceptual Building  
and System Design**

Christian Struck

nr 174

**Numerical Modeling of Micro-Scale  
Wind-Induced Pollutant Dispersion  
in the Built Environment**

Pierre Gousseau

nr 175

**Modeling Recreation Choices  
over the Family Lifecycle**

Anna Beatriz Grigolon

nr 176

**Experimental and Numerical Analysis of  
Mixing Ventilation at Laminar, Transitional  
and Turbulent Slot Reynolds Numbers**

Twan van Hooff

nr 177

**Collaborative Design Support:  
Workshops to Stimulate Interaction and  
Knowledge Exchange Between Practitioners**

Emile M.C.J. Quanjel

nr 178

**Future-Proof Platforms for Aging-in-Place**

Michiel Brink

nr 179

**Motivate:  
A Context-Aware Mobile Application for  
Physical Activity Promotion**

Yuzhong Lin

nr 180

**Experience the City:  
Analysis of Space-Time Behaviour and  
Spatial Learning**

Anastasia Moiseeva

nr 181

**Unbonded Post-Tensioned Shear Walls of  
Calcium Silicate Element Masonry**

Lex van der Meer

nr 182

**Construction and Demolition Waste  
Recycling into Innovative Building Materials  
for Sustainable Construction in Tanzania**

Mwita M. Sabai

nr 183

**Durability of Concrete  
with Emphasis on Chloride Migration**

Przemysław Spiesz

nr 184

**Computational Modeling of Urban  
Wind Flow and Natural Ventilation Potential  
of Buildings**

Rubina Ramponi

nr 185

**A Distributed Dynamic Simulation  
Mechanism for Buildings Automation  
and Control Systems**

Azzedine Yahiaoui

nr 186

**Modeling Cognitive Learning of Urban  
Networks in Daily Activity-Travel Behavior**

Şehnaz Cenani Durmazoğlu

nr 187

**Functionality and Adaptability of Design  
Solutions for Public Apartment Buildings  
in Ghana**

Stephen Agyefi-Mensah

nr 188

**A Construction Waste Generation Model  
for Developing Countries**

Lilliana Abarca-Guerrero

nr 189

**Synchronizing Networks:  
The Modeling of Supernetworks for  
Activity-Travel Behavior**

Feixiong Liao

nr 190

**Time and Money Allocation Decisions  
in Out-of-Home Leisure Activity Choices**

Gamze Zeynep Dane

nr 191

**How to Measure Added Value of CRE and  
Building Design**

Rianne Appel-Meulenbroek

nr 192

**Secondary Materials in Cement-Based  
Products:  
Treatment, Modeling and Environmental  
Interaction**

Miruna Florea

nr 193

**Concepts for the Robustness Improvement  
of Self-Compacting Concrete:**

**Effects of Admixtures and Mixture  
Components on the Rheology and Early  
Hydration at Varying Temperatures**

Wolfram Schmidt

nr 194

**Modelling and Simulation of Virtual Natural Lighting Solutions in Buildings**

Rizki A. Mangkuto

nr 195

**Nano-silica production at low temperatures from the dissolution of olivine – Synthesis, tailoring and modelling**

Alberto Lazaro Garcia

nr 196

**Building Energy Simulation Based Assessment of Industrial Halls for Design Support**

Bruno Lee

nr 197

**Computational Performance Prediction of the Potential of Hybrid Adaptable Thermal Storage Concepts for Lightweight Low-Energy Houses**

Pieter-Jan Hoes

nr 198

**Application of Nano-Silica in Concrete**

George Quercia Bianchi

nr 199

**Dynamics of Social Networks and Activity Travel Behaviour**

Fariya Sharmeen

nr 200

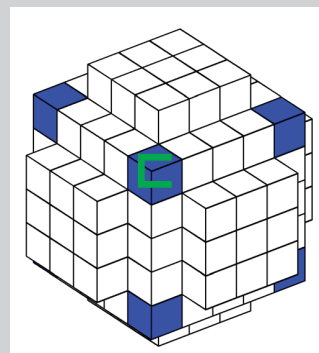
**Building Structural Design Generation and Optimisation including Spatial Modification**

Juan Manuel Davila Delgado

This thesis aims to extend existing insights on micro-structural development of cement / gypsum-based materials during hydration, usage and fire using cellular automata, experiments and mathematical models in order to further understand and optimize these cement/gypsum-based materials.

The main findings in this thesis are the following;

- Cellular automata systems can be applied for regular and random packing of digitized spheres.
- A hybrid model, combining chemical reaction controlled and diffusion controlled models has been successfully introduced and tested.
- CEMHYD3D has been successfully modified for multi-cycle and multi-scale modelling of ordinary Portland cement with a particle size distribution.
- Ultrasonic sound measurements can be applied for determining the hydration curve of calcium sulphate based materials.
- The thermal conductivity of gypsum plasterboard at room and elevated temperature can be modelled using a three-phase model.
- A combination of slag cement, calcium sulphate hemihydrate and quicklime can be applied for the stabilization and solidification of contaminated soil.



F

F

B

W

H

E

H

U

/ Department of the Built Environment

**TU** / **e**

Technische Universiteit  
**Eindhoven**  
University of Technology